Summer 8-2018

A Glacial History of Roberts Massif, Central Transantarctic Mountains, Antarctica, Using Cosmogenic 3He, 10Be, and 21Ne Surface Exposure Ages

Alexandra M. Balter
University of Maine, alexandra.balter@maine.edu

A GLACIAL HISTORY OF ROBERTS MASSIF, CENTRAL TRANSANTARCTIC MOUNTAINS, ANTARCTICA, USING COSMOGENIC ^{3}HE, ^{10}BE, AND ^{21}NE SURFACE EXPOSURE AGES

By

Alexandra Michelle Balter

B.S. Bates College, 2014

A THESIS

Submitted in Partial Fulfillment of the

Requirements for the Degree of

Master of Science

(in Earth and Climate Sciences)

The Graduate School

The University of Maine

August 2018

Advisory Committee:

Gordon R.M. Bromley, Adjunct Research Professor of Earth and Climate Sciences, Advisor

Brenda L. Hall, Professor of Earth and Climate Sciences, Advisor

George H. Denton, Professor of Earth and Climate Sciences

Aaron E. Putnam, Assistant Professor of Earth and Climate Sciences

Karl J. Kreutz, Professor of Earth and Climate Sciences

A GLACIAL HISTORY OF ROBERTS MASSIF, CENTRAL TRANSANTARCTIC MOUNTAINS, ANTARCTICA, USING COSMOGENIC ^{3}HE, ^{10}BE, AND ^{21}NE SURFACE EXPOSURE AGES

By Alexandra Michelle Balter

Thesis Advisors: Dr. Gordon R.M. Bromley

Dr. Brenda L. Hall

An Abstract of the Thesis Presented
in Partial Fulfillment of the Requirements for the
Degree of Master of Science
(in Earth and Climate Sciences)

August 2018

Ice-free areas at high elevation in the central Transantarctic Mountains preserve moraines and drift deposits that delineate the former thickness and extent of the East Antarctic Ice Sheet (EAIS); cosmogenic exposure ages on these features indicate when the ice sheet was as or more extensive than today. Approximately 30 existing cosmogenic-nuclide exposure ages from scattered locations within these deposits suggest that some moraines and drift sheets are at least 5 Ma old. Those ages imply that the age range of these deposits may span warm periods during the Miocene and Pliocene, during which the EAIS is hypothesized to have been much smaller than present and which constitute potentially important geologic analogues for future warm climates. Therefore, to evaluate the long-term stability of the ice sheet, I have obtained ^{3}He, ^{10}Be, and ^{21}Ne exposure ages from 150 glacially-transported clasts on distinct ice-marginal landforms at Roberts Massif at the head of Shackleton Glacier. The majority of these data comprise ^{3}He measurements

on pyroxene extracted from Ferrar dolerite clasts and prepared using a refined HF etching method that improves both measurement throughput and reproducibility. I address the common problem of scatter in exposure ages due to cosmogenic-nuclide inheritance by (i) measuring large numbers of exposure ages, including ~7 from each landform, and (ii) resampling and averaging approaches based on both statistical criteria and field observations of boulder characteristics and geomorphic context.

Moraines at Roberts Massif are openwork boulder belts characteristic of deposition by cold-based ice, which is consistent with present climate and glaciological conditions. Additionally, the lack of glaciofluvial deposits at Roberts Massif suggests that temperatures have not been sufficiently warm to induce surface melting of the ice at this location since at least the beginning of my glacial record. Apparent exposure ages at this site range from ~400 ka to 13 Ma, with individual moraine ages as old as ~8 Ma, which shows that these landforms record glacial events in the central Transantarctic Mountains since the mid-Miocene. I also use the $^{10}Be/^{21}Ne$ nuclide pair to constrain erosion rates of Beacon Sandstone boulders to <3.5 cm/Ma, a testament to the long-term stability of this landscape. My glacial chronology, combined with geomorphic mapping and calculated erosion rates, point to cold-based glaciation in the central Transantarctic Mountains since at least ~8 Ma and likely since ~15 Ma. Further, I show that the EAIS in this region was of similar thickness or thicker than present for long periods since ~15 Ma, including parts of the Pliocene and Miocene, indicating that temperature-precipitation feedbacks may be a major control for the long-term mass balance of the EAIS.

ACKNOWLEDGEMENTS

I am indebted to my advisors, Gordon Bromley and Brenda Hall, who have guided me through this project, instilling in me a passion for glacial geology through stimulating conversation and field experience. I am also grateful for the mentorship of Greg Balco, who hosted me at the Berkeley Geochronology Center, taught me about ^{3}He measurements, and who continues to help me understand and apply the fundamentals of cosmogenic dating. Thank you to my committee: George Denton, Aaron Putnam, and Karl Kreutz. For guidance and training in the lab, I thank Gordon Bromley, Brenda Hall, Peter Strand and Mary Yates. Thank you to Kaj Overturf for crushing dolerites, and to Jill Pelto and Mariah Radue for their help in the laboratory. Additionally, I would like to acknowledge Holly Thomas for her tireless and precise work on the samples from Upper Roberts, the ages for which I present in this thesis. I am grateful to Maggie Jackson for thought-provoking conversations and field wisdom. And of course, to my family, friends, and my wonderful partner Brian Kennedy, who keep things in perspective. My experience at Berkeley Geochronology Center was funded by the Geological Society of America and this project was funded by the National Science Foundation, grant number OPP-1443321.

TABLE OF CONTENTS

LIST OF TABLES

LIST OF FIGURES

CHAPTER 1

INTRODUCTION

Extensive drift deposits and well-preserved moraines in ice-free areas of the upper Transantarctic Mountains delineate the former thickness and extent of the East Antarctic Ice Sheet (EAIS); cosmogenic exposure ages for these features indicate when the ice sheet was as or more extensive than today. In this thesis, I present 150 ^{3}He, ^{21}Ne, and ^{10}Be cosmogenic exposure-age dates from moraine and drift boulders at Roberts Massif in the central Transantarctic Mountains (Figure 1.1). This glacial history records EAIS change for the past ~15 Ma and affords insight into EAIS stability under warmer-than-present climate conditions.

The Antarctic Ice Sheet exerts a major control on global sea level, with the marine-based West Antarctic Ice Sheet (WAIS) and the larger, land-based EAIS holding 5 m and 53 m sea-level rise equivalent, respectively (Fretwell et al., 2013). Yet, in the face of continued anthropogenic climate change, the resilience of Antarctica generally and the EAIS in particular to climate warming is poorly constrained: Will the EAIS retreat into sub-marine basins, resulting in destabilization and drawdown of large portions of the ice sheet? Or will temperature-precipitation feedbacks offset ice loss along the ice sheet's margins? Studies of modern EAIS mass-balance address these questions, and offer conflicting views whereby both increasing and decreasing mass-balance are suggested over the 20th century (e.g., Shepherd et al., 2012; Hanna et al., 2013; Zwally et al., 2015). A more complete understanding of the mechanisms controlling EAIS change in the face of climate warming can be gained from looking at the ice sheet's past variability.

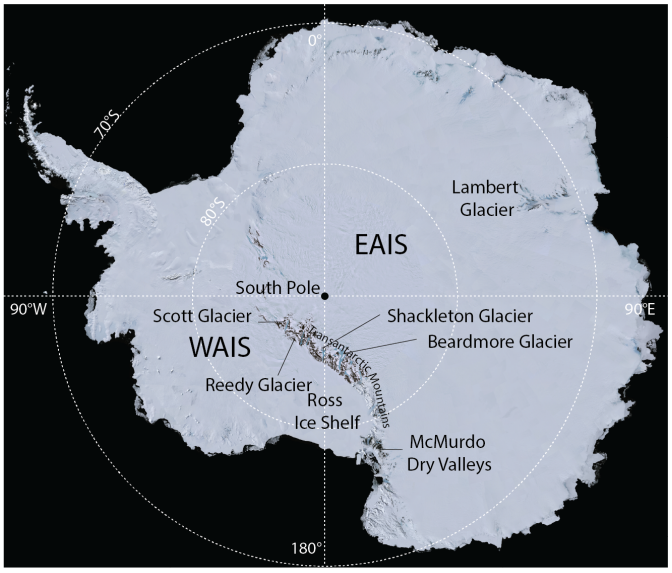

Figure 1.1 Map of Antarctica. Key places mentioned in text are labeled.

Constraints on EAIS variability over millions of years afford insight into ice sheet response to periods of warmer-than-present climate, such as the Pliocene (~5–3 Ma) and the Miocene (~23–5 Ma). Therefore, my thesis addresses two principal questions regarding the long-term behavior of the EAIS: 1) How stable has the EAIS been on a time scale of millions of years, including the Pliocene and Miocene periods? and 2) How long have current glaciological (cold-based) and environmental (polar desert) conditions persisted in the central Transantarctic Mountains? Ultimately, my results provide direct geologic constraint of ice sheet behavior in East Antarctica since the middle Miocene and provide much needed insight into the impact of warmer climate conditions on ice sheet stability.

1.1 EAIS Evolution: Insights and Conflicting Histories

The onset of Antarctic glaciation is marked by a pronounced increase in the benthic $\delta^{18}O$ of deep-sea sediment cores at the Eocene-Oligocene boundary at ~34 Ma (Shackleton and Kennett, 1976, 1975; Zachos et al., 1992). The inception of Antarctic glaciation therefore has

been linked to the tectonic opening of major Southern Ocean gateways and establishment of the Antarctic Circumpolar Current (Kennett, 1977; Scher et al., 2015). The resulting decrease in temperature and increase in precipitation provided conditions conducive for glaciation (Kennett, 1977). Furthermore, modeling studies suggest that declining concentrations of atmospheric CO_2 throughout the Cenozoic played a major role in initiating Antarctic cryosphere expansion (DeConto and Pollard, 2003).

During the ensuing ~20 Ma, the volume of the Antarctic ice sheets likely fluctuated on orbital timescales (Holbourn et al., 2005; Naish et al., 2001), with the EAIS grounding line positioned on the outer continental shelf by the middle Miocene at ~15–14 Ma despite warm Southern Ocean temperatures (Naish et al., 2001; Shevenell et al., 2008, 2004). Shevenell et al. (2008) highlight the crucial role that moisture flux to the Antarctic played in ice sheet expansion ~15 Ma, citing the further tectonic and oceanic isolation of Antarctica as major drivers of cryosphere evolution throughout the Cenozoic. Areal scouring and large-scale meltwater features in the Dry Valleys sector of Antarctica provide congruent terrestrial evidence of a large, overriding ice sheet during the Miocene (e.g., Denton and Sugden, 2005; Margerison et al., 2005).

A second key step in the establishment of the modern Antarctic Ice Sheet occurred ~14 Ma, when sea-surface temperatures cooled in both the southwest Pacific and the Southern Ocean by ~6–7°C and ~0–4°C, respectively (Shevenell et al., 2008, 2004). In the Olympus Range in the Dry Valleys sector of Antarctica, ash-bearing fossiliferous sediments record an ~8°C summertime temperature cooling, marked by changes in fossil assemblages, between 14.1

and 13.9 Ma (Lewis et al., 2008), a transition that might also signify a fundamental switch from wet- to cold-based glaciation in the Antarctic. Ashfall deposits in the Asgard Range, Dry Valleys, suggest this major climatic shift occurred between ~15 and 13.6 Ma (Marchant et al., 1993).

Although the transition to cold-based glaciation at ~14 Ma is well-supported by existing evidence, primarily from the Dry Valleys, the behavior of the EAIS since that time remains unclear. Several studies have argued for persistent polar desert conditions and ice sheet stability since the mid-Miocene (e.g., Sugden et al., 1993), while others contend that that the ice sheet was significantly smaller during the Mid-Pliocene Warm Period (~3.3–3.0 Ma) (e.g., Scherer et al., 2016). A key feature of the debate over EAIS resilience during the Pliocene is the age of the Sirius Group deposits, a series of clay-rich lodgement tills that were deposited by temperate ice and are found today at high altitudes throughout the Transantarctic Mountains (Mayewski, 1975; Mercer, 1972). Overlying the Sirius Group are extensive cold-based deposits, which represent deposition under the dry, polar conditions that typify the region today. The presence of Pliocene-aged diatoms in the Sirius Group, which were once argued to provide a maximum age for the deposits (e.g., Webb and Harwood, 1987), was later attributed to windblown deposition (Burckle and Potter, 1996; Kellogg and Kellogg, 1996). Nevertheless, Scherer et al. (2016) suggest that this mechanism of aeolian emplacement does not preclude a Pliocene age for the Sirius Group.

In contrast, cosmogenic exposure-age dating of boulders from Sirius Group lag deposits at Mt. Fleming, Mt. Feather, and Table Mountain in the Dry Valleys region, yield minimum age ranges for the Sirius Group of 2.9–4.8 Ma (Ivy-Ochs et al., 1995), 4.3 Ma (Brook et al., 1995), and > 6.5–10 Ma (Schaefer et al., 1999). Similarly, at the Dominion Range in the central Transantarctic Mountains, a cold-based moraine overlying Sirius Group deposits dates to 5.2 Ma

(Ackert and Kurz, 2004). These apparent exposure ages do not consider the effect of boulder erosion, which is estimated at 0–30 cm/Ma (Brook et al., 1995; Ivy-Ochs et al., 1995; Schaefer et al., 1999). If erosion *is* considered, Schaefer et al. (1999) concluded that the Sirius Group is > 15 Ma in age. Furthermore, previous expansions of the cold-based EAIS are recorded in Wright Valley, where $^{39}Ar/^{40}Ar$ dating of reworked basalt cobbles provides a limiting chronology, suggesting that the earliest event implied by the glacial record occurred > 3.6 Ma (Hall et al., 1993). Together, the majority of terrestrial-based studies indicate that the Sirius Group was certainly deposited prior to the Pliocene, and likely before the mid-Miocene.

Conflicting views on EAIS resilience during the Pliocene are also apparent in more distal records. For instance, far-field sea-level estimates, based on both geomorphic shoreline data and benthic $\delta^{18}O$ records, allow for EAIS retreat within uncertainty (Miller et al., 2012; Rovere et al., 2014). Conversely, when accounting for the higher $\delta^{18}O$ of Antarctic ice during the Pliocene, Winnick and Caves (2015) show that the EAIS likely did not contribute to Pliocene sea level. Furthermore, Cook et al. (2013) constrain the provenance of Pliocene-aged iceberg rafted debris in a sediment core off the coast of the Adélie Land to the Wilkes Subglacial Basin, a scenario that, the authors contend, would require considerable retreat of the EAIS into the basin during the Pliocene. However, that argument relies on an incomplete understanding both of subglacial geology (Ferraccioli et al., 2009) and basal ice conditions/erosional ice sheet regimes at the EAIS margins. Until recently, glaciological models could not simulate EAIS retreat during the Pliocene (Pollard and DeConto, 2009), and in fact showed EAIS expansion due to temperature-precipitation feedbacks in Antarctica (Huybrechts, 1993). In the past several years, however, updated models incorporating such processes as ice shelf hydrofracturing and the theoretical

failure of ice cliffs have simulated significant EAIS retreat into submarine basins under Pliocene conditions (Pollard et al., 2015).

In sum, direct geologic constraints of EAIS change over millions of years, although tantalizing, are severely limited and the questions regarding EAIS response to warmer climate conditions remain unanswered. My thesis adds to this discussion by providing an exhaustive glacial record from one ice-free massif in the central Transantarctic Mountains. While this record cannot denote times when the EAIS was smaller than today—information that is key for projecting future sea-level rise—it does indicate when the ice sheet was more extensive than present, thereby enabling me to evaluate long-term patterns of ice sheet stability.

1.2 Cosmogenic Exposure-Age Dating in Antarctica: Common Pitfalls

Although cosmogenic nuclides have been used to date surfaces in Antarctica since the early 1990s (e.g., Brook et al., 1993; Brown et al., 1991; Ivy-Ochs et al., 1995), refinement of these methods is ongoing. Therefore, another key component of my thesis addresses common pitfalls of the cosmogenic exposure-age dating method in Antarctica, including inherited nuclide inventories and moraine age scatter. If a glacial erratic was exposed to cosmogenic radiation prior to the most recent glacial transport (i.e., exposure on cliff face, reincorporated from older glacial drift), it will contain an "inherited" nuclide component that will make its apparent age older than the true age of deposition. Whereas in temperate regimes inherited nuclides typically are stripped from the boulder by glacial erosion, cold-based ice is minimally erosive and thus the potential for inheritance is much greater. Further, cold-based ice typically does not disturb underlying substrate during re-advance, meaning that thin drifts of younger boulders are often draped over older deposits.

These unique characteristics of cold-based ice pose a challenge for cosmogenic exposure-age dating, which relies on the assumption that a boulder has experienced a single period of exposure. In some moraine chronologies, boulders with inheritance are easy to reject as obvious outliers (e.g., Balco et al., 2002). However, in the Antarctic, moraines commonly exhibit a significant amount of scatter, potentially because: 1) the glacier has advanced to/over a moraine more than once throughout the landform's exposure history, depositing new boulders without disturbing the moraine; 2) boulders contain inherited nuclides, as they were recycled from previously exposed deposits; and/or 3) boulders derived from rock fall contain inherited nuclides remnant of exposure on the cliff face, which are not stripped during transport. To counter these limitations, I describe new boulder selection criteria for cold-based deposits and suggest collecting a large number of samples to better estimate the "true age" of each moraine.

1.3 Site Description

The Transantarctic Mountains form a 3000 km-long geographic barrier separating the EAIS from the WAIS, through which large outlet glaciers flow from the EAIS into the Ross Sea Embayment. My study site, Roberts Massif (86.374°S, 177.135°W), is a ~100 km^2 ice-free area located at the head of Shackleton Glacier in the central Transantarctic Mountains (Figure 1.2). Bounded to the south and east by the EAIS, to the north and west by the "headwaters" of Shackleton Glacier, and to the northeast by an unnamed spur of Zaneveld Glacier, the landscape at Roberts Massif is characterized by abundant moraine ridges that record periods during which

the surface of the EAIS was higher than today. Local bedrock at Roberts Massif is dominated by pyroxene-rich (Jurrasic) Ferrar dolerite and sandstones of the (Devonian-Triassic) Beacon Supergroup.

Throughout the massif, topography is defined by large normal faults, resulting in topographic relief of as much as ~1200 m below Misery Peak. These faults delineate a lower elevation platform, referred to here as Lower Roberts; a middle elevation platform, which I call Roberts Col; and the high peaks of Roberts Massif, including Misery Peak (2725 m) and Arena Peak (2700 m) (Figure 1.3). In the central portion of the massif, a complex of faults has incised tills of the Sirius Group to create a deep, back-tilted basin, which I call the Southern Basin (Hambrey et al., 2003) (Figure 1.3). With the exception of a 100 m-relief bedrock hill, which I will refer to as the Central Rise, and the Southern Basin, the Lower Roberts area exhibits

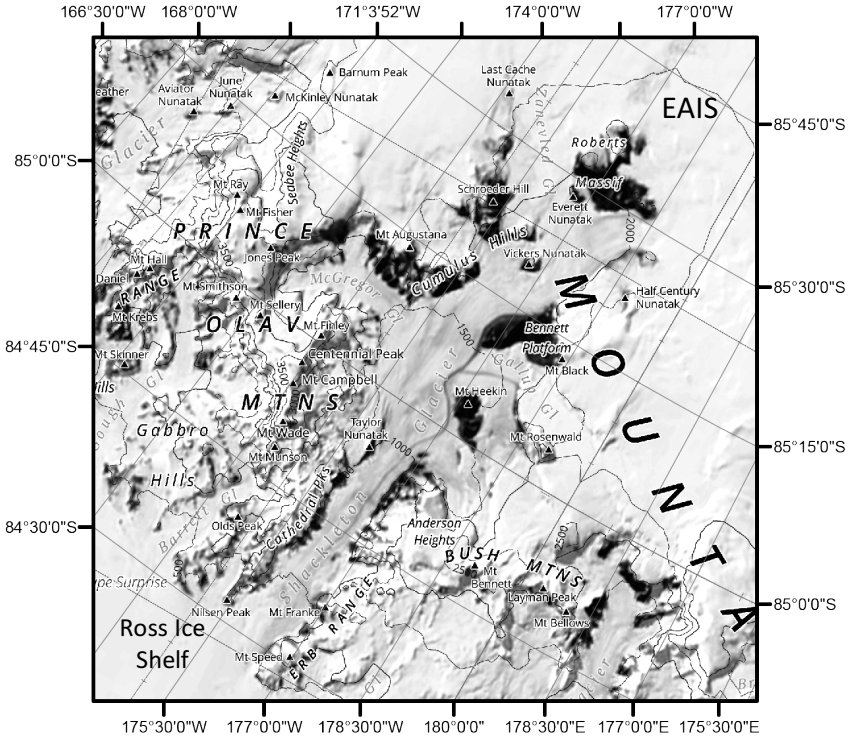

Figure 1.2 Location of Roberts Massif at the head of Shackleton Glacier. Also note the position of the massif at the edge of the EAIS.

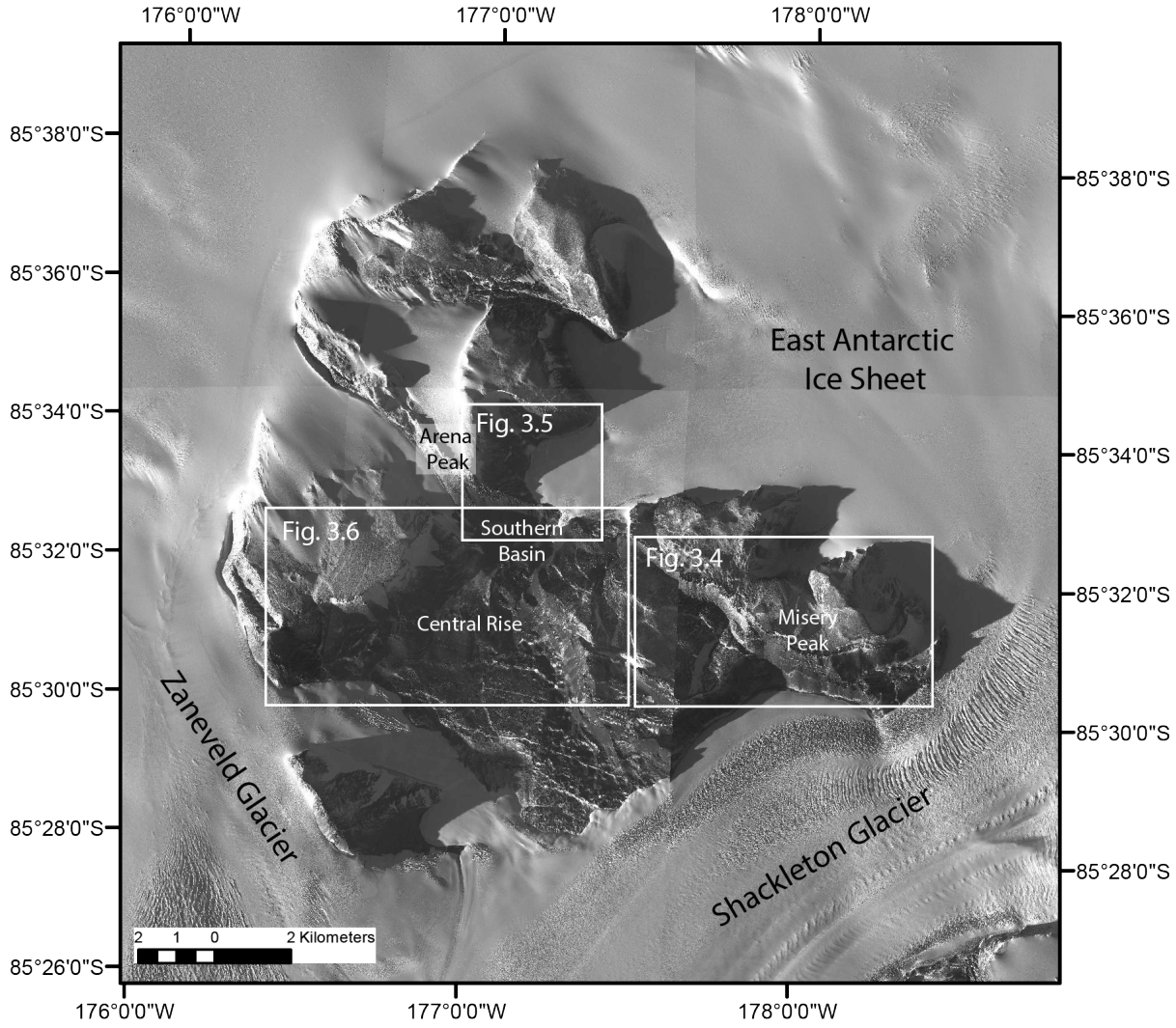

Figure 1.3 Map of Roberts Massif. Labels denote places commonly referred to throughout my thesis. The extent of Figure 3.4 denotes the Roberts Col area, the extent of Figure 3.5 shows the Upper Roberts location, and the location of Figure 3.6 is referred to as Lower Roberts.

relatively gentle topography (Figure 1.3). Smaller "*sackungen*" features, a result of gravitational spreading of the landscape following the removal of a glacial buttress, cut both the cold-based drift deposits and the Sirius Group, especially on the sides of the Central Rise, but do not cut any of the moraines themselves (Ackert and Kurz, 2004).

CHAPTER 2

METHODS

2.1 Fieldwork and Mapping

As part of a larger University of Maine-led investigation into ice sheet stability, I conducted fieldwork at Roberts Massif during the 2016–2017 Antarctic field season. Specifically, I mapped moraines, drift limits, and other geomorphic features using satellite imagery and ground-truthing. I then described the geomorphology and collected GPS locations and elevations of each moraine. Following the field season, I digitized the field maps using ArcGIS to create a glacial geomorphic map of Roberts Massif.

While geomorphic mapping illuminates the past configurations of the EAIS at Roberts Massif, a precise chronology for the moraines provides crucial information about when the ice sheet occupied each position. Therefore, I used cosmogenic helium-3 (^{3}He), neon-21 (^{21}Ne), and beryllium-10 (^{10}Be) surface-exposure dating of glacially transported boulders perched atop moraine crests to build a detailed chronology of past glacial change. The premise of this method is straightforward. A boulder transported within a glacier is shielded from incoming cosmogenic radiation. Upon deposition, the boulder is bombarded by cosmic radiation—primarily composed of high-energy neutrons—inducing nuclear reactions within the elements (i.e., aluminum, silicon) of pyroxene or quartz minerals. These reactions produce the rare isotopes ^{3}He in pyroxene, and ^{10}Be and ^{21}Ne in quartz. If both the production rate (in atoms/gram/year) and concentration of the cosmogenic isotope of interest are known, one can calculate the time elapsed since the glacier deposited the boulder. Recent improvements of exposure-age dating methods allow for the development of high-resolution chronologies with associated uncertainties of less than 2%.

To reduce the probability of sampling boulders with nuclide inheritance, I employed a refined approach to selecting boulders for cosmogenic surface exposure-age dating in the field. Previous studies highlight the need to distinguish between subglacial and supraglacial sources in Antarctica, as the latter is more likely to contain inherited nuclide inventories (e.g., Stone et al., 2003; Todd et al., 2010). Therefore, sampling teams typically select glacially molded clasts which may also exhibit glacial polish and striations, as these boulders show clear evidence of sub- or englacial transport. Instead, in this location where the morphology of the drifts and moraines suggest deposition by cold-based ice, I opted to sample the more angular, least weathered boulders on each moraine, operating under the assumption that significantly molded clasts were more likely to have been formed at a time when the ice sheet was more temperate than today, and therefore more erosive. If so, the glacially molded clasts might originally have been formed many millions of years ago and subsequently subjected to multiple periods of exposure, and thus would actually be more inheritance-prone. In addition to those updated selection criteria, I chose stable boulders that show no sign of having moved since deposition (i.e., perched atop other boulders, not broken), as post-depositional remobilization (e.g., rolling) will decrease the apparent age of the boulder.

After boulders were selected, I photographed, sketched, and described the characteristics of each one, and determined the degree of horizon shielding using a clinometer. I then collected ~500 g from the upper exposed surface of each boulder using either a hammer and chisel or by drilling holes and splitting the rock with shims and wedges. To establish precisely the elevation of each sampled boulder, I first set a Trimble differential GPS on the respective moraine crest to serve as a temporary base station. I then used two handheld altimeters to measure the elevation of each sample relative to the base station. Concurrently, I maintained a fixed base station at

camp, comprising a Trimble differential GPS and an altimeter, for the duration of the field season. Upon return to McMurdo Station, elevation data were corrected by UNAVCO for the variability recorded in the base station data set. Finally, I recorded coordinates for each sample using a handheld Garmin GPS.

2.2 Mineral Separation

All rock samples were sent to the University of Maine for mineral extraction and sample preparation. First, each sample was drawn, described, photographed, weighed and measured for thickness. Samples then were crushed, pulverized, and sieved to isolate the required size fraction: 125–250 μm for ^{3}He and 250–500 μm for both ^{21}Ne and ^{10}Be. For the ^{3}He method, crushed dolerites were boiled in 10% nitric acid for ~2 hours to remove metal oxides. Samples then underwent heavy-liquid treatment to isolate pyroxene from the bulk rock, followed by leaching in 5% hydrofluoric acid (HF) to 1) dissolve any groundmass adhering to the grains and 2) remove the outer few microns of each pyroxene grain, which typically contain higher concentrations of non-cosmogenic ^{4}He produced by U-Th decay (Blard and Farley, 2008; Bromley et al., 2014). Lastly, pyroxene grains underwent magnetic separation and hand picking to ensure separates were pure. Clean pyroxene separates were sent to Berkeley Geochronology Center in Berkeley, CA, for analysis by ^{3}He mass spectrometry (see Section 2.3). The above pyroxene separation methods are described in full in Appendix A.

For the ^{10}Be method, the 250–500 μm fraction of crushed sandstone was boiled in 6 M hydrochloric acid to remove iron oxides, after which each sample was etched in 5% HF for ~1 week to remove adhering groundmass. If quartz grains had remaining cement following HF leaching, they were boiled in 50% sodium hydroxide to remove amorphous silica, and then

placed back in 2% HF for another round of etching. Some samples underwent several rounds of treatment in NaOH and HF before they are deemed clean enough by visible inspection. Subsequently, their purity was checked via ICP-OES. Once the samples were sufficiently clean, I extracted beryllium in the University of Maine Cosmogenic Isotope Laboratory following established extraction protocols. Packed beryllium targets were submitted to the Center for Accelerator Mass Spectrometry at the Lawrence Livermore National Laboratory in Livermore, CA. I also sent aliquots of clean quartz to the Berkeley Geochronology Center for analysis by ^{21}Ne mass spectrometry.

2.3 Noble Gas Mass Spectrometry

All pyroxene separates were measured for ^{3}He on the Berkeley Geochronology Center "Ohio" system equipped with fully automated gas extraction and purification lines. First, ~25 mg aliquots of pure pyroxene separates were enclosed in tantalum packets, after which the packets were heated under vacuum using a 150w diode laser to extract the gases. The laser is equipped with a feedback control mechanism, monitored by a coaxial optical pyrometer, which maintains the prescribed laser temperature. Packets generally underwent two 15-minute heating steps at 1225°C and 1325°C to ensure full degassing of each sample. Gases released into the extraction line were purified by reaction with SAES getters and were frozen to activated charcoal at 12.5 K. Helium then was released into the MAP-215 noble gas mass spectrometer at 33 K, in which ^{4}He was measured on a Faraday cup and ^{3}He on a continuous dynode electron multiplier operated in pulse-counting mode.

Total helium sensitivity was quantified by peak height comparison with aliquots of custom-mixed helium gas standards containing between 1.57 x 10^{-18} and 4.71 x 10^{-16} mol ^{3}He and between 4.39 x 10^{-14} and 1.26 x 10^{-11} mol ^{4}He (Figure 2.1; sensitivity calculations are described in Appendix B). Concentrations of ^{3}He and ^{4}He in each standard were calculated with direct pressure measurements using Baratron capacitance manometers. Reported uncertainties for helium concentrations include error from counting statistics and reproducibility of gas standard analyses. Tantalum blank analyses showed negligible amounts of ^{3}He, thus I did not subtract blank concentrations. For a given ^{3}He measurement period, two to five aliquots of the CRONUS-P standard were measured. Means and standard deviations of the aliquots run during each distinct measurement period ranged from (4.97 ± 0.1) x 10^{9} atoms g^{-1} to (5.14 ± 0.1) x 10^{9} atoms g^{-1}. I used these data to derive correction factors to normalize all samples from each measurement period to the accepted CRONUS-P value of 5.02 atoms g^{-1} (Blard et al., 2015). Correction factors therefore ranged between 0.969 and 1.031.

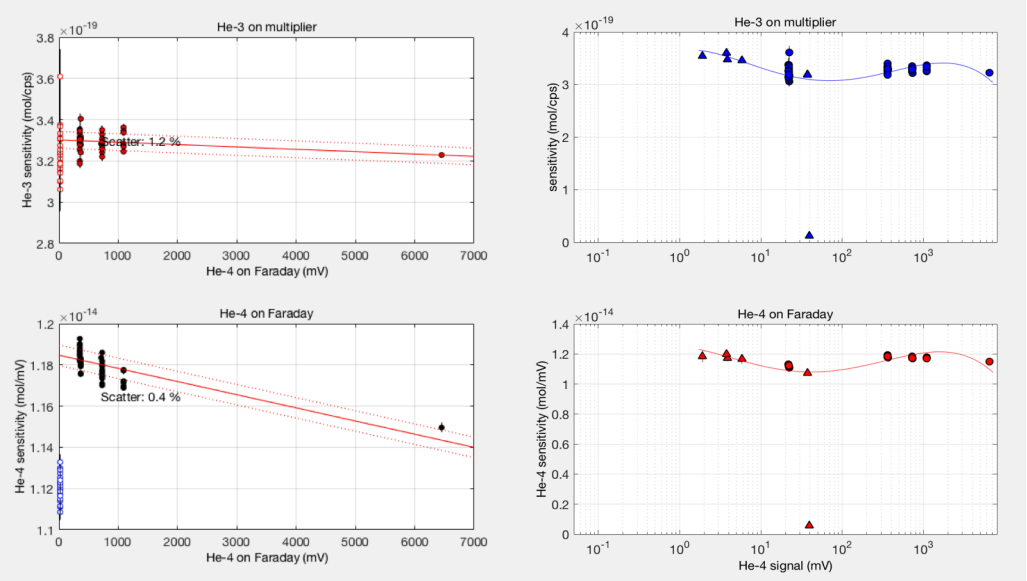

Figure 2.1 Noble gas mass spectrometer sensitivity plots. These graphs show concentrations of ^{3}He and ^{4}He in standards in mol/cps and mol/mV, respectively, during calibration of the BGC "Ohio" noble gas mass spectrometer in linear (left) and log (right) scales. These plots demonstrate that the calculated concentrations both of ^{3}He and ^{4}He are dependent on the amount of ^{4}He in each sample.

2.4 Error Propagation

In many of the samples, I measured helium and neon concentrations in multiple aliquots. With each concentration, I calculated the cosmogenic exposure-age and internal error of the aliquot using the CRONUS-Earth online exposure-age calculator (Balco et al., 2008). To test whether the resulting ages of each aliquot agreed within error, I performed a chi-squared test. For those populations which passed the chi-squared test with 95% confidence that the ages agreed within error, I took the error-weighted mean as the true age of the sample and the standard error as the uncertainty. For those populations that did not pass the chi-squared test, the true age of the sample was taken as the mean and the uncertainty as the standard deviation. Measurements of the CRONUS-P standard on the BGC Ohio noble gas mass spectrometer are replicable to ~2%, meaning that the absolute calibration uncertainty of Ohio is ~2%. If the calculated uncertainty of a sample (using either the standard error or the standard deviation) was < 2%, I took the uncertainty to be 2% of the sample age. A MATLAB script that determines the exposure-age and uncertainty from multiple aliquots is provided in Appendix E.

CHAPTER 3

GLACIAL GEOMORPHOLOGY

Well-preserved moraines and drift sheets exposed in ice-free areas of Roberts Massif provide evidence for past expansions of the EAIS and delineate previous ice sheet margins. Small (~1–2 m relief), openwork boulder moraines, along with an absence of glaciofluvial deposits throughout the massif, are indicative of deposition by cold-based ice (Atkins, 2013). At Roberts Massif, I identified two distinct drift types and 23 moraines, which are described below.

3.1 Principal Drift Units

3.1.1 Wet-Based Till

First identified by Mercer (1965), sediments associated with the so-called Sirius Group occur as erosional remnants of clay-rich tills located at high elevations (> ~2000 m) throughout the Transantarctic Mountains, and correspond to at least one period of past temperate glaciation. At Roberts Massif, where Sirius Group sediments have been described in detail by Hambrey et al. (2003), I observed outcrops of the deposits throughout Lower Roberts, and immediately below Roberts Col. These tills contain abundant striated, glacially molded cobbles and boulders that are imbricated in a semi-lithified gray clay matrix (Figure 3.1). The Sirius Group is exposed beneath overlying cold-based drifts (described below) both at post-depositional fault scarps and where the overlying drift has been removed by subsequent glacial scouring. At these exposures, a boulder lag often mantles the deposits. Importantly, all of the moraines at lower Roberts overlie, and are therefore stratigraphically younger than, the Sirius Group.

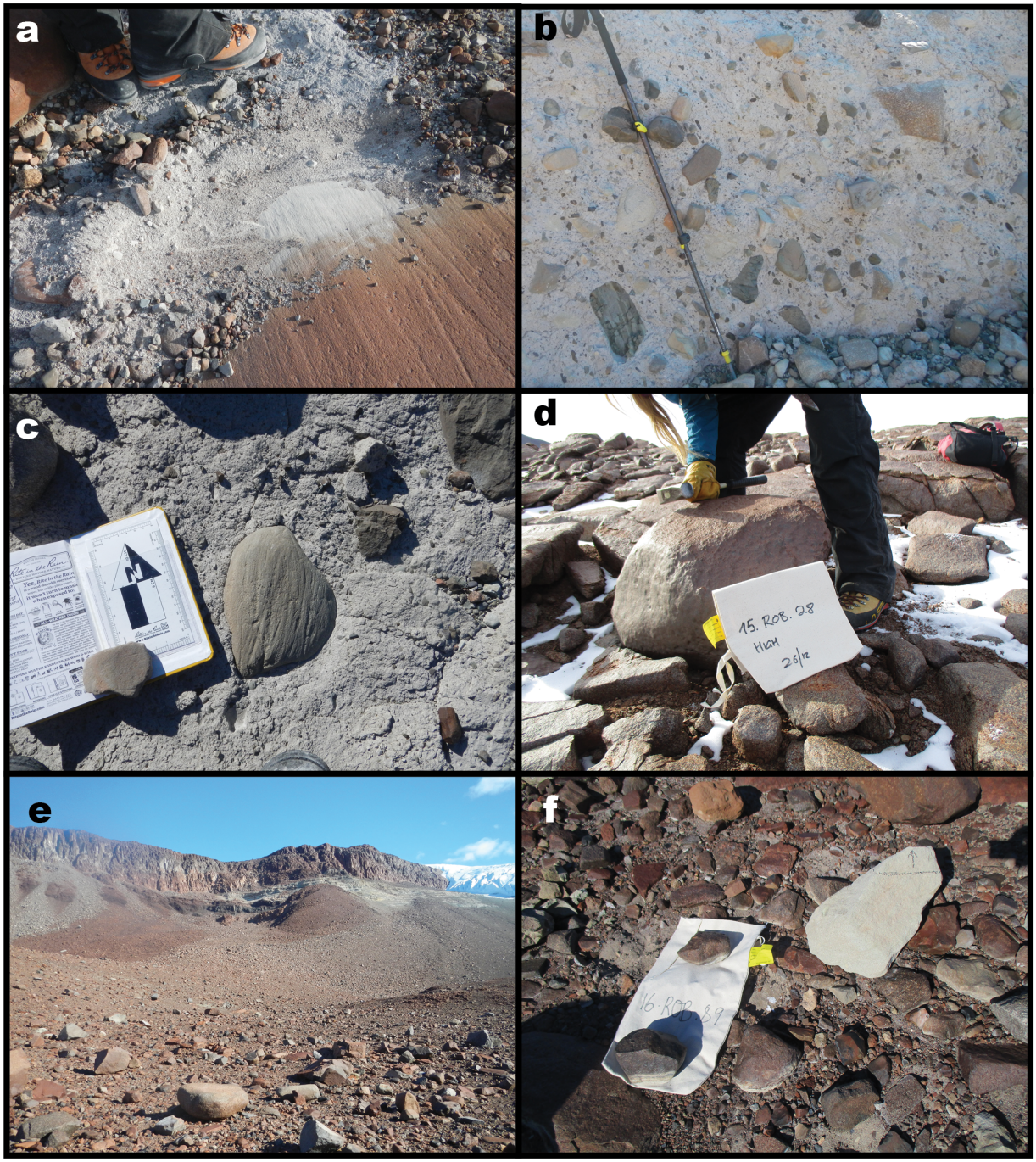

Figure 3.1 Photographs of drift units described at Roberts Massif. a) The gray, fine-grained Sirius Group deposits atop striated dolerite bedrock; b) Sirius Group exposed in section in the Southern Basin; c) Striated, glacially molded Sirius cobble embedded in a fine-grained matrix; d) Sample 15-ROB-028-COL of the Roberts Col drift, which yields the oldest apparent exposure age in the record; e) cold-based drift in the Southern Basin at Roberts Massif; f) freshly scoured sandstone clast likely deposited as a thin drift sheet atop older deposits during a Late Quaternary expansion of the EAIS.

Underlying the Sirius Group tills, glacially molded and polished dolerite bedrock exhibits abundant striae that indicate southeast-northwest flow during the overriding glacial event, corroborating the observations of Hambrey et al. (2003). Furthermore, the immaculate preservation of striae and glacial polish is a testament both to the resistance of the Ferrar Dolerite and the negligible long-term erosion rates at Roberts Massif.

3.1.2 Cold-Based Drifts

Cold-based ice, which characterizes much of East Antarctica today, is below the pressure melting point throughout and does not slide along the bed, meaning that it is minimally erosive (Drewry, 1986). In contrast to the wet-based tills described above, deposits associated with cold-based glaciation are typically thin, patchy, clast-supported drifts with little to no fine-grained material (Figure 3.1). Furthermore, clasts lack the striations, polish, and molding associated with erosive wet-based ice. Multiple such drifts comprising large, angular, red-stained dolerite boulders and occasional sandstones are widespread throughout Roberts Massif. Differential weathering among the boulders and the presence of reworked clasts from the underlying wet-based tills demonstrate the unique ability of cold-based ice to preserve older landscapes with each ice advance. Although each drift may include boulders of different depositional ages, the drift appears generally more weathered (i.e., redder, more wind-affected surfaces) with increasing distance from the modern glacier margin, suggesting a general increase in age (Figure 3.2). There is no evidence of flowing water, such as meltwater channels or outwash deposits (e.g., kame terraces, deltas, etc.), associated with the cold-based drifts throughout the massif. Had temperatures been warm enough to melt the surface of the ice sheet at any time since the

beginning of the glacial record, I would expect to see such meltwater features. The mapped and sampled moraines (described in detail below) are associated with these cold-based drifts and provide direct geologic constraints on the extent and timing of past expansions of the EAIS.

The youngest drift(s) at Roberts Massif, denoted by minimal weathering and fresh scuff marks [abrasions formed as cold-based ice drags entrained boulders across underlying surfaces (Atkins et al., 2002)], comprise a thin layer of debris that extends several tens of meters beyond the current ice margins (Figure 3.1). This drift occurs up to ~1810 m elevation on the northern edge of Lower Roberts and ~1750 m elevation on the southern edge, where the unit was deposited by the north-flowing ice tongue (Figure 3.2). Farther south at Upper Roberts, the fresh drift extends up to ~2165 m elevation, approximately 20 m above the modern ice margin, where it overlaps the lowest moraine on that hillside. Based on the its stratigraphy and appearance, I tentatively correlate this unit with the youngest deposits described at Reedy and Scott Glaciers, southern Transantarctic Mountains, which were attributed to the Last Glacial Maximum (Todd et al., 2010; Bromley et al., 2012). Notably, this younger drift is not typically associated with a moraine at Roberts Massif.

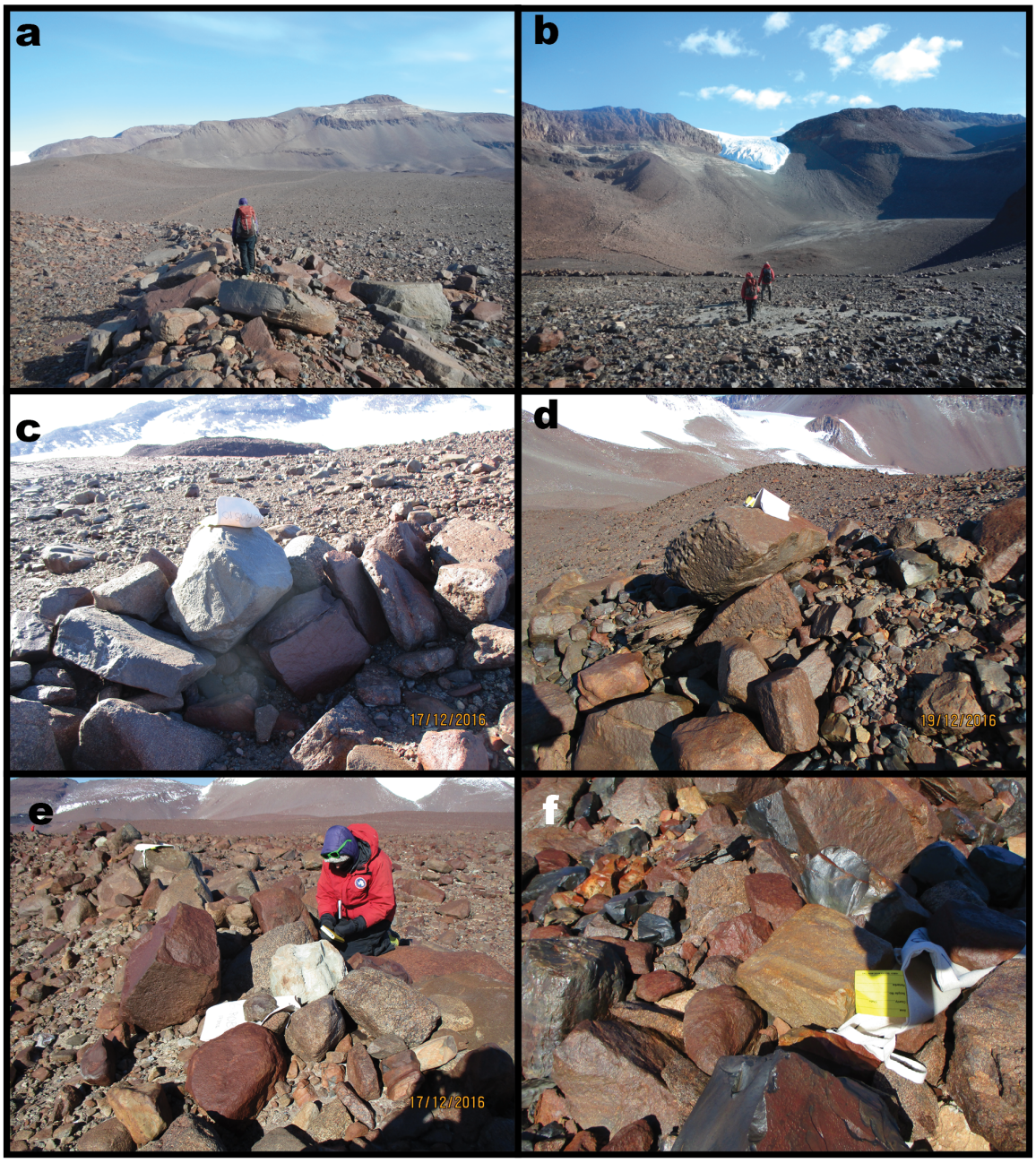

Figure 3.2 Photos of moraines and sampled boulders at Roberts Massif. a) AND moraine in the Lower Roberts area. Moraine is 1-2 m high and made up primarily of angular boulders; b) WIN, MON and MNM moraines mapped in the Southern Basin. The associated drifts appear more weathered farther from the ice tongue. Sirius Group deposits (gray) are also visible beneath the drift; c) Angular, perched dolerite boulder sampled on the NLO moraine; d) angular dolerite boulder perched atop the RIN moraine. It is clear that boulders on the RIN moraine, which is, stratigraphically, the oldest moraine at Lower Roberts, are significantly more weathered (i.e., redder, more pitting) than those on NLO. e) example of a sampled sandstone boulder on the NLO moraine, which appears fresher in color compared to the sampled sandstone on RIN (f).

3.2 Moraines

The primary focus of my thesis is those moraines associated with the cold-based drift deposits at Roberts Massif, 23 of which I mapped and sampled for cosmogenic exposure-age dating. Moraines are typically 1–2 m high and made up primarily of angular dolerite boulders (Figure 3.2). Sandstone boulders also occur on several moraines but, due to their less resistant nature, they exhibit clear signs of surface erosion, such as pitting and exfoliation. All moraines investigated for my thesis were deposited directly by the EAIS, which flowed into Roberts Massif from both the north and south. The morphology and bouldery nature of the moraines, as well as the absence of meltwater features described above, indicates deposition by cold-based ice (Atkins, 2013). To describe this chronology, I have divided Roberts Massif into three sub-sites: Roberts Col, Upper Roberts, and Lower Roberts.

3.2.1 Roberts Col

The Misery moraines are located on a gently sloping plateau ~1 km east of the Roberts Col, where they form a series of concentric terminal moraines at the base of the 450 m-high north-facing escarpment of Misery Peak (2725 m) (Figure 3.3; Figure 3.4). This complex was deposited by a north-flowing tongue of the EAIS that crossed the lower slopes on the southern side of Misery Peak before cascading down the escarpment, and represents a period when the ice sheet surface was at least 450 m higher than today. These moraines overlie a thin drift of primarily angular boulders which extends beyond the moraine complex to Roberts Col and represents a period of earlier, more extensive glaciation. In descending stratigraphic order, I analyzed samples collected from the following units below Misery Peak: Roberts Col Drift

Figure 3.3 Photos of the Misery Moraines. a) Misery B moraine at the Roberts Col site. Although the Misery moraines comprise primarily boulders, some smaller cobbles are present and the moraines are slightly larger (~2-5 m) than moraines elsewhere at Roberts. b) Example of a boulder sampled on the Misery C moraine. Like most boulders at Roberts Col, this exhibits deep red staining and significant pitting compared to the boulders at Lower and Upper Roberts.

(underlying deposit), Misery D (outer moraine), Misery A, Misery B, and Misery C (inner moraine) (Figure 3.4). The Misery B moraine cross-cuts, and therefore post-dates, the Misery A moraine, demonstrating clear stratigraphic succession.

Compared to other moraines at Roberts Massif, the Misery moraines are relatively large landforms, exhibiting ~2–5 m of relief and comprising a large proportion of smaller boulders and cobbles in addition to large boulders. In both appearance and position, the Misery moraines are similar to the Reedy E deposits at Reedy Glacier, southern Transantarctic Mountains, which represent the earliest preserved record of ice thickening conformable with the present landscape at that site (Bromley et al., 2010). The dolerite boulders perched atop the Misery moraines display a deep-red weathering rind and are considerably more ventifacted than boulders on the lower, younger moraines.

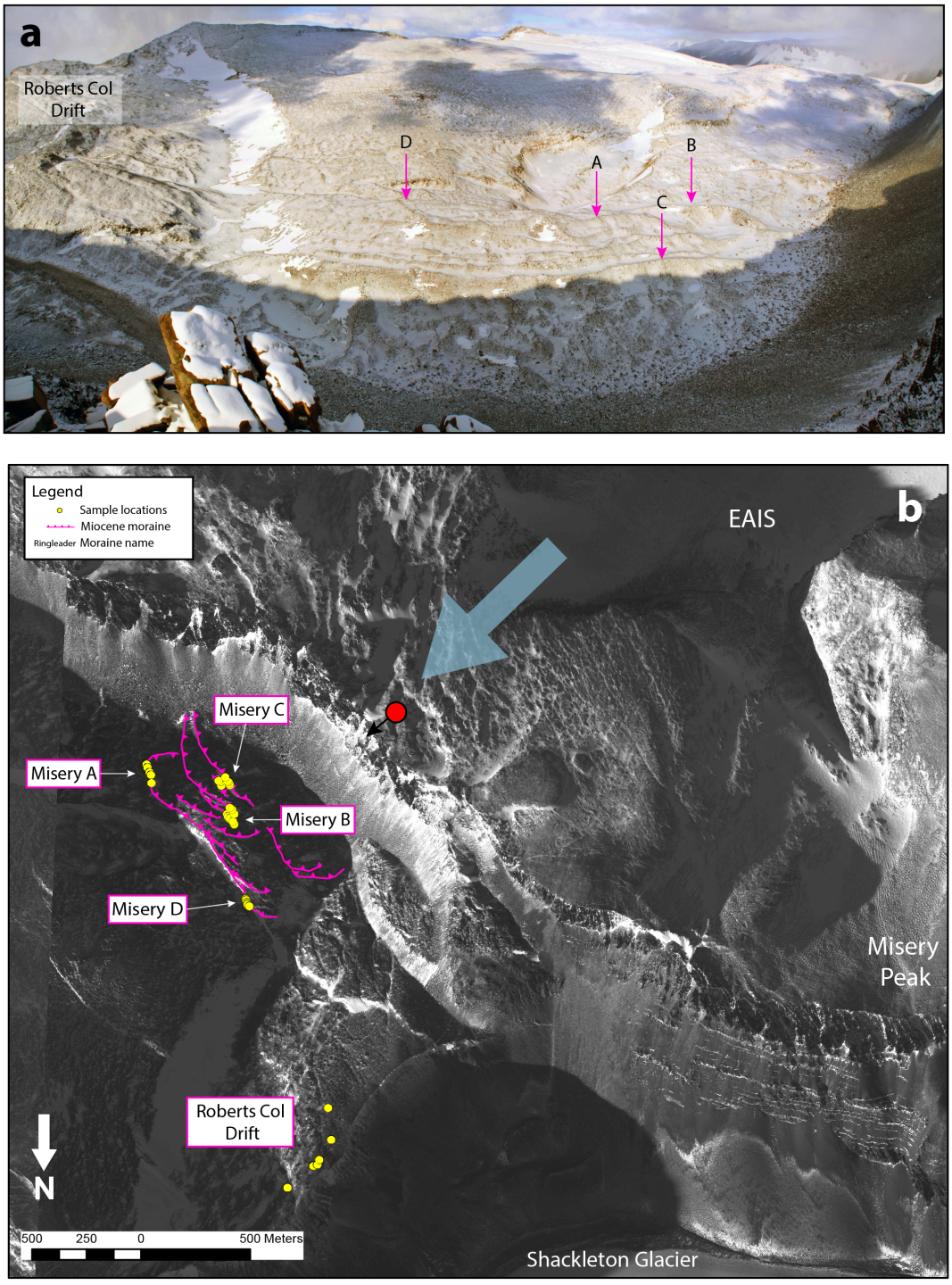

Figure 3.4 Map of Roberts Col. a) Photo of the Roberts Col area. Pink arrows point to the sampled Misery Moraines and are labelled with the corresponding moraine letter. The location of the Roberts Col drift is also labeled. The photo was taken from the location of the red circle in (b) looking in the direction of the black arrow (vantage to the northeast). b) Simple geomorphic map of the Roberts Col area. The Roberts Drift mantles the bedrock outboard of the Misery moraines. The blue arrow denotes the direction of ice flow when the Misery Moraines were deposited.

3.2.2 Upper Roberts

A vertical transect of moraines at Upper Roberts were deposited directly by a north-flowing lobe of the EAIS on a steep west-facing slope, between approximately 60 m and 150 m above the modern ice surface. In descending stratigraphic order, I mapped and analyzed samples collected from the following moraines: Arena, Eine, Kleine, Nacht, Musik (informal names) (Figure 3.5). While additional moraines exist both above and below the Arena moraine, representing more extensive glaciation beyond the Arena and Eine moraines, respectively, those landforms were deemed unsuitable for cosmogenic exposure-age dating due to the high slope angle and unstable nature of the hillside.

3.2.3 Lower Roberts

The distribution of relict moraines indicates that the modern ice-flow pattern, where the EAIS flows into Lower Roberts from both the north and south, existed during past periods when the EAIS was more extensive than today (Figure 3.6). During the most extensive glaciation recorded at this site, north- and south-flowing ice converged near the Central Rise, depositing the Ringleader moraine (stratigraphically, the oldest moraine in the Lower Roberts sequence), which encircles the hill's summit. Furthermore, drift is present between the two ridges of Ringleader, suggesting that the EAIS was, at some time prior to the deposition of Ringleader, continuous across the lower Roberts area and at least ~260 m higher than the modern ice surface to the north. Based purely on relative weathering, it appears that moraines are progressively younger with increasing proximity to both ice margins.

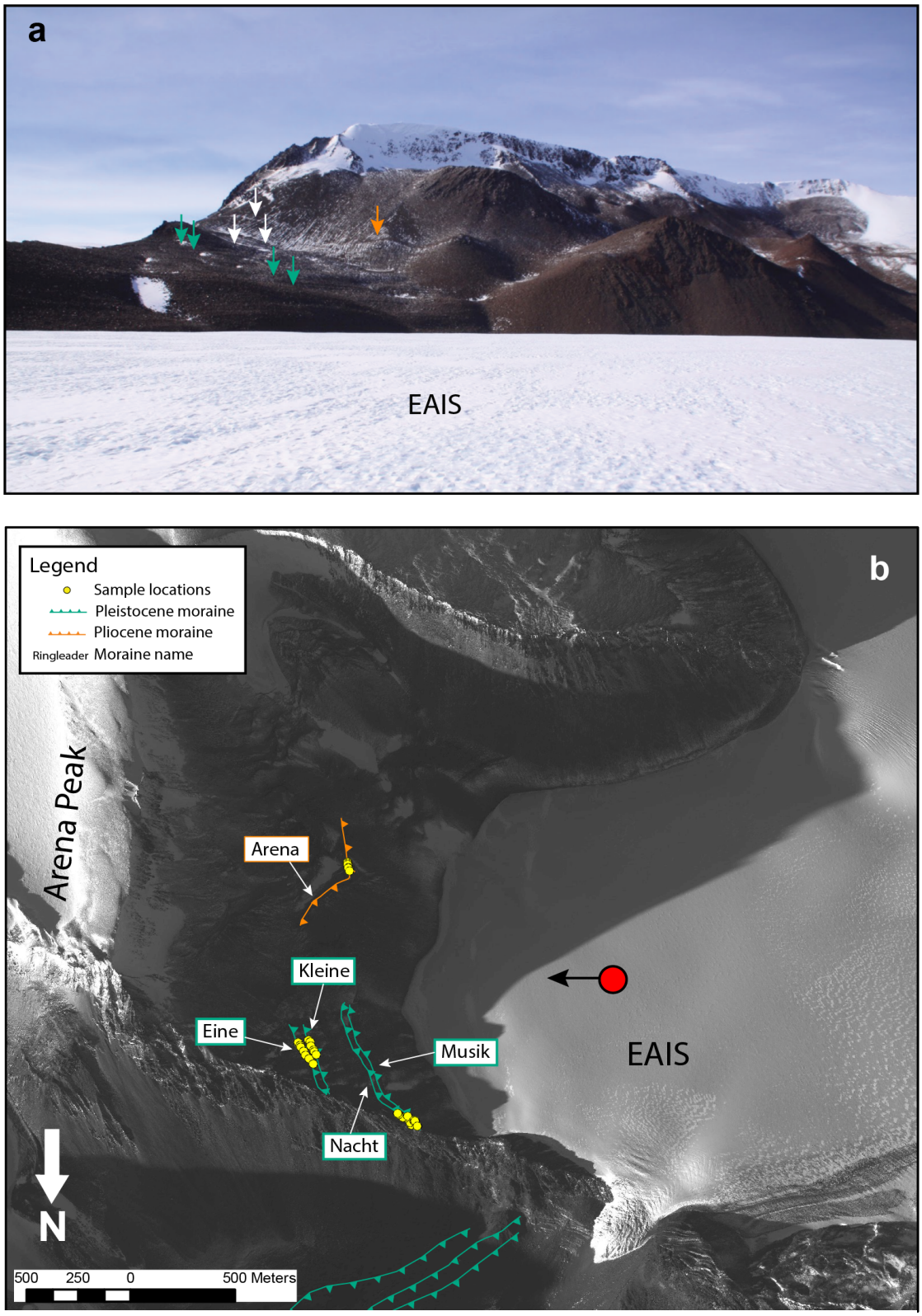

Figure 3.5 Map of Upper Roberts. a) Photo of the Upper Roberts transect with moraines marked by arrows colored by age as indicated in the legend in (b), while white arrows denote undated moraines visible in the photo. b) geomorphic map of Upper Roberts. The red circle and arrow shows the location and vantage of the photo in (a).

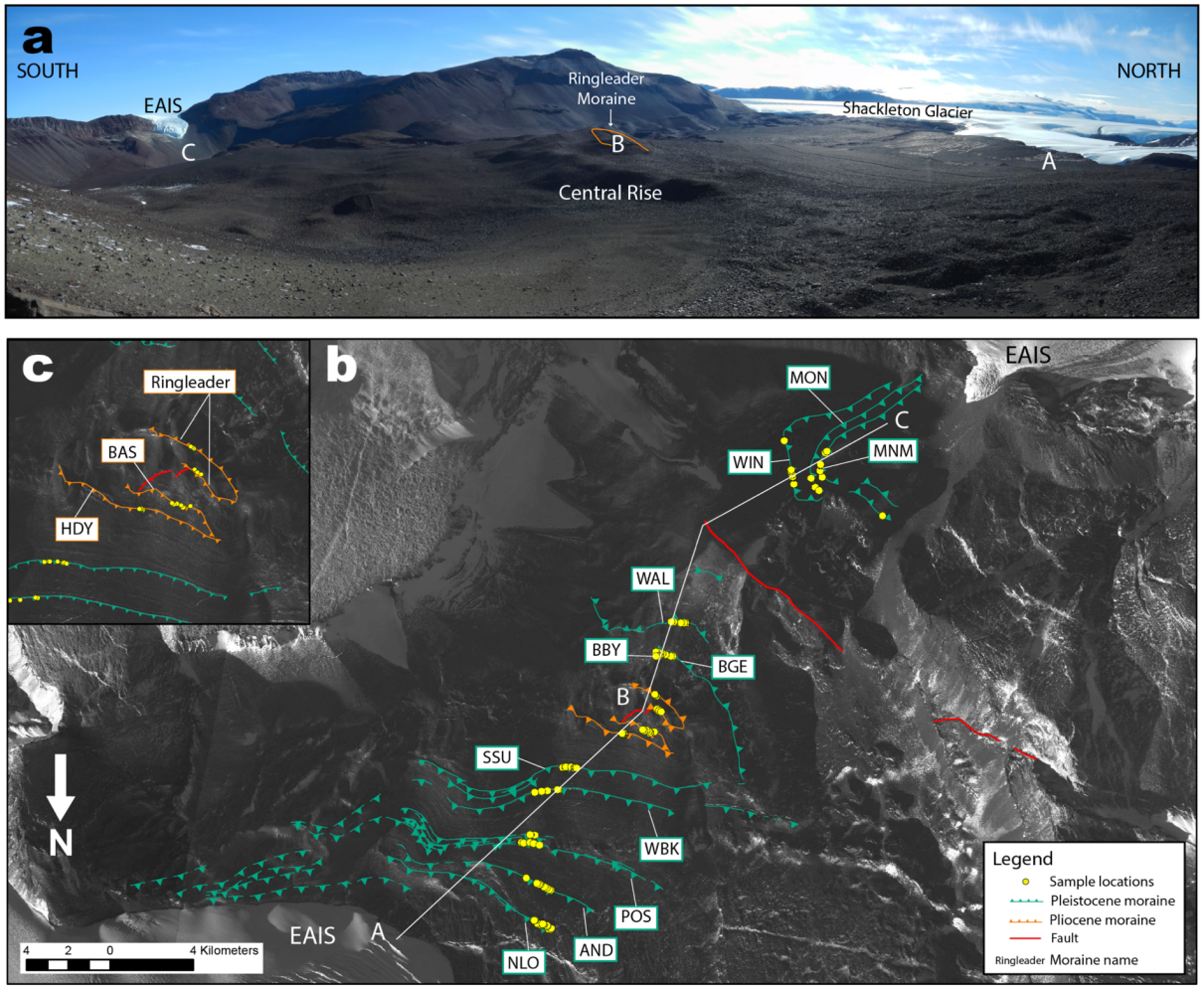

Figure 3.6 Map of Lower Roberts. a) Photo of the Lower Roberts area, with key places labeled. Letters A, B, and C correspond to transect positions in (b). b) Glacial geomorphic map of Lower Roberts. Moraine names are shown in boxes. Moraines on the Central Rise are not labeled in (b), but shown in larger scale in (c). The Lower Roberts northern transect extends from points A to B, while the Lower Roberts southern transect follows point B to C.

Viewed in descending stratigraphic order from the summit of the Central Rise northward, I sampled the following moraines: BAS, HDY, SSU, WBK, POS, AND, and NLO/NLI (moraine initials correspond to informal names and sample ID suffixes listed in the ICE-D Antarctica online database). Both the BAS and HDY moraines, which are located on the north-facing slope of the Central rise, can be traced westward to where they join similar landforms sloping from the south, thus representing the former confluence of separate ice masses. Both moraines become diffuse to the east and are poorly preserved on the south side of the bedrock rise, although discontinuous segments can be seen in the satellite imagery. Continuing north towards the modern glacier, the moraines are nearly identical in their size and morphology, comprising boulder ridges as much as 2 m in relief. Notably, the POS moraines constitute a complex of three main ridges and multiple isolated moraine ridge segments, which, based on relative weathering and position, were likely deposited during the same glacial event. Similarly, two ridges comprise the NLO/NLI moraines, the stratigraphically youngest moraines in the northern part of the massif.

In descending stratigraphic order, the moraines located south of the bedrock rise and descending into the southern basin include: BBY, BGE, WAL, WIN, MON, and MNM. These moraines are similar in appearance and morphology to those described on the northern side of the Central Rise. The BBY moraine is a short, diffuse moraine segment that may be associated with the more continuous BGE moraine. I also observed a moraine between WAL and WIN (stratigraphically, the oldest moraine in the Southern Basin) in the satellite imagery, but was unable to find a prominent ridge on the ground. In the southern basin, the stratigraphically youngest and oldest moraines—WIN and MNM, respectively—form prominent, well-developed ridges. However, the MON moraine, between WIN and MNM, is noticeably more diffuse.

Notably, I avoided sampling boulders on the southernmost portion of the MNM moraine, as a freshly scoured drift is draped atop that part of the ridge, and likely post-dates the original deposition of the moraine.

CHAPTER 4

CHRONOLOGY

I made a total of 249 ^{3}He, ^{21}Ne, and ^{10}Be measurements in 150 samples collected from moraines and drift boulders at Roberts Massif. Of these 150 samples, I measured ^{3}He concentrations in pyroxenes isolated from 137 Ferrar dolerite boulders (including multiple aliquots for 86 of those samples) and ^{10}Be in quartz from 13 Beacon sandstone boulders. Additionally, ^{21}Ne measurements were made on multiple aliquots from four of those sandstone boulders. Nuclide concentrations are summarized in Table 4.1 and Table 4.2 and apparent exposure ages are presented in Table 4.3. "Apparent" exposure ages refer to the calculated age of the boulder given the measured nuclide inventory, assuming that the boulder has experienced only one period of exposure, with no erosion or burial during that time. Complete step-degassing results for ^{3}He measurements are presented in Appendix C, while the full exposure-age data set is accessible both in Appendix D and online at http://antarctica.ice-d.org/allsites. Apparent exposure ages, calculated using the scaling framework of Lifton et al. (2014) (hereby referred to as LSD scaling) and the primary production rate calibration data set of Borchers et al. (2016), are presented below. Complete discussions of outlier elimination methods, landform ages, and justification for employing the LSD scaling method are found in Chapter 5.

4.1 Roberts Col

At the Roberts Col site, I measured ^{3}He concentrations in three dolerite boulders and ^{10}Be and ^{21}Ne concentrations in four sandstone erratics from the Roberts Col drift. ^{3}He ages range from 8.74–11.19 Ma and ^{21}Ne ages are between 9.26 Ma and 12.92 Ma (Figure 4.1). All four

^{10}Be ages are saturated with respect to St scaling (discussed further in Chapter 5) and, although ages are calculated using LSD scaling, the internal errors are ~30–50 % of the calculated age due to the position of the [^{10}Be] near the asymptote of the concentration vs. age curve.

I also measured ^{3}He concentrations in 27 dolerite boulders from the Misery moraines. Listed in descending stratigraphic order, the age ranges obtained on these moraines are: 7.52–8.32 Ma (Misery D, n = 5), 4.38–8.03 Ma (Misery A, n = 5), 7.98–8.19 Ma (Misery B, n = 8), and 4.76–8.06 Ma (Misery C, n = 7) (Figure 4.1). Notably, the ages of the Misery D and Misery B moraines display excellent internal consistency, with coefficients of variance (CV) of 4% and 1%, respectively, even before outliers were eliminated.

4.2 Upper Roberts

Along the Upper Roberts transect, I measured ^{3}He in 22 boulders from four moraine crests. In stratrigraphically descending order, the age ranges for each moraine are: 2.53–2.89 Ma (Arena, n = 6), 0.90–2.09 Ma (Eine, n = 7), 0.99–1.38 Ma (Kleine, n = 6), 1.04–1.54 Ma (Nacht, N = 7), and 0.62–1.12 Ma (Musik, n = 3) (Figure 4.2). In general, these data show decent agreement among ages on each landform, especially for the Arena, Kleine, and Nacht moraines, even before eliminating outliers.

4.3 Lower Roberts

The Ringleader moraine, which is situated atop the Central Rise, is the oldest moraine in the Lower Roberts area, with seven apparent exposure ages ranging from 2.11–4.09 Ma (Figure 4.4). Within the Ringleader data set, the two sandstone boulders give ^{10}Be ages that are

consistent with the ^{3}He ages on the moraine. Below, I present ages for both the northern and southern transects at Lower Roberts, which both begin at the Ringleader moraine (Figure 3.6).

Along the Lower Roberts northern transect, I measured ^{3}He in 34 dolerite boulders and ^{10}Be in two sandstone boulders. Listed with decreasing elevation, the moraines gave apparent exposure age ranges of: 2.70–3.09 Ma (BAS, n = 7), 2.03–3.45 Ma (HDY, n = 7), 1.90–2.93 Ma (SSU, n = 7), 1.78–3.65 Ma (WBK, n = 7), 1.17–2.05 Ma (POS, n = 5), 1.30–1.63 Ma (AND, n = 3), and 1.20 Ma (NLO, n = 1) (Figure 4.4). The moraines in the middle of the transect (particularly WBK and POS) show the most scatter, while the BAS and HDY moraine display excellent internal consistency. Analyses on the AND and NLO/NLI moraines are incomplete, thus these results are preliminary. However, the one ^{10}Be age on AND is consistent with the two ^{3}He ages on that moraine. Further, the one ^{10}Be age on NLO, the moraine closest to the modern ice, displays the youngest age in the transect.

Lastly, I measured ^{3}He in 35 dolerite boulders and ^{10}Be in 5 sandstone boulders along the Lower Roberts southern transect. In order of decreasing distance from the current ice margin, these moraines afford age ranges of: 1.51–2.62 (BBY, n = 5), 1.38–4.04 (BGE, n = 7), 1.51–2.75 (WAL, n = 7), 0.38–0.98 (WIN, n = 7), 0.53–1.03 (MON, n = 6), 0.39–1.87 (MNM, n = 7) (Figure 4.4; Figure 4.5). One ^{10}Be age on WIN is significantly younger than the rest of the age population on that moraine, which is not surprising as that boulder displayed signs of heavy erosion, including considerable exfoliation and rounding. On the MON moraine, the four ^{10}Be ages are systematically older than the two ^{3}He ages, which give nearly identical ages. In general, the moraines in this transect yielded the highest degree of scatter in the Roberts Massif chronology, possible reasons for which are discussed in Chapter 5.

Table 4.1 Dolerite sample information and ^{3}He concentrations in pyroxenes.

Sample ID	Aliquot	Weight (g)	Latitude (DD)	Longitude (DD)	Elevation (m)	Shielding Factor	Sample Thickness (cm)	Measured [He-3] (10^9 atoms/g)	δ[He-3] (10^7 atoms/g)	Standardized [He-3] (10^9 atoms/g)	Standardized δ[He-3] (10^7 atoms/g)	[He-4] (10^{14} atoms/g)	δ[He-4] (10^{13} atoms/g)	Measured [He-3] of CRONUS-P Standard (10^9 atoms/g)	δ[He-3] of CRONUS-P Standard (10^8 atoms/g)
Roberts Col															
15-ROB-001-MZA	a	0.02447	-85.52805	-177.68282	2199.0	0.9847	1.4	8.73	7.99	8.82	8.07	9.18	0.39	4.97	1.03
15-ROB-001-MZA	b	0.02238						8.44	7.42	8.53	7.50	8.80	0.36	4.97	1.03
15-ROB-002-MZA	a	0.01956	-85.52792	-177.68332	2200.0	0.98785	2.5	6.05	5.15	6.11	5.20	2.66	0.58	4.97	1.03
15-ROB-002-MZA	b	0.01424						6.05	5.22	6.11	5.27	2.71	0.58	4.97	1.03
15-ROB-003-MZA	a	0.01414	-85.52768	-177.6839	2198.5	0.98785	1.1	6.57	5.70	6.63	5.75	3.73	0.80	4.97	1.03
15-ROB-003-MZA	b	0.02288						6.58	5.82	6.64	5.87	3.82	0.79	4.97	1.03
15-ROB-004-MZA	a	0.01857	-85.52757	-177.68553	2197.0	0.98785	0.95	4.56	3.68	4.60	3.72	8.66	1.68	4.97	1.03
15-ROB-004-MZA	b	0.02489						4.86	4.49	4.91	4.53	8.59	1.72	4.97	1.03
15-ROB-005-MZA	a	0.0202	-85.5271	-177.69048	2195.5	0.991	1.6	6.67	5.66	6.74	5.72	10.36	2.05	4.97	1.03
15-ROB-005-MZA	b	0.01876						6.67	5.33	6.73	5.38	10.14	2.02	4.97	1.03
15-ROB-006-MZB	a	0.01801	-85.52575	-177.7179	2248.0	0.9939	2.2	9.06	16.35	9.15	16.52	6.50	1.05	4.97	1.03
15-ROB-006-MZB	b	0.02164						8.73	14.91	8.82	15.06	6.45	1.03	4.97	1.03
15-ROB-007-MZB	a	0.02269	-85.52488	-177.7249	2255.0	0.9939	2	9.32	16.03	9.41	16.19	9.26	1.43	4.97	1.03
15-ROB-007-MZB	b	0.0181						9.07	14.12	9.16	14.27	9.33	1.33	4.97	1.03
15-ROB-008-MZB	a	0.02381	-85.52478	-177.72667	2253.0	0.9939	1.5	9.11	14.87	9.20	15.02	9.73	1.78	4.97	1.03
15-ROB-008-MZB	b	0.01564						9.06	14.37	9.15	14.52	10.26	1.50	4.97	1.03
15-ROB-009-MZB	a	0.02098	-85.52438	-177.73138	2252.0	0.9939	1.7	9.21	17.89	9.30	18.07	2.06	0.37	4.97	1.03
15-ROB-009-MZB	b	0.01882						9.03	14.43	9.13	14.58	2.03	0.30	4.97	1.03
15-ROB-010-MZB	a	0.0227	-85.5245	-177.7315	2250.0	0.9939	1.1	9.06	16.33	9.15	16.50	8.43	1.41	4.97	1.03
15-ROB-010-MZB	b	0.01836						9.11	12.51	9.20	12.64	8.19	1.02	4.97	1.03
15-ROB-011-MZB	a	0.02252	-85.52508	-177.73225	2252.0	0.9939	1.2	9.12	17.59	9.21	17.77	4.18	0.76	4.97	1.03
15-ROB-011-MZB	b	0.0221						9.09	14.43	9.18	14.58	4.08	0.61	4.97	1.03
15-ROB-012-MZB	a	0.02141	-85.52528	-177.73147	2254.0	0.9939	2.1	9.13	15.90	9.22	16.06	8.63	1.35	4.97	1.03
15-ROB-013-MZB	a	0.02077	-85.52537	-177.73098	2253.0	0.9939	2.2	9.02	17.37	9.11	17.54	4.69	0.84	4.97	1.03
15-ROB-014-MZC	a	0.0261	-85.5267	-177.72797	2221.0	0.9869	1.8	8.64	14.56	8.73	14.71	8.72	1.34	4.97	1.03
15-ROB-014-MZC	b	0.02079						8.59	12.58	8.67	12.70	8.60	1.18	4.97	0.94
15-ROB-015-MZC	a	0.02368	-85.52687	-177.72652	2222.0	0.9936	1.8	8.75	14.60	8.84	14.74	8.00	1.24	4.97	1.03
15-ROB-015-MZC	b	0.02097						8.74	13.33	8.83	13.46	7.98	1.12	4.97	0.94
15-ROB-016-MZC	a	0.02365	-85.52687	-177.7264	2222.0	0.9869	1.5	8.49	14.59	8.58	14.73	2.70	0.44	4.97	1.03
15-ROB-016-MZC	b	0.0197						8.53	13.07	8.62	13.20	2.47	0.35	4.97	0.94
15-ROB-017-MZC	a	0.0173	-85.5269	-177.72513	2220.0	0.9869	1.1	8.81	13.79	8.90	13.92	7.26	1.02	4.97	1.03
15-ROB-018-MZC	a	0.02305	-85.52747	-177.72853	2212.0	0.9802	3.4	8.08	8.24	8.16	8.33	9.75	0.43	4.97	1.03
15-ROB-018-MZC	b	0.01757						7.82	7.90	7.90	7.98	9.58	0.44	4.97	1.03
15-ROB-018-MZC	c	0.01778						8.02	14.20	8.10	14.35	9.56	1.54	4.97	1.03
15-ROB-019-MZC	a	0.0198	-85.52748	-177.72743	2210.0	0.9869	2.2	7.79	8.03	7.87	8.11	4.72	0.23	4.97	1.03
15-ROB-019-MZC	b	0.01687						7.92	8.24	8.00	8.32	4.93	0.24	4.97	1.03
15-ROB-020-MZC	a	0.02127	-85.52758	-177.72627	2211.0	0.9802	4	7.66	7.36	7.73	7.43	5.85	0.26	4.97	1.03
15-ROB-020-MZC	b	0.03215						7.97	7.76	8.05	7.83	6.14	0.28	4.97	1.03
15-ROB-021-MZC	a	0.02149	-85.5276	-177.72593	2211.0	0.9869	1.7	5.45	5.68	5.50	5.74	8.00	0.35	4.97	1.03
15-ROB-021-MZC	b	0.0194						5.37	5.40	5.42	5.45	8.08	0.37	4.97	1.03
15-ROB-022-MZC	a	0.01789	-85.52782	-177.72097	2206.0	0.9802	2.5	5.01	5.32	5.06	5.37	6.52	0.32	4.97	1.03
15-ROB-022-MZC	b	0.0174						5.08	5.28	5.13	5.33	6.68	0.31	4.97	1.03
15-ROB-023-MZD	a	0.01957	-85.52222	-177.72617	2251.0	0.9959	1.5	9.02	15.59	9.11	15.74	3.44	0.56	4.97	1.03
15-ROB-024-MZD	a	0.02031	-85.52218	-177.72677	2247.0	0.9959	1.9	8.66	13.96	8.75	14.10	7.39	1.07	4.97	1.03
15-ROB-025-MZD	a	0.01761	-85.52205	-177.72725	2250.0	0.9959	2.9	8.97	14.90	9.06	15.05	7.24	1.11	4.97	1.03
15-ROB-026-MZD	a	0.02186	-85.52198	-177.72737	2252.0	0.9959	2.4	8.40	14.47	8.48	14.61	5.04	0.82	4.97	1.03
15-ROB-027-MZD	a	0.02371	-85.52188	-177.72793	2247.0	0.9959	4.8	8.98	14.97	9.07	15.12	5.77	0.90	4.97	1.03
15-ROB-027-MZD	b	0.01958						9.12	14.26	9.21	14.40	5.69	0.83	4.97	1.03

Table 4.1 continued.

Sample ID	Aliquot	Weight (g)	Latitude (DD)	Longitude (DD)	Elevation (m)	Shielding Factor	Sample Thickness (cm)	Measured [He-3] (10^9 atoms/g)	δ[He-3] (10^7 atoms/g)	Standardized [He-3] (10^9 atoms/g)	Standardized δ[He-3] (10^7 atoms/g)	[He-4] (10^{14} atoms/g)	δ[He-4] (10^{13} atoms/g)	Measured [He-3] of CRONUS-P Standard (10^9 atoms/g)	δ[He-3] of CRONUS-P Standard (10^8 atoms/g)
Roberts Col continued															
15-ROB-028-COL	a	0.0416	-85.50998	-177.79202	2378.0	1	3	13.86	13.71	14.00	13.85	1.68	0.06	4.97	1.03
15-ROB-028-COL	b	0.03272						13.54	17.19	13.67	17.37	1.63	0.07	4.97	1.03
15-ROB-030-COL	a	0.0562	-85.51005	-177.79427	2385.0	1	4.4	12.46	16.25	12.58	16.41	5.64	0.27	4.97	1.03
15-ROB-030-COL	b	0.01884						11.96	16.91	12.08	17.08	-	-	4.97	1.03
15-ROB-031-COL	a	0.0468	-85.50902	-177.77877	2369.0	1	4.3	10.68	14.00	10.78	14.14	4.34	0.20	4.97	1.03
15-ROB-031-COL	b	0.01399						10.40	14.41	10.51	14.55	4.48	0.22	4.97	1.03
15-ROB-031-COL	c	0.02112						10.46	20.29	10.57	20.50	4.21	0.76	4.97	1.03
Upper Roberts															
15-ROB-035-ARM	a	0.0382	-85.5627	-177.10017	2305.0	0.9835	1.1	3.00	3.13	3.03	3.16	6.28	0.23	4.97	1.03
15-ROB-035-ARM	b	0.01302						3.11	4.14	3.14	4.18	6.50	0.29	4.97	1.03
15-ROB-036-ARM	a	0.0537	-85.56265	-177.1002	2304.0	0.9835	2	3.36	4.36	3.39	4.41	4.76	0.19	4.97	1.03
15-ROB-036-ARM	b	0.02276						3.29	4.55	3.32	4.59	4.83	0.23	4.97	1.03
15-ROB-038-ARM	a	0.0267	-85.56262	-177.10047	2305.0	0.9835	3.4	2.83	3.28	2.86	3.31	1.79	0.08	4.97	1.03
15-ROB-038-ARM	b	0.03429						3.03	4.19	3.06	4.23	1.97	0.09	4.97	1.03
15-ROB-039-ARM	a	0.0263	-85.56248	-177.10112	2308.0	0.9835	1.8	2.87	4.00	2.90	4.04	6.07	0.28	4.97	1.03
15-ROB-039-ARM	b	0.0222						2.99	3.72	3.02	3.76	6.24	0.25	4.97	1.03
15-ROB-040-ARM	a	0.0386	-85.56245	-177.10132	2299.0	0.9835	2	3.10	3.57	3.14	3.61	3.56	0.14	4.97	1.03
15-ROB-040-ARM	b	0.02628						3.07	4.25	3.10	4.29	3.43	0.16	4.97	1.03
15-ROB-041-ARM	a	0.0233	-85.56233	-177.10185	2299.0	0.9835	3.1	3.09	3.89	3.12	3.93	7.18	0.31	4.97	1.03
15-ROB-041-ARM	b	0.0158						3.17	3.26	3.20	3.29	6.95	0.23	4.97	1.03
15-ROB-042-EIN	a	0.0435	-85.5553	-177.08377	2253.0	0.9857	1.4	1.46	1.99	1.48	2.01	6.00	0.28	4.97	1.03
15-ROB-042-EIN	b	0.0192						1.45	1.79	1.47	1.80	6.11	0.23	4.97	1.03
15-ROB-042-EIN	c	0.01948						1.38	1.53	1.40	1.55	6.01	0.28	4.97	1.03
15-ROB-043-EIN	a	0.0404	-85.5552	-177.08398	2254.0	0.9866	1.6	1.39	2.03	1.40	2.05	4.52	0.22	4.97	1.03
15-ROB-043-EIN	b	0.0196						1.39	2.62	1.40	2.65	4.65	0.18	4.97	1.03
15-ROB-043-EIN	c	0.02263						1.33	1.93	1.35	1.95	4.86	0.23	4.97	1.03
15-ROB-044-EIN	a	0.024	-85.55507	-177.08367	2254.0	0.9866	3.8	0.92	1.37	0.93	1.39	2.16	0.10	4.97	1.03
15-ROB-044-EIN	b	0.0378						1.01	1.41	1.02	1.43	2.50	0.11	4.97	1.03
15-ROB-044-EIN	c	0.01755						1.02	1.61	1.03	1.62	2.27	0.11	4.97	1.03
15-ROB-045-EIN	a	0.058	-85.55487	-177.08478	2257.0	0.9866	1.5	1.55	1.91	1.56	1.93	2.95	0.13	4.97	1.03
15-ROB-045-EIN	b	0.01776						1.57	2.35	1.59	2.37	2.80	0.13	4.97	1.03
15-ROB-046-EIN	a	0.0242	-85.55467	-177.08555	2256.0	0.9866	2.4	2.37	2.92	2.40	2.95	3.47	0.15	4.97	1.03
15-ROB-046-EIN	b	0.01795						2.27	3.29	2.30	3.32	3.66	0.18	4.97	1.03
15-ROB-047-EIN	a	0.0201	-85.55453	-177.0861	2251.0	0.9866	2.5	1.15	1.68	1.16	1.69	5.04	0.23	4.97	1.03
15-ROB-047-EIN	b	0.01952						1.31	1.98	1.32	2.00	5.68	0.27	4.97	1.03
15-ROB-048-EIN	a	0.01827	-85.55425	-177.08798	2257.0	0.9875	1.5	1.16	1.71	1.17	1.72	7.67	0.36	4.97	1.03
15-ROB-048-EIN	b	0.02339						1.17	1.72	1.19	1.74	6.57	0.31	4.97	1.03
15-ROB-049-KLE	a	0.01849	-85.55425	-177.0954	2245.0	0.9893	3.1	1.19	2.09	1.20	2.12	2.53	0.38	4.97	1.03
15-ROB-050-KLE	a	0.02146	-85.55418	-177.09543	2239.0	0.9865	4	1.17	1.73	1.18	1.75	10.14	0.47	4.97	1.03
15-ROB-050-KLE	b	0.02086						1.20	1.79	1.22	1.81	9.52	0.45	4.97	1.03
15-ROB-050-KLE	c	0.01869						1.15	1.24	1.17	1.25	4.95	0.22	4.97	1.03
15-ROB-051-KLE	a	0.01997	-85.554	-177.09607	2244.0	0.9865	2	1.53	2.23	1.54	2.25	7.85	0.38	4.97	1.03
15-ROB-052-KLE	a	0.02037	-85.55382	-177.09787	2231.0	0.9865	1.1	1.43	2.11	1.45	2.13	3.54	0.17	4.97	1.03
15-ROB-053-KLE	a	0.01771	-85.55382	-177.09898	2248.0	0.9865	2	1.11	1.70	1.12	1.71	6.41	0.30	4.97	1.03
15-ROB-053-KLE	b	0.01958						1.08	1.62	1.09	1.64	7.41	0.34	4.97	1.03
15-ROB-054-KLE	a	0.02272	-85.5537	-177.10042	2238.0	0.9865	1.8	1.45	1.42	1.47	1.43	2.07	0.45	4.97	1.03
15-ROB-054-KLE	b	0.01772						1.46	1.50	1.47	1.52	2.05	0.44	4.97	1.03

Table 4.1 continued.

Sample ID	Aliquot	Weight (g)	Latitude (DD)	Longitude (DD)	Elevation (m)	Shielding Factor	Sample Thickness (cm)	Measured [He-3] (10^9 atoms/g)	δ[He-3] (10^7 atoms/g)	Standardized [He-3] (10^9 atoms/g)	Standardized δ[He-3] (10^7 atoms/g)	[He-4] (10^{14} atoms/g)	δ[He-4] (10^{13} atoms/g)	Measured [He-3] of CRONUS-P Standard (10^9 atoms/g)	δ[He-3] of CRONUS-P Standard (10^8 atoms/g)
Upper Roberts continued															
15-ROB-055-NAC	a	0.01832	-85.55098	-177.13638	2220.5	0.9973	3.3	1.15	1.71	1.17	1.73	4.97	0.23	4.97	1.03
15-ROB-055-NAC	b	0.01729						1.16	1.81	1.17	1.83	5.84	0.28	4.97	1.03
15-ROB-056-NAC	a	0.02432	-85.55108	-177.13538	2224.0	0.99665	2.7	1.17	1.73	1.18	1.75	8.68	0.41	4.97	1.03
15-ROB-056-NAC	b	0.02118						1.11	1.66	1.12	1.68	8.21	0.39	4.97	1.03
15-ROB-057-NAC	a	0.0189	-85.55127	-177.13258	2227.5	0.99665	2.7	1.34	2.72	1.36	2.75	-	-	4.97	1.03
15-ROB-057-NAC	b	0.0249						1.42	2.44	1.43	2.47	3.24	0.42	4.97	0.94
15-ROB-058-NAC	a	0.02304	-85.5513	-177.13137	2220.5	0.99665	2.3	1.36	2.57	1.37	2.59	2.62	0.42	4.97	1.03
15-ROB-059-NAC	a	0.01986	-85.5513	-177.13137	2220.5	0.99665	2.1	1.15	2.14	1.17	2.16	6.77	1.06	4.97	1.03
15-ROB-059-NAC	b	0.02136						1.21	2.20	1.22	2.23	6.57	0.85	4.97	0.94
15-ROB-060-NAC	a	0.02426	-85.55142	-177.12885	2216.0	0.99665	1.4	1.68	2.83	1.70	2.86	5.52	0.81	4.97	1.03
15-ROB-061-NAC	a	0.02287	-85.55147	-177.12807	2216.0	0.996	1.5	1.19	2.02	1.20	2.04	4.68	0.69	4.97	1.03
15-ROB-062-MUS	a	0.01851	-85.55135	-177.1353	2217.0	0.9952	1.8	1.22	2.26	1.23	2.29	6.44	0.98	4.97	1.03
15-ROB-063-MUS	a	0.01749	-85.55118	-177.13863	2215.0	0.9951	2.8	1.16	2.07	1.17	2.09	6.24	0.91	4.97	1.03
15-ROB-064-MUS	a	0.02156	-85.55115	-177.13932	2212.0	0.9951	2.1	0.67	1.22	0.68	1.24	5.95	0.81	4.97	1.03
Lower Roberts															
16-ROB-015-AND	a	0.01923	-85.507698	-176.87601	1829.4	0.9988	1.54	1.31	3.18	1.30	3.16	2.90	0.27	5.05	1.14
16-ROB-015-AND	b	0.02337						1.36	3.18	1.35	3.16	2.83	0.26	5.05	1.14
16-ROB-016-AND	a	0.02749	-85.507797	-176.875	1829.9	0.9988	1.95	1.06	2.51	1.06	2.50	2.54	0.23	5.05	1.14
16-ROB-016-AND	b	0.02125						1.07	2.56	1.06	2.55	2.52	0.23	5.05	1.14
16-ROB-023-PSO	a	0.02133	-85.5112	-176.855	1869.6	0.9983	1.03	1.19	2.84	1.18	2.82	4.00	0.40	5.05	1.14
16-ROB-023-PSO	b	0.02386						1.17	2.74	1.17	2.72	4.11	0.37	5.05	1.14
16-ROB-024-PSO	a	0.02479	-85.511703	-176.854	1866.1	0.9984	1.5	0.99	2.34	0.98	2.32	0.46	0.04	5.05	1.14
16-ROB-028-PSI	a	0.02276	-85.5112	-176.855	1862.5	0.9978	1.84	1.52	3.44	1.51	3.42	0.52	0.05	5.05	1.14
16-ROB-028-PSI	b	0.02098						1.48	3.43	1.47	3.40	0.53	0.05	5.05	1.14
16-ROB-029-PSI	a	0.02377	-85.511101	-176.858	1863.0	0.9986	1.47	1.73	3.93	1.72	3.91	1.18	0.11	5.05	1.14
16-ROB-030-PSI	a	0.02349	-85.511002	-176.86301	1865.0	0.9986	2.09	1.32	3.07	1.31	3.06	0.39	0.04	5.05	1.14
16-ROB-031-WIN	a	0.02086	-85.515198	-176.877	1876.0	0.9978	2.31	2.05	3.48	2.04	3.46	7.56	1.96	5.05	1.14
16-ROB-031-WIN	b	0.01885						2.19	3.76	2.17	3.73	7.97	2.06	5.05	1.14
16-ROB-032-WIN	a	0.02159	-85.515198	-176.877	1877.0	0.9978	1.99	2.43	5.57	2.41	5.53	1.75	0.18	5.05	1.14
16-ROB-032-WIN	b	0.01979						2.39	5.50	2.37	5.47	1.74	0.16	5.05	1.14
16-ROB-033-WIN	a	0.02109	-85.515099	-176.87399	1877.5	0.9978	1.85	1.51	3.59	1.51	3.57	5.46	0.50	5.05	1.14
16-ROB-034-WIN	a	0.02729	-85.515099	-176.87199	1877.0	0.9975	2.35	3.08	4.94	3.06	4.91	1.24	0.33	5.05	1.14
16-ROB-034-WIN	b	0.0206						3.10	5.04	3.08	5.01	1.30	0.33	5.05	1.14
16-ROB-036-WIN	a	0.02265	-85.514999	-176.86301	1876.0	0.9975	1.91	2.39	3.89	2.37	3.87	0.51	0.13	5.05	1.14
16-ROB-036-WIN	b	0.02251						2.40	3.92	2.38	3.90	0.60	0.16	5.05	1.14
16-ROB-037-WIN	a	0.02509	-85.5149	-176.856	1876.0	0.9972	2.11	1.99	4.49	1.98	4.46	0.62	0.06	5.05	1.14
16-ROB-037-WIN	b	0.01837						2.02	4.70	2.01	4.67	0.59	0.06	5.05	1.14
16-ROB-038-SSU	a	0.02228	-85.516899	-176.884	1871.2	0.9972	2.32	1.74	2.86	1.73	2.84	5.01	1.24	5.05	1.14
16-ROB-038-SSU	b	0.01775						1.79	3.10	1.78	3.08	5.59	1.46	5.05	1.14
16-ROB-039-SSU	a	0.02121	-85.516899	-176.885	1872.7	0.9972	2.68	1.69	2.84	1.68	2.82	3.60	0.92	5.05	1.14
16-ROB-039-SSU	b	0.01932						1.77	3.02	1.76	3.00	3.77	0.97	5.05	1.14
16-ROB-040-SSU	a	0.02195	-85.516899	-176.88901	1872.7	0.9972	1.88	2.10	3.51	2.09	3.49	0.80	0.21	5.05	1.14
16-ROB-040-SSU	b	0.01792						2.12	3.55	2.11	3.52	0.73	0.19	5.05	1.14
16-ROB-041-SSU	a	0.02029	-85.5168	-176.89301	1872.7	0.9972	1.57	2.12	3.52	2.11	3.50	0.64	0.16	5.05	1.14
16-ROB-041-SSU	b	0.01826						2.11	3.52	2.10	3.50	0.58	0.24	5.05	1.14
16-ROB-042-SSU	a	0.01847	-85.526899	-176.89301	1871.7	0.9979	1.34	2.17	3.66	2.16	3.63	3.85	0.99	5.05	1.14
16-ROB-042-SSU	b	0.01844						2.23	3.77	2.21	3.74	3.78	1.13	5.05	1.14
16-ROB-043-SSU	a	0.02189	-85.5168	-176.895	1872.2	0.9979	1.31	2.53	4.04	2.52	4.01	0.58	0.15	5.05	1.14
16-ROB-043-SSU	b	0.01804						2.46	4.03	2.44	4.00	0.43	0.11	5.05	1.14
16-ROB-044-SSU	a	0.022	-85.5168	-176.877	1872.7	0.9979	1.55	1.64	2.81	1.63	2.79	0.33	0.09	5.05	1.14
16-ROB-044-SSU	b	0.02314						1.58	2.70	1.57	2.68	0.33	0.09	5.05	1.14

Table 4.1 continued.

Sample ID	Aliquot	Weight (g)	Latitude (DD)	Longitude (DD)	Elevation (m)	Shielding Factor	Sample Thickness (cm)	Measured [He-3] (10^9 atoms/g)	δ[He-3] (10^7 atoms/g)	Standardized [He-3] (10^9 atoms/g)	Standardized δ[He-3] (10^7 atoms/g)	[He-4] (10^{14} atoms/g)	δ[He-4] (10^{13} atoms/g)	Measured [He-3] of CRONUS-P Standard (10^9 atoms/g)	δ[He-3] of CRONUS-P Standard (10^8 atoms/g)
Lower Roberts continued															
16-ROB-045-HDY	a	0.02066	-85.5196	-176.918	1895.6	0.997	1.69	2.42	6.34	2.37	6.20	3.59	0.29	5.14	1.01
16-ROB-046-HDY	a	0.02501	-85.519501	-176.938	1895.6	0.9974	1.96	2.39	6.96	2.32	6.74	2.46	0.32	5.18	0.73
16-ROB-046-HDY	b	0.02045						2.43	6.39	2.37	6.24	2.38	0.19	5.14	1.01
16-ROB-046-HDY	c	0.02375						2.53	7.36	2.47	7.19	2.71	0.22	5.14	1.01
16-ROB-047-HDY	a	0.05299	-85.519501	-176.938	1893.6	0.9974	2.3	1.79	5.13	1.73	4.97	0.62	0.08	5.18	0.73
16-ROB-048-HDY	a	0.02891	-85.519501	-176.937	1893.6	0.9974	1.6	2.39	6.95	2.32	6.74	2.76	0.35	5.18	0.73
16-ROB-048-HDY	b	0.02022						2.35	6.14	2.30	6.00	2.69	0.21	5.14	1.01
16-ROB-049-HDY	a	0.02445	-85.519501	-176.937	1893.6	0.9974	1.48	2.56	7.45	2.48	7.23	2.57	0.33	5.18	0.73
16-ROB-050-HDY	a	0.02593	-85.519501	-176.93601	1894.6	0.9974	2.14	3.02	8.53	2.95	8.33	4.66	0.42	5.14	1.01
16-ROB-051-HDY	a	0.02034	-85.519501	-176.93601	1898.6	0.9974	1.98	2.43	6.94	2.38	6.78	4.73	0.43	5.14	1.01
16-ROB-052-BAS	a	0.03916	-85.519798	-176.966	1917.7	0.9961	1.22	2.59	6.64	2.53	6.49	0.91	0.07	5.14	1.01
16-ROB-053-BAS	a	0.0211	-85.519699	-176.96201	1914.2	0.9963	2.22	2.65	8.00	2.57	7.76	4.51	0.60	5.18	0.73
16-ROB-053-BAS	c	0.0251						2.64	8.03	2.56	7.79	4.24	0.56	5.18	0.73
16-ROB-054-BAS	a	0.02201	-85.519699	-176.961	1913.2	0.9963	1.49	2.53	7.20	2.47	7.04	8.80	0.80	5.14	1.01
16-ROB-055-BAS	a	0.04472	-85.5215	-176.968	1911.2	0.9943	1.74	2.76	7.81	2.68	7.57	0.66	0.08	5.18	0.73
16-ROB-056-BAS	a	0.0361	-85.519897	-176.95799	1914.2	0.9959	1.96	2.40	6.15	2.34	6.01	0.75	0.06	5.14	1.01
16-ROB-057-BAS	a	0.02454	-85.519798	-176.95599	1913.7	0.9961	1.53	2.49	7.04	2.42	6.82	2.89	0.36	5.18	0.73
16-ROB-057-BAS	b	0.02421						2.59	7.89	2.53	7.71	3.65	0.31	5.14	1.01
16-ROB-058-BAS	a	0.02605	-85.519897	-176.955	1911.7	0.9961	1.8	2.50	5.69	2.52	5.75	0.84	0.18	4.97	0.94
16-ROB-058-BAS	b	0.03973						2.48	3.74	2.49	3.76	0.93	0.11	4.99	0.95
16-ROB-059-RIN	a	0.01769	-85.5214	-176.96899	1956.7	0.9989	2.9	2.73	4.63	2.76	4.67	3.48	0.46	4.97	0.94
16-ROB-061-RIN	a	0.02169	-85.521301	-176.97099	1963.7	0.999	2.9	2.56	5.83	2.59	5.89	0.49	0.10	4.97	0.94
16-ROB-061-RIN	b	0.04304						2.51	5.66	2.53	5.70	0.52	0.11	4.99	0.95
16-ROB-063-RIN	a	0.01894	-85.522499	-176.965	1952.7	0.9988	2.8	3.65	6.06	3.69	6.12	3.61	0.50	4.97	0.94
16-ROB-063-RIN	b	0.02426						3.57	12.80	3.48	12.51	4.09	0.26	5.14	1.01
16-ROB-064-RIN	a	0.02211	-85.522499	-176.964	1954.7	0.9988	2.1	3.03	6.91	3.06	6.98	0.54	0.11	4.97	0.94
16-ROB-065-RIN	a	0.02609	-85.522499	-176.968	1956.7	0.9988	1.78	2.06	6.42	2.00	6.22	3.79	0.52	5.18	0.73
16-ROB-065-RIN	b	0.02068						1.85	6.88	1.81	6.73	3.60	0.33	5.14	1.01
16-ROB-066-MNM	a	0.02515	-85.539001	-177.11301	1769.6	0.9801	1.78	1.46	4.54	1.42	4.44	5.99	0.52	5.14	1.01
16-ROB-067-MNM	a	0.02229	-85.5392	-177.11099	1770.1	0.984	2.4	0.68	2.10	0.66	2.05	2.86	0.24	5.14	1.01
16-ROB-067-MNM	b	0.02168						0.64	2.45	0.62	2.39	2.95	0.27	5.14	1.01
16-ROB-068-MNM	a	0.02562	-85.539597	-177.10899	1772.6	0.9862	1.57	1.15	3.74	1.12	3.65	4.05	0.36	5.14	1.01
16-ROB-069-MNM	a	0.02831	-85.540001	-177.10899	1773.6	0.9862	2.24	0.40	1.49	0.39	1.46	6.86	0.44	5.14	1.01
16-ROB-070-MNM	a	0.03093	-85.5401	-177.10899	1773.6	0.9862	1.83	1.16	4.20	1.14	4.10	3.10	0.20	5.14	1.01
16-ROB-070-MNM	b	0.01938						1.09	4.11	1.06	4.02	2.84	0.26	5.14	1.01
16-ROB-071-MNM	a	0.02645	-85.5401	-177.10899	1779.1	0.9882	4.74	0.54	2.00	0.53	1.95	5.53	0.35	5.14	1.01
16-ROB-072-MNM	a	0.02535	-85.539497	-177.11501	1779.1	0.9882	2	0.31	1.04	0.31	1.02	3.05	0.25	5.14	1.01
16-ROB-072-MNM	b	0.02446						0.31	1.22	0.30	1.19	3.22	0.29	5.14	1.01
16-ROB-076-MON	a	0.02788	-85.538399	-177.105	1789.1	0.981	1.33	0.42	1.36	0.41	1.33	10.20	0.88	5.14	1.01
16-ROB-077-MON	a	0.02499	-85.5382	-177.10899	1792.1	0.9821	1.31	0.42	1.36	0.41	1.33	2.89	0.24	5.14	1.01
16-ROB-077-MON	b	0.03115						0.44	1.65	0.43	1.61	2.96	0.19	5.14	1.01
16-ROB-079-WIN	a	0.0247	-85.538696	-177.108	1834.6	0.9749	2	0.64	2.00	0.63	1.95	1.97	0.16	5.14	1.01
16-ROB-080-WIN	a	0.02503	-85.5383	-177.08701	1822.2	0.9924	3.15	0.67	2.43	0.66	2.37	9.21	0.57	5.14	1.01
16-ROB-081-WIN	a	0.02652	-85.538597	-177.08501	1819.7	0.9865	1.55	0.60	1.77	0.59	1.73	0.33	0.13	5.14	1.01
16-ROB-081-WIN	b	0.02716						0.58	2.07	0.57	2.02	0.35	0.15	5.14	1.01
16-ROB-082-WIN	a	0.02759	-85.539001	-177.08299	1819.7	0.9916	1.34	0.41	1.39	0.40	1.36	0.58	0.30	5.14	1.01
16-ROB-082-WIN	b	0.04487						0.42	1.58	0.41	1.54	0.58	0.05	5.14	1.01
16-ROB-083-WIN	a	0.02835	-85.539101	-177.08299	1819.7	0.9916	1.44	0.75	2.80	0.74	2.73	3.58	0.23	5.14	1.01
16-ROB-084-WIN	a	0.02928	-85.539101	-177.08299	1818.2	0.9914	2.13	0.63	1.95	0.61	1.91	1.09	0.09	5.14	1.01
16-ROB-084-WIN	b	0.02119						0.64	2.46	0.63	2.41	1.16	0.10	5.14	1.01
16-ROB-085-WIN	a	0.03074	-85.539299	-177.082	1816.7	0.9915	1.5	0.79	2.52	0.77	2.46	3.75	0.33	5.14	1.01

Table 4.1 continued.

Sample ID	Aliquot	Weight (g)	Latitude (DD)	Longitude (DD)	Elevation (m)	Shielding Factor	Sample Thickness (cm)	Measured [He-3] (10^9 atoms/g)	δ[He-3] (10^7 atoms/g)	Standardized [He-3] (10^9 atoms/g)	Standardized δ[He-3] (10^7 atoms/g)	[He-4] (10^{14} atoms/g)	δ[He-4] (10^{13} atoms/g)	Measured [He-3] of CRONUS-P Standard (10^9 atoms/g)	δ[He-3] of CRONUS-P Standard (10^8 atoms/g)
Lower Roberts continued															
16-ROB-104-WAL	a	0.02831	-85.527901	-176.989	1900.7	0.9974	2.31	1.71	4.88	1.67	4.77	3.91	0.35	5.14	1.01
16-ROB-104-WAL	b	0.02438						1.68	4.83	1.64	4.72	3.42	0.31	5.14	1.01
16-ROB-105-WAL	a	0.0245	-85.527901	-176.99001	1900.7	0.9974	2.14	2.02	5.79	1.98	5.66	6.16	0.55	5.14	1.01
16-ROB-106-WAL	a	0.02546	-85.528	-176.99801	1899.7	0.9951	4.22	2.38	6.77	2.32	6.61	5.09	0.46	5.14	1.01
16-ROB-106-WAL	b	0.02033						2.34	8.33	2.29	8.14	5.06	0.32	5.14	1.01
16-ROB-107-WAL	a	0.02529	-85.527901	-176.985	1896.7	0.995	1.93	1.36	3.79	1.33	3.70	5.58	0.49	5.14	1.01
16-ROB-108-WAL	a	0.02605	-85.528	-176.979	1893.2	0.9967	2.25	2.01	5.65	1.96	5.52	3.88	0.35	5.14	1.01
16-ROB-109-WAL	a	0.0231	-85.528	-176.976	1890.2	0.9967	4.45	1.28	3.75	1.25	3.66	4.15	0.37	5.14	1.01
16-ROB-110-WAL	a	0.02601	-85.527702	-176.966	1889.2	0.9941	1.34	1.57	4.14	1.54	4.05	2.26	0.18	5.14	1.01
16-ROB-110-WAL	b	0.02829						1.57	5.82	1.53	5.69	2.59	0.24	5.14	1.01
16-ROB-111-BGE	a	0.01655	-85.525398	-176.979	1908.7	0.9978	1.43	1.53	4.12	1.50	4.03	2.50	0.20	5.14	1.01
16-ROB-111-BGE	b	0.02633						1.54	5.71	1.51	5.58	2.54	0.23	5.14	1.01
16-ROB-112-BGE	a	0.02879	-85.525497	-176.97701	1909.2	0.9978	1.82	1.28	3.95	1.24	3.83	4.80	0.64	5.18	0.73
16-ROB-112-BGE	b	0.01852						1.17	4.15	1.14	4.05	4.73	0.32	5.14	1.01
16-ROB-113-BGE	a	0.02742	-85.525597	-176.972	1906.2	0.9978	1.95	2.54	7.85	2.46	7.61	6.67	0.90	5.18	0.73
16-ROB-114-BGE	a	0.02563	-85.525597	-176.96899	1905.7	0.9979	1.56	2.08	5.87	2.03	5.74	3.94	0.35	5.14	1.01
16-ROB-114-BGE	b	0.02044						2.11	7.60	2.07	7.42	4.18	0.27	5.14	1.01
16-ROB-115-BGE	a	0.02197	-85.525597	-176.967	1905.2	0.998	2.13	2.45	6.91	2.39	6.76	4.72	0.42	5.14	1.01
16-ROB-116-BGE	a	0.0276	-85.525703	-176.966	1905.2	0.9976	2.28	3.63	9.95	3.54	9.72	7.51	0.66	5.14	1.01
16-ROB-116-BGE	b	0.0149						3.44	12.15	3.36	11.88	6.96	0.44	5.14	1.01
16-ROB-117-BGE	a	0.02473	-85.525703	-176.963	1905.2	0.9974	2.21	2.45	7.15	2.38	6.93	0.88	0.11	5.18	0.73
16-ROB-118-BBY	a	0.02426	-85.525398	-176.966	1903.7	0.9972	3.67	2.29	7.10	2.22	6.88	3.79	0.52	5.18	0.73
16-ROB-119-BBY	a	0.02529	-85.525398	-176.967	1905.2	0.9972	1.82	1.47	4.36	1.42	4.23	5.52	0.70	5.18	0.73
16-ROB-120-BBY	a	0.02924	-85.525398	-176.966	1904.7	0.9972	2.83	1.41	4.00	1.38	3.91	2.91	0.26	5.14	1.01
16-ROB-121-BBY	a	0.02683	-85.525398	-176.965	1905.2	0.9972	3.16	1.34	4.09	1.30	3.97	4.79	0.63	5.18	0.73
16-ROB-121-BBY	b	0.0177						1.31	3.87	1.28	3.78	4.31	0.34	5.14	1.01
16-ROB-122-BBY	a	0.02592	-85.525398	-176.963	1905.2	0.9972	1.75	2.03	6.30	1.96	6.10	5.12	0.67	5.18	0.73
Shielded Sample															
15-ROB-SHIELD1	a	0.04282	-	-	-	-	-	2.83	3.28	2.86	3.32	1.79	0.08	4.97	1.03

Table 4.2 Sandstone sample information and ^{21}Ne and ^{10}Be concentrations measured in quartz.

Sample ID	Aliquot	Weight for Ne-21 Analysis (g)	Weight for Be-10 Analysis (g)	Latitude (DD)	Longitude (DD)	Elevation (m)	Shielding Factor	Sample Thickness (cm)	Measured [Ne-21]* (10^9 atoms/g)	δ[Ne-21]* (10^7 atoms/g)	Measured [Ne-21] of CRONUS-A Standard (10^8 atoms/g)	δ[Ne-21] of CRONUS-A Standard (10^6 atoms/g)	Measured [Be-10] (10^7 atoms/g)	δ[Be-10] (10^5 atoms/g)
15-ROB-029-COL	a	0.1081	5.4288	-85.50998	-177.79202	2378	1	2	2.14	4.44	3.19	1.70	8.18	8.78
	b	0.1049	-						2.09	3.40	3.19	1.70	-	-
	c	0.1196	-						2.07	2.73	3.19	1.70	-	-
	d	0.1723	-						2.12	2.50	3.19	1.70	-	-
15-ROB-032-COL	a	0.1332	3.4951	-85.51025	-177.79535	2376	1	1.8	2.36	4.82	3.19	1.70	8.47	9.75
	b	0.1244	-						2.33	3.70	3.19	1.70	-	-
	c	0.1519	-						2.30	3.07	3.19	1.70	-	-
	d	0.1578	-						2.30	2.67	3.19	1.70	-	-
15-ROB-033-COL	a	0.1173	3.347	-85.5111	-177.80135	2388	1	2	2.16	3.43	3.19	1.70	8.50	11.38
	b	0.1184	-						2.15	2.73	3.19	1.70	-	-
	c	0.1228	-						2.14	2.55	3.19	1.70	-	-
15-ROB-034-COL	a	0.1066	3.1821	-85.51245	-177.79913	2361	1	2.8	1.65	2.68	3.19	1.70	7.85	8.84
	b	0.1393	-						1.63	2.14	3.19	1.70	-	-
	c	0.131	-						1.62	1.90	3.19	1.70	-	-
16-ROB-009-NLO	a	0.1452	4.105	-85.505203	-176.871	1829.52	0.9982	1.9	-	-	-	-	2.56	3.36
16-ROB-020-AND	a	0.1334	3.9744	-85.508102	-176.86501	1843.4	0.9993	2.3	-	-	-	-	2.93	3.77
16-ROB-060-RIN	a	0.1455	1.1961	-85.5214	-176.96899	1963.7	0.9948	2.1	-	-	-	-	4.62	6.36
16-ROB-062-RIN	a	0.1387	1.1245	-85.522499	-176.966	1957.2	0.9989	4.5	-	-	-	-	4.81	6.48
16-ROB-073-MON	a	0.1342	4.1403	-85.539101	-177.101	1786.56	0.9853	2.3	-	-	-	-	1.49	1.72
16-ROB-074-MON	a	0.1257	3.913	-85.538498	-177.105	1788.06	0.9812	2.2	-	-	-	-	1.81	2.18
16-ROB-075-MON	a	-	4.1403	-85.538498	-177.105	1792.56	0.9812	2.1	-	-	-	-	2.18	2.69
16-ROB-078-MON	a	-	3.913	-85.538696	-177.108	1834.56	0.9749	2	-	-	-	-	2.08	2.50
16-ROB-086-WIN	a	-	4.3681	-85.539597	-177.08099	1797.69	0.9857	2	-	-	-	-	0.94	1.38

*Assumed nucleogenic component is (7.7 ± 2.0) x 10^6 atoms $g^{-1,}$ which is subtracted from the measured [Ne-21] and δ[Ne-21] concentrations for age calculations.

Table 4.3 Apparent ^{3}He, ^{10}Be, and ^{21}Ne exposure ages. Italicized samples are considered outliers and samples listed in red are saturated with respect to St Scaling.

Sample ID	No.	Nuclide	Age (LSDn) (Ma)	Age (St) (Ma)
Roberts Col				
Misery A				
15-ROB-001-MZA	2	^{3}He	8.03 ± 0.19	8.99 ± 0.21
15-ROB-002-MZA	*2*	*^{3}He*	*5.69 ± 0.11*	*6.37 ± 0.13*
15-ROB-003-MZA	*2*	*^{3}He*	*6.11 ± 0.12*	*6.84 ± 0.14*
15-ROB-004-MZA	*2*	*^{3}He*	*4.38 ± 0.2*	*4.9 ± 0.23*
15-ROB-005-MZA	*2*	*^{3}He*	*6.22 ± 0.12*	*6.97 ± 0.14*
Misery B				
15-ROB-006-MZB	2	^{3}He	7.98 ± 0.16	8.97 ± 0.18
15-ROB-007-MZB	2	^{3}He	8.19 ± 0.16	9.21 ± 0.18
15-ROB-008-MZB	2	^{3}He	8.08 ± 0.16	9.09 ± 0.18
15-ROB-009-MZB	2	^{3}He	8.12 ± 0.16	9.13 ± 0.18
15-ROB-010-MZB	2	^{3}He	8.07 ± 0.16	9.08 ± 0.18
15-ROB-011-MZB	2	^{3}He	8.08 ± 0.16	9.09 ± 0.18
15-ROB-012-MZB	1	^{3}He	8.15 ± 0.16	9.17 ± 0.18
15-ROB-013-MZB	1	^{3}He	8.07 ± 0.16	9.08 ± 0.18
Misery C				
15-ROB-014-MZC	2	^{3}He	7.93 ± 0.16	8.89 ± 0.18
15-ROB-015-MZC	2	^{3}He	7.99 ± 0.16	8.96 ± 0.18
15-ROB-016-MZC	2	^{3}He	7.81 ± 0.16	8.76 ± 0.18
15-ROB-017-MZC	1	^{3}He	8.06 ± 0.16	9.04 ± 0.18
15-ROB-018-MZC	3	^{3}He	7.55 ± 0.15	8.46 ± 0.17
15-ROB-019-MZC	2	^{3}He	7.32 ± 0.15	8.2 ± 0.16
15-ROB-020-MZC	2	^{3}He	7.44 ± 0.21	8.34 ± 0.24
15-ROB-021-MZC	*2*	*^{3}He*	*5.01 ± 0.1*	*5.61 ± 0.11*
15-ROB-022-MZC	*2*	*^{3}He*	*4.76 ± 0.1*	*5.33 ± 0.11*
Misery D				
15-ROB-023-MZD	1	^{3}He	8.02 ± 0.16	9.02 ± 0.18
15-ROB-024-MZD	1	^{3}He	7.75 ± 0.16	8.72 ± 0.17
15-ROB-025-MZD	1	^{3}He	8.08 ± 0.16	9.09 ± 0.18
15-ROB-026-MZD	*1*	*^{3}He*	*7.52 ± 0.15*	*8.46 ± 0.17*
15-ROB-027-MZD	2	^{3}He	8.32 ± 0.17	9.35 ± 0.19
Roberts Col				
15-ROB-028-COL	2	^{3}He	11.19 ± 0.22	12.72 ± 0.25
15-ROB-029-COL	1	^{10}Be	9.88 ± 2.97	0 ± 0
15-ROB-029-COL	4	^{21}Ne	11.73 ± 0.23	14.28 ± 0.29
15-ROB-030-COL	2	^{3}He	10.02 ± 0.29	11.4 ± 0.33
15-ROB-031-COL	3	^{3}He	8.74 ± 0.17	9.92 ± 0.2
15-ROB-032-COL	1	^{10}Be	10.7 ± 4.82	0 ± 0
15-ROB-032-COL	4	^{21}Ne	12.92 ± 0.26	15.72 ± 0.31
15-ROB-033-COL	1	^{10}Be	10.61 ± 5.36	0 ± 0
15-ROB-033-COL	3	^{21}Ne	11.9 ± 0.24	14.5 ± 0.29
15-ROB-034-COL	1	^{10}Be	9.33 ± 2.37	0 ± 0
15-ROB-034-COL	3	^{21}Ne	9.26 ± 0.19	11.26 ± 0.23

Sample ID	No.	Nuclide	Age (LSDn) (Ma)	Age (St) (Ma)
Upper Roberts				
Arena Moraine				
15-ROB-035-ARM	2	^{3}He	2.63 ± 0.07	2.97 ± 0.08
15-ROB-036-ARM	2	^{3}He	2.89 ± 0.06	3.26 ± 0.07
15-ROB-038-ARM	2	^{3}He	2.58 ± 0.12	2.91 ± 0.14
15-ROB-039-ARM	2	^{3}He	2.53 ± 0.07	2.86 ± 0.08
15-ROB-040-ARM	2	^{3}He	2.69 ± 0.05	3.04 ± 0.06
15-ROB-041-ARM	2	^{3}He	2.76 ± 0.06	3.12 ± 0.06
Eine Moraine				
15-ROB-042-EIN	3	^{3}He	1.28 ± 0.04	1.45 ± 0.04
15-ROB-043-EIN	3	^{3}He	1.23 ± 0.03	1.38 ± 0.03
15-ROB-044-EIN	*3*	*^{3}He*	*0.9 ± 0.05*	*1.01 ± 0.06*
15-ROB-045-EIN	2	^{3}He	1.39 ± 0.03	1.56 ± 0.03
15-ROB-046-EIN	2	^{3}He	2.09 ± 0.06	2.36 ± 0.07
15-ROB-047-EIN	2	^{3}He	1.11 ± 0.1	1.25 ± 0.12
15-ROB-048-EIN	2	^{3}He	1.04 ± 0.02	1.17 ± 0.02
Kleine Moraine				
15-ROB-049-KLE	1	^{3}He	1.08 ± 0.02	1.22 ± 0.02
15-ROB-050-KLE	3	^{3}He	1.09 ± 0.02	1.23 ± 0.03
15-ROB-051-KLE	1	^{3}He	1.38 ± 0.03	1.56 ± 0.03
15-ROB-052-KLE	1	^{3}He	1.3 ± 0.03	1.46 ± 0.03
15-ROB-053-KLE	2	^{3}He	0.99 ± 0.02	1.11 ± 0.02
15-ROB-054-KLE	2	^{3}He	1.32 ± 0.03	1.49 ± 0.03
Nacht Moraine				
15-ROB-055-NAC	2	^{3}He	1.07 ± 0.02	1.2 ± 0.02
15-ROB-056-NAC	2	^{3}He	1.04 ± 0.04	1.17 ± 0.04
15-ROB-057-NAC	2	^{3}He	1.26 ± 0.05	1.42 ± 0.05
15-ROB-058-NAC	1	^{3}He	1.25 ± 0.02	1.4 ± 0.03
15-ROB-059-NAC	2	^{3}He	1.08 ± 0.03	1.21 ± 0.03
15-ROB-060-NAC	*1*	*^{3}He*	*1.54 ± 0.03*	*1.72 ± 0.03*
15-ROB-061-NAC	1	^{3}He	1.08 ± 0.02	1.21 ± 0.02
Musik Moraine				
15-ROB-062-MUS	1	^{3}He	1.12 ± 0.02	1.25 ± 0.03
15-ROB-063-MUS	1	^{3}He	1.07 ± 0.02	1.2 ± 0.02
15-ROB-064-MUS	*1*	*^{3}He*	*0.62 ± 0.01*	*0.69 ± 0.01*
Lower Roberts				
No Lunch Moraine				
16-ROB-009-NLO	1	^{10}Be	1.2 ± 0.02	1.37 ± 0.03
Andrew Moraine				
16-ROB-015-AND	2	^{3}He	1.63 ± 0.03	1.77 ± 0.04
16-ROB-016-AND	2	^{3}He	1.3 ± 0.03	1.42 ± 0.03
16-ROB-020-AND	1	^{10}Be	1.43 ± 0.03	1.66 ± 0.03
Pot of Stew Moraines				
16-ROB-023-PSO	2	^{3}He	1.39 ± 0.03	1.51 ± 0.03
16-ROB-024-PSO	*1*	*^{3}He*	*1.17 ± 0.03*	*1.27 ± 0.03*
16-ROB-028-PSI	2	^{3}He	1.79 ± 0.04	1.95 ± 0.04
16-ROB-029-PSI	1	^{3}He	2.05 ± 0.05	2.24 ± 0.05
16-ROB-030-PSI	1	^{3}He	1.57 ± 0.04	1.72 ± 0.04

Table 4.3 continued.

Sample ID	No.	Nuclide	Age (LSDn) (Ma)	Age (St) (Ma)
Lower Roberts continued				
Windbreaker Moraine				
16-ROB-031-WBK	2	^{3}He	2.51 ± 0.11	2.74 ± 0.12
16-ROB-032-WBK	2	^{3}He	2.83 ± 0.06	3.1 ± 0.06
16-ROB-033-WBK	1	^{3}He	1.78 ± 0.04	1.95 ± 0.05
16-ROB-034-WBK	*2*	*^{3}He*	*3.65 ± 0.07*	*3.99 ± 0.08*
16-ROB-036-WBK	2	^{3}He	2.82 ± 0.06	3.08 ± 0.06
16-ROB-037-WBK	2	^{3}He	2.37 ± 0.05	2.59 ± 0.05
Sunnyside Up Moraine				
16-ROB-038-SSU	2	^{3}He	2.09 ± 0.04	2.29 ± 0.05
16-ROB-039-SSU	2	^{3}He	2.06 ± 0.07	2.25 ± 0.08
16-ROB-040-SSU	2	^{3}He	2.5 ± 0.05	2.73 ± 0.05
16-ROB-041-SSU	2	^{3}He	2.5 ± 0.05	2.73 ± 0.05
16-ROB-042-SSU	2	^{3}He	2.59 ± 0.05	2.82 ± 0.06
16-ROB-043-SSU	2	^{3}He	2.93 ± 0.06	3.2 ± 0.06
16-ROB-044-SSU	2	^{3}He	1.9 ± 0.04	2.07 ± 0.04
Hunky Dory Moraine				
16-ROB-045-HDY	1	^{3}He	2.76 ± 0.07	3.02 ± 0.08
16-ROB-046-HDY	3	^{3}He	2.78 ± 0.06	3.04 ± 0.06
16-ROB-047-HDY	1	^{3}He	2.03 ± 0.06	2.22 ± 0.06
16-ROB-048-HDY	2	^{3}He	2.69 ± 0.05	2.94 ± 0.06
16-ROB-049-HDY	1	^{3}He	2.89 ± 0.08	3.16 ± 0.09
16-ROB-050-HDY	*1*	*^{3}He*	*3.45 ± 0.1*	*3.77 ± 0.11*
16-ROB-051-HDY	1	^{3}He	2.77 ± 0.08	3.03 ± 0.09
Banana Split Moraine				
16-ROB-052-BAS	1	^{3}He	2.89 ± 0.07	3.17 ± 0.08
16-ROB-053-BAS	2	^{3}He	2.96 ± 0.06	3.24 ± 0.06
16-ROB-054-BAS	1	^{3}He	2.84 ± 0.08	3.11 ± 0.09
16-ROB-055-BAS	1	^{3}He	3.09 ± 0.09	3.39 ± 0.1
16-ROB-056-BAS	1	^{3}He	2.7 ± 0.07	2.96 ± 0.08
16-ROB-057-BAS	2	^{3}He	2.83 ± 0.07	3.1 ± 0.07
16-ROB-058-BAS	2	^{3}He	2.88 ± 0.06	3.16 ± 0.06
Ringleader Moraine				
16-ROB-059-RIN	1	^{3}He	3.09 ± 0.06	3.4 ± 0.07
16-ROB-060-RIN	1	^{10}Be	2.67 ± 0.08	3.39 ± 0.12
16-ROB-061-RIN	2	^{3}He	2.85 ± 0.06	3.13 ± 0.06
16-ROB-062-RIN	1	^{10}Be	3.03 ± 0.1	4 ± 0.17
16-ROB-063-RIN	*2*	*^{3}He*	*4.09 ± 0.11*	*4.49 ± 0.12*
16-ROB-064-RIN	1	^{3}He	3.41 ± 0.08	3.75 ± 0.09
16-ROB-065-RIN	*2*	*^{3}He*	*2.11 ± 0.14*	*2.32 ± 0.16*
Slim Shady Moraine				
16-ROB-066-MNM	*1*	*^{3}He*	*1.87 ± 0.06*	*2.03 ± 0.06*
16-ROB-067-MNM	2	^{3}He	0.85 ± 0.03	0.92 ± 0.03
16-ROB-068-MNM	*1*	*^{3}He*	*1.46 ± 0.05*	*1.58 ± 0.05*
16-ROB-069-MNM	1	^{3}He	0.51 ± 0.02	0.56 ± 0.02
16-ROB-070-MNM	*2*	*^{3}He*	*1.43 ± 0.05*	*1.55 ± 0.05*
16-ROB-071-MNM	1	^{3}He	0.7 ± 0.03	0.76 ± 0.03
16-ROB-072-MNM	2	^{3}He	0.39 ± 0.01	0.43 ± 0.01

Sample ID	No.	Nuclide	Age (LSDn) (Ma)	Age (St) (Ma)
Lower Roberts continued				
Monet Moraine				
16-ROB-073-MON	1	^{10}Be	0.65 ± 0.01	0.72 ± 0.01
16-ROB-074-MON	1	^{10}Be	0.82 ± 0.02	0.92 ± 0.02
16-ROB-075-MON	1	^{10}Be	1.03 ± 0.02	1.17 ± 0.02
16-ROB-076-MON	1	^{3}He	0.53 ± 0.02	0.57 ± 0.02
16-ROB-077-MON	2	^{3}He	0.54 ± 0.01	0.58 ± 0.01
16-ROB-078-MON	1	^{10}Be	0.94 ± 0.02	1.07 ± 0.02
Winterfell Moraine				
16-ROB-079-WIN	1	^{3}He	0.79 ± 0.02	0.86 ± 0.03
16-ROB-080-WIN	1	^{3}He	0.82 ± 0.03	0.89 ± 0.03
16-ROB-081-WIN	2	^{3}He	0.72 ± 0.01	0.78 ± 0.02
16-ROB-082-WIN	2	^{3}He	0.5 ± 0.01	0.54 ± 0.01
16-ROB-083-WIN	1	^{3}He	0.92 ± 0.03	1 ± 0.04
16-ROB-084-WIN	2	^{3}He	0.77 ± 0.02	0.84 ± 0.02
16-ROB-085-WIN	1	^{3}He	0.98 ± 0.03	1.06 ± 0.03
16-ROB-086-WIN	*1*	*^{10} Be*	*0.38 ± 0.01*	*0.42 ± 0.01*
The Wall Moraine				
16-ROB-104-WAL	2	^{3}He	1.93 ± 0.04	2.12 ± 0.04
16-ROB-105-WAL	1	^{3}He	2.3 ± 0.07	2.52 ± 0.07
16-ROB-106-WAL	2	^{3}He	2.75 ± 0.05	3.01 ± 0.06
16-ROB-107-WAL	1	^{3}He	1.56 ± 0.04	1.7 ± 0.05
16-ROB-108-WAL	1	^{3}He	2.3 ± 0.06	2.52 ± 0.07
16-ROB-109-WAL	1	^{3}He	1.51 ± 0.04	1.65 ± 0.05
16-ROB-110-WAL	2	^{3}He	1.8 ± 0.04	1.97 ± 0.04
Barrage Moraine				
16-ROB-111-BGE	2	^{3}He	1.72 ± 0.03	1.89 ± 0.04
16-ROB-112-BGE	*2*	*^{3}He*	*1.38 ± 0.05*	*1.51 ± 0.06*
16-ROB-113-BGE	1	^{3}He	2.85 ± 0.09	3.12 ± 0.1
16-ROB-114-BGE	2	^{3}He	2.36 ± 0.05	2.58 ± 0.05
16-ROB-115-BGE	1	^{3}He	2.78 ± 0.08	3.04 ± 0.09
16-ROB-116-BGE	*2*	*^{3}He*	*4.04 ± 0.1*	*4.42 ± 0.11*
16-ROB-117-BGE	1	^{3}He	2.76 ± 0.08	3.02 ± 0.09
Baby Moraine				
16-ROB-118-BBY	1	^{3}He	2.62 ± 0.08	2.86 ± 0.09
16-ROB-119-BBY	1	^{3}He	1.65 ± 0.05	1.8 ± 0.05
16-ROB-120-BBY	*1*	*^{3}He*	*1.61 ± 0.05*	*1.76 ± 0.05*
16-ROB-121-BBY	*2*	*^{3}He*	*1.51 ± 0.03*	*1.66 ± 0.03*
16-ROB-122-BBY	1	^{3}He	2.27 ± 0.07	2.49 ± 0.08

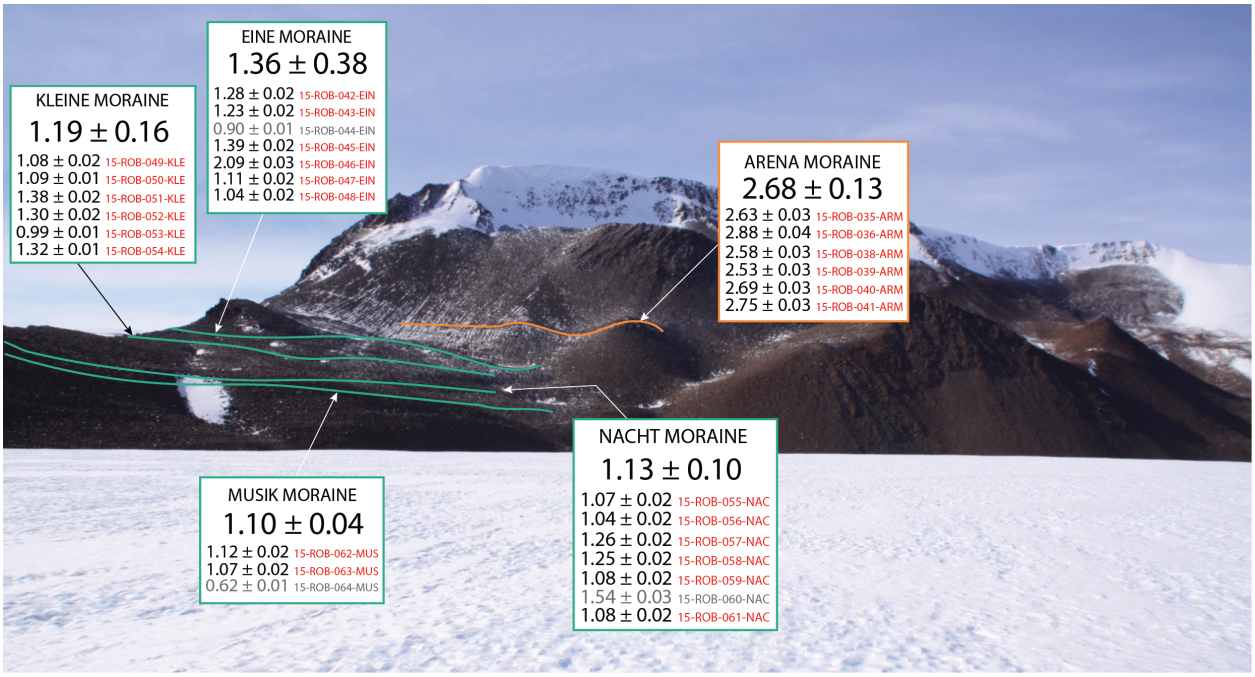

Figure 4.2 Apparent ^{3}He exposure ages at Upper Roberts. Gray text marks samples eliminated as outliers and not included when calculating mean landform age, shown in large text beneath each moraine name.

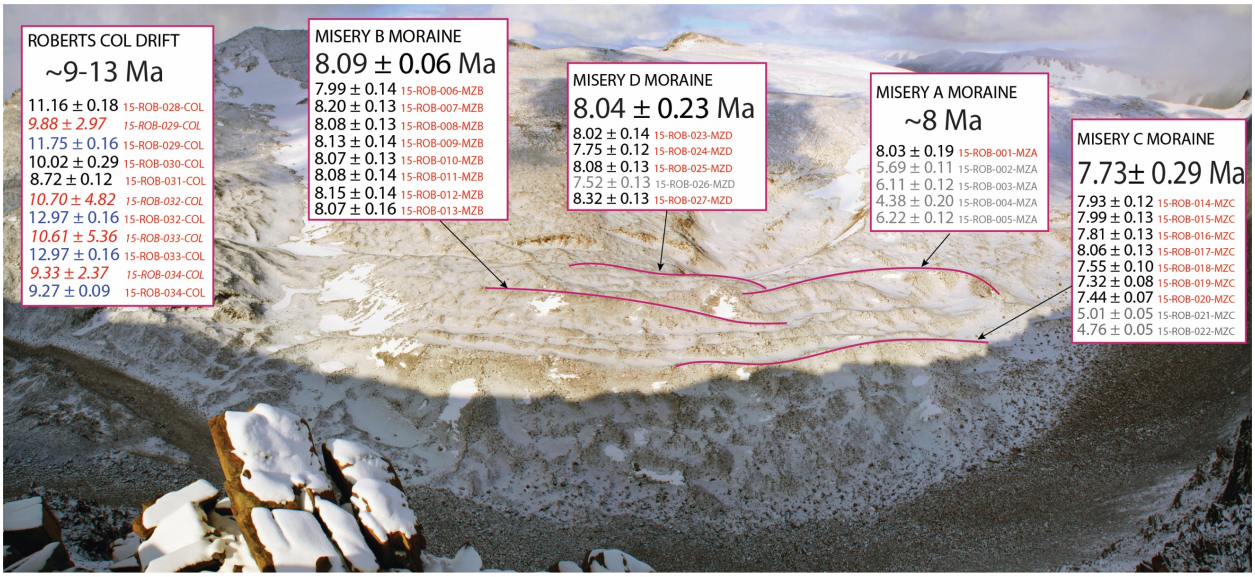

Figure 4.1 Apparent exposure ages Roberts Col. Black, blue, and red text denote ^{3}He, ^{21}Ne, and ^{10}Be ages, respectively. Gray text marks samples eliminated as outliers and not included when calculating mean landform age, shown in large text beneath each moraine name. As the age of the Misery A moraine is based only on one sample, the age of the landform is considered approximate. Similarly, I provide an approximate age range for the Roberts Col drift, which may represent more than one expansion of the EAIS.

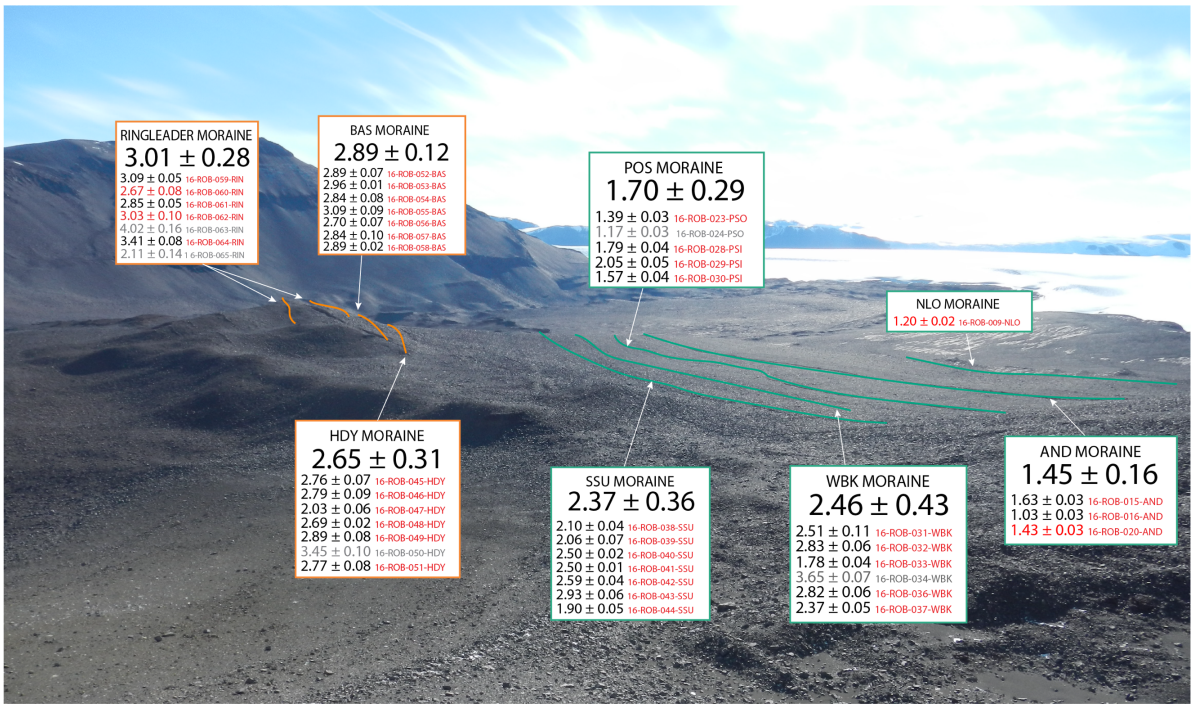

Figure 4.4 Apparent exposure ages along the Lower Roberts northern transect (A–B in Figure 3.6). Black and red text denote ^{3}He and ^{10}Be ages, respectively. Gray text marks samples eliminated as outliers and not included when calculating mean landform age, shown in large text beneath each moraine name.

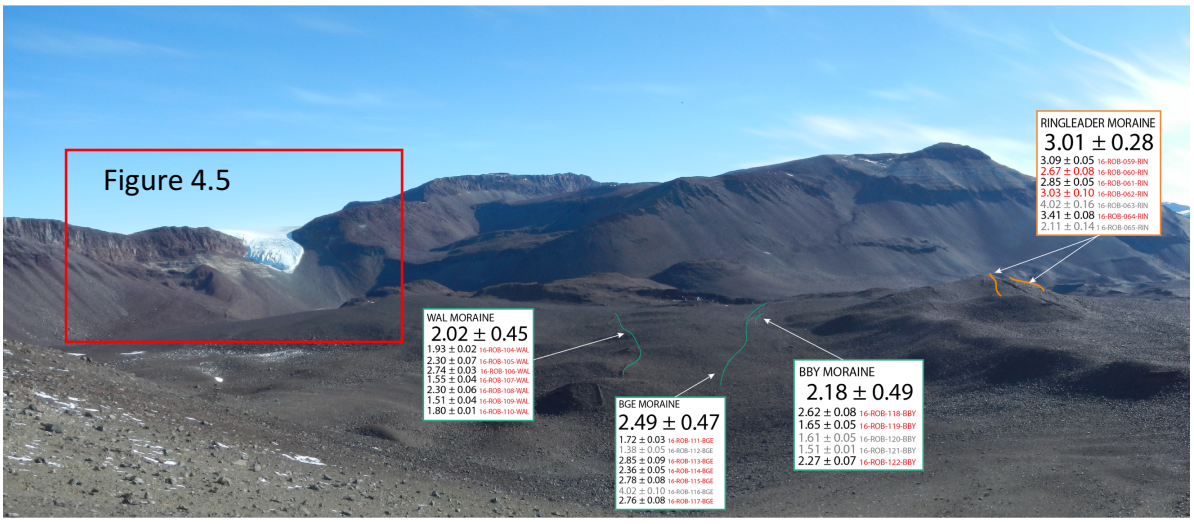

Figure 4.3 Apparent exposure ages along the Lower Roberts southern transect (B–C in Figure 3.6). Black and red text denote ^{3}He and ^{10}Be ages, respectively. Gray text marks samples eliminated as outliers and not included when calculating mean landform age, shown in large text beneath each moraine name. The location of Figure 4.5, which shows the lower portion of the southern transect, is marked by the red box.

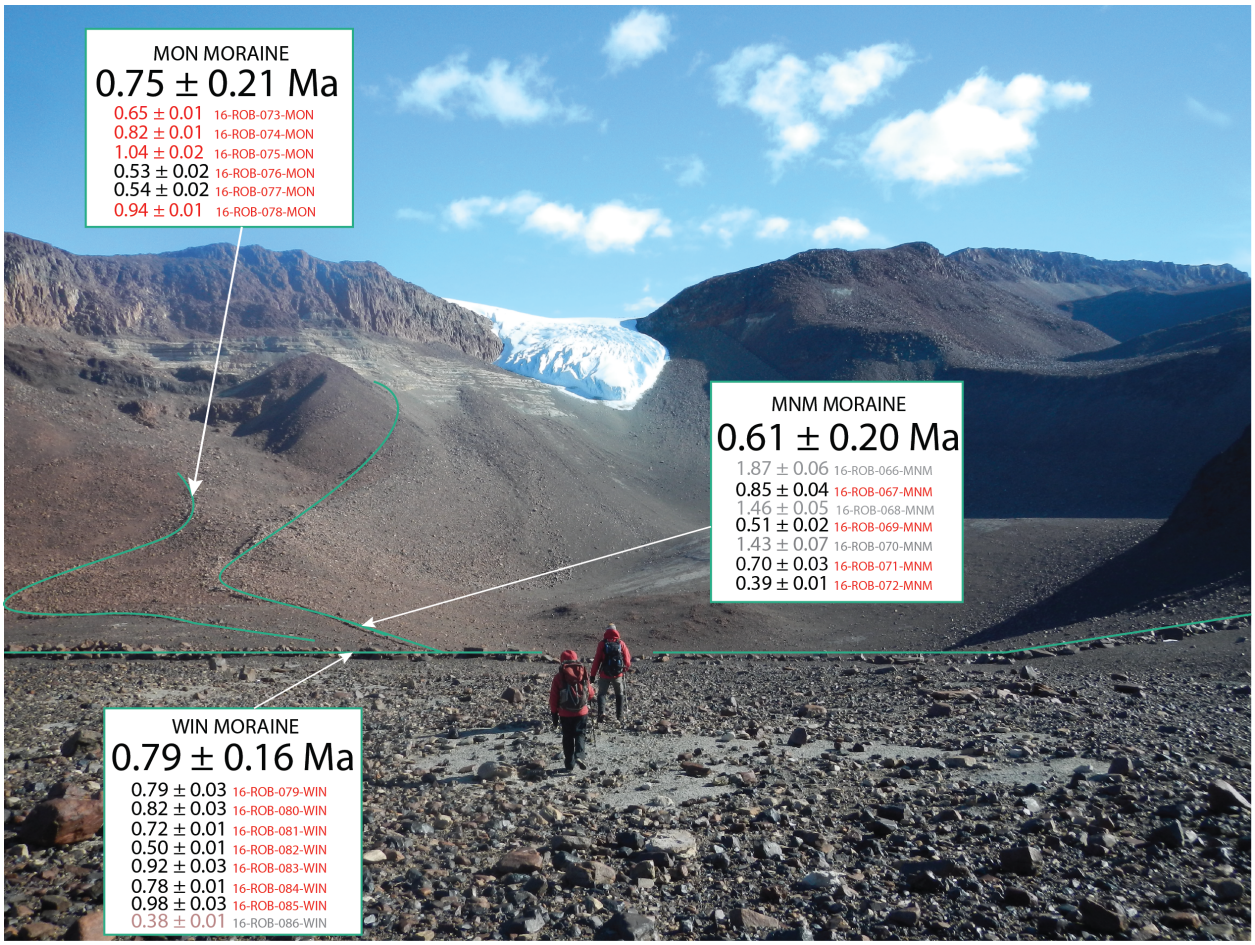

Figure 4.5 Apparent exposure ages in the Southern Basin. This Southern Basin is in southernmost portion of the Lower Roberts southern transect (B–C in Figure 3.6). Black and red text denote ^{3}He and ^{10}Be ages, respectively. Gray text marks samples eliminated as outliers and not included when calculating mean landform age, shown in large text beneath each moraine name. The glacier shown in the photo is a tongue of the EAIS itself.

CHAPTER 5

DISCUSSION

The glacial record at Roberts Massif extends back to the middle Miocene, with apparent exposure ages ranging from ~13 Ma to 0.4 Ma. Generally, these ages indicate that the EAIS was larger than present during the periods ~13–8 Ma and ~3 – < 0.6 Ma. In addition to discussing the implications of this glacial record for ice sheet sensitivity to climate, I explore potential reasons for the reduced moraine scatter in this chronology compared with previous Antarctic records.

5.1 Reduced moraine age scatter

For 86 of the dolerite samples, I measured ^{3}He concentrations in multiple aliquots of purified pyroxene separates. With a few exceptions, the standard deviation of ^{3}He concentrations for the multiple aliquots was generally equal to or less than the analytical precision of the measurements (Figure 5.1). I attribute the high degree of reproducibility among these measurements to the etching of pyroxenes in hydrofluoric acid, which serves to improve nuclide measurement in two ways: 1) by removing groundmass adhering to the pyroxene grains, such as feldspar, whose mineral structure does not retain ^{3}He, but whose weight effectively dilutes the ^{3}He concentration; 2) by removing the outer few microns of the pyroxene grains, which typically contain higher concentrations of non-cosmogenic radiogenic ^{4}He due to implantation (Blard and Farley, 2008; Bromley et al., 2014). Removing this non-cosmogenic component increases the ^{3}He/^{4}He ratio significantly, resulting in more precise measurement of cosmogenic ^{3}He, which in turn may reduce overall scatter in the data set.

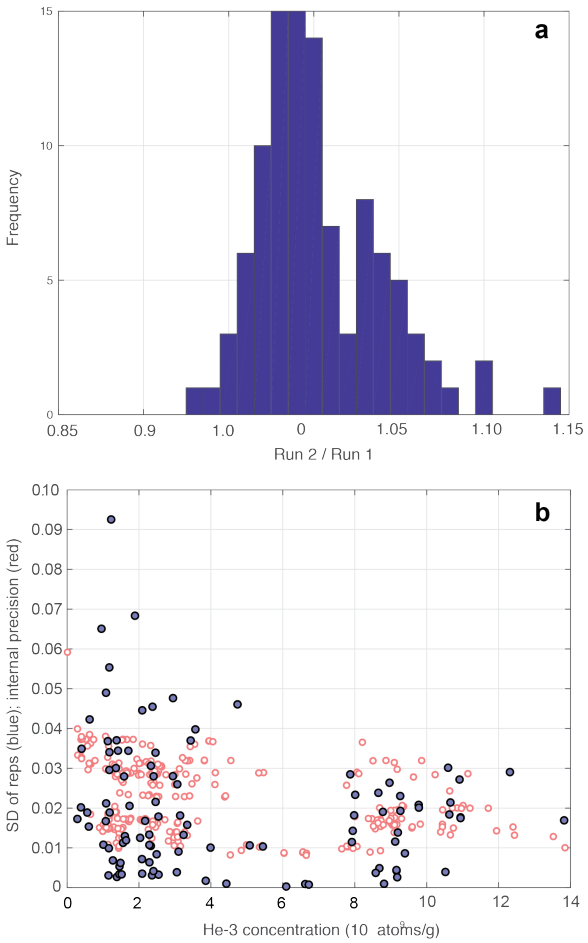

Figure 5.1 ^{3}He concentration reproducibility plots . a) Histogram showing the ratio of ^{3}He concentrations between two different aliquots of the same sample. This difference is typically < 5%. b) scatter plot showing that, for the most part, the standard deviation of ^{3}He concentrations measured in multiple aliquots of the same sample is comparable to the analytical precision.

In addition to the high inter-aliquot reproducibility of my ^{3}He measurements, the generally low degree of age scatter in this moraine record represents an improvement over previous Antarctic studies (e.g., Brown, 1991). For example, Brook et al. (1993) sampled three moraines for which the coefficient of variance (CV) of the raw age populations are > 70%. However, the standard deviation on their fourth and oldest moraine is only 6% of the mean. Similarly, at the Dominion Range, central Transantarctic Mountains, the CV on the Oliver Platform moraine is 38% (Ackert and Kurz, 2004). At Roberts Massif, there are varying degrees

of age scatter, but generally, the CVs on the raw ages are < 30% and on 9 moraines are < 15%. Once outliers were eliminated (discussed below), CVs are typically < 20% and on 8 moraines are < 10%. Although I have not eliminated geologic scatter in the moraine record, the overall moraine scatter at Roberts Massif is low relative to previous records.

I attribute the improvement in moraine scatter to 1) the updated boulder selection criteria discussed in the Methods chapter and 2) the relatively large number of exposure samples measured from each landform (typically seven from each moraine). Only nine boulders in the record at Roberts Massif were eliminated as obvious old outliers thought to have inherited nuclides. Thus, it appears that applying these boulder selection criteria when sampling cold-based deposits may reduce the frequency of sampling boulders with considerable inheritance.

Figure 5.2 shows the results of a resampling exercise that I performed to highlight the importance of collecting many samples from each landform. To establish how much the average moraine age could change if fewer boulders were sampled, I calculated the average age of every combination of 6, 5, 4, and 3 boulders on a given moraine and displayed these mean ages in a histogram (the results for Ringleader are shown in Figure 5.2, but the results are similar for all moraines where seven boulders were sampled; MATLAB script provided in Appendix H). When I subsampled three boulders, the average age of the moraine ranged from 2.54 Ma to 3.53 Ma (~1 Ma range); when I subsampled six boulders, the average age range for the moraine became from 2.86–3.19 Ma (~0.3 Ma range). Even prior to rejecting outliers, it is apparent that the possible range of average moraine age narrows when more data are included, thus highlighting the value of measuring large number of samples on each landform in the Antarctic, where geologic scatter remains a persistent limitation in surface-exposure chronologies.

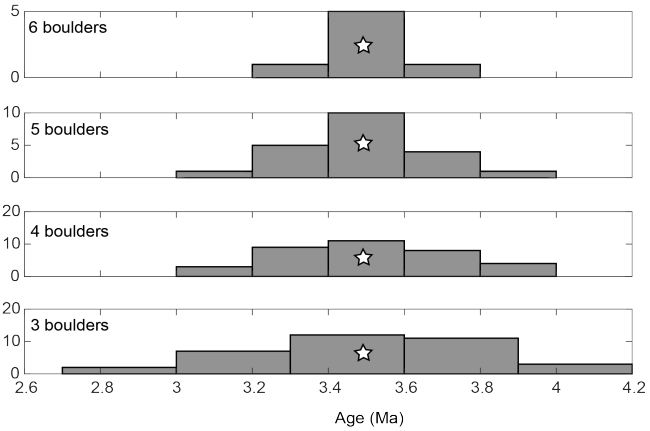

Figure 5.2 Resampling results for the Ringleader moraine (Lower Roberts). These histograms depict the distribution of averages ages of each combination of 6, 5, 4, and 3 boulders on that moraine. White stars indicate the average of all seven ages on the moraine.

5.2 Determining Moraine Age

I employed geomorphic indicators, such as relative weathering characteristics, and, where applicable, cross-cutting relationships, to determine that moraines further from the current ice sheet margins are generally older than more proximal moraines. In temperate settings, where glacial readvances are likely to "erase" evidence of previous glacial positions, this assumption is not usually problematic. However, under cold-based glacial conditions, such as in the Antarctic, the ice can advance over older landforms without disturbing those deposits. Despite this, both the raw ages in our study and the amount of boulder weathering (i.e., redness, pitting) generally decrease in stratigraphic order (with both elevation and distance) towards modern ice sheet. Based on these observations, and on previous work done by Bromley et al. (2010) at Reedy Glacier and Staiger et al. (2006) adjacent to Ferrar Glacier showing that older limits are typically more extensive, I have chosen to operate under the assumption that the moraines do, in general, get younger towards the current ice sheet margins.

Using this model, I eliminated likely outliers by inferring that no boulders on a given moraine should be older than all boulders on the moraine above/outboard of it or younger than every boulder on the moraine below/inboard of it within the analytical uncertainty of the boulder age. To maintain internal consistency with this method, the maximum/minimum of each moraine, which serves as the bounding limit for eliminating outliers on the surrounding moraines, was recalculated with each successive elimination. On the Ringleader moraine, where there is no older moraine to provide a bounding maximum age, I eliminated the oldest age as an outlier because it was well beyond of 1σ of the mean. Similarly, I eliminated the two youngest boulders on the Misery C moraine, (stratigraphically, the youngest moraine in the complex), and the youngest boulder on the Musik moraine (the lowest moraine limit at Upper Roberts), as they gave ages < 1σ of the mean. A MATLAB script that performs this outlier elimination based on morphostratigraphic relationships is provided in APPENDIX F.

Typically, the method employed eliminates only extreme outliers at each subsite. However, along the Lower Roberts southern transect, a number of outlier samples are close in age to those that were not eliminated (on the BBY and BGE moraines), indicating that this may not be the ideal outlier elimination method for those moraines. Possible explanations for the scatter on those moraines are addressed in Section 5.4, but as the inclusion or rejection of those ages as outliers does not change the moraine age beyond 1σ of the mean, my conclusions are not affected. In sum, this method eliminates only a few boulders per site, constituting 17% of the total data, whereas the rejection of all ages beyond 2σ of the mean removes only one outlier in the entire record (despite clear scatter on some moraines), while removing ages beyond 1σ of the mean would result in me eliminating 30% of the data set.

Despite this elimination procedure, the presence of geologic scatter in the data set is indicated by 1) the fact that the uncertainty in moraine ages is significantly greater than the analytical uncertainty of each measurement, and 2) the high reduced-χ^2 and CV values of some moraines (Table 5.1). Exceptions to this pattern include the Misery moraines and the ARM & BAS moraines. Nonetheless, since the age distributions of most moraines at Roberts do not appear to exhibit either young or old biases (skewness values are between -1 and 1; Table 5.1; method modified from Applegate et al., 2010), I have chosen the mean age to represent the timing of moraine occupation and the standard deviation of the population as the uncertainty. However, I recognize that the spread of ages may represent real geologic events. For example, if cold-based ice occupied the same area on multiple occasions without disturbing the underlying deposits, the minimum age of a particular moraine population might then represent the last time ice last occupied a particular position. Thus, I also present the age range of each moraine displayed as a boxplot rather than a probability density function to enable ready evaluation of the whole population of boulder ages (Figure 5.3, Figure 5.4). A MATLAB script that generates the boxplots is provided in Appendix G. Other considerations regarding the true moraine ages and their geologic context are discussed below.

Table 5.1 Moraine ages and statistics.

			Raw Data						*St Scaling**		*LSDn Scaling**				
Moraine	Elevation	Number of samples kept (number excluded)	Mean LSDn age (Ma)	Mean St age (Ma)	LSDn Age Range (Ma)	Skewness	CV	Reduced χ^2	Mean Age (Ma)	Range (Ma)	Mean age (Ma)	Range (Ma)	Skewness	CV	Reduced χ^2
Roberts Col															
Roberts Col	2377	11 (0)	-	-	8.74 - 12.92	-	-	-	-	9.92 - 15.72	-	8.74 - 12.92	-	-	31.04
Misery D	2249	4 (1)	7.94 ± 0.31	8.93 ± 0.35	7.52 - 8.32	-0.20	4%	3.87	9.04 ± 0.26	8.72 - 9.35	8.04 ± 0.23	7.75 - 8.32	-0.11	3%	2.11
Misery A	2198	1 (4)	6.09 ± 1.31	6.81 ± 1.47	4.38 - 8.03	-0.28	22%	47.45	8.99 ± 0.19	8.99 - 8.99	8.03 ± 0.19	8.03 - 8.03	-0.28	-	-
Misery B	2252	8 (0)	8.09 ± 0.06	9.1 ± 0.07	7.98 - 8.19	-0.28	1%	0.15	9.10 ± 0.07	8.97 - 9.21	8.09 ± 0.06	7.98 - 8.19	-0.28	1%	0.15
Misery C	2215	5 (2)	7.09 ± 1.28	7.96 ± 1.44	4.76 - 8.06	-1.21	18%	145.47	8.66 ± 0.33	8.2 - 9.04	7.73 ± 0.29	7.32 - 8.06	-0.26	4%	3.35
Upper Roberts															
Arena	2303	6 (0)	2.68 ± 0.13	3.03 ± 0.15	2.53 - 2.89	0.51	5%	4.18	3.03 ± 0.15	2.86 - 3.26	2.68 ± 0.13	2.53 - 2.89	0.51	5%	4.18
Eine	2255	6 (1)	1.29 ± 0.39	1.45 ± 0.44	0.9 - 2.09	1.06	30%	64.53	1.53 ± 0.43	1.17 - 2.36	1.36 ± 0.38	1.04 - 2.09	1.38	28%	81.41
Kleine	2241	6 (0)	1.19 ± 0.16	1.34 ± 0.18	0.99 - 1.38	-0.07	13%	49.95	1.34 ± 0.18	1.11 - 1.56	1.19 ± 0.16	0.99 - 1.38	-0.07	13%	49.95
Nacht	2221	6 (1)	1.19 ± 0.18	1.33 ± 0.2	1.04 - 1.54	1.15	15%	37	1.27 ± 0.11	1.17 - 1.42	1.13 ± 0.10	1.04 - 1.26	0.64	9%	10.31
Musik	2215	3 (1)	0.94 ± 0.28	1.05 ± 0.31	0.62 - 1.12	-0.69	30%	390.88	1.23 ± 0.36	1.20 - 1.25	1.10 ± 0.04	1.07 - 1.12	-	4%	3.13
Lower Roberts															
Ringleader	1957	5 (2)	3.04 ± 0.62	3.5 ± 0.69	2.11 - 4.09	0.29	20%	31.23	3.53 ± 0.34	3.13 - 4.00	3.01 ± 0.28	2.67 - 3.41	0.27	9%	14.17
Banana	1914	7 (0)	2.89 ± 0.12	3.16 ± 0.13	2.7 - 3.09	0.32	4%	2.51	3.16 ± 0.13	2.96 - 3.39	2.89 ± 0.12	2.70 - 3.09	0.32	4%	2.51
Hunky	1895	6 (1)	2.77 ± 0.41	3.03 ± 0.45	2.03 - 3.45	-0.20	15%	35.29	2.90 ± 0.34	2.22 - 3.16	2.65 ± 0.31	2.03 - 2.89	-1.62	12%	26.20
Sunnyside Up	1872	7 (0)	2.37 ± 0.36	2.58 ± 0.4	1.9 - 2.93	0.17	15%	56.42	2.58 ± 0.40	2.07 - 3.2	2.37 ± 0.36	1.90 - 2.93	0.17	15%	56.42
Windbreaker	1877	5 (2)	2.66 ± 0.62	2.91 ± 0.68	1.78 - 3.65	0.26	23%	134.72	2.69 ± 0.47	1.95 - 3.10	2.46 ± 0.43	1.78 - 2.83	-0.77	17%	86.54
Pot 'O Stew	1865	4 (1)	1.59 ± 0.34	1.74 ± 0.38	1.17 - 2.05	0.13	21%	105.19	1.85 ± 0.31	1.51 - 2.24	1.70 ± 0.29	1.39 - 2.05	0.19	17%	67.96
Andrew	1830	3 (0)	1.45 ± 0.16	1.62 ± 0.18	1.3 - 1.63	0.22	11%	31.04	1.62 ± 0.18	1.42 - 1.77	1.45 ± 0.16	1.30 - 1.63	0.22	11%	31.04
No Lunch	1830	1 (0)	1.20 ± 0.02	1.37 ± 0.02	-	-	-	-	1.37 ± 0.02	1.37 - 1.37	1.20 ± 0	1.20 - 1.20	-	-	-
Baby	1905	3 (2)	1.93 ± 0.49	2.11 ± 0.53	1.51 - 2.62	0.56	25%	92.72	2.39 ± 0.54	1.8 - 2.86	2.18 ± 0.49	1.65 - 2.62	-0.34	22%	74.64
Barrage	1906	5 (2)	2.55 ± 0.87	2.8 ± 0.95	1.38 - 4.04	0.30	34%	218.54	2.73 ± 0.52	1.89 - 3.12	2.49 ± 0.47	1.72 - 2.85	-1.00	19%	178.08
The Wall	1896	7 (0)	2.02 ± 0.45	2.21 ± 0.49	1.51 - 2.75	0.35	22%	84.77	2.21 ± 0.49	1.65 - 3.01	2.02 ± 0.45	1.51 - 2.75	0.35	22%	84.77
Winterfell	1818	7 (1)	0.74 ± 0.2	0.8 ± 0.22	0.38 - 0.98	-0.67	27%	415.36	0.86 ± 0.17	0.54 - 1.06	0.79 ± 0.16	0.50 - 0.98	-0.69	20%	151.38
Monet	1791	6 (0)	0.75 ± 0.21	0.84 ± 0.25	0.53 - 1.03	0.17	28%	193.65	0.84 ± 0.25	0.58 - 1.17	0.75 ± 0.21	0.53 - 1.03	0.17	28%	193.65
Slim Shady	1774	4 (3)	1.03 ± 0.56	1.12 ± 0.6	0.39 - 1.87	0.31	54%	1309.13	0.67 ± 0.22	0.43 - 0.92	0.61 ± 0.20	0.39 - 0.85	0.10	33%	304.37

*Landform ages after outliers were eliminated.

.

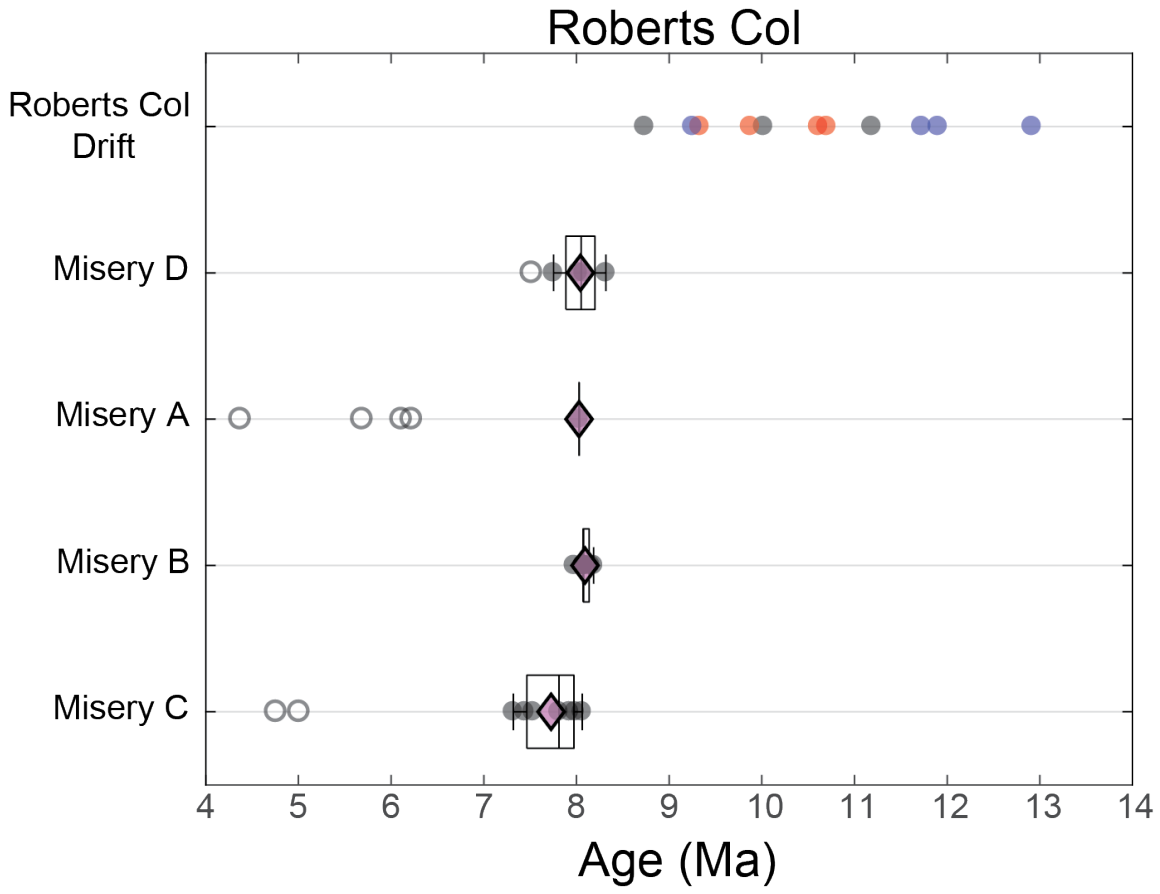

Figure 5.3 Boxplots of age ranges at Roberts Col. Boxes show the interquartile range and the line in the center of the box denotes the median of the data set. Closed circles are included data and open circles are outliers. Black, red, and blue circles denote ^{3}He, ^{10}Be and ^{21}Ne ages, respectively. Pink diamonds show the mean age of the landform with outliers excluded. Landforms are displayed in stratigraphically descending order, with the stratigraphically oldest unit at the top of the plot.

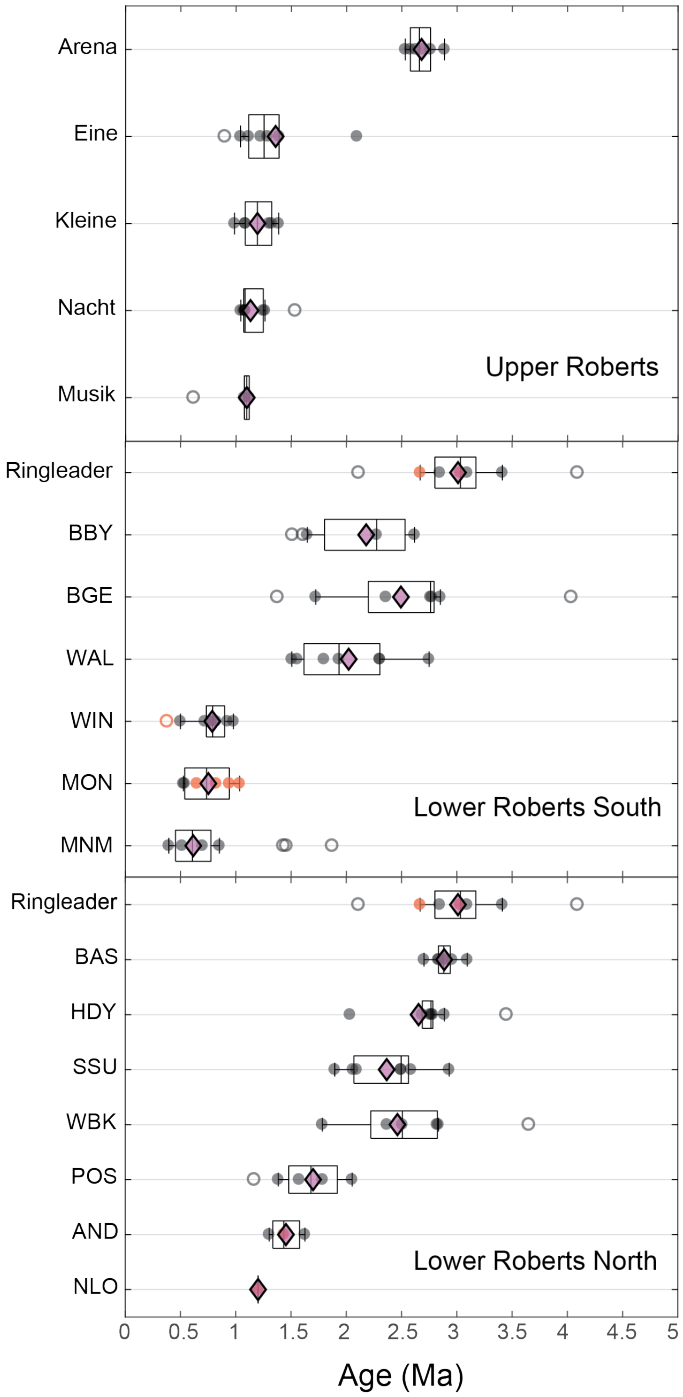

Figure 5.4 Boxplots with age ranges at Upper and Lower Roberts. Boxes show the interquartile range and the line in the center of the box denotes the median of the data set. Closed circles are included data and open circles are outliers. Black and red circles represent ^{3}He and ^{10}Be ages, respectively. Pink diamonds show the mean age of the unit with outliers excluded. Moraines at each site are displayed in stratigraphically descending order, with the stratigraphically oldest moraine at the top of the plot. Note that the Ringleader moraine is shown on the plots for both the Lower Roberts northern and southern transects.

5.2.1 Cosmogenic ^{3}He Production Rates

Exposure ages are best calculated when applying a production rate calibrated on landforms close in proximity, altitude, and, ideally, age to the landform of interest. As a result, numerous studies provide robust production rate calibration data in regions where exposure-age dating is commonly used (e.g., Balco et al., 2009; Goehring et al., 2010; Putnam et al., 2010; Young et al., 2013). Unfortunately, there are no calibration data for any nuclide in Antarctica to apply to my exposure-age calculations (Balco, 2017). Furthermore, existing ^{3}He calibration data only date landforms up to ~200 ka, which is significantly younger than most boulders in my glacial record, and thus presents a complication when using time-dependent scaling frameworks. Perhaps most importantly, the overall uncertainty in current ^{3}He production rates is ~9% (Borchers et al., 2016). Not only is this uncertainty considerably greater than the ~2% analytical error of most of my ^{3}He concentrations, it also hinders the assessment of EAIS behavior in response to specific climatic events, such as the mid-Pliocene Warm Period (3.3–3.0 Ma), since the duration of these events are often equivalent to the range of possible exposure-ages calculated using such uncertain production rates. For example, the Ringleader moraine, which I date to 3.01 Ma, can be dated to ~3.3 Ma using a 9% lower production rate. In the scenario that I present, the EAIS was present at Roberts Massif at the end of the mid-Pliocene Warm Period; however, in the alternative scenario, the EAIS was more extensive *throughout* that warm time. Although some recent studies have aimed to improve the uncertainty and scatter in ^{3}He production rate calibration using advanced statistical techniques (Borchers et al., 2016; Goehring et al., 2018), a local production rate for Antarctica is needed to improve the accuracy of exposure-age calculations. Therefore, I discuss the Roberts Massif chronology with regard to

long-term EAIS stability, rather than focusing on individual, relatively short-lived climatic events.

5.3 Glacial history of Roberts Massif

The exposure-age chronology at Roberts Massif affords insight into glacial activity during the mid to late Miocene, ~13–8 Ma, and during the Late Pliocene to Late Pleistocene, ~3 Ma to 0.6 Ma. Below, I discuss the glacial history implied by the chronology at each area of Roberts Massif.

5.3.1 Miocene Glaciation

5.3.1.1 Roberts Col

The oldest glacial deposits sampled at Roberts Massif comprise Roberts Col Drift, located approximately 400 m above the margin of Shackleton Glacier, which gave apparent exposure ages between ~13 and 9 Ma (Figure 4.1, Figure 5.3). This thin, bouldery drift not only represents a time during which the glacier surface was considerably higher than today, but also provides a minimum-limiting age constraint for the underlying surface of striated bedrock and Sirius Group, and thus for temperate glaciation in the central Transantarctic Mountains. The oldest dolerite boulder collected from this drift, sample 15-ROB-028-COL (Figure 3.1), gave an apparent exposure age of 11.19 ± 0.22 Ma and contains potentially the highest measured concentration of *in situ* ^{3}He ever measured in a terrestrial sample (1.38 x 10^{10} atoms g^{-1}). Similarly, the oldest sandstone boulder on Roberts Col, sample15-ROB-032-COL, affords an apparent ^{21}Ne age of 12.92 ± 0.26 Ma, and may have the highest concentration of terrestrial *in situ* ^{21}Ne measured to date (2.32 x 10^{9} atoms $g^{-1)}$. Four ^{10}Be measurements from sandstone samples, 15-ROB-029-COL, 15-ROB-032-COL, 15-ROB-033-COL, and 15-ROB-034-COL, are

saturated with respect to St scaling thereby indicating that ^{10}Be production and ^{10}Be loss (via radioactive decay and erosion) have reached equilibrium. While such ^{10}Be measurements cannot provide meaningful exposure-ages, they nonetheless afford unique opportunity to test aspects of production rate scaling frameworks, and, when paired with ^{21}Ne measurements, to learn about long-term erosion rates, both of which are discussed below.

5.3.1.2 Scaling Methods

Two commonly used scaling methods, St (after Stone (2000)) and LSD (a time-dependent scaling framework after Lifton et al. (2014)) yield apparent exposure ages that differ by up to ~20%. Beyond the fact that this equates to an age difference of ~3 Ma in the oldest sample (15-ROB-032-COL), this discrepancy becomes particularly important when comparing the moraine ages at Roberts Massif to global climatic data sets. For example, using St scaling and the primary production rate calibration set of Borchers et al. (2016), the Arena moraine is 3.03 Ma and the RIN, BAS, and HDY moraines are 3.53 Ma, 3.16 Ma, and 2.90 Ma, respectively. Such a distribution implies that the EAIS was present in the central Transantarctic Mountains for the entire duration of the mid-Pliocene Warm Period. Yet, when calculated according to the LSD scaling framework, the Arena moraine becomes 2.68 Ma and the RIN, BAS, and HDY moraines 3.01 Ma, 2.89 Ma, and 2.65 Ma, respectively. Calculated in this way, the data set suggests that the EAIS was present at the culmination of the mid-Pliocene Warm Period, yet does not preclude a smaller EAIS prior to ~3 Ma. The high nuclide concentrations measured in boulders on Roberts Col provide a unique opportunity for testing nuclide production rate scaling frameworks. This discussion appears in a post on Dr. Greg Balco's blog, entitled "Saturated Surfaces in Antarctica" and is summarized below (Balco, 2016).

The ^{10}Be inventory in a non-eroding boulder can be quantified using the differential equation,

$$\frac{dN}{dt} = P - N\lambda$$

where N in the nuclide concentration, t is exposure time, and P is the local production rate. Saturation (when nuclide production and nuclide decay equilibrate) occurs in the sample when $\frac{dN}{dt} = 0$, or, rearranging the equation, when $N = \frac{P}{\lambda}$. This equation can be used to calculate the saturation concentration of ^{10}Be given a specific, local production rate determined by the scaling method. According to the Borchers et al. (2016) primary production rate (4.13 ± 1.55 atoms g^{-1} yr^{-1}) and St scaling, the local production rate on Roberts Col is ~38.4 atoms g^{-1}. Given these parameters, the saturation concentration of ^{10}Be (i.e., the highest possible concentration one would expect to see at the altitude of the sampled boulder) is 7.70 x 10^7 atoms g^{-1}. However, the ^{10}Be concentration of 15-ROB-032-COL, the sandstone boulder with the highest ^{21}Ne concentration, is 8.47 x 10^7 atoms g^{-1}, which exceeds the saturation concentration by ~10%. Using a lower ^{10}Be reference production rate, such as the New Zealand rate (3.84 ± 0.08 atoms g^{-1} yr^{-1}, (Putnam et al. 2010)), exacerbates this problem.

In contrast, the LSD scaling method, for which production rates have higher altitude dependence, yields a greater saturation concentration (~8.90 x 10^7 atoms g^{-1}) for the location and altitude of 15-ROB-032-COL, which is higher than the ^{10}Be concentration of the boulder. This pattern, whereby high-elevation boulders have ^{10}Be concentrations which are "oversaturated" with respect to St scaling, but not with LSD scaling, holds for other samples in the ICE-D database and highlights that, at least at high elevations in Antarctica, LSD is probably the most appropriate method for scaling cosmogenic nuclide production rates.

5.3.1.3 Boulder Erosion

Because many of the boulders in the Roberts data set have been exposed for millions of years, I assess the effect of erosion on boulder nuclide inventories and, thus, exposure age. There are two ways to do this: i) calculate the "apparent erosion rate" from the measured nuclide concentration, and ii), when measurements of multiple nuclides are available, solve a system of differential equations to obtain the best fitting range of erosion rates. The "apparent erosion rate" is that implied by the nuclide inventory assuming that the rock surface has eroded sufficiently for nuclide production and nuclide loss to balance. Effectively, this gives a maximum erosion rate for that boulder.

The first approach calculates the apparent erosion rate using the equation,

$$\varepsilon = \frac{P\Lambda}{N}$$

where ε is the erosion rate in g cm^{-2} yr^{-1}, P is the production rate in atoms g^{-1} yr^{-1}, Λ is the attenuation rate of cosmic rays in dolerite (140 g cm^{-2}), and N is the concentration of a stable nuclide (in this case, ^{3}He). Using this equation for the oldest dolerite sample in this record (15-ROB-028-COL), which also provides the highest ^{3}He concentration, yields an erosion rate of 4.82 cm Ma^{-1}.

When concentrations of multiple nuclides with different decay rates are available, such as ^{10}Be (decay constant, λ, of 4.99 x 10^{-7} yr^{-1} and ^{21}Ne (stable nuclide, $\lambda = 0$ yr^{-1}), both the age and erosion rate are more accurately determined. Although ^{10}Be and ^{21}Ne are produced at a fixed ratio in quartz (~1:4), the ratio of [^{10}Be]/[^{21}Ne] decreases over time due to differing decay rates. Erosion, which removes nuclides from the boulder's inventory, serves to hasten the decay/removal of *in situ* nuclides from the rock. Therefore, the boulder has been exposed to cosmogenic rays for a longer period than the nuclide concentration implies for the zero-erosion

scenario. This concept is illustrated by the fact that a boulder that has been exposed for 12 Ma and subject to an erosion rate of 2 cm Ma^{-1} will exhibit a lower [^{21}Ne], but a higher [^{10}Be]/[^{21}Ne] ratio, than a boulder exposed for 12 Ma with an erosion rate of 1 cm Ma^{-1}. Although those theoretical boulders have been exposed for the same amount of time, the "half-life" is greater for the faster eroding boulder (i.e., more of the nuclide inventory is removed in the same amount of time) so the exposure age implied by the nuclide inventory at that erosion rate is reached more quickly.

This concept is the basis for the two-nuclide diagram, commonly referred to as a "banana plot," in which lines of constant age and lines of constant erosion are plotted in [^{10}Be]/[^{21}Ne] - [^{21}Ne] space. Where the nuclide concentrations of a boulder fall in relation to the age and erosion lines then gives information about both the exposure-age of the boulder and the time-integrated erosion rate that boulder has experienced, solving the system of equations,

$$N_{^{21}Ne} = \frac{P_{^{21}Ne}}{\frac{\varepsilon}{\Lambda}}\left(1 - e^{-t\left(\frac{\varepsilon}{\Lambda}\right)}\right)$$

$$N_{^{10}Be} = \frac{P_{^{10}Be}}{\lambda + \frac{\varepsilon}{\Lambda}}\left(1 - e^{-t\left(\lambda + \frac{\varepsilon}{\Lambda}\right)}\right)$$

where λ is the decay constant for ^{10}Be and t is the exposure age in years (all other variables have the same definitions as Eqn. 5.2). The only unknowns in these equations are ε and t. The upper limit of this diagram denotes the "simple exposure line"; samples plotting close to that line have likely experienced a single exposure period and negligible erosion. Samples that plot close to the steady-state erosion line, which forms the lower limit of the "steady-erosion island" (i.e., the banana), have reached the steady-state of net zero nuclide accumulation. Any samples plotting below the steady-state erosion line have likely experienced burial or ice-cover during their exposure history.

The four sandstones which have paired ^{10}Be and ^{21}Ne measurements yield erosion rates between ~1 and 3.5 cm/Ma and exposure ages of ~12–15 Ma (Figure 5.5). The apparent erosion rate of 4.82 cm Ma^{-1} for the dolerites serves as a maximum erosion rate. However, given the inherent hardness of dolerite compared to the softer sandstones, this erosion rate is probably far too high, and I suggest that the dolerites at Roberts Massif have experienced negligible erosion since deposition. Further, the dolerite boulders at Roberts Massif have clearly experienced less erosion than those in the Dry Valleys, as I observed minimal pitting on boulders younger than ~8 Ma, compared with ~0.5 Ma boulders in the Dry Valleys that exhibited a similar level of ventifaction (Swanger et al., 2011).

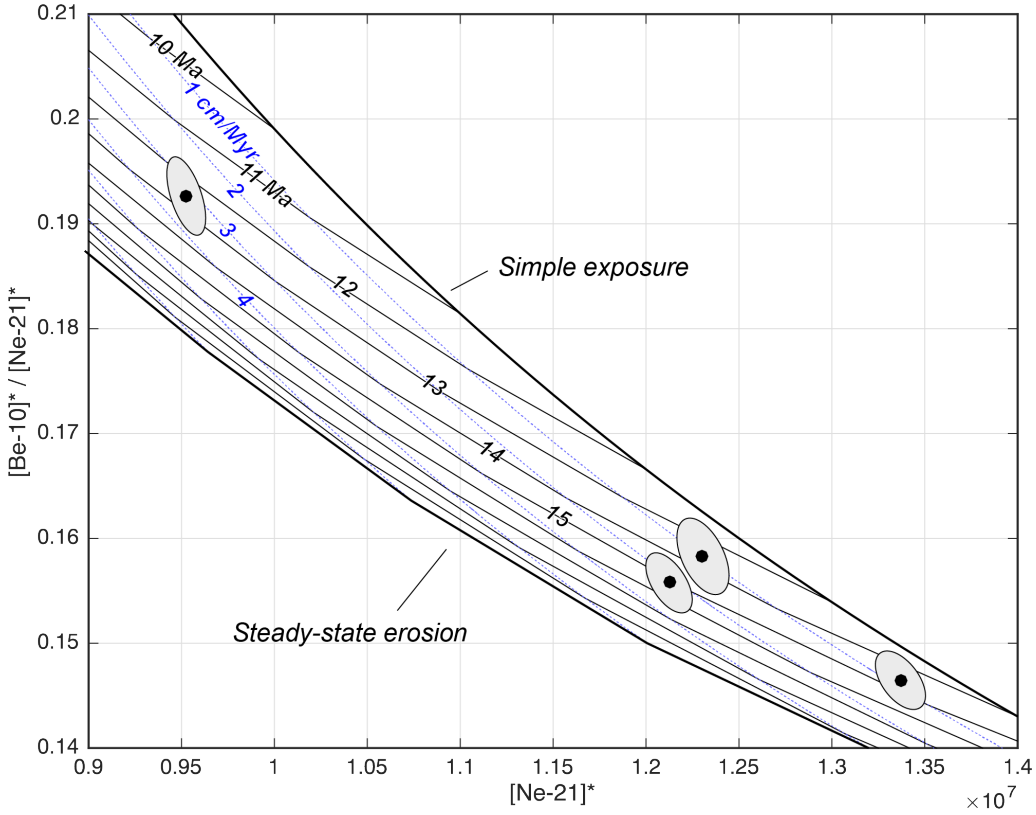

Figure 5.5 Two-nuclide diagram for Roberts Col. The simple exposure and steady-state erosion lines, which bound the "steady-erosion island," are labeled. Lines of constant age are displayed in black, while lines of constant erosion rates are represented in blue. Black circles represent measured nuclide concentrations and gray circles bound the uncertainty associated with calculating the erosion rate and age of each boulder.

5.3.1.4 Implications for the Age of the Roberts Col Drift

When the effects of erosion are included, the Roberts Col drift dates to between 12 and 15 Ma, placing a limiting age on the transition from temperate to cold-based glaciation in the central Transantarctic Mountains. The mid-Miocene age of the Roberts Col deposit is consistent with $^{40}Ar/^{39}Ar$ ages of *in situ* ash deposits in the Dry Valleys region, which suggest that cold, polar desert conditions and cold-based glaciation have persisted in the northern Transantarctic Mountains since ~14–15 Ma (Marchant et al., 1993). This climatic shift is also recorded by well-preserved terrestrial and lacustrine fossils interbedded with ash fall deposits in the Olympus Range in the Dry Valleys, which indicate summertime cooling of 8°C around 14 Ma (Lewis et al., 2008).

5.3.2 Misery Moraines

Inboard of the Roberts Col drift are the four Misery Moraines, which cluster around ~8 Ma in age (Table 5.1, Figure 5.3). The internal consistency of ^{3}He concentrations of dolerite boulders on these landforms, particularly the Misery B and D moraines, suggests that little post-depositional modification of these landforms has occurred. Further, on these long timescales, it is possible that geologic scatter becomes insignificant in cosmogenic nuclide data sets, since the internal error for individual boulder ages is roughly the same as the standard deviation of younger moraine ages. Additionally, the absence of water-lain sediments, finer grain sizes, and glaciofluvial features suggest that the ice was cold-based at the time of deposition. Indeed, the distinct lack of outwash deposits throughout Roberts Massif suggests that temperatures have not been sufficiently warm to induce surface melting since at least 8 Ma, and, based on the age of the Roberts Col drift, likely since ~15 Ma.

5.4 Late Pliocene to Pleistocene Glaciation

5.4.1 Upper Roberts

The Upper Roberts area is a hypsometrically simple moraine transect that affords insight into ice sheet change since ~3 Ma. In order of descending elevation, the moraines date to 2.68 ± 0.13 Ma (Arena moraine, 2300 m), 1.36 ± 0.38 Ma (Eine moraine, 2255 m), 1.19 ± 0.16 Ma (Kleine moraine, 2241 m), 1.13 ± 0.10 (Nacht moraine, 2220 m), and 1.10 ± 0.04 Ma (Musik moraine, 2215 m) (Figure 5.6). Additionally, I observed moraine segments on the slope above the Arena moraine, which denote larger positions of the EAIS, likely before ~2.7 Ma, as well as lower moraine segments situated between the Arena and Eine moraines, which are ~45 m apart in elevation. These lower, undated limits may account for the temporal gap between the Arena and Eine moraines. Exposure ages become consistently younger with decreasing elevation, indicating that the surface of the EAIS, on average, has lowered since > 2.7 Ma.

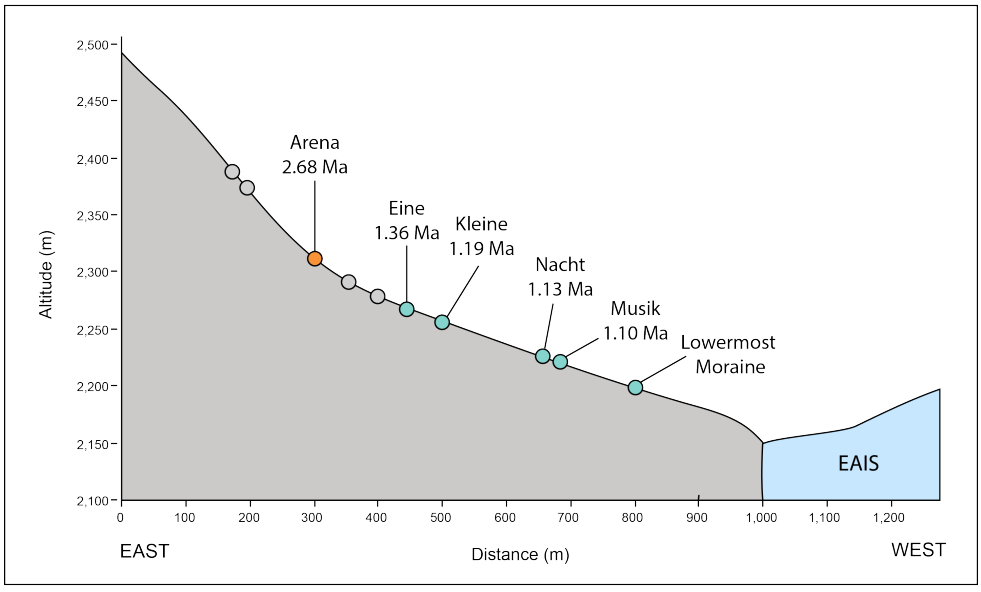

Figure 5.6 Topographic profile of Upper Roberts with moraine ages. In accordance with the geomorphic maps, orange circles show Pliocene moraines while teal circles represent Pleistocene moraines. Gray circles denote undated moraines observed in the imagery.

Although deposits from the last several glaciations are not the focus of this thesis, one prominent moraine does exist below Musik at ~2185 m. Two fresh looking sandstone boulders collected from that limit date to the last deglaciation, ~9 ka (Margaret Jackson, Personal Comm; ICE-D database), as do samples collected from a drift of fresh sandstone boulders extending from the moraine to modern ice margin. While the implications of this youngest deposit are beyond the scope of my thesis, these preliminary ages demonstrate that the EAIS adjacent to Upper Roberts was smaller during the Late Quaternary than it was during the period ~2.7–0.9 Ma.

5.4.2 Lower Roberts

The moraine ages at Lower Roberts are summarized according to their elevation in Figure 5.7. The oldest moraine at Lower Roberts (Ringleader moraine, 1956 m) gives an age of 3.01 ± 0.28 Ma. The presence of drift boulders distal to this landform (between the two moraine ridges) indicates that at some time, likely prior to ~3 Ma, the ice sheet completely overtopped the Central Rise. However, the topography at Lower Roberts is such that any moraine corresponding to that greater ice extent is unlikely to have been well-preserved on the steep talus slopes flanking the basin. To aid the discussion of the remaining exposure ages at Lower Roberts, I have split the area into northern (A–B; Figure 3.6) and southern transects (B–C; Figure 3.6), both of which begin at the Ringleader moraine and end at the northern and southern ice margins, respectively.

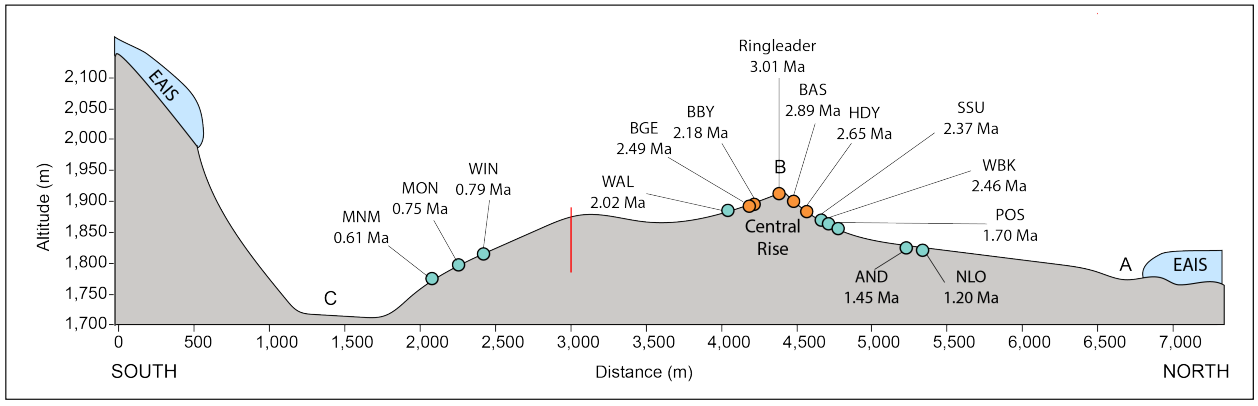

Figure 5.7 Topographic profile of Lower Roberts with moraine ages. In accordance with the geomorphic maps, orange circles show Pliocene moraines while teal circles represent Pleistocene moraines. A, B, and C correspond to the transect labels in Figure 3.6. The red line shows the fault scarp mapped in Figure 3.6.

5.4.2.1 Lower Roberts Northern Transect

Along the Lower Roberts northern transect, mean moraine ages generally decrease with declining elevation, being youngest close to the modern ice sheet margin. Listed in morphostratigraphic order, the moraines to the north of Ringleader are: 2.89 ± 0.12 Ma (BAS, 1914 m), 2.65 ± 0.31 Ma (HDY, 1895 m), 2.37 ± 0.36 Ma (1872 m), 2.46 ± 0.43 Ma (WBK, 1877 m), 1.70 ± 0.29 Ma (POS, 1865 m), 1.45 ± 0.16 Ma (AND, 1830 m), and 1.20 ± 0.02 Ma (NLO, 1830 m). The tight age distribution exhibited by the BAS moraine, reflected by the CV of 4%, indicates that there is little geologic scatter in this part of the data set. Similarly, with the exception of the youngest age (which is retained by the outlier elimination method), the distribution of ages on the HDY moraine is also internally consistent. If that young age is removed, the moraine becomes 2.78 ± 0.07 Ma, with a CV of 2.5%. Although this results in a significantly lower age uncertainty, I recognize that these two results agree within error, and thus do not influence my interpretations. To maintain consistency in my outlier elimination method, I take the 2.56 Ma age as the age of the HDY moraine.

Between the HDY and SSU moraines are several diffuse moraine crests that were difficult to distinguish from the surrounding drift on the ground, and thus were not sampled. The next two moraines in the dated transect, SSU and WBK, each exhibit a considerable spread in ages that overlap with one another. Although I eliminated outliers stratigraphically, the mean age of SSU (2.37 ± 0.36 Ma) is younger than that of WBK (2.46 ± 0.43 Ma), despite the latter being located closer to the modern ice margin. Of course, it is possible that the SSU was in fact deposited at its more extensive position *after* the WBK moraine, meaning that the cold-based ice overrode WBK without disturbing it. Acknowledging that the two data sets are indistinguishable within 1σ uncertainty, I suggest two possible explanations for the chronologic overlap between the SSU and WBK moraines. In the first, both data sets contain a relatively high degree of geologic scatter compared to other moraines in this record, potentially due to nuclide inheritance (i.e., ice has covered older till without disturbing it, or has re-entrained boulders with existing nuclide inventories). If this is true, the minimum population of ages may best reflect the time of moraine occupation.

The second possible scenario is that the spread of ages reflects real geologic activity, such as the repeated expansion and contraction of cold-based ice over this area during the period indicated by the SSU and WBK moraines ages (1.90–2.93 Ma). To assess the potential impact of the latter scenario, I considered the boulder ages from the SSU and WBK moraines as if they were all from the same depositional event. In doing so, three distinct age populations emerged (Figure 5.8): 1.96 ± 0.15 Ma, 2.49 ± 0.08 Ma, and 2.86 ± 0.06 Ma. At face value, therefore, it is possible that the fluctuating ice margin reached or overrode both moraine crests on at least three occasions between ~2.9 and 2 Ma. If so, the mean age of each landform approximates the period

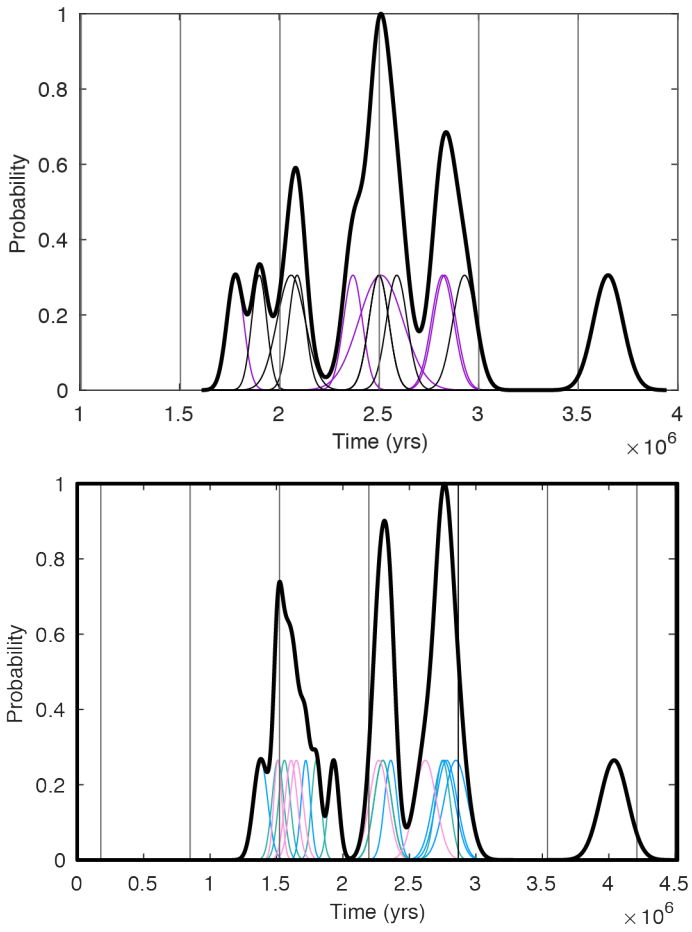

Figure 5.8 Camel plots with ages from multiple moraines. Top: Camel plot of all ages from WBK and SSU moraines along the Lower Roberts northern transect. Purple lines represent ages from WBK and thin black lines show ages from the SSU moraine. Bottom: Camel plot of all ages from the WAL, BGE, and BBY moraines. Blue lines show ages from BGE, teal lines represent ages from WAL, and pink lines denote ages from BBY.

during which the ice margin occupied these extended positions, while the minimum age of each moraine indicates the last time that the ice sheet was that extensive (~2 Ma). One way to test this hypothesis would be to measure multiple nuclides in these boulders to assess whether they have experienced any significant period(s) of burial. Unfortunately, I did not find any sandstone erratics on these moraines and, at present, other nuclides are not reliably measured in pyroxenes.

As the measurement of samples collected from the POS, AND, and NLO moraines is currently incomplete, the moraine ages presented here are preliminary. The POS moraines, which include numerous discontinuous ridge segments, are considered here as a single complex and give an apparent age of 1.70 ± 0.29 Ma. Farther down the transect, the AND moraine gives a younger mean age (1.45 ± 0.16 Ma), while a single ^{10}Be measurement from the NLO moraine gives an age of 1.20 ± 0.02 Ma. Together, the data comprising this northern transect depict a gradually lowering ice sheet surface at Lower Roberts transect since ~3 Ma. This lowering trend is further implicated by the presence of freshly scoured dolerite and sandstone boulders extending ~100 m above the modern glacier margin, which I attribute to the late Pleistocene glaciations based on morphostratigraphic correlation with Late Quaternary drifts observed in other areas of Roberts (Maggie Jackson, Personal Comm.) and throughout the Transantarctic Mountains (e.g., Bromley et al., 2012; Denton et al., 1989; Todd et al., 2010).

5.4.2.2 Lower Roberts Southern Transect

A similar pattern of ice sheet lowering over the past 3 Ma is suggested by the moraine chronology along the Lower Roberts southern transect, for which the Ringleader moraine also forms the highest point. On the southern flank of the Central Rise, immediately downslope of the Ringleader moraine, there are several moraine segments that, although visible in the satellite imagery, I chose not to sample due to their diffuse and discontinuous nature on the ground. Thus, the next highest landforms sampled along this transect were the BBY and BGE moraines (~30 m distance apart), with mean ages of 2.18 ± 0.49 Ma and 2.40 ± 0.49 Ma, respectively. Continuing down the transect, the next moraine, WAL, comprises a relatively discontinuous ridge and gives a similar age range to the BBY and BGE limits (2.02 ± 0.45 Ma). To explore the chronologic

overlap in the BBY, BGE, and WAL moraines, I performed the same exercise as I did for the SSU and WBK moraines on the northern transect, whereby I considered the ages on the BBY, BGE, and WAL moraines as comprising related depositional events. When considering the ages on these three moraines together, three distinct age populations emerged: 1.66 ± 0.05 Ma, 2.31 ± 0.04 Ma, and 2.75 ± 0.08 Ma (Figure 5.8). Therefore, it is possible that the glacier occupied the general vicinity of the BBY, BGE, and WAL moraines from ~2.75 to 1.66 Ma, with the ice margin reaching or overriding these moraine limits at least three times during that period.

The next moraines in the transect are located in the Southern Basin (Figure 1.3) and give ages, in descending order, of 0.79 ± 0.16 Ma (WIN), 0.75 ± 0.21 Ma (MON), and 0.61 ± 0.20 Ma (MNM). Although their CV values are high, at 20%, 28%, and 33%, these three limits do not exhibit distinct age groupings, unlike other high-scatter moraines at Lower Roberts (e.g., SSU and WBK, and BBY, BGE, and WAL). Nonetheless, I can infer from the data set that the ice sheet has become progressively less extensive from ~800–600 ka. Notably, there are no moraines preserved proximal to the MNM moraine. Instead, a thin drift of relatively fresh boulders represents deposition during more recent glacial events (dates < 500,000 years; Maggie Jackson, Personal Comm.; ICE-D). Together with the other moraine ages along the southern transect, it appears that the surface of the EAIS has progressively lowered over the past ~3 Ma.

In general, the Lower Roberts southern transect displays the highest degree of scatter among all the moraines in the Roberts Massif chronology. I hypothesize that at least some of this scatter can be attributed to the large cliff-face bordering the Southern Basin, which would provide a significant source of inheritance-prone material to the glacier. Although this suggestion is difficult to test, I would expect multi-nuclide measurements on some boulders from moraines along the southern transect to yield nuclide concentration ratios that plot close to the steady-state

erosion line. Given the low erosion rates in the central Transantarctic Mountains, this finding would be consistent with material exposed at a cliff-face for a significant period, rather than a boulder that has experienced one period of simple exposure following glacial deposition. Although not included in my thesis, future work will test this hypothesis using ^{10}Be and ^{21}Ne in sandstones on moraines throughout Roberts.

5.4.3 Implications of Pliocene-Pleistocene Moraine Ages

The significant chronologic overlap (within 1σ) evident among several of the moraine groups at Lower Roberts potentially reflects geologic scatter, especially as I am dealing with highly precise nuclide concentration measurements on relatively long timescales. Alternatively, these age distributions might also reflect actual geologic variability, for instance, the repeated waxing and waning of the ice margin over tens to hundreds of thousands of years. On a first-order basis, however, I can draw two principal conclusions from this record: 1) the EAIS was present in the central Transantarctic Mountains from ≥ 3 Ma to ≤ 0.6 Ma and 2) that the ice sheet surface appears to have lowered over the past ≥ 3 Ma (Figure 5.6, Figure 5.7). This pattern is corroborated by the fact that fresh boulders deposited during the most recent period of greater ice extent, attributed to the late Pleistocene (Maggie Jackson, Personal Comm.), do not extend beyond the lowermost moraines anywhere at Roberts Massif.

Plausible explanations for the apparent lowering of the EAIS surface over the last ~3 Ma include 1) uplift, either due to tectonism or isostatic effects of downcutting by outlet glaciers or ice sheet unloading, or 2) climatic feedbacks. In general, tectonic uplift in the Transantarctic Mountains is thought have been minimal since the mid-Miocene. Uplift data in the Shackleton Glacier region, which rely on the vertical displacement of piedmont erosion surfaces at the

lowest reaches of the glacier, imply a maximum range of uplift between 290 m and 790 m since ~14 Ma and constrain the majority of faulting along the Transantarctic Mountain Front to > 14 Ma (Miller et al., 2010). Farther north, $^{40}Ar/^{39}Ar$ ages on subaerial volcanic cones limit uplift to 300 m over the past 3 Ma in the McMurdo Dry Valleys and to < 67 m over the past 7.8 Ma in the Royal Society Range (Sugden et al., 1999; Wilch et al., 1993). Similarly, model simulations incorporating the effects of dynamic topography show ~50 m of uplift in the Dominion Range over the past ~3 Ma, in agreement with existing geomorphic and surface exposure-age data suggesting that surfaces in the Dominion Range have been close to their current elevation for > 4 Ma (Austermann, 2014; Ackert & Kurz, 2004). Such low uplift rates are in accord with low rates of exhumation since ~15 Ma (Fitzgerald, 2002). In my study area, minimal uplift at Roberts Massif is also implied by an absence of moraines dissected by faults.

Isostatic rebound, resulting from incision of the Transantarctic Mountains by large, locally wet-based outlet glaciers, such as Shackleton Glacier, lifts the mountain summits relative to the ice sheet surface. Stern et al. (2005) show that this process of uplift might account for ~1.5 km of total peak elevations south of the Beardmore-Nimrod region of the Transantarctic Mountains since the onset of polar desert conditions in the mid-Miocene. While this process potentially comprises at least part of the apparent lowering of the EAIS evident in the Roberts Massif moraine record, it is likely that the majority of valley incision was complete prior to the mid-Miocene. For example, landscape studies of the Dry Valleys, which were incised by EAIS outlet glaciers similar to Shackleton Glacier, indicate that those valleys were carved prior to ~15 Ma (Sugden et al., 1995). Further, geo- and thermo-chronologic data from detrital sediments in Prydz Bay, delivered by Lambert Glacier, a much larger (and likely more erosive) outlet glacier than Shackleton, suggest that the majority of trough incision was complete by the late Miocene,

which marks the beginning of the glacial record at Roberts Massif (Thomson et al., 2013; Tochilin et al., 2012). While some downcutting by EAIS outlet glaciers may have taken place since the mid-Miocene, this process may have been more important prior to that time.

An alternative scenario posits that the volume of the EAIS itself has decreased over the last 3 Ma due to climatic mechanisms. Changes in snowfall exert major control on EAIS mass balance and, increased (decreased) accumulation rates across the Antarctic are closely coupled with higher (lower) temperatures (Frieler et al., 2015; Medley et al., 2018). Therefore, it is possible that progressive cooling over the last 3 Ma has driven a gradual decrease in precipitation and, consequently, ice sheet extent. Boening et al. (2012) show that this process is in place today, with the EAIS mass balance being slightly positive resulting from warming-driven increase in precipitation. Indeed, a decrease in EAIS volume would be accompanied by isostatic uplift due to glacial unloading. Therefore, I suggest that the apparent ice sheet thinning over the course of the Roberts Massif glacial record reflects the interdependent effects of climate-induced shrinkage of the EAIS and accompanying rebound.

The notion of ice sheet lowering over the last ~3 Ma is consistent with previous glacial histories in the Antarctic (e.g., Brook et al., 1993; Denton et al., 1989). For example, in the Dry Valleys region, Taylor Glacier was thicker than present ~3 Ma and has been thinning for the past ~4 Ma (Brook et al., 1993; Staiger et al., 2006). Based on cosmogenic exposure-ages of moraine boulders in the Dominion Range, Ackert and Kurz (2004) also concluded that the EAIS surface has lowered over the Pliocene-Pleistocene period. Farther south, progressive thinning of Reedy Glacier over the past > ~5 Ma is implied by the increasing age of glacial deposits with elevation

(Bromley et al., 2010). The glacial history at Roberts Massif, in conjunction with these other chronologies throughout the Transantarctic Mountains, provides evidence for a general thinning of the EAIS over the past ~3 Ma and possibly longer.

5.5 Drivers of Ice Sheet Stability

The Roberts Massif moraine record represents periods during which the EAIS in the central Transantarctic Mountains was of similar size or slightly larger than today. The earliest time for which I have evidence that the ice sheet was larger than today is ~9–13 Ma, or ~12–15 Ma if the effects of erosion are considered. This finding is consistent with the onset of permanent glaciation in the Antarctic during the middle Miocene (Shackleton and Kennett, 1976; Zachos et al., 1992). While some glacially molded bedrock surfaces have been dated to that time (unpublished; see ICE-D Antarctica database), the Roberts Massif data set includes the first glacial erratics dated to the mid-Miocene, and thus affords robust evidence that the ice sheet was larger in the central Transantarctic Mountains at that time.

Secondly, these data enable me to infer that the EAIS surface was sufficiently high at ~8 Ma for ice to override a col ~450 m above the current ice sheet surface and deposit the Misery moraine complex. Few terrestrial records document glacial activity in Antarctica at that time, thus the Misery moraines provide new insight into glaciological conditions, showing that the EAIS was cold-based and more extensive than today during the mid-Miocene. This expansion of the EAIS was concurrent with high atmospheric CO_2 concentrations and sea-surface and bottom water temperatures significantly warmer than today (Figure 5.9; Lear et al., 2015; Mejía et al., 2017; Pagani et al., 1999; Zhang et al., 2013). Thus, the correlation of a larger EAIS with

warmer conditions globally suggests that temperature-precipitation feedbacks may play an important role in controlling EAIS mass-balance, especially on the timescale of millions of years (Frieler et al., 2015; Fudge et al., 2016; Huybrechts, 1993).

With the exception of several individual boulder ages, there is a conspicuous absence of moraines in the Roberts Massif data set dating to between ~8 and ~3 Ma, part of which encompasses the Pliocene Warm Period (Figure 5.9). However, the moraine evidence for cold-based conditions during the earlier and warmer Miocene suggests that a climatic mechanism for a smaller Pliocene EAIS is unlikely. Instead, I suggest that the ice sheet may have remained sufficiently large at that time to cover Lower Roberts, even if it had retreated slightly from its 8 Ma position. This scenario is indicated both by drift outboard of the Ringleader moraine, as well as higher, undated moraines evident at Upper Roberts. Although I was unable to date the stratigraphically older deposits, other studies suggest ice was larger > 5 Ma at Reedy Glacier (Bromley et al., 2010) and the Dominion Range (Ackert and Kurz, 2004). However, I recognize the limitations of my data set, whereby I can only infer when the glacier was larger than today, but not when it was less extensive.

Finally, as discussed in Section 5.4.3, thinning of the EAIS over the last ~3 Ma is implied by the fact that, in general, Pliocene-Pleistocene moraines become progressively older with increasing distance from the modern ice margins. Although some of the apparent change in ice surface elevation may be due to minimal tectonic uplift or isostatic rebound, I suggest that global cooling since at least the late Pliocene (Figure 5.9; e.g., Lariviere et al., 2012; Lear et al., 2015), may have resulted in decreased precipitation over the Antarctic, contributing at least in part to EAIS thinning in the Roberts record. Interestingly, this thinning of the ice sheet is also

coincident with declining atmospheric CO_2, suggesting that CO_2 does not drive EAIS extent (Figure 5.9; Bartoli et al., 2011; Hönisch et al., 2009).

Altogether, this exhaustive glacial chronology at Roberts Massif shows that the EAIS was present in the central Transantarctic Mountains, and potentially slightly larger than now, for long periods when climate has been significantly warmer than today, including the mid-Miocene, the late Pliocene, and the early Pleistocene. The result of more extensive ice during past periods of warmer-than-present climate suggests that temperature-precipitation feedbacks may play a significant role in controlling EAIS mass balance on the timescales of hundreds of thousands to millions of years. Overall, the glacial chronology of Roberts Massif bolsters the argument for the long-term stability of the EAIS.

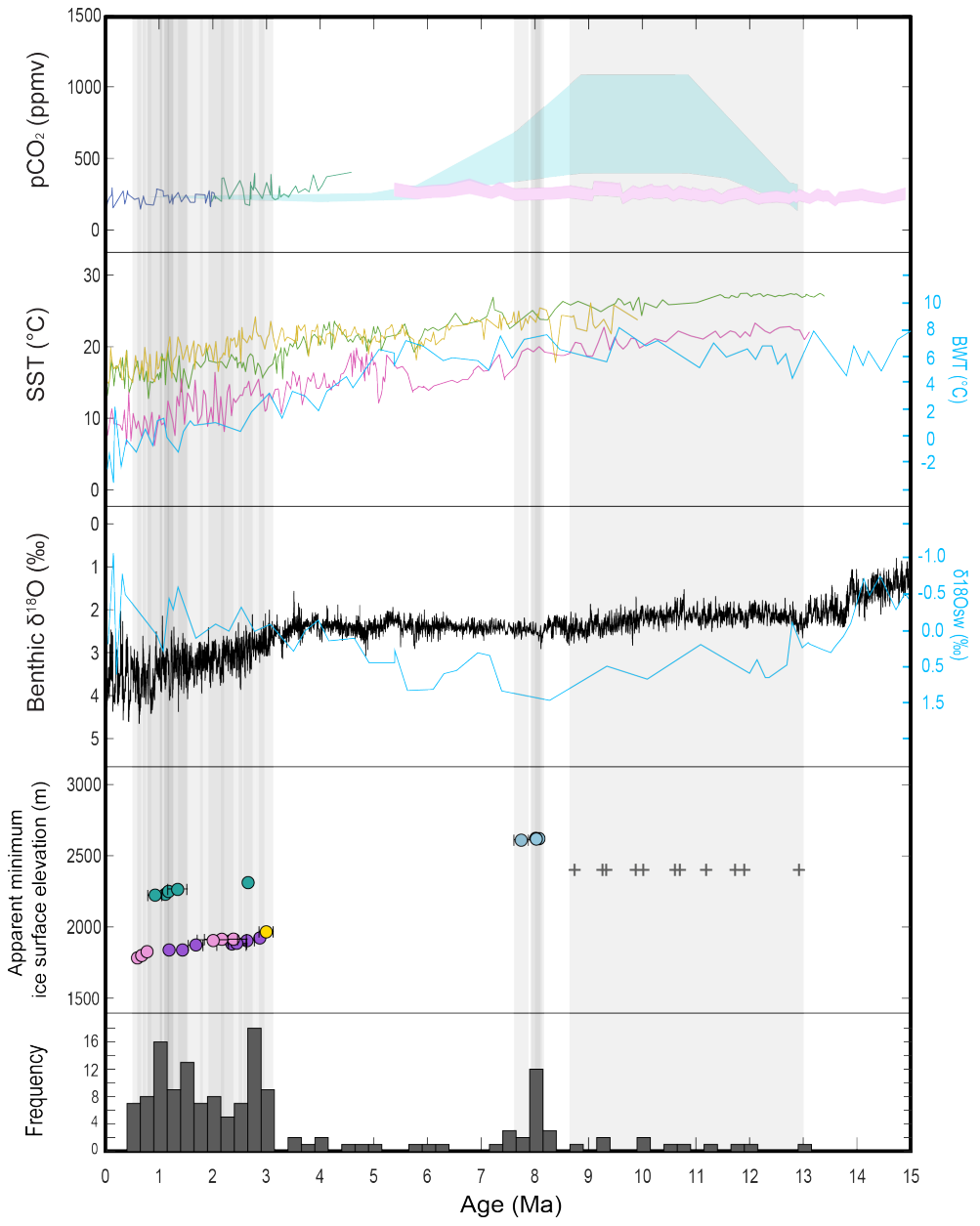

Figure 5.9 Comparison of the Roberts Massif glacial chronology with paleoclimate records. a) CO_2 records: blue, Ocean Drilling Program (ODP) site 668B, Eastern Equatorial Atlantic (Hönisch et al., 2009); green, ODP site 999 in the Caribbean (Bartoli et al., 2011); light blue, ODP site 846 Eastern Equatorial Pacific (Mejía et al., 2017); pink, Deep Sea Drilling Project site 588, southwest Pacific (Pagani et al., 1999); b) Sea surface temperatures: green, ODP site 1010, Subtropical east Pacific (Lariviere et al., 2012); pink, ODP site 1021, Northeast Pacific (Lariviere et al., 2012); yellow, ODP site 1208, Northwest Pacific (Lariviere et al., 2012); and bottom water temperatures: blue, ODP site 806, southwest Pacific (Lear et al., 2015); c) Black, spliced benthic $\delta^{18}O$ curve (De Vleeschouwer et al., 2017); and blue, $\delta^{18}O_{sw}$, ODP site 806, southwest Pacific (Lear et al., 2015); continued on next page.

Figure 5.9 (continued) d) Moraine ages from this study plotted against the minimum ice surface elevation implied by the elevation and location of each landform (i.e., the elevation of the moraine or drift boulder, or, for the Misery Moraines, the elevation of the col the ice must have overtopped to deposit the moraines): plus signs show boulder ages from the Roberts Col drift, light blue circles represent the Misery moraines, teal circles denote moraines at Upper Roberts, the yellow circle shows the Ringleader moraine, purple circles denote moraines on the Lower Roberts northern transect, and pink circles represent moraines from the Lower Roberts southern transect. e) histogram showing all individual boulder ages (including outliers) at Roberts Massif. Grey bars spanning the figure show the mean moraine ages, with width equal to moraine age uncertainty, and represent times in this record when the EAIS was more expansive than today.

CHAPTER 6

CONCLUSIONS

This exhaustive glacial history of Roberts Massif contributes new evidence for the long-term stability of the East Antarctic ice sheet. The key findings of my thesis are:

1) Selecting boulders for cosmogenic exposure-age dating that are the most angular and least weathered on a given cold-based landform may reduce the number of boulders rejected as outliers due to inheritance. Further, collecting a large number of samples ($n = \geq 7$) on each landform may allow for better approximation of the "true" moraine age.
2) At least at high elevations in Antarctica, the LSD scaling framework appears to give more realistic nuclide production rates than does the more commonly used St scaling.
3) At Roberts Col, a drift deposit ~400 m above the current ice margin dates to ~12–15 Ma, providing a minimum limiting age for temperate glaciation in the central Transantarctic Mountains.
4) The tightly-clustered ages of the four Misery Moraines show that at ~8 Ma, the EAIS was sufficiently large to override a col ~450 m above the current ice surface and cross the eastern flank of Misery Peak. These landforms not only indicate that the ice sheet was larger during the warm mid-Miocene, but also show that cold-based glaciation has persisted since at least that time.
5) Low sandstone erosion rates of ~1–3.5 cm/Ma, determined from ^{21}Ne and ^{10}Be concentrations, provide further evidence for long-term landscape stability and persistent polar desert conditions in the central Transantarctic Mountains. Additionally, the presence of striated dolerite bedrock pre-dating ~15 Ma suggests that dolerite erosion is negligible at this location.

6) Ages on 19 moraines at Upper and Lower Roberts indicate that the EAIS surface has become progressively lower over the last ~3 Ma and possibly longer, even as global temperatures apparently cooled since the late Pliocene, meaning that temperature-precipitation feedbacks may play a crucial role in driving long-term ice sheet mass balance.
7) Despite a conspicuous absence of moraines deposited between 8 Ma and 3 Ma, the EAIS has been present in the central Transantarctic Mountains for long periods since at least ~15 Ma, and has potentially been larger during periods of warmer-than-present climate in the middle to late Miocene, the late Pliocene, and the early Pleistocene.

BIBLIOGRAPHY

Ackert, R.P., Kurz, M.D., 2004. Age and uplift rates of Sirius Group sediments in the Dominion Range, Antarctica, from surface exposure dating and geomorphology. Glob. Planet. Change 42, 207–225.

Applegate, P.J., Urban, N.M., Laabs, B.J.C., Keller, K., Alley, R.B., 2010. Modeling the statistical distributions of cosmogenic exposure dates from moraines. Geosci. Model Dev. 3, 293–307. doi:10.5194/gmd-3-293-2010

Atkins, C.B., 2013. Geomorphological evidence of cold-based glacier activity in South Victoria Land, Antarctica. Geol. Soc. London, Spec. Publ. 381, 299–318. doi:10.1144/SP381.18

Atkins, C.B., Barrett, P.J., Hicock, S.R., 2002. Cold glaciers erode and deposit: Evidence from Allan Hills, Antarctica. Geology 30, 659–662. doi:10.1130/0091-7613(2002)030<0659:CGEADE>2.0.CO;2

Balco, G., 2017. The uneven distribution of production rate calibration data.

Balco, G., 2016. Saturated Surfaces in Antarctica [WWW Document]. www.cosmognosis.wordpress.com/2016/09/09/saturated-surfaces-in-antarctica/.

Balco, G., Briner, J., Finkel, R.C., Rayburn, J.A., Ridge, J.C., Schaefer, J.M., 2009. Regional beryllium-10 production rate calibration for late-glacial northeastern North America. Quat. Geochronol. 4, 93–107. doi:10.1016/j.quageo.2008.09.001

Balco, G., Stone, J.O., Lifton, N.A., Dunai, T.J., 2008. A complete and easily accessible means of calculating surface exposure ages or erosion rates from 10Be and 26Al measurements. Quat. Geochronol. 3, 174–195. doi:10.1016/j.quageo.2007.12.001

Balco, G., Stone, J.O.H., Porter, S.C., Caffee, M.W., 2002. Cosmogenic-nuclide ages for New England coastal moraines, Martha's Vineyard and Cape Cod, Massachusetts, USA. Quat. Sci. Rev. 21, 2127–2135. doi:10.1016/S0277-3791(02)00085-9

Bartoli, G., Hönisch, B., Zeebe, R.E., 2011. Atmospheric CO<inf>2</inf> decline during the Pliocene intensification of Northern Hemisphere glaciations. Paleoceanography 26, 1–14. doi:10.1029/2010PA002055

Blard, P.H., Balco, G., Burnard, P.G., Farley, K.A., Fenton, C.R., Friedrich, R., Jull, A.J.T., Niedermann, S., Pik, R., Schaefer, J.M., Scott, E.M., Shuster, D.L., Stuart, F.M., Stute, M., Tibari, B., Winckler, G., Zimmermann, L., 2015. An inter-laboratory comparison of cosmogenic 3He and radiogenic 4He in the CRONUS-P pyroxene standard. Quat. Geochronol. 26, 11–19. doi:10.1016/j.quageo.2014.08.004

Blard, P.H., Farley, K.A., 2008. The influence of radiogenic 4He on cosmogenic 3He determinations in volcanic olivine and pyroxene. Earth Planet. Sci. Lett. 276, 20–29. doi:10.1016/j.epsl.2008.09.003

Borchers, B., Marrero, S., Balco, G., Caffee, M., Goehring, B., Lifton, N., Nishiizumi, K., Phillips, F., Schaefer, J., Stone, J., 2016. Geological calibration of spallation production rates in the CRONUS-Earth project. Quat. Geochronol. 31, 188–198. doi:10.1016/j.quageo.2015.01.009

Bromley, G.R.M., Hall, B.L., Stone, J.O., Conway, H., 2012. Late Pleistocene evolution of Scott Glacier, southern Transantarctic Mountains: Implications for the Antarctic contribution to deglacial sea level. Quat. Sci. Rev. 50, 1–13. doi:10.1016/j.quascirev.2012.06.010

Bromley, G.R.M., Hall, B.L., Stone, J.O., Conway, H., Todd, C.E., 2010. Late Cenozoic deposits at Reedy Glacier, Transantarctic Mountains: implications for former thickness of the West Antarctic Ice Sheet. Quat. Sci. Rev. 29, 384–398. doi:10.1016/j.quascirev.2009.07.001

Bromley, G.R.M., Winckler, G., Schaefer, J.M., Kaplan, M.R., Licht, K.J., Hall, B.L., 2014. Pyroxene separation by HF leaching and its impact on helium surface-exposure dating. Quat. Geochronol. 23, 1–8. doi:10.1016/j.quageo.2014.04.003

Brook, E.J., Brown, E.T., Kurz, M.D., Ackert, R.P., Raisbeck, G.M., Yiou, F., 1995. Constraints on Age, Erosion, and Uplift of Neogene Glacial Deposits in the Transantarctic-Mountains Determined From in-Situ Cosmogenic Be-10 and Al-26. Geology 23, 1063–1066. doi:10.1130/0091-7613(1995)0232.3.CO;2

Brook, E.J., Kurz, M.D., Ackert Jr., R.P., Denton, G.H., Brown, E.T., Raisbeck, G.M., Yiou, F., 1993. Chronology of Taylor Glacier Advances in Arena Valley, Antarctica, Using in Situ Cosmogenic 3He and 10Be. Quat. Res. 39, 11–23.

Brown, E.T., Edmond, J.M., Raisbeck, G.M., Yiou, F., Kurz, M.D., Brook, E.J., 1991. Examination of surface exposure ages of Antarctic moraines using in situ produced 10Be and 26Al. Geochim. Cosmochim. Acta 55, 2269–2283. doi:10.1016/0016-7037(91)90103-C

Burckle, L.H., Potter, N., 1996. Pliocene-Pleistocene diatoms in Paleozoic and Mesozoic sedimentary and igneous rocks from Antarctica: A Sirius problem solved. Geology 24, 235–238. doi:10.1130/0091-7613(1996)024<0235:PPDIPA>2.3.CO;2

Cook, C.P., van de Flierdt, T., Williams, T., Hemming, S.R., Iwai, M., Kobayashi, M., Jimenez-Espejo, F.J., Escutia, C., González, J.J., Khim, B.-K., McKay, R.M., Passchier, S., Bohaty, S.M., Riesselman, C.R., Tauxe, L., Sugisaki, S., Galindo, A.L., Patterson, M.O., Sangiorgi, F., Pierce, E.L., Brinkhuis, H., Klaus, A., Fehr, A., Bendle, J. a. P., Bijl, P.K., Carr, S. a., Dunbar, R.B., Flores, J.A., Hayden, T.G., Katsuki, K., Kong, G.S., Nakai, M., Olney, M.P., Pekar, S.F., Pross, J., Röhl, U., Sakai, T., Shrivastava, P.K., Stickley, C.E., Tuo, S., Welsh, K., Yamane, M., 2013. Dynamic behaviour of the East Antarctic ice sheet during Pliocene warmth. Nat. Geosci. 6, 765–769. doi:10.1038/ngeo1889

De Vleeschouwer, D., Vahlenkamp, M., Crucifix, M., Pälike, H., 2017. Alternating Southern and Northern Hemisphere climate response to astronomical forcing during the past 35 m.y. Geology 45, 375–378. doi:10.1130/G38663.1

DeConto, R.M., Pollard, D., 2003. Rapid Cenozoic glaciation of Antarctica induced by declining atmospheric CO 2 1317, 1313–1317.

Denton, G.H., Bockheim, J.G., Wilson, S.C., Leide, J.E., Andersen, B.G., 1989. Late Quaternary Ice-Surface Fluctuations of Beardmore Glacier, Transantarctic Mountains. Quat. Res. 31, 183–209. doi:10.1016/0033-5894(89)90007-0

Denton, G.H., Sugden, D.E., 2005. Meltwater features that suggest Miocene ice-sheet overriding of the Transantarctic Mountains in Victoria Land, Antarctica. Geogr. Ann. 87 A, 67–85.

Ferraccioli, F., Armadillo, E., Jordan, T., Bozzo, E., Corr, H., 2009. Aeromagnetic exploration over the East Antarctic Ice Sheet: A new view of the Wilkes Subglacial Basin. Tectonophysics 478, 62–77. doi:10.1016/j.tecto.2009.03.013

Fretwell, P., Pritchard, H.D., Vaughan, D.G., Bamber, J.L., Barrand, N.E., Bell, R., Bianchi, C., Bingham, R.G., Blankenship, D.D., Casassa, G., Catania, G., Callens, D., Conway, H., Cook, A.J., Corr, H.F.J., Damaske, D., Damm, V., Ferraccioli, F., Forsberg, R., Fujita, S., Gim, Y., Gogineni, P., Griggs, J.A., Hindmarsh, R.C.A., Holmlund, P., Holt, J.W., Jacobel, R.W., Jenkins, A., Jokat, W., Jordan, T., King, E.C., Kohler, J., Krabill, W., Riger-Kusk, M., Langley, K.A., Leitchenkov, G., Leuschen, C., Luyendyk, B.P., Matsuoka, K., Mouginot, J., Nitsche, F.O., Nogi, Y., Nost, O.A., Popov, S. V., Rignot, E., Rippin, D.M., Rivera, A., Roberts, J., Ross, N., Siegert, M.J., Smith, A.M., Steinhage, D., Studinger, M., Sun, B., Tinto, B.K., Welch, B.C., Wilson, D., Young, D.A., Xiangbin, C., Zirizzotti, A., 2013. Bedmap2: Improved ice bed, surface and thickness datasets for Antarctica. Cryosphere 7, 375–393. doi:10.5194/tc-7-375-2013

Frieler, K., Clark, P.U., He, F., Buizert, C., Reese, R., Ligtenberg, S.R.M., Van Den Broeke, M.R., Winkelmann, R., Levermann, A., 2015. Consistent evidence of increasing Antarctic accumulation with warming. Nat. Clim. Chang. 5, 348–352. doi:10.1038/nclimate2574

Fudge, T.J., Markle, B.R., Cuffey, K.M., Buizert, C., Taylor, K.C., Steig, E.J., Waddington, E.D., Conway, H., Koutnik, M., 2016. Variable relationship between accumulation and temperature in West Antarctica for the past 31,000 years. Geophys. Res. Lett. 43, 3795–3803. doi:10.1002/2016GL068356

Goehring, B.M., Kurz, M.D., Balco, G., Schaefer, J.M., Licciardi, J., Lifton, N., 2010. A reevaluation of in situ cosmogenic 3He production rates. Quat. Geochronol. 5, 410–418. doi:10.1016/j.quageo.2010.03.001

Goehring, B.M., Muzikar, P., Lifton, N.A., 2018. Establishing a Bayesian approach to determining cosmogenic nuclide reference production rates using He-3. Earth Planet. Sci. Lett. 481, 91–100. doi:10.1016/j.epsl.2017.10.025

Hall, B.L., Denton, G.H., Lux, D.R., Bockheim, J.G., 1993. Late Tertiary Antarctic Paleoclimate and Ice-Sheet Dynamics Inferred from Surficial Deposits in Wright Valley Source. Geogr. Ann. Ser. A Phys. Geogr. 75, 239–267.

Hanna, E., Navarro, F.J., Pattyn, F., Domingues, C.M., Fettweis, X., Ivins, E.R., Nicholls, R.J., Ritz, C., Smith, B., Tulaczyk, S., Whitehouse, P.L., Jay Zwally, H., 2013. Ice-sheet mass balance and climate change. Nature 498, 51–59. doi:10.1038/nature12238

Holbourn, A., Kuhnt, W., Schulz, M., Erlenkeuser, H., 2005. Impacts of orbital forcing and atmospheric carbon dioxide on Miocene ice-sheet expansion. Nature 438, 483–487. doi:10.1038/nature04123

Hönisch, B., Hemming, N.G., Archer, D., Siddall, M., McManus, J.F., 2009. Atmospheric Carbon Dioxide Concentration across the Mid-Pleistocene Transition. Science (80-.). 324, 1551–1554. doi:10.1007/sl0869-007-9037-x

Huybrechts, P., 1993. Glaciological Modelling of the Late Cenezoic East Antarctic Ice Sheet: Stability or Dynamism. Geogr. Ann. 75 A, 221–238.

Ivy-Ochs, S., Schluchter, C., Kubik, P.W., Dittrich-Hannen, B., Beer, J., 1995. Minimum 10Be exposure ages of early Pliocene for the Table Mountain plateau and the Sirius Group at Mount Fleming, Dry Valleys, Antarctica. Geology 23, 1007–1010. doi:10.1130/0091-7613(1995)023<1007:MBEAOE>2.3.CO;2

Kellogg, D.E., Kellogg, T.B., 1996. Diatoms in South Pole ice: Implications for eolian contamination of Sirius Group deposits. Geology 24, 115–118. doi:10.1130/0091-7613(1996)024<0115:DISPII>2.3.CO;2

Kennett, J.P., 1977. Cenozoic evolution of Antarctic glaciation, the circum-Antarctic Ocean, and their impact on global paleoceanography. J. Geophys. Res. 82, 3843–3860.

Lariviere, J.P., Ravelo, A.C., Crimmins, A., Dekens, P.S., Ford, H.L., Lyle, M., Wara, M.W., 2012. Late Miocene decoupling of oceanic warmth and atmospheric carbon dioxide forcing. Nature 486, 97–100. doi:10.1038/nature11200

Lear, C.H., Coxall, H., Foster, G.L., Lunt, D.J., Mawbey, E.M., Rosenthal, Y., Sosdian, S.M., Thomas, E., Wilson, P.A., 2015. Neogene ice volume and ocean temperatures: Insights from infaunal foraminiferal Mg/Ca paleothermometry. Paleoceanography 30, 1437–1454. doi:10.1002/2015PA002833.Received

Lewis, A.R., Marchant, D.R., Ashworth, A.C., Hedenas, L., Hemming, S.R., Johnson, J. V., Leng, M.J., Machlus, M.L., Newton, A.E., Raine, J.I., Willenbring, J.K., Williams, M., Wolfe, A.P., 2008. Mid-Miocene cooling and the extinction of tundra in continental Antarctica. Proc. Natl. Acad. Sci. 105, 10676–10680. doi:10.1073/pnas.0802501105

Lifton, N., Sato, T., Dunai, T.J., 2014. Scaling in situ cosmogenic nuclide production rates using analytical approximations to atmospheric cosmic-ray fluxes. Earth Planet. Sci. Lett. 386, 149–160. doi:10.1016/j.epsl.2013.10.052

Marchant, D.R., Denton, G.H., Sugden, D.E., Swisher, C.C., 1993. Miocene Glacial Stratigraphy and Landscape Evolution of the Western Asgard Range, Antarctica. Geogr. Ann. Ser. A Phys. Geogr. 75, 303–330.

Margerison, H.R., Phillips, W.M., Stuart, F.M., Sugden, D.E., 2005. Cosmogenic 3He concentrations in ancient flood deposits from the Coombs Hills, northern Dry Valleys, East Antarctica: Interpreting exposure ages and erosion rates. Earth Planet. Sci. Lett. 230, 163–175. doi:10.1016/j.epsl.2004.11.007

Mayewski, P.A., 1975. Glacial geology and late Cenozoic history of the Transantarctic Mountains, Antarctica. Inst. Polar Stud. Ohio State Univ. Report 56, 168.

Medley, B., McConnell, J.R., Neumann, T.A., Reijmer, C.H., Chellman, N., Sigl, M., Kipfstuhl, S., 2018. Temperature and Snowfall in Western Queen Maud Land Increasing Faster Than Climate Model Projections. Geophys. Res. Lett. 45, 1472–1480. doi:10.1002/2017GL075992

Mejía, L.M., Méndez-Vicente, A., Abrevaya, L., Lawrence, K.T., Ladlow, C., Bolton, C., Cacho, I., Stoll, H., 2017. A diatom record of CO2 decline since the late Miocene. Earth Planet. Sci. Lett. 479, 18–33. doi:10.1016/j.epsl.2017.08.034

Mercer, J.H., 1972. Some observations on the glacial geology of the Beardmore Glacier area. Antarct. Geol. Geophys.

Miller, K.G., Wright, J.D., Browning, J. V., Kulpecz, A., Kominz, M., Naish, T.R., Cramer, B.S., Rosenthal, Y., Peltier, W.R., Sosdian, S., 2012. High tide of the warm Pliocene: Implications of global sea level for Antarctic deglaciation. Geology 40, 407–410. doi:10.1130/G32869.1

Miller, S.R., Fitzgerald, P.G., Baldwin, S.L., 2010. Cenozoic range-front faulting and development of the Transantarctic Mountains near Cape Surprise, Antarctica: Thermochronologic and geomorphologic constraints. Tectonics 29, 1–21. doi:10.1029/2009TC002457

Naish, T.R., Barrett, P.J., Dunbar, G.B., Woolfe, K.J., Dunn, A.G., Henrys, S.A., Claps, M., Powell, R.D., Fielding, C.R., 2001. Sedimentary cyclicity in CRP drillcore, Victoria Land Basin, Antarctica. Terra Antarct. 8, 225–244.

Pagani, M., Freeman, K.H., Arthur, M.A., 1999. Late Miocene Atmospheric CO_2 Concentrations and the Expansion of C_4 Grasses Published by : American Association for the Advancement of Science Linked references are available on JSTOR for this article : Late Miocene Atmospheric CO2 Concentrations and the. Science (80-.). 285, 876–879.

Pollard, D., DeConto, R.M., 2009. Modelling West Antarctic ice sheet growth and collapse through the past five million years. Nature 458, 329–332. doi:10.1038/nature07809

Pollard, D., DeConto, R.M., Alley, R.B., 2015. Potential Antarctic Ice Sheet retreat driven by hydrofracturing and ice cliff failure. Earth Planet. Sci. Lett. 412, 112–121. doi:10.1016/j.epsl.2014.12.035

Putnam, A.E., Schaefer, J.M., Barrell, D.J.A., Vandergoes, M., Denton, G.H., Kaplan, M.R., Finkel, R.C., Schwartz, R., Goehring, B.M., Kelley, S.E., 2010. In situ cosmogenic10Be production-rate calibration from the Southern Alps, New Zealand. Quat. Geochronol. 5, 392–409. doi:10.1016/j.quageo.2009.12.001

Rovere, A., Raymo, M.E., Mitrovica, J.X., Hearty, P.J., O'Leary, M.J., Inglis, J.D., Leary, M.J.O., Inglis, J.D., 2014. The Mid-Pliocene sea-level conundrum: Glacial isostasy, eustasy and dynamic topography. Earth Planet. Sci. Lett. 387, 27–33. doi:10.1016/j.epsl.2013.10.030

Schaefer, J.M., Ivy-Ochs, S., Wieler, R., Leya, I., Baur, Denton, G.H., Schluchter, C., 1999. Cosmogenic noble gas studies in the oldest landscape on Earth: surface exposure age of the Dry Valleys, Antarctica. Earth Planet. Sci. Lett. 167, 215–226.

Scher, H.D., Whittaker, J.M., Williams, S.E., Latimer, J.C., Kordesch, W.E.C., Delaney, M.L., 2015. Onset of Antarctic Circumpolar Current 30 million years ago as Tasmanian Gateway aligned with westerlies. Nature 523, 580–583. doi:10.1038/nature14598

Scherer, R.P., DeConto, R.M., Pollard, D., Alley, R.B., 2016. Windblown Pliocene diatoms and East Antarctic Ice Sheet retreat. Nat. Commun. 7, 1–9. doi:10.1038/ncomms12957

Shackleton, N.J., Kennett, J.P., 1976. Paleotemperature history of the Cenozoic and the initiation of Antarctic glaciation; Oxygen and carbon isotope analyses in DSDP sites 277, 279 and 281. Initial Reports Deep Sea Drill. Proj. 29, 743–755. doi:10.2973/dsdp.proc.37.1977

Shackleton, N.J., Kennett, J.P., 1975. Late Cenozoic oxygen and carbon isotopic changes at DSDP Site 284: implications for glacial history of the Northern Hemisphere and Antarctica. Initial Reports Deep Sea Drill. Proj. 29, 801–807.

Shepherd, A., Ivins, E.R., Geruo, A., Barletta, V.R., Bentley, M.J., Bettadpur, S., Briggs, K.H., Bromwich, D.H., Forsberg, R., Galin, N., Horwath, M., Jacobs, S., Joughin, I., King, M.A., Lenaerts, J.T.M., Li, J., Ligtenberg, S.R.M., Luckman, A., Luthcke, S.B., McMillan, M., Meister, R., Milne, G., Mouginot, J., Muir, A., Nicolas, J.P., Paden, J., Payne, A.J., Pritchard, H., Rignot, E., Rott, H., Sørensen, L.S., Scambos, T.A., Scheuchl, B., Schrama, E.J.O., Smith, B., Sundal, A. V., Van Angelen, J.H., Van De Berg, W.J., Van Den Broeke, M.R., Vaughan, D.G., Velicogna, I., Wahr, J., Whitehouse, P.L., Wingham, D.J., Yi, D., Young, D., Zwally, H.J., 2012. A reconciled estimate of ice-sheet mass balance. Science (80-.). 338, 1183–1189. doi:10.1126/science.1228102

Shevenell, A.E., Kennett, J.P., Lea, D.W., 2008. Middle Miocene ice sheet dynamics, deep-sea temperatures, and carbon cycling: A Southern Ocean perspective. doi:10.1029/2007GC001736

Shevenell, A.E., Kennett, J.P., Lea, D.W., 2004. Middle Miocene Southern Ocean Cooling and Antarctic Cryosphere Expansion. Science (80-.). 305, 1766–1770.

Staiger, J.W., Marchant, D.R., Schaefer, J.M., Oberholzer, P., Johnson, J. V, Lewis, A.R., Swanger, K.M., 2006. Plio-Pleistocene history of Ferrar Glacier , Antarctica : Implications for climate and ice sheet stability 243, 489–503. doi:10.1016/j.epsl.2006.01.037

Stone, J.O., 2000. Air pressure and cosmogenic isotope production. J. Geophys. Res. 105, 23,753-23,759.

Stone, J.O., Balco, G., Sugden, D.E., Caffee, M.W., Sass, L.C.I., Cowdery, S.G., Siddoway, C., 2003. Holcene Deglaciation of Marie Byrd Land, West Antarctica. Science (80-.). 299, 99–102. doi:10.1126/science.1115233

Sugden, D.E.., Marchant, D.R.., Denton, G.H.., 1993. The Case for a Stable East Antarctic Ice Sheet. Geogr. Ann. Ser. A Phys. Geogr. 75, 151–154.

Sugden, D.E., Denton, G.H., Marchant, D.R., 1995. Landscape Evolution of the Dry Valleys, Transantarctic Mountains - Tectonic Implications. J. Geophys. Res. Earth 100, 9949–9967.

Sugden, D.E., Summerfield, M.A., Denton, G.H., Wilch, T.I., McIntosh, W.C., Marchant, D.R., Rutford, R.H., 1999. Landscape development in the Royal Society Range, southern Victoria Land, Antarctica: stability since the mid-Miocene. Geomorphology 28, 181–200. doi:10.1016/S0169-555X(98)00108-1

Swanger, K.M., Marchant, D.R., Schaefer, J.M., Winckler, G., Head, J.W., 2011. Elevated East Antarctic outlet glaciers during warmer-than-present climates in southern Victoria Land. Glob. Planet. Change 79, 61–72. doi:10.1016/j.gloplacha.2011.07.012

Thomson, S.N., Reiners, P.W., Hemming, S.R., Gehrels, G.E., 2013. The contribution of glacial erosion to shaping the hidden landscape of East Antarctica. Nat. Geosci. 6, 203–207. doi:10.1038/ngeo1722

Tochilin, C.J., Reiners, P.W., Thomson, S.N., Gehrels, G.E., Hemming, S.R., Pierce, E.L., 2012. Erosional history of the Prydz Bay sector of East Antarctica from detrital apatite and zircon geo-and thermochronology multidating. Geochemistry, Geophys. Geosystems 13. doi:10.1029/2012GC004364

Todd, C., Stone, J., Conway, H., Hall, B., Bromley, G., 2010. Late Quaternary evolution of Reedy Glacier, Antarctica. Quat. Sci. Rev. 29, 1328–1341. doi:10.1016/j.quascirev.2010.02.001

Webb, P.N., Harwood, D.M., 1987. Terrestrial flora of the Sirius Formation: its significance for Late Cenozoic glacial history. Antarct. J. United States 22, 7–11.

Wilch, T.I., Lux, D.R., Denton, G.H., McIntosh, W.C., 1993. Minimal Pliocene-Pleistocene uplift of the dry valleys sector of the Transantarctic Mountains: a key parameter in ice-sheet reconstructions. Geology 21, 841–844. doi:10.1130/0091-7613(1993)021<0841:MPPUOT>2.3.CO;2

Winnick, M.J., Caves, J.K., 2015. Oxygen isotope mass-balance constraints on Pliocene sea level and East Antarctic Ice Sheet stability. Geology 43, 879–882. doi:10.1130/G36999.1

Young, N.E., Schaefer, J.M., Briner, J.P., Goehring, B.M., 2013. A 10Be production-rate calibration for the Arctic. J. Quat. Sci. 28, 515–526. doi:10.1002/jqs.2642

Zachos, J.C., Breza, J.R., Wise, S.W., 1992. Early Oligocene ice sheet expansion on Antarctica: stable isotope and sedimentological evidence from Kerguelen Plateau, Southern Indian Ocean. Geology 20, 569–573. doi:10.1130/0091-7613(1992)020<0569:EOISEO>2.3.CO;2

Zhang, Y.G.Y.G., Pagani, M., Liu, Z., Bohaty, S.M.S.M., DeConto, R., 2013. A 40-million-year history of atmospheric CO2. Philos. Trans. Math. Phys. Sngineering Sci. 371, 1–20.

Zwally, H.J., Li, J., Robbins, J.W., Saba, J.L., Yi, D., Brenner, A.C., 2015. Mass gains of the Antarctic ice sheet exceed losses. J. Glaciol. 61, 1019–1036. doi:10.3189/2015JoG15J071

APPENDIX A

PYROXENE SEPARATION FOR ^{3}HE DATING

The following procedure, used to purify pyroxene grains for cosmogenic ^{3}He exposure-age dating, is modified from Bromley et al. (2014). A flow chart for the procedure is provided below:

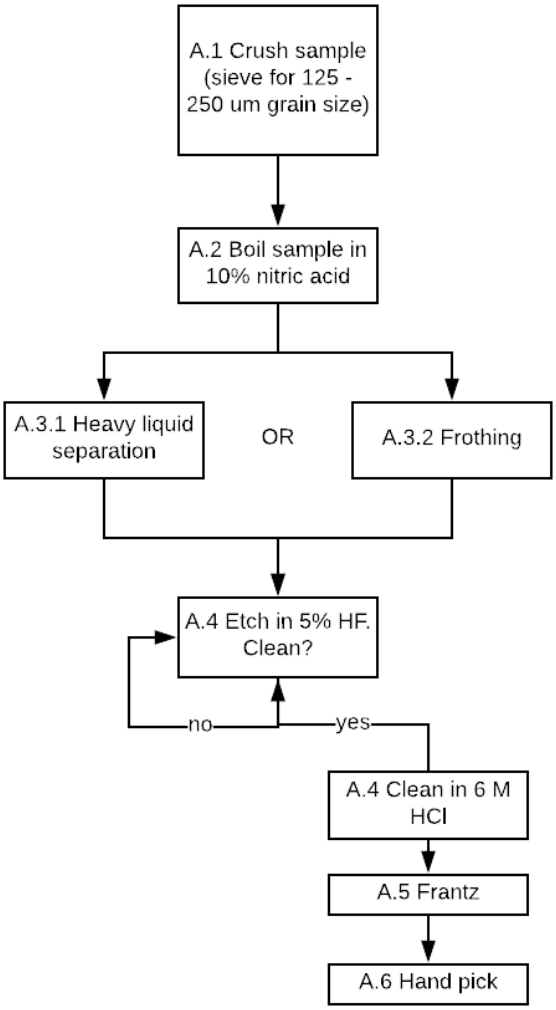

Pyroxene Separation

Detailed below are methods for obtaining purified pyroxene from a whole rock. The preparation of the rock involves both physical and chemical separation methods. The procedure detailed below is a modified version of the Lamont-Doherty Earth Observatory Laboratory methods (http://www.ldeo.columbia.edu/cosmo/methods).

A.1 Rock Crushing

Safety information: The crushing, grinding, and sieving of rocks produces high amounts of dust, and inhalation of dust particles should be avoided. Review the procedures for operating the ventilation systems for these pieces of equipment and procedures. ALWAYS WEAR A DUST MASK (NIOSH approved, N95), safety goggles, work gloves, long pants, and closed shoes.

1. Ensure that work area and machinery are thoroughly cleaned.

2. Rock samples may need to be cut using a saw to fit in jaw crusher.

3. The samples are crushed into small pieces using a jaw crusher. Use a piece of wood to guide samples into crusher to ensure that they do not fly away.

4. Samples are then crushed using a disk mill. Place the nozzle of the vent into the whole at the top of the box around the disk mill. This will remove the majority of the dust particles from the source area. Crush rock pieces into sand-sized grains (generally < 0.7mm). It is necessary to put the sample through the disk mill numerous times and progressively move the disks closer together to achieve the desired grain size without producing excess fine-grained sediment.

5. The crushed rock can then be put through a column of sieves to sort the sample by grain size. Use 125-250 μm size sieves.

Cleaning: Saws and rock crushing machines should be thoroughly cleaned after each sample. Rinse saws with water and dry them completely afterward. Use methanol to protect the metal pieces from oxidation. Clean the disk mill using a vacuum, air compressor, and small broom or brush. After cleaning the disk mill, turn it on and let it run for a few seconds without putting a sample in and observe to see if grains are in the pan. Clean sieves with a brush and put in a small ultrasonic bath. Then, dry sieves in an oven and inspect them for cleanliness. If grains are still present in sieves, clean further with a brush or air compressor.

A.2 Nitric Acid Boiling

Samples are boiled in nitric acid to remove iron oxides.

1. Check the beakers thoroughly for cracks and clearly label them.

2. Be careful of cross contamination if you are boiling more than 1 sample.

3. Set up the hotplate in the hood. As the beakers can jump around during this process, you may wish you use the hotplates with metal cages.

4. Pour crushed sample into 500 ml beakers. Try not to fill above the 300 ml line on the beaker. Rinse with DI water in the sink 5-6 times, or until water is clear, to remove fines.

5. In the fume hood, add 10% nitric acid to each beaker so that there the liquid is ~100 ml above the sample. Cover the beakers with a watch glass. Set the hotplate to about 325°C and bring the samples to a boil. The boiling can be very vigorous at first, so you must stay in the lab until it has reached a steady rolling boil. Make sure that vigorous boiling isn't causing the beakers to "walk" off the hotplate. Boil for 2 hours, checking often to ensure that the liquid has not dried down. After 2 hours, unplug hot plate and let samples cool for about an hour.

6. Once the beakers are cool (lukewarm is ok), the waste nitric acid must be either stored in waste containers or neutralized. To neutralize, place several spoonfuls of sodium bicarbonate into a large plastic bucket. Decant nitric acid into container. Rinse each sample 2 more times with DI water, each time decanting the water into the bucket. Test pH with litmus paper. Continue adding sodium bicarbonate until solution is neutral (pH = 7). The neutralized acid can then be poured down the sink.

7. At the sink, rinse the samples 3 more times with DI water, or until the water is clear.

8. Dry samples overnight in hood.

Beaker Cleaning: If they have iron oxide staining on the bottom, you may need to pour a thin layer of 6M HCl in the bottom of each beaker to remove the staining. Do this in the hood. Place a watch glass on the beaker and let sit in the hood until staining has dissolved (this is usually quite fast). Scrub the beakers in the sink using a brush if necessary and rinse thoroughly so that no sample grains remain in the beakers. If they are really filthy, you can soak them in a soapy solution. Use DI-water for the final rinse. Dry beakers on the drying rack.

A.3.1 Heavy Liquid Separation

Purpose: To separate pyroxene grains from sand samples.

In this procedure, you will separate pyroxenes using LST heavy liquid. LST is non-toxic and does not pose any hazard.
Take care to save the LST – even small droplets on stirrers or in beakers. This stuff is expensive!

1. Make up LST at appropriate density (≥ 2.68 g/cm^3). Measure the LST density with the hygrometer. You can also check the density by placing the piece of pure quartz in the LST – if it is the right density, the quartz will just barely float. If LST is too dense, you can dilute it with DI water. If it is too dilute, you can place the beaker of LST in the oven or on the hot plate at ~300°F until the quartz floats.
2. Make sure the stopper is shut on the separatory funnel. Place an Erlenmayer flask under it, as the liquid will likely still drip out of the funnel even when stopper is shut. Pour the LST into the funnel so that it is approximately half full (you can adjust the amount of LST used based on the size of your sample). Take care that LST doesn't get on the lip of the funnel (wipe if it does) as this will cause the top to stick later on.
3. Using a funnel, pour your sample into the liquid. Smaller samples work better, so split your sample if necessary and do 2-3 runs. Stir using a plastic rod. Rinse rod with DI water over waste beaker when done stirring.

4. Let sit about half an hour, or until grains are done settling.
5. Prepare Buchner funnel and Erlenmayer flask with a coffee filter. Attach vacuum hose and make sure vacuum knobs are set correctly. Wet the coffee filter to make sure it has a good seal.
6. Turn on pump and open the stopper until the heavy minerals settled on the bottom have flushed through. Continuously rinse sample in coffee filter to allow LST to run through filter. Keep an eye on the LST level in the separatory funnel, as it can begin to rush out quickly. If that starts to happen, close stop cock quickly and wait for grains to settle again.
7. Once all of the heavy minerals are in the coffee filter, rinse thoroughly with DI water to make sure all LST rinses through filter. Remove coffee filter and rinse heavy minerals into a clean beaker labeled with the sample name and 'PYROXENE.' Rinse once in the sink, then place in the oven to dry.
8. Replace coffee filter (can reuse the same one if it is not ripped). Allow rest of LST and minerals to drain into the coffee filter. Again, rinse thoroughly with DI water to make sure that all LST passes through filter. Rinse into another clean clean beaker labeled with the sample name and 'FELDSPAR.' Rinse once in the sink, then place in the oven to dry.
9. Replace coffee filter and rinse out separatory funnel completely with DI water, allowing liquid to drain into coffee filter and flask beneath. You can turn the stopcock a few times as the liquid is draining to clean any grains from the opening. Once separatory funnel is thoroughly clean, place coffee filter in LST waste container for later cleaning.
10. Place dilute LST in beaker and dry down on hot plate or in oven for next use.

Procedure for cleaning LST and waste (a bit of a messy process, but does recover quite a lot of LST from waste):

1. Fill LST waste beaker with DI water. With gloved hands, squeeze all liquid out of each piece of waste (i.e. coffee filter, Kim wipe) back into beaker. Place dry waste into new beaker. Repeat until all waste items have been squeezed dry.
2. Repeat step 1, so that each piece of waste is soaked with DI water and squeezed out twice.
3. Filter the waste water from both rinses through a coffee filter into an Erlenmayer flask to remove any grains in liquid. The LST in the Erlenmayer flask will be very dilute.
4. To clean dilute LST, run through a coffee filter into an Erlenmayer flask to remove any grains.
5. Combine clean LST from steps 3 and 4 and dry down on hotplate or in oven.
6. LST should be cleaned if grains are observed in the liquid, and whenever waste containers are full.

A.3.2 Froth Flotation

This method is used to separate feldspar and mica from quartz. It is based on the froth flotation method developed at the PRIME lab (http://www.physics.purdue.edu/primelab/MSL/froth_ floatation.html). Although this procedure is typically used for quartz separations, it works well for separating pyroxenes from Ferrar dolerites, which contain mostly pyroxene and feldspar. However, if using a different rock type, you will need to carefully inspect both the sinking and floating fraction to ensure that the separation was successful.

Grain size for ^{3}He measurement is typically 125-250 μm but you should evaluate your sample and select a size that minimizes poly-mineral grains. We have successfully processed 63-125 μm. Pyroxene with attached feldspars or mica will float, in which case smaller is better. You can froth as much as 300 g in one bottle, otherwise split it into 2 bottles.

Preparation and Pretreatment -- 1% HF leach

1. Record all information in the froth flotation log.

2. Weigh the sample and record the weight (weigh it directly into a tared 2000 ml leaching bottle. Pour the sample in the hood to reduce dust inhalation and lab contamination).

3. Rinse the sample with DI-water to remove dust.

4. Take a small split (<1g) of the rinsed sample with a spatula and place it in a labeled petri dish for examination under the microscope (it is easier to look at the minerals after the sample has been rinsed of dust). Set the sample aside to describe while the sample is leaching.

5. Add 1% HF solution to the jar filling it approximate 2x the depth of the sample. Place it on the shaker table for 45-60 minutes. Do one sample at a time so the sample isn't sitting in the HF solution for too long. You can start the next sample leaching when you begin frothing the current sample.

6. Meanwhile describe the sample and record this in the log. Roughly estimate the percent composition of pyroxene and feldspar and any other significant minerals. If you don't know the mineral, at lead describe color, luster, shape, etc.

Frothing Set Up

1. Fill the 10-liter carboy next to the carbonator with the frothing solution: the final should contain 0.01 ml/1 glacial acetic acid and 0.01 ml/ lauryl amine (surfactant).

2. A concentrated solution is stored in the cabinet below the hood. Add 10 ml of concentrate per liter of DI-water and mix well (this does not have to be precise).

3. Rinse off the carbonator tube before placing it into the frothing solution in the carboy. Make sure it is completely submerged. The solution will be sucked into the carbonator after it's been dispensed. Keep at lead a few liters in the carboy so the carbonator does not suck up air.

4. Hard open the CO_2 tank. It is pre-set to ~100 psi (it should not exceed 100 psi).

5. Plug in the carbonator. There is no on/off switch.

Frothing Process

1. After 45-50 minutes, decant the 1% HF solution from the sample into a labeled waste container. DO NOT rinse the sample.

2. Keep the sample in the 2L leaching bottle and add a few drops of mineral oil to the sample and swirl it around. All mineral oil seems to work-pine, eucalyptus, tea tree (Do not use vegetable oils. Although they will work, they are impossible to clean up. Mineral oils are aromatic hydrocarbons and will evaporate as opposed to vegetable oils that are long chain fatty acids).

3. Dispense some frothing solution onto the sample. Carefully swirl around the bottle at the same time. Decant the solution with the floating grains into a plastic collection jar or directly into a filter funnel hooked up to the pump. The first 2-3 additions might not work very well but with each repetition the frothing with get "foamier" and more grains will float. The floating minerals will look clumpy, fluffy, and bubbly and after a few repetitions of froth and decanting, the sinking fraction and floating fraction will look distinct. If the frothing seems to slow down yet you can see there is still feldspar to remove, try added more oil.

4. When you think the separation is complete, take a split from the sinking pyroxene fraction and check under the microscope to see if any feldspar remains. Difficult samples can be deceiving, so use this as a guide to check what you naked eye sees. Do not finish the sample without looking at this split or you may quit too early.

Once the separation is complete…

1. Take a tiny split from the floating fraction and record what is in it. Take note of any pyroxene that floated off with the feldspar fraction. Poly-mineral grains of pyroxenes and feldspars will float.

2. Rinse the floating fraction in the filter with DI-water.

3. Finish filter the floating fraction, neutralize it with baking soda, and pour down the sink.

Sinking and Floating Fractions

Quartz & Recovery:

1. Rinse the sinking fraction with DI water.

2. Either transfer into 500 ml beaker and dry in oven over night or proceed to HF/HNO_3 leaching.

A.4 Hydrofluoric Acid Leaching

The following steps require the use of strong acids that present skin and inhalation exposure risks, and for HF, systemic toxicity. Review the MSDS sheets and any other documentation

provided. Understand the risks associated with handling the chemicals you are working with, the procedures for reducing any risks, and emergency procedures in the event of an accident.

- Always work in a fume hood with the sash as low as is practical.

- Wear safety/splash goggles and use a full-coverage face shield if there is any risk of splashing.

- Wear appropriate gloves: for work with hot acids, use heavyweight (22 mil) neoprene gloves. For work with HF, you must wear HF-resistant gloves- not all materials are HF resistant (for example, latex). Check your gloves regularly for holes and excessive wear and replace as needed.

- You must wear long pants and closed shoes. Shorts, skirts, and open-toed or fabric shoes are not permitted when working with chemicals.

- Know where the eyewash stations, safety showers, spill kits, and tubes of calcium gluconate gel are located. Small spills contained in a hood can be cleaned up. In the event of a large spill or accident, call your institution's building manager.

- All HF exposures must be treated as medical emergencies. Flush the exposed area with water until medical help arrives.

- All chemical waste is collected in labeled containers and picked up as hazardous waste. Understand the procedures for collecting, labeling, and disposing of your waste.

- Empty bottles must be thoroughly rinsed out. Fill the bottle with water in the hood to avoid breathing vapors, and then rinse out at least 3 times in the sink. Deface the label, and write very clearly on the bottle, "RINSED."

Hydrofluoric Leach:

Samples are leached in a dilute hydrofluoric acid solution in order to dissolve minerals other than pyroxene and to remove radiogenic ^{3}He from the outer surfaces of the pyroxene graines. Samples are generally leached once in ~100 ml of a 5% HF/HNO_3 solution and placed in a heated ultrasonic bath for 3-4 days. Some samples require additional (4-10) leaching steps before they are sufficiently clean.

Measure 5-7 g of sample into a 125 ml plastic bottle. Make sure that you are using the low density polyethylene (LDPE) containers *not* the high density polyethylene (HDPE) containers, as the HDPE bottles are more brittle and may crack over time.

- Add 100 ml DI-H_2O. Then, working in the fume hood, add 10 ml concentrated (49%) HF. NOTE: ALWAYS ADD WATER FIRST! NEVER ADD WATER TO ACID!

- Place bottles in the small ultrasonic (this one has an on/off switch rather than timed sonication). Make sure there are no drips of acid on the sides of the bottles. You can leave the ultrasonic running each day, but make sure to turn it off each night to give the ultrasonic a "rest" so that the motor does not burn out. Make sure to check the water level before turning on the ultrasonic each morning. The water line should be roughly flush with the top of the ultrasonic.

- Pyroxene dissolves relatively slowly in HF compared to quartz, but make sure to check the sample periodically to make sure that you have not lost too much. It also helps to shake up the sample a few times a day.

- After 3-4 days, you are ready to decant the HF. In the hood, pour the acid solution into a properly labeled waste container being careful not to pour out your sample.

- While working in the fume hood, add ~100 ml of DI-H_2O to each bottle. Shake them vigorously, and then decant the water into the waste container, again being careful not to spill any sample. The acid is dilute enough to now work outside of the hood. Rinse the samples two more times, filling the bottles about a third of the way and shaking them vigorously each time. The vigorous shaking will work to break up weaker feldspar grains.

- For larger samples, or those that seem to still have some feldspars in them, it may help to do a second leaching in 5% HF for 4-6 hours.

- If there is a lot of calcium in the pyroxenes, fluorides may develop. To dissolve the fluorides, cover the sample (still in the 125 ml bottles) in 6 M HCl and allow to sit for at least an hour (can let sit overnight). If the ultrasonic is on, you can place the bottles in the ultrasonic.

- In the hood, decant the HCl into a waste container or neutralize the acid.

- Rinse samples thoroughly in DI water (5-6 times) to remove any trace HCl. Dry samples in plastic bottles in the oven on a low temperature overnight.

- Wash your bottles. Make sure you remove all sample grains from the bottles before adding a new sample! Rinse the bottles thoroughly and scrub with brush. You can turn the bottle upside down and forcefully clean off any grains that may be stuck to the bottom and sides. Once your bottles are cleaned, remove all labels and put them away.

A.5 Magnetic Mineral Separation

- Sieve samples using a 0.125 mm sieve to remove any small grains that have broken down in the etching process, which make hand picking more difficult. You can also use a 0.250 mm sieve to remove any remaining fluorides that did not dissolve completely in HCl.

- Put the sieved sample through a frantz isodynamic separator at ~1.0 Amps and a 5-degree tilt to remove any remaining feldspars or other non-magnetic minerals. The non-magnetic

fraction should be white in color. All of the pyroxenes should remain in the magnetic fraction.

- Put the magnetic fraction attained in the previous step back through the frantz, this time set to ~0.20 Amps. This will remove any highly magnetic minerals, such as ilmenite. Keep the non-magnetic fraction.

- Cleaning: Clean the chute magnet thoroughly after each sample. Wipe the frantz and the collection cups with the brush and then with the air hose.

A.6 Hand-picking

- The final step in preparing samples for ^{3}He analysis is hand picking. Materials needed are a diatom tray, paintbrush, small water vessel, and a microscope.

- Label a small glass vial and place on the balance. Zero the balance.

- Place pyroxene grains in a thin layer along the bottom of the trough in the diatom tray. Picking will be most effective if the grains are not too dense in the tray and grains are not piled atop one another. Also, make sure that grains have not stuck to the sides of "trough" in the diatom tray, as they will be difficult to see in the microscope.

- Wet the paintbrush slightly and pick out any grains that are not pyroxenes. After picking up each unwanted grain, the paintbrush can be rinsed in the small container of water.

- NOTE: Depending on the type of pyroxene, the pyroxene grains may have lost their color in the HF leaching making it more difficult to distinguish them from any remaining feldspars. Typically, if a few feldspar grains remain, they are a milky white while the pyroxenes are more translucent. If you are unsure how to identify the altered pyroxenes, it may be helpful to identify at a few grains in the scanning electron microscope to get a sense for what each mineral looks like after it has been etched.

- After picking through the entire tray, you can transfer the grains into the glass vial using a piece of paper. Turn the diatom tray over on the paper and tap the bottom of the tray so that all the grains fall off onto the paper. If needed, you can use a Kimwipe to remove any grains remaining in the tray. Pour grains into the glass vial. Return vial to balance to retrieve mass of purified pyroxene.

- In the end, you should have 100-200 mg, which is enough pyroxene to analyze multiple aliquots for ^{3}He. This will probably require picking 2-4 diatom trays.

APPENDIX B

^{3}HE DATA REDUCTION

The following equations are used to calculate ^{3}He and ^{4}He concentrations and uncertainties from noble gas mass spectrometry outputs.

B.1 Calculate Helium-3 Concentrations

The equation used to calculate ^{3}He concentration is:

$$[\,^3He] = \frac{^3He * s_3 * 6.022 * 10^{23}}{m}$$

where ^{3}He is the amount of ^{3}He measured on the mass spectrometer in counts per second (cps), s_3 is the ^{3}He sensitivity (instructions to calculate below), and m is the mass of the sample in grams. If multiple heating steps were performed, the total [^{3}He] is the sum of the [^{3}He] from all steps.

B.1.1 Mass spectrometer sensitivity to ^{3}He

The sensitivity of the mass spectrometer to ^{3}He is dependent on the ^{4}He concentration in the sample. Therefore, the sensitivity of the mass spectrometer is determined from gas standard runs. The following steps can be used to calculate s_3:

1) Determine which standards are applicable to dataset. Ideally, you have run samples with both lower and higher ^{3}He concentrations than you expect to find in your unknowns.
2) Calculate s_3 by interpolating between ^{3}He concentrations of various gas standards.
    a. Divide the known amount of ^{3}He (in atoms) in the gas standard by the measured ^{3}He (in cps) in the gas standard to determine s_3 (in atoms/cps) for each gas standard.

b. Plot s_3 vs. measured ^{4}He (in mV) for all gas standards (can be done in either linear or log scale). Plot a line of best fit and view the associated equation.

c. Use the equation for the line of best fit determined in 2b, and the measured ^{4}He (in mV) for each standard, calculate s_3 for all standards plotted in Step 2b.

d. Take the standard deviation of all values in 2c. Find δs_3 (in mol/cps) for each sample by multiplying s_3 (in mol/cps) for each sample by the standard deviation.

B.1.2 ^{3}He Uncertainty Calculation

The equation for the uncertainty associated with the ^{3}He concentration of each heating step is:

$$\delta[\,^3He] = \frac{6.022 * 10^{23}}{m} * \sqrt{(\,^3He * \delta s_3)^2 + (s_3 * \delta\,^3He)^2}$$

where m is the sample mass in g, ^{3}He is the measured amount of ^{3}He in cps, δs_3 is the value calculated for each heating step in step 2d of section A.1.1, s_3 is the sensitivity value calculated for each heating step in step 2c of section A.1.1., and δ^3He is the measured uncertainty (in mol/cps). Use the following equation to find the uncertainty in the ^{3}He concentration for the whole sample:

$$\delta[\,^3He] = \sqrt{(\delta[\,^3He]_{@\ heating\ step\ 1})^2 + \cdots + (\delta[\,^3He]_{@\ heating\ step\ n})^2}$$

NOTE: The same procedure is used to calculate the ^{4}He concentrations and uncertainties using the measured amount of ^{4}He in the standards and samples (in mol/mV).

Table C.1 continued.

APPENDIX C

STEP DEGASSING RESULTS FOR ^{3}HE MEASUREMENTS

Table C.1 Complete step degassing results for ^{3}He measurements

Sample ID	Date analyzed	Aliquot	Heating temperature (°C)	Heating time (min)	Aliquot weight (g)	[He-3] (atoms/g)	δ[He-3] (atoms/g)	[He-3] (atoms/g)	δ[He-3] (atoms/g)	% error	[He-4] (atoms/g)	δ[He-4] (atoms/g)	[He-4] (atoms/g)	δ[He-4] (atoms/g)
15-ROB-001-MZA	2016_10_1	a	1150	15	0.02447	7.59E+09	7.89E+07	8.73E+09	7.99E+07	0.92	7.96E+14	3.89E+12	9.18E+14	3.94E+12
15-ROB-001-MZA	2016_10_1	a	1300	15	0.02447	1.14E+09	1.30E+07				1.21E+14	5.95E+11		
15-ROB-001-MZA	2016_10_2	b	1150	15	0.02238	7.00E+09	7.24E+07	8.44E+09	7.42E+07	0.88	7.28E+14	3.56E+12	8.80E+14	3.64E+12
15-ROB-001-MZA	2016_10_2	b	1300	15	0.02238	1.45E+09	1.62E+07				1.52E+14	7.46E+11		
15-ROB-002-MZA	2016_10_2	a	1150	15	0.01956	6.03E+09	5.15E+07	6.05E+09	5.15E+07	0.85	2.65E+14	5.75E+12	2.66E+14	5.75E+12
15-ROB-002-MZA	2016_10_2	a	1300	15	0.01956	2.31E+07	1.77E+06				1.09E+12	3.67E+10		
15-ROB-002-MZA	2016_10_2	b	1150	15	0.01424	6.01E+09	5.21E+07	6.05E+09	5.22E+07	0.86	2.68E+14	5.82E+12	2.71E+14	5.82E+12
15-ROB-002-MZA	2016_10_2	b	1300	15	0.01424	3.66E+07	2.64E+06				2.77E+12	6.80E+10		
15-ROB-003-MZA	2016_10_2	a	1150	15	0.01414	6.48E+09	5.67E+07	6.57E+09	5.70E+07	0.87	3.68E+14	7.98E+12	3.73E+14	7.98E+12
15-ROB-003-MZA	2016_10_2	a	1300	15	0.01414	9.02E+07	5.33E+06				5.26E+12	1.19E+11		
15-ROB-003-MZA	2016_10_2	b	1150	15	0.02288	6.44E+09	5.81E+07	6.58E+09	5.82E+07	0.88	3.63E+14	7.88E+12	3.82E+14	7.89E+12
15-ROB-003-MZA	2016_10_2	b	1300	15	0.02288	1.34E+08	2.87E+06				1.89E+13	4.12E+11		
15-ROB-004-MZA	2016_10_2	a	1150	15	0.01857	4.15E+09	3.64E+07	4.56E+09	3.68E+07	0.81	7.67E+14	1.66E+13	8.66E+14	1.68E+13
15-ROB-004-MZA	2016_10_2	a	1300	15	0.01857	4.02E+08	5.43E+06				9.95E+13	2.16E+12		
15-ROB-004-MZA	2016_10_2	b	1150	15	0.02489	4.60E+09	4.47E+07	4.86E+09	4.49E+07	0.92	7.90E+14	1.71E+13	8.59E+14	1.72E+13
15-ROB-004-MZA	2016_10_2	b	1300	15	0.02489	2.66E+08	4.11E+06				6.85E+13	1.49E+12		
15-ROB-005-MZA	2016_10_2	a	1150	15	0.0202	6.06E+09	5.61E+07	6.67E+09	5.66E+07	0.85	9.39E+14	2.04E+13	1.04E+15	2.05E+13
15-ROB-005-MZA	2016_10_2	a	1300	15	0.0202	6.10E+08	7.25E+06				9.70E+13	2.11E+12		
15-ROB-005-MZA	2016_10_2	b	1150	15	0.01876	6.10E+09	5.28E+07	6.67E+09	5.33E+07	0.80	9.22E+14	2.01E+13	1.01E+15	2.02E+13
15-ROB-005-MZA	2016_10_2	b	1300	15	0.01876	5.67E+08	7.18E+06				9.19E+13	1.99E+12		

Table C.1 continued.

Sample ID	Date analyzed	Aliquot	Heating temperature (°C)	Heating time (min)	Aliquot weight (g)	[He-3] (atoms/g)	δ[He-3] (atoms/g)	[He-3] (atoms/g)	δ[He-3] (atoms/g)	% error	[He-4] (atoms/g)	δ[He-4] (atoms/g)	[He-4] (atoms/g)	δ[He-4] (atoms/g)
15-ROB-006-MZB	2017_05_1	a	1250	15	0.01801	8.33E+09	1.63E+08	9.06E+09	1.64E+08	1.80	5.76E+14	1.05E+13	6.49E+14	1.05E+13
15-ROB-006-MZB	2017_05_1	a	1300	15	0.01801	4.60E+08	1.17E+07				4.62E+13	8.64E+11		
15-ROB-006-MZB	2017_05_1	a	1350	15	0.01801	2.73E+08	7.95E+06				2.73E+13	5.13E+11		
15-ROB-006-MZB	2017_05_2	b	1275	15	0.02164	8.58E+09	1.49E+08	8.73E+09	1.49E+08	1.71	6.28E+14	1.03E+13	6.45E+14	1.03E+13
15-ROB-006-MZB	2017_05_2	b	1350	15	0.02164	1.48E+08	4.93E+06				1.67E+13	3.02E+11		
15-ROB-006-MZB	2017_05_2	b	1375	15	0.02164	5.31E+06	1.16E+06				4.79E+11	1.02E+11		
15-ROB-007-MZB	2017_05_1	a	1250	15	0.02269	8.12E+09	1.59E+08	9.32E+09	1.60E+08	1.72	7.72E+14	1.42E+13	9.26E+14	1.43E+13
15-ROB-007-MZB	2017_05_1	a	1300	15	0.02269	6.77E+08	1.64E+07				8.59E+13	1.62E+12		
15-ROB-007-MZB	2017_05_1	a	1350	15	0.02269	5.25E+08	1.24E+07				6.84E+13	1.28E+12		
15-ROB-007-MZB	2017_05_2	b	1275	15	0.0181	8.01E+09	1.40E+08	9.07E+09	1.41E+08	1.56	7.99E+14	1.32E+13	9.33E+14	1.33E+13
15-ROB-007-MZB	2017_05_2	b	1350	15	0.0181	8.26E+08	1.92E+07				1.04E+14	1.84E+12		
15-ROB-007-MZB	2017_05_2	b	1375	15	0.0181	2.35E+08	7.46E+06				2.97E+13	5.29E+11		
15-ROB-008-MZB	2017_05_1	a	1250	15	0.02381	7.52E+09	1.46E+08	9.11E+09	1.49E+08	1.63	7.71E+14	1.76E+13	9.73E+14	1.78E+13
15-ROB-008-MZB	2017_05_1	a	1300	15	0.02381	9.11E+08	1.97E+07				1.14E+14	2.08E+12		
15-ROB-008-MZB	2017_05_1	a	1350	15	0.02381	6.84E+08	1.62E+07				8.72E+13	1.63E+12		
15-ROB-008-MZB	2017_05_2	b	1275	15	0.01564	8.10E+09	1.42E+08	9.06E+09	1.44E+08	1.59	9.04E+14	1.48E+13	1.03E+15	1.50E+13
15-ROB-008-MZB	2017_05_2	b	1350	15	0.01564	8.94E+08	2.06E+07				1.14E+14	2.02E+12		
15-ROB-008-MZB	2017_05_2	b	1375	15	0.01564	6.93E+07	3.79E+06				8.33E+12	1.75E+11		
15-ROB-009-MZB	2017_05_1	a	1250	15	0.02098	9.18E+09	1.79E+08	9.21E+09	1.79E+08	1.94	2.05E+14	3.74E+12	2.06E+14	3.74E+12
15-ROB-009-MZB	2017_05_1	a	1300	15	0.02098	2.84E+07	2.16E+06				7.50E+11	6.22E+10		
15-ROB-009-MZB	2017_05_3	b	1275	15	0.01882	9.00E+09	1.44E+08	9.03E+09	1.44E+08	1.60	2.02E+14	3.03E+12	2.03E+14	3.03E+12
15-ROB-009-MZB	2017_05_3	b	1350	15	0.01882	3.32E+07	2.24E+06				9.36E+11	8.11E+10		
15-ROB-010-MZB	2017_05_1	a	1250	15	0.0227	8.33E+09	1.63E+08	9.06E+09	1.63E+08	1.80	7.65E+14	1.40E+13	8.43E+14	1.41E+13
15-ROB-010-MZB	2017_05_1	a	1300	15	0.0227	6.02E+08	1.45E+07				6.48E+13	1.20E+12		
15-ROB-010-MZB	2017_05_1	a	1350	15	0.0227	1.25E+08	4.30E+06				1.33E+13	2.51E+11		

Table C.1 continued.

Sample ID	Date analyzed	Aliquot	Heating temperature (°C)	Heating time (min)	Aliquot weight (g)	[He-3] (atoms/g)	δ[He-3] (atoms/g)	[He-3] (atoms/g)	δ[He-3] (atoms/g)	% error	[He-4] (atoms/g)	δ[He-4] (atoms/g)	[He-4] (atoms/g)	δ[He-4] (atoms/g)
15-ROB-010-MZB	2017_05_3	b	1275	15	0.01836	7.61E+09	1.23E+08	9.11E+09	1.25E+08	1.37	6.62E+14	9.97E+12	8.19E+14	1.02E+13
15-ROB-010-MZB	2017_05_3	b	1350	15	0.01836	1.43E+09	2.49E+07				1.50E+14	2.28E+12		
15-ROB-010-MZB	2017_05_3	b	1375	15	0.01836	7.60E+07	3.31E+06				7.34E+12	1.75E+11		
15-ROB-011-MZB	2017_05_1	a	1250	15	0.02252	9.05E+09	1.76E+08	9.12E+09	1.76E+08	1.93	4.12E+14	7.57E+12	4.18E+14	7.57E+12
15-ROB-011-MZB	2017_05_1	a	1300	15	0.02252	6.65E+07	3.17E+06				5.31E+12	1.10E+11		
15-ROB-011-MZB	2017_05_3	b	1275	15	0.0221	9.00E+09	1.44E+08	9.09E+09	1.44E+08	1.59	4.02E+14	6.07E+12	4.08E+14	6.07E+12
15-ROB-011-MZB	2017_05_3	b	1350	15	0.0221	8.55E+07	3.60E+06				5.85E+12	1.38E+11		
15-ROB-012-MZB	2017_05_1	a	1250	15	0.02141	8.09E+09	1.58E+08	9.13E+09	1.59E+08	1.74	7.37E+14	1.34E+13	8.63E+14	1.35E+13
15-ROB-012-MZB	2017_05_1	a	1300	15	0.02141	6.81E+08	1.68E+07				8.17E+13	1.55E+12		
15-ROB-012-MZB	2017_05_1	a	1350	15	0.02141	3.56E+08	9.40E+06				4.37E+13	8.19E+11		
15-ROB-013-MZB	2017_05_1	a	1250	15	0.02077	8.92E+09	1.74E+08	9.02E+09	1.74E+08	1.93	4.62E+14	8.42E+12	4.69E+14	8.42E+12
15-ROB-013-MZB	2017_05_1	a	1300	15	0.02077	9.86E+07	4.26E+06				6.75E+12	1.38E+11		
15-ROB-014-MZC	2017_05_1	a	1250	15	0.0261	7.43E+09	1.44E+08	8.64E+09	1.46E+08	1.68	7.27E+14	1.33E+13	8.72E+14	1.34E+13
15-ROB-014-MZC	2017_05_1	a	1300	15	0.0261	8.10E+08	1.73E+07				9.79E+13	1.79E+12		
15-ROB-014-MZC	2017_05_1	a	1350	15	0.0261	4.07E+08	1.02E+07				4.70E+13	8.75E+11		
15-ROB-014-MZC	2017_05_4	b	1275	15	0.02079	8.23E+09	1.25E+08	8.59E+09	1.26E+08	1.46	8.20E+14	1.17E+13	8.60E+14	1.18E+13
15-ROB-014-MZC	2017_05_4	b	1350	15	0.02079	3.58E+08	9.38E+06				4.02E+13	9.15E+11		
15-ROB-015-MZC	2017_05_1	a	1250	15	0.02368	7.41E+09	1.44E+08	8.75E+09	1.46E+08	1.67	6.66E+14	1.22E+13	8.00E+14	1.24E+13
15-ROB-015-MZC	2017_05_1	a	1300	15	0.02368	8.60E+08	1.98E+07				8.84E+13	1.65E+12		
15-ROB-015-MZC	2017_05_1	a	1350	15	0.02368	4.77E+08	1.18E+07				4.56E+13	8.48E+11		
15-ROB-015-MZC	2017_05_4	b	1275	15	0.02097	8.73E+09	1.33E+08	8.74E+09	1.33E+08	1.53	7.97E+14	1.12E+13	7.98E+14	1.12E+13
15-ROB-015-MZC	2017_05_4	b	1350	15	0.02097	1.09E+07	1.69E+06				1.22E+12	8.83E+10		
15-ROB-016-MZC	2017_05_2	a	1275	15	0.02365	8.39E+09	1.46E+08	8.49E+09	1.46E+08	1.72	2.65E+14	4.37E+12	2.70E+14	4.37E+12
15-ROB-016-MZC	2017_05_2	a	1300	15	0.02365	9.94E+07	4.11E+06				4.39E+12	9.06E+10		
15-ROB-016-MZC	2017_05_4	b	1275	15	0.0197	8.51E+09	1.31E+08	8.53E+09	1.31E+08	1.53	2.47E+14	3.46E+12	2.47E+14	3.47E+12

Table C.1 continued.

Sample ID	Date analyzed	Aliquot	Heating temperature (°C)	Heating time (min)	Aliquot weight (g)	[He-3] (atoms/g)	δ[He-3] (atoms/g)	[He-3] (atoms/g)	δ[He-3] (atoms/g)	% error	[He-4] (atoms/g)	δ[He-4] (atoms/g)	[He-4] (atoms/g)	δ[He-4] (atoms/g)
15-ROB-016-MZC	2017_05_4	b	1350	15	0.0197	2.21E+07	1.97E+06				4.69E+11	9.13E+10		
15-ROB-017-MZC	2017_05_2	a	1275	15	0.0173	7.71E+09	1.36E+08	8.81E+09	1.38E+08	1.57	6.07E+14	1.00E+13	7.26E+14	1.02E+13
15-ROB-017-MZC	2017_05_2	a	1350	15	0.0173	9.81E+08	2.32E+07				1.05E+14	1.86E+12		
15-ROB-017-MZC	2017_05_2	a	1375	15	0.0173	1.15E+08	4.26E+06				1.38E+13	2.50E+11		
15-ROB-018-MZC	2016_10_1	a	1150	15	0.02305	7.44E+09	8.20E+07	8.08E+09	8.24E+07	1.02	8.86E+14	4.33E+12	9.75E+14	4.35E+12
15-ROB-018-MZC	2016_10_1	a	1300	15	0.02305	6.39E+08	8.06E+06				8.92E+13	4.37E+11		
15-ROB-018-MZC	2016_10_2	b	1150	15	0.01757	7.45E+09	7.87E+07	7.82E+09	7.90E+07	1.01	9.03E+14	4.41E+12	9.58E+14	4.42E+12
15-ROB-018-MZC	2016_10_2	b	1300	15	0.01757	3.70E+08	6.09E+06				5.46E+13	2.69E+11		
15-ROB-018-MZC	2017_05_1	c	1250	15	0.01778	7.23E+09	1.41E+08	8.02E+09	1.42E+08	1.77	8.39E+14	1.53E+13	9.56E+14	1.53E+13
15-ROB-018-MZC	2017_05_1	c	1300	15	0.01778	4.94E+08	1.32E+07				7.33E+13	1.37E+12		
15-ROB-018-MZC	2017_05_1	c	1350	15	0.01778	2.96E+08	8.62E+06				4.38E+13	8.21E+11		
15-ROB-019-MZC	2016_10_1	a	1150	15	0.0198	7.68E+09	7.99E+07	7.79E+09	8.03E+07	1.03	4.67E+14	2.28E+12	4.72E+14	2.29E+12
15-ROB-019-MZC	2016_10_1	a	1300	15	0.0198	1.13E+08	7.45E+06				5.66E+12	1.89E+11		
15-ROB-019-MZC	2016_10_2	b	1150	15	0.01687	7.79E+09	8.20E+07	7.92E+09	8.24E+07	1.04	4.86E+14	2.38E+12	4.93E+14	2.39E+12
15-ROB-019-MZC	2016_10_2	b	1300	15	0.01687	1.25E+08	8.23E+06				6.71E+12	2.23E+11		
15-ROB-020-MZC	2016_10_1	a	1150	15	0.02127	7.02E+09	7.31E+07	7.66E+09	7.36E+07	0.96	5.36E+14	2.62E+12	5.85E+14	2.63E+12
15-ROB-020-MZC	2016_10_1	a	1300	15	0.02127	6.31E+08	8.38E+06				4.96E+13	2.45E+11		
15-ROB-020-MZC	2016_10_2	b	1150	15	0.03215	7.55E+09	7.74E+07	7.97E+09	7.76E+07	0.97	5.80E+14	2.83E+12	6.14E+14	2.84E+12
15-ROB-020-MZC	2016_10_2	b	1300	15	0.03215	4.20E+08	5.45E+06				3.41E+13	1.68E+11		
15-ROB-021-MZC	2016_10_1	a	1150	15	0.02149	5.08E+09	5.65E+07	5.45E+09	5.68E+07	1.04	7.18E+14	3.51E+12	8.00E+14	3.53E+12
15-ROB-021-MZC	2016_10_1	a	1300	15	0.02149	3.67E+08	5.77E+06				8.14E+13	3.99E+11		
15-ROB-021-MZC	2016_10_2	b	1150	15	0.0194	5.09E+09	5.38E+07	5.37E+09	5.40E+07	1.01	7.47E+14	3.65E+12	8.08E+14	3.66E+12
15-ROB-021-MZC	2016_10_2	b	1300	15	0.0194	2.74E+08	4.31E+06				6.10E+13	3.00E+11		
15-ROB-022-MZC	2016_10_1	a	1150	15	0.01789	4.93E+09	5.29E+07	5.01E+09	5.32E+07	1.06	6.43E+14	3.14E+12	6.52E+14	3.15E+12
15-ROB-022-MZC	2016_10_1	a	1300	15	0.01789	8.11E+07	5.55E+06				8.85E+12	2.94E+11		

Table C.1 continued.

Sample ID	Date analyzed	Aliquot	Heating temperature (°C)	Heating time (min)	Aliquot weight (g)	[He-3] (atoms/g)	δ[He-3] (atoms/g)	[He-3] (atoms/g)	δ[He-3] (atoms/g)	% error	[He-4] (atoms/g)	δ[He-4] (atoms/g)	[He-4] (atoms/g)	δ[He-4] (atoms/g)
15-ROB-022-MZC	2016_10_2	b	1150	15	0.0174	4.92E+09	5.27E+07	5.08E+09	5.28E+07	1.04	6.41E+14	3.13E+12	6.68E+14	3.13E+12
15-ROB-022-MZC	2016_10_2	b	1300	15	0.0174	1.61E+08	3.56E+06				2.77E+13	1.41E+11		
15-ROB-023-MZD	2017_05_2	a	1275	15	0.01957	8.96E+09	1.56E+08	9.02E+09	1.56E+08	1.73	3.41E+14	5.60E+12	3.44E+14	5.60E+12
15-ROB-023-MZD	2017_05_2	a	1300	15	0.01957	5.96E+07	3.03E+06				2.90E+12	1.03E+11		
15-ROB-024-MZD	2017_05_2	a	1275	15	0.02031	8.00E+09	1.39E+08	8.66E+09	1.40E+08	1.61	6.49E+14	1.07E+13	7.39E+14	1.07E+13
15-ROB-024-MZD	2017_05_2	a	1350	15	0.02031	4.90E+08	1.23E+07				6.71E+13	1.19E+12		
15-ROB-024-MZD	2017_05_2	a	1375	15	0.02031	1.70E+08	5.83E+06				2.26E+13	4.02E+11		
15-ROB-025-MZD	2017_05_2	a	1275	15	0.01761	8.51E+09	1.49E+08	8.97E+09	1.49E+08	1.66	6.74E+14	1.11E+13	7.24E+14	1.11E+13
15-ROB-025-MZD	2017_05_2	a	1350	15	0.01761	4.18E+08	1.14E+07				4.56E+13	8.08E+11		
15-ROB-025-MZD	2017_05_2	a	1375	15	0.01761	4.33E+07	2.54E+06				4.27E+12	1.04E+11		
15-ROB-026-MZD	2017_05_2	a	1275	15	0.02186	8.33E+09	1.45E+08	8.40E+09	1.45E+08	1.72	4.99E+14	8.23E+12	5.04E+14	8.23E+12
15-ROB-026-MZD	2017_05_2	a	1300	15	0.02186	6.74E+07	2.97E+06				5.11E+12	1.08E+11		
15-ROB-027-MZD	2017_05_2	a	1275	15	0.02371	8.63E+09	1.49E+08	8.98E+09	1.50E+08	1.67	5.49E+14	9.02E+12	5.77E+14	9.03E+12
15-ROB-027-MZD	2017_05_2	a	1300	15	0.02371	3.44E+08	9.15E+06				2.86E+13	5.11E+11		
15-ROB-027-MZD	2017_05_3	b	1275	15	0.01958	8.87E+09	1.42E+08	9.12E+09	1.43E+08	1.56	5.49E+14	8.29E+12	5.69E+14	8.30E+12
15-ROB-027-MZD	2017_05_3	b	1350	15	0.01958	2.53E+08	7.44E+06				2.00E+13	4.20E+11		
15-ROB-028-COL	2016_08_2	a	650	15	0.0416	8.14E+09	1.12E+08	1.39E+10	1.37E+08	0.99	9.70E+13	4.67E+11	1.68E+14	5.82E+11
15-ROB-028-COL	2016_08_2	a	1300	15	0.0416	5.73E+09	7.91E+07				7.08E+13	3.46E+11		
15-ROB-028-COL	2016_08_3	b	1150	15	0.03272	1.25E+10	1.71E+08	1.35E+10	1.72E+08	1.27	1.54E+14	7.42E+11	1.62E+14	7.44E+11
15-ROB-028-COL	2016_08_3	b	1300	15	0.03272	1.04E+09	1.54E+07				8.98E+12	4.62E+10		
15-ROB-030-COL	2016_08_2	a	650	15	0.0562	1.19E+10	1.62E+08	1.25E+10	1.62E+08	1.30	5.40E+14	2.66E+12	5.64E+14	2.66E+12
15-ROB-030-COL	2016_08_2	a	1300	15	0.0562	6.04E+08	8.89E+06				2.43E+13	1.18E+11		
15-ROB-030-COL	2016_08_3	b	1150	15	0.01884	1.19E+10	1.69E+08	1.20E+10	1.69E+08	1.41	5.35E+14	2.59E+12	#VALUE!	#VALUE!
15-ROB-030-COL	2016_08_3	b	1300	15	0.01884	3.64E+07	7.94E+06				NaN	NaN		
15-ROB-031-COL	2016_08_2	a	650	15	0.0468	1.02E+10	1.40E+08	1.07E+10	1.40E+08	1.31	4.12E+14	2.03E+12	4.34E+14	2.03E+12

Table C.1 continued.

Sample ID	Date analyzed	Aliquot	Heating temperature (°C)	Heating time (min)	Aliquot weight (g)	[He-3] (atoms/g)	δ[He-3] (atoms/g)	[He-3] (atoms/g)	δ[He-3] (atoms/g)	% error	[He-4] (atoms/g)	δ[He-4] (atoms/g)	[He-4] (atoms/g)	δ[He-4] (atoms/g)
15-ROB-031-COL	2016_08_2	a	1300	15	0.0468	4.91E+08	7.31E+06				2.22E+13	1.08E+11		
15-ROB-031-COL	2016_08_3	b	1150	15	0.01399	1.04E+10	1.44E+08	1.04E+10	1.44E+08	1.38	4.48E+14	2.16E+12	4.48E+14	2.16E+12
15-ROB-031-COL	2016_08_3	b	1300	15	0.01399	1.65E+07	1.64E+06				5.66E+11	3.64E+10		
15-ROB-031-COL	2017_05_1	c	1250	15	0.02112	1.04E+10	2.03E+08	1.05E+10	2.03E+08	1.94	4.20E+14	7.64E+12	4.21E+14	7.64E+12
15-ROB-031-COL	2017_05_1	c	1300	15	0.02112	1.15E+07	1.89E+06				4.85E+11	6.77E+10		
15-ROB-035-ARM	2016_08_2	a	650	15	0.0382	1.91E+09	2.70E+07	3.00E+09	3.13E+07	1.05	4.27E+14	2.07E+12	6.28E+14	2.29E+12
15-ROB-035-ARM	2016_08_2	a	1300	15	0.0382	1.09E+09	1.59E+07				2.02E+14	9.71E+11		
15-ROB-035-ARM	2016_08_3	b	1150	15	0.01302	2.78E+09	4.08E+07	3.11E+09	4.14E+07	1.33	5.96E+14	2.86E+12	6.50E+14	2.87E+12
15-ROB-035-ARM	2016_08_3	b	1300	15	0.01302	3.31E+08	6.82E+06				5.53E+13	2.70E+11		
15-ROB-036-ARM	2016_08_2	a	650	15	0.0537	2.83E+09	4.29E+07	3.36E+09	4.36E+07	1.30	3.78E+14	1.86E+12	4.76E+14	1.92E+12
15-ROB-036-ARM	2016_08_2	a	1300	15	0.0537	5.35E+08	7.79E+06				9.75E+13	4.79E+11		
15-ROB-036-ARM	2016_08_3	b	1150	15	0.02276	3.23E+09	4.54E+07	3.29E+09	4.55E+07	1.38	4.75E+14	2.30E+12	4.83E+14	2.30E+12
15-ROB-036-ARM	2016_08_3	b	1300	15	0.02276	5.80E+07	1.86E+06				8.70E+12	4.81E+10		
15-ROB-038-ARM	2016_08_2	a	650	15	0.0267	2.18E+09	3.11E+07	2.83E+09	3.28E+07	1.16	1.57E+14	7.62E+11	1.79E+14	7.71E+11
15-ROB-038-ARM	2016_08_2	a	1300	15	0.0267	6.59E+08	1.04E+07				2.27E+13	1.12E+11		
15-ROB-038-ARM	2016_08_3	b	1150	15	0.03429	3.00E+09	4.19E+07	3.03E+09	4.19E+07	1.38	1.95E+14	9.36E+11	1.97E+14	9.36E+11
15-ROB-038-ARM	2016_08_3	b	1300	15	0.03429	3.81E+07	1.11E+06				1.70E+12	1.56E+10		
15-ROB-039-ARM	2016_08_1	a	1150	15	0.0263	2.80E+09	4.00E+07	2.87E+09	4.00E+07	1.39	5.90E+14	2.83E+12	6.07E+14	2.83E+12
15-ROB-039-ARM	2016_08_1	a	1300	15	0.0263	7.87E+07	1.92E+06				1.72E+13	8.92E+10		
15-ROB-039-ARM	2016_08_2	b	750	15	0.0222	2.59E+09	3.67E+07	2.99E+09	3.72E+07	1.25	5.19E+14	2.49E+12	6.24E+14	2.52E+12
15-ROB-039-ARM	2016_08_2	b	900	15	0.0222	1.13E+08	2.66E+06				3.72E+13	1.87E+11		
15-ROB-039-ARM	2016_08_2	b	1300	15	0.0222	2.93E+08	5.41E+06				6.80E+13	3.29E+11		
15-ROB-040-ARM	2016_08_2	a	650	15	0.0386	2.46E+09	3.44E+07	3.10E+09	3.57E+07	1.15	2.63E+14	1.29E+12	3.56E+14	1.37E+12
15-ROB-040-ARM	2016_08_2	a	1300	15	0.0386	6.48E+08	9.67E+06				9.29E+13	4.50E+11		
15-ROB-040-ARM	2016_08_3	b	1150	15	0.02628	3.01E+09	4.24E+07	3.07E+09	4.25E+07	1.39	3.36E+14	1.62E+12	3.43E+14	1.62E+12

Table C.1 continued.

Sample ID	Date analyzed	Aliquot	Heating temperature (°C)	Heating time (min)	Aliquot weight (g)	[He-3] (atoms/g)	δ[He-3] (atoms/g)	[He-3] (atoms/g)	δ[He-3] (atoms/g)	% error	[He-4] (atoms/g)	δ[He-4] (atoms/g)	[He-4] (atoms/g)	δ[He-4] (atoms/g)
15-ROB-040-ARM	2016_08_3	b	1300	15	0.02628	5.66E+07	1.64E+06				6.98E+12	4.05E+10		
15-ROB-041-ARM	2016_08_1	a	1150	15	0.0233	2.72E+09	3.83E+07	3.09E+09	3.89E+07	1.26	6.49E+14	3.11E+12	7.18E+14	3.13E+12
15-ROB-041-ARM	2016_08_1	a	1300	15	0.0233	3.76E+08	6.53E+06				7.00E+13	3.49E+11		
15-ROB-041-ARM	2016_08_2	b	650	15	0.0158	1.92E+09	2.85E+07	3.17E+09	3.26E+07	1.03	4.15E+14	2.05E+12	6.95E+14	2.27E+12
15-ROB-041-ARM	2016_08_2	b	900	15	0.0158	3.73E+08	6.90E+06				1.01E+14	4.85E+11		
15-ROB-041-ARM	2016_08_2	b	1300	15	0.0158	8.79E+08	1.41E+07				1.80E+14	8.67E+11		
15-ROB-042-EIN	2016_08_1	a	1150	15	0.0435	1.38E+09	1.98E+07	1.46E+09	1.99E+07	1.36	5.69E+14	2.75E+12	6.00E+14	2.75E+12
15-ROB-042-EIN	2016_08_1	a	1300	15	0.0435	8.59E+07	1.86E+06				3.13E+13	1.54E+11		
15-ROB-042-EIN	2016_08_2	b	650	15	0.0192	1.12E+09	1.69E+07	1.45E+09	1.79E+07	1.23	4.68E+14	2.28E+12	6.11E+14	2.33E+12
15-ROB-042-EIN	2016_08_2	b	900	15	0.0192	1.27E+08	3.33E+06				5.96E+13	2.88E+11		
15-ROB-042-EIN	2016_08_2	b	1300	15	0.0192	2.15E+08	4.54E+06				8.36E+13	4.05E+11		
15-ROB-042-EIN	2016_10_1	c	1150	15	0.01948	1.28E+09	1.51E+07	1.38E+09	1.53E+07	1.11	5.62E+14	2.75E+12	6.01E+14	2.76E+12
15-ROB-042-EIN	2016_10_1	c	1300	15	0.01948	1.06E+08	2.41E+06				3.83E+13	1.91E+11		
15-ROB-043-EIN	2016_08_1	a	1150	15	0.0404	1.39E+09	2.03E+07	1.39E+09	2.03E+07	1.47	4.53E+14	2.20E+12	4.52E+14	2.20E+12
15-ROB-043-EIN	2016_08_2	b	650	15	0.0196	1.06E+09	2.56E+07	1.39E+09	2.62E+07	1.89	3.62E+14	1.75E+12	4.65E+14	1.79E+12
15-ROB-043-EIN	2016_08_2	b	900	15	0.0196	1.98E+08	4.00E+06				5.90E+13	2.86E+11		
15-ROB-043-EIN	2016_08_2	b	1300	15	0.0196	1.39E+08	3.62E+06				4.50E+13	2.19E+11		
15-ROB-043-EIN	2016_08_3	c	1150	15	0.02263	1.29E+09	1.92E+07	1.33E+09	1.93E+07	1.45	4.72E+14	2.30E+12	4.86E+14	2.30E+12
15-ROB-043-EIN	2016_08_3	c	1300	15	0.02263	4.55E+07	1.55E+06				1.46E+13	7.41E+10		
15-ROB-044-EIN	2016_08_1	a	1150	15	0.024	9.20E+08	1.37E+07	9.19E+08	1.37E+07	1.49	2.16E+14	1.03E+12	2.16E+14	1.03E+12
15-ROB-044-EIN	2016_08_1	a	1300	15	0.024	3.22E+06	5.32E+05				6.31E+11	1.93E+10		
15-ROB-044-EIN	2016_08_2	b	650	15	0.0378	9.62E+08	1.41E+07	1.01E+09	1.41E+07	1.40	2.36E+14	1.13E+12	2.50E+14	1.14E+12
15-ROB-044-EIN	2016_08_2	b	1300	15	0.0378	4.84E+07	1.31E+06				1.41E+13	7.13E+10		
15-ROB-044-EIN	2016_08_4	c	1150	15	0.01755	1.02E+09	1.59E+07	1.02E+09	1.61E+07	1.57	2.27E+14	1.11E+12	2.27E+14	1.12E+12
15-ROB-044-EIN	2016_08_4	c	1300	15	0.01755	4.75E+06	1.08E+06				9.90E+11	3.74E+10		

Table C.1 continued.

Sample ID	Date analyzed	Aliquot	Heating temperature (°C)	Heating time (min)	Aliquot weight (g)	[He-3] (atoms/g)	δ[He-3] (atoms/g)	[He-3] (atoms/g)	δ[He-3] (atoms/g)	% error	[He-4] (atoms/g)	δ[He-4] (atoms/g)	[He-4] (atoms/g)	δ[He-4] (atoms/g)
15-ROB-045-EIN	2016_08_2	a	650	15	0.058	1.33E+09	1.88E+07	1.55E+09	1.91E+07	1.24	2.67E+14	1.30E+12	2.95E+14	1.30E+12
15-ROB-045-EIN	2016_08_2	a	1300	15	0.058	2.19E+08	3.57E+06				2.78E+13	1.35E+11		
15-ROB-045-EIN	2016_08_3	b	1150	15	0.01776	1.57E+09	2.34E+07	1.57E+09	2.35E+07	1.50	2.79E+14	1.35E+12	2.80E+14	1.35E+12
15-ROB-045-EIN	2016_08_3	b	1300	15	0.01776	6.50E+06	8.67E+05				7.82E+11	2.44E+10		
15-ROB-046-EIN	2016_08_2	a	650	15	0.0242	1.99E+09	2.85E+07	2.37E+09	2.92E+07	1.23	3.02E+14	1.47E+12	3.47E+14	1.49E+12
15-ROB-046-EIN	2016_08_2	a	1300	15	0.0242	3.89E+08	6.36E+06				4.52E+13	2.21E+11		
15-ROB-046-EIN	2016_08_3	b	1150	15	0.01795	2.26E+09	3.28E+07	2.27E+09	3.29E+07	1.45	3.64E+14	1.78E+12	3.66E+14	1.78E+12
15-ROB-046-EIN	2016_08_3	b	1300	15	0.01795	1.57E+07	1.09E+06				2.12E+12	2.93E+10		
15-ROB-047-EIN	2016_08_3	a	1150	15	0.0201	1.09E+09	1.66E+07	1.15E+09	1.68E+07	1.46	4.68E+14	2.24E+12	5.04E+14	2.25E+12
15-ROB-047-EIN	2016_08_3	a	1300	15	0.0201	6.79E+07	2.02E+06				3.69E+13	1.81E+11		
15-ROB-047-EIN	2016_08_4	b	1150	15	0.01952	1.28E+09	1.96E+07	1.31E+09	1.98E+07	1.51	5.53E+14	2.69E+12	5.68E+14	2.69E+12
15-ROB-047-EIN	2016_08_4	b	1300	15	0.01952	3.01E+07	1.52E+06				1.53E+13	7.89E+10		
15-ROB-048-EIN	2016_08_3	a	1150	15	0.01827	1.11E+09	1.69E+07	1.16E+09	1.71E+07	1.47	7.39E+14	3.61E+12	7.67E+14	3.61E+12
15-ROB-048-EIN	2016_08_3	a	1300	15	0.01827	5.76E+07	2.21E+06				2.83E+13	1.44E+11		
15-ROB-048-EIN	2016_08_4	b	1150	15	0.02339	1.15E+09	1.71E+07	1.17E+09	1.72E+07	1.46	6.35E+14	3.07E+12	6.57E+14	3.07E+12
15-ROB-048-EIN	2016_08_4	b	1300	15	0.02339	3.02E+07	1.45E+06				2.26E+13	1.12E+11		
15-ROB-049-KLE	2017_05_3	a	1275	15	0.01849	1.17E+09	2.09E+07	1.19E+09	2.09E+07	1.76	2.49E+14	3.75E+12	2.53E+14	3.75E+12
15-ROB-049-KLE	2017_05_3	a	1350	15	0.01849	1.90E+07	1.76E+06				3.87E+12	1.11E+11		
15-ROB-050-KLE	2016_08_4	a	1150	15	0.02146	1.12E+09	1.71E+07	1.17E+09	1.73E+07	1.47	9.78E+14	4.70E+12	1.01E+15	4.71E+12
15-ROB-050-KLE	2016_08_4	a	1300	15	0.02146	6.03E+07	2.03E+06				3.65E+13	1.78E+11		
15-ROB-050-KLE	2016_08_4	b	1150	15	0.02086	1.15E+09	1.77E+07	1.20E+09	1.79E+07	1.48	9.19E+14	4.46E+12	9.52E+14	4.46E+12
15-ROB-050-KLE	2016_08_4	b	1300	15	0.02086	5.41E+07	1.95E+06				3.35E+13	1.63E+11		
15-ROB-050-KLE	2016_10_1	c	1150	15	0.01869	1.03E+09	1.20E+07	1.15E+09	1.24E+07	1.07	4.40E+14	2.15E+12	4.95E+14	2.17E+12
15-ROB-050-KLE	2016_10_1	c	1300	15	0.01869	1.21E+08	3.05E+06				5.43E+13	2.68E+11		
15-ROB-051-KLE	2016_08_4	a	1150	15	0.01997	1.48E+09	2.21E+07	1.53E+09	2.23E+07	1.46	7.66E+14	3.76E+12	7.85E+14	3.76E+12

Table C.1 continued.

Sample ID	Date analyzed	Aliquot	Heating temperature (°C)	Heating time (min)	Aliquot weight (g)	[He-3] (atoms/g)	δ[He-3] (atoms/g)	[He-3] (atoms/g)	δ[He-3] (atoms/g)	% error	[He-4] (atoms/g)	δ[He-4] (atoms/g)	[He-4] (atoms/g)	δ[He-4] (atoms/g)
15-ROB-051-KLE	2016_08_4	a	1300	15	0.01997	4.95E+07	2.39E+06				2.02E+13	1.02E+11		
15-ROB-052-KLE	2016_08_4	a	1150	15	0.02037	1.43E+09	2.10E+07	1.43E+09	2.11E+07	1.47	3.53E+14	1.71E+12	3.54E+14	1.71E+12
15-ROB-052-KLE	2016_08_4	a	1300	15	0.02037	1.03E+07	1.09E+06				1.92E+12	2.89E+10		
15-ROB-053-KLE	2016_08_4	a	1150	15	0.01771	1.06E+09	1.68E+07	1.11E+09	1.70E+07	1.53	6.20E+14	2.99E+12	6.41E+14	2.99E+12
15-ROB-053-KLE	2016_08_4	a	1300	15	0.01771	5.46E+07	1.81E+06				2.11E+13	1.07E+11		
15-ROB-053-KLE	2016_08_4	b	1150	15	0.01958	1.03E+09	1.60E+07	1.08E+09	1.62E+07	1.51	7.13E+14	3.44E+12	7.41E+14	3.45E+12
15-ROB-053-KLE	2016_08_4	b	1300	15	0.01958	5.42E+07	2.06E+06				2.88E+13	1.42E+11		
15-ROB-054-KLE	2016_10_2	a	1150	15	0.02272	1.44E+09	1.41E+07	1.45E+09	1.42E+07	0.98	2.05E+14	4.45E+12	2.07E+14	4.45E+12
15-ROB-054-KLE	2016_10_2	a	1300	15	0.02272	1.51E+07	1.46E+06				1.64E+12	4.02E+10		
15-ROB-054-KLE	2016_10_2	b	1150	15	0.01772	1.44E+09	1.50E+07	1.46E+09	1.50E+07	1.03	2.04E+14	4.42E+12	2.05E+14	4.42E+12
15-ROB-054-KLE	2016_10_2	b	1300	15	0.01772	1.48E+07	1.43E+06				1.60E+12	4.54E+10		
15-ROB-055-NAC	2016_08_4	a	1150	15	0.01832	1.13E+09	1.70E+07	1.15E+09	1.71E+07	1.48	4.78E+14	2.34E+12	4.97E+14	2.34E+12
15-ROB-055-NAC	2016_08_4	a	1300	15	0.01832	2.96E+07	1.57E+06				1.97E+13	1.02E+11		
15-ROB-055-NAC	2016_08_4	b	1150	15	0.01729	1.14E+09	1.79E+07	1.16E+09	1.81E+07	1.56	5.74E+14	2.77E+12	5.84E+14	2.77E+12
15-ROB-055-NAC	2016_08_4	b	1300	15	0.01729	2.57E+07	1.47E+06				1.06E+13	7.47E+10		
15-ROB-056-NAC	2016_08_4	a	1150	15	0.02432	1.14E+09	1.72E+07	1.17E+09	1.73E+07	1.48	8.52E+14	4.11E+12	8.68E+14	4.11E+12
15-ROB-056-NAC	2016_08_4	a	1300	15	0.02432	2.83E+07	1.32E+06				1.63E+13	8.31E+10		
15-ROB-056-NAC	2016_08_4	b	1150	15	0.02118	1.09E+09	1.65E+07	1.11E+09	1.66E+07	1.50	8.05E+14	3.86E+12	8.21E+14	3.86E+12
15-ROB-056-NAC	2016_08_4	b	1300	15	0.02118	2.48E+07	1.35E+06				1.63E+13	8.36E+10		
15-ROB-057-NAC	2017_05_2	a	1275	15	0.0189	1.32E+09	2.72E+07	1.34E+09	2.72E+07	2.03	3.28E+14	5.38E+12	3.35E+14	5.38E+12
15-ROB-057-NAC	2017_05_2	a	1300	15	0.0189	2.21E+07	2.20E+06				7.04E+12	1.56E+11		
15-ROB-057-NAC	2017_05_5	b	1275	15	0.0249	1.41E+09	2.44E+07	1.42E+09	2.44E+07	1.73	3.23E+14	4.19E+12	3.24E+14	4.19E+12
15-ROB-057-NAC	2017_05_5	b	1350	15	0.0249	3.55E+06	1.10E+06				3.55E+11	4.90E+10		
15-ROB-058-NAC	2017_05_2	a	1275	15	0.02304	1.34E+09	2.56E+07	1.36E+09	2.57E+07	1.89	2.57E+14	4.21E+12	2.62E+14	4.21E+12
15-ROB-058-NAC	2017_05_2	a	1300	15	0.02304	2.25E+07	1.66E+06				4.94E+12	1.08E+11		

Table C.1 continued.

Sample ID	Date analyzed	Aliquot	Heating temperature (°C)	Heating time (min)	Aliquot weight (g)	[He-3] (atoms/g)	δ[He-3] (atoms/g)	[He-3] (atoms/g)	δ[He-3] (atoms/g)	% error	[He-4] (atoms/g)	δ[He-4] (atoms/g)	[He-4] (atoms/g)	δ[He-4] (atoms/g)
15-ROB-059-NAC	2017_05_2	a	1275	15	0.01986	1.09E+09	2.11E+07	1.15E+09	2.14E+07	1.85	6.45E+14	1.06E+13	6.77E+14	1.06E+13
15-ROB-059-NAC	2017_05_2	a	1350	15	0.01986	5.38E+07	2.67E+06				2.60E+13	4.64E+11		
15-ROB-059-NAC	2017_05_2	a	1375	15	0.01986	1.38E+07	1.59E+06				5.48E+12	1.22E+11		
15-ROB-059-NAC	2017_05_5	b	1275	15	0.02136	1.21E+09	2.20E+07	1.21E+09	2.20E+07	1.82	6.54E+14	8.54E+12	6.57E+14	8.54E+12
15-ROB-059-NAC	2017_05_5	b	1350	15	0.02136	4.93E+06	1.20E+06				2.30E+12	7.19E+10		
15-ROB-060-NAC	2017_05_3	a	1275	15	0.02426	1.64E+09	2.83E+07	1.68E+09	2.83E+07	1.68	5.39E+14	8.09E+12	5.52E+14	8.09E+12
15-ROB-060-NAC	2017_05_3	a	1350	15	0.02426	4.51E+07	2.23E+06				1.28E+13	2.74E+11		
15-ROB-061-NAC	2017_05_3	a	1275	15	0.02287	1.15E+09	2.00E+07	1.19E+09	2.02E+07	1.70	4.58E+14	6.90E+12	4.68E+14	6.91E+12
15-ROB-061-NAC	2017_05_3	a	1350	15	0.02287	3.20E+07	2.08E+06				1.05E+13	2.23E+11		
15-ROB-062-MUS	2017_05_3	a	1275	15	0.01851	1.22E+09	2.26E+07	1.22E+09	2.26E+07	1.85	6.43E+14	9.75E+12	6.44E+14	9.75E+12
15-ROB-062-MUS	2017_05_3	a	1350	15	0.01851	2.33E+06	1.21E+06				9.88E+11	7.60E+10		
15-ROB-063-MUS	2017_05_3	a	1275	15	0.01749	1.12E+09	2.06E+07	1.16E+09	2.07E+07	1.79	6.08E+14	9.13E+12	6.24E+14	9.13E+12
15-ROB-063-MUS	2017_05_3	a	1350	15	0.01749	3.39E+07	2.26E+06				1.56E+13	3.40E+11		
15-ROB-064-MUS	2017_05_3	a	1275	15	0.02156	5.92E+08	1.18E+07	6.69E+08	1.22E+07	1.83	5.30E+14	7.99E+12	5.95E+14	8.06E+12
15-ROB-064-MUS	2017_05_3	a	1350	15	0.02156	6.12E+07	2.77E+06				5.19E+13	1.07E+12		
15-ROB-064-MUS	2017_05_3	a	1375	15	0.02156	1.63E+07	1.46E+06				1.30E+13	2.77E+11		
15-ROB-SHIELD1	2017_05_4	a	1275	15	0.04282	2.40E+07	1.45E+06	2.57E+07	1.52E+06	5.90	3.70E+14	5.22E+12	3.86E+14	5.23E+12
15-ROB-SHIELD1	2017_05_4	a	1350	15	0.04282	1.74E+06	4.42E+05				1.64E+13	3.73E+11		
16-ROB-015-AND	2018_04_17	a	1225	15	0.01923	1.29E+09	3.18E+07	1.31E+09	3.18E+07	2.43	2.89E+14	2.67E+12	2.90E+14	2.67E+12
16-ROB-015-AND	2018_04_17	a	1325	15	0.01923	1.32E+07	1.65E+06				9.17E+11	6.34E+10		
16-ROB-015-AND	2018_04_19	b	1225	15	0.02337	1.33E+09	3.17E+07	1.36E+09	3.18E+07	2.33	2.80E+14	2.63E+12	2.8344E+14	2.63355E+12
16-ROB-015-AND	2018_04_19	b	1325	15	0.02337	2.75E+07	1.73E+06				3.30E+12	8.08E+10		
16-ROB-016-AND	2018_04_17	a	1225	15	0.02749	1.06E+09	2.51E+07	1.06E+09	2.51E+07	2.36	2.52E+14	2.33E+12	2.54E+14	2.33E+12
16-ROB-016-AND	2018_04_17	a	1325	15	0.02749	6.89E+06	1.12E+06				1.73E+12	4.73E+10		
16-ROB-016-AND	2018_04_19	b	1225	15	0.02125	1.06E+09	2.56E+07	1.07E+09	2.56E+07	2.40	2.50E+14	2.32E+12	2.52415E+14	2.31926E+12

Table C.1 continued.

Sample ID	Date analyzed	Aliquot	Heating temperature (°C)	Heating time (min)	Aliquot weight (g)	[He-3] (atoms/g)	δ[He-3] (atoms/g)	[He-3] (atoms/g)	δ[He-3] (atoms/g)	% error	[He-4] (atoms/g)	δ[He-4] (atoms/g)	[He-4] (atoms/g)	δ[He-4] (atoms/g)
16-ROB-016-AND	2018_04_19	b	1325	15	0.02125	1.29E+07	1.50E+06				2.32E+12	5.69E+10		
16-ROB-023-PSO	2018_04_17	a	1225	15	0.02133	1.17E+09	2.83E+07	1.19E+09	2.84E+07	2.39	3.95E+14	4.02E+12	4.00E+14	4.02E+12
16-ROB-023-PSO	2018_04_17	a	1325	15	0.02133	1.78E+07	1.46E+06				5.12E+12	6.89E+10		
16-ROB-023-PSO	2018_04_19	b	1225	15	0.02386	1.15E+09	2.73E+07	1.17E+09	2.74E+07	2.33	4.02E+14	3.70E+12	4.11065E+14	3.69959E+12
16-ROB-023-PSO	2018_04_19	b	1325	15	0.02386	2.73E+07	1.74E+06				9.43E+12	9.98E+10		
16-ROB-024-PSO	2018_04_17	a	1225	15	0.02479	9.75E+08	2.33E+07	9.87E+08	2.34E+07	2.37	4.53E+13	4.30E+11	4.56E+13	4.33E+11
16-ROB-024-PSO	2018_04_17	a	1325	15	0.02479	1.23E+07	1.42E+06				2.73E+11	4.61E+10		
16-ROB-028-PSI	2018_04_17	a	1225	15	0.02276	1.48E+09	3.44E+07	1.52E+09	3.44E+07	2.26	5.18E+13	4.97E+11	5.23E+13	4.99E+11
16-ROB-028-PSI	2018_04_17	a	1325	15	0.02276	3.83E+07	2.33E+06				5.35E+11	4.41E+10		
16-ROB-028-PSI	2018_04_19	b	1225	15	0.02098	1.43E+09	3.42E+07	1.48E+09	3.43E+07	2.31	5.20E+13	4.89E+11	5.33005E+13	4.91383E+11
16-ROB-028-PSI	2018_04_19	b	1325	15	0.02098	5.00E+07	2.59E+06				1.31E+12	4.37E+10		
16-ROB-029-PSI	2018_04_17	a	1225	15	0.02377	1.70E+09	3.93E+07	1.73E+09	3.93E+07	2.27	1.17E+14	1.08E+12	1.18E+14	1.08E+12
16-ROB-029-PSI	2018_04_17	a	1325	15	0.02377	3.29E+07	1.77E+06				1.50E+12	5.20E+10		
16-ROB-030-PSI	2018_04_17	a	1225	15	0.02349	1.29E+09	3.07E+07	1.32E+09	3.07E+07	2.32	3.80E+13	3.62E+11	3.86E+13	3.66E+11
16-ROB-030-PSI	2018_04_17	a	1325	15	0.02349	3.22E+07	2.10E+06				6.18E+11	5.46E+10		
16-ROB-031-WIN	2018_03_29	a	1225	15	2.09E-02	2.05E+09	3.48E+07	2.05E+09	3.48E+07	1.70E+00	7.54E+14	1.96E+13	7.56E+14	1.95507E+13
16-ROB-031-WIN	2018_03_29	a	1325	15	2.09E-02	4.82E+06	1.65E+06				1.29E+12	7.02E+10		
16-ROB-031-WIN	2018_03_29	b	1225	15	1.89E-02	2.18E+09	3.75E+07	2.19E+09	3.76E+07	1.72E+00	7.95E+14	2.06E+13	7.97E+14	2.05564E+13
16-ROB-031-WIN	2018_03_29	b	1325	15	1.89E-02	5.76E+06	1.80E+06				1.20E+12	6.15E+10		
16-ROB-032-WIN	2018_04_17	a	1225	15	0.02159	2.40E+09	5.56E+07	2.43E+09	5.57E+07	2.30	1.74E+14	1.80E+12	1.75E+14	1.80E+12
16-ROB-032-WIN	2018_04_17	a	1325	15	0.02159	2.28E+07	1.72E+06				7.94E+11	3.91E+10		
16-ROB-032-WIN	2018_04_19	b	1225	15	0.01979	2.35E+09	5.50E+07	2.39E+09	5.50E+07	2.31	1.72E+14	1.59E+12	1.73856E+14	1.59257E+12
16-ROB-032-WIN	2018_04_19	b	1325	15	0.01979	3.07E+07	2.02E+06				1.38E+12	6.84E+10		
16-ROB-033-WIN	2018_04_19	a	1225	15	0.02109	1.50E+09	3.59E+07	1.51E+09	3.59E+07	2.37	5.45E+14	5.04E+12	5.46E+14	5.04E+12
16-ROB-033-WIN	2018_04_19	a	1325	15	0.02109	1.02E+07	1.38E+06				1.92E+12	5.60E+10		

Table C.1 continued.

Sample ID	Date analyzed	Aliquot	Heating temperature (°C)	Heating time (min)	Aliquot weight (g)	[He-3] (atoms/g)	δ[He-3] (atoms/g)	[He-3] (atoms/g)	δ[He-3] (atoms/g)	% error	[He-4] (atoms/g)	δ[He-4] (atoms/g)	[He-4] (atoms/g)	δ[He-4] (atoms/g)
16-ROB-034-WIN	2018_03_29	a	1225	15	2.73E-02	2.99E+09	4.93E+07	3.08E+09	4.94E+07	1.60E+00	1.20E+14	3.32E+12	1.23E+14	3.31712E+12
16-ROB-034-WIN	2018_03_29	a	1325	15	2.73E-02	8.69E+07	2.70E+06				3.15E+12	8.76E+10		
16-ROB-034-WIN	2018_03_29	b	1225	15	2.06E-02	3.02E+09	5.03E+07	3.10E+09	5.04E+07	1.63E+00	1.27E+14	3.29E+12	1.30E+14	3.29587E+12
16-ROB-034-WIN	2018_03_29	b	1325	15	2.06E-02	7.62E+07	2.81E+06				2.52E+12	8.91E+10		
16-ROB-036-WIN	2018_03_29	a	1225	15	2.27E-02	2.33E+09	3.88E+07	2.39E+09	3.89E+07	1.63E+00	5.07E+13	1.32E+12	5.14E+13	1.31915E+12
16-ROB-036-WIN	2018_03_29	a	1325	15	2.27E-02	5.62E+07	2.39E+06				7.08E+11	5.55E+10		
16-ROB-036-WIN	2018_03_29	b	1225	15	2.25E-02	2.35E+09	3.91E+07	2.40E+09	3.92E+07	1.63E+00	5.86E+13	1.62E+12	5.98E+13	1.62159E+12
16-ROB-036-WIN	2018_03_29	b	1325	15	2.25E-02	4.89E+07	2.22E+06				1.14E+12	5.00E+10		
16-ROB-037-WIN	2018_04_19	a	1225	15	0.02509	1.92E+09	4.48E+07	1.99E+09	4.49E+07	2.25	6.05E+13	5.61E+11	6.18E+13	5.63E+11
16-ROB-037-WIN	2018_04_19	a	1325	15	0.02509	6.87E+07	2.79E+06				1.26E+12	5.09E+10		
16-ROB-037-WIN	2018_04_19	b	1225	15	0.01837	2.00E+09	4.69E+07	2.02E+09	4.70E+07	2.33	5.82E+13	5.47E+11	5.85259E+13	5.50188E+11
16-ROB-037-WIN	2018_04_19	b	1325	15	0.01837	2.21E+07	2.18E+06				3.00E+11	6.27E+10		
16-ROB-038-SSU	2018_03_29	a	1225	15	2.23E-02	1.67E+09	2.85E+07	1.74E+09	2.86E+07	1.65E+00	4.80E+14	1.24E+13	5.01E+14	1.24256E+13
16-ROB-038-SSU	2018_03_29	a	1325	15	2.23E-02	7.15E+07	2.97E+06				2.10E+13	5.51E+11		
16-ROB-038-SSU	2018_03_29	b	1225	15	1.78E-02	1.77E+09	3.09E+07	1.79E+09	3.10E+07	1.73E+00	5.52E+14	1.46E+13	5.59E+14	1.45798E+13
16-ROB-038-SSU	2018_03_29	b	1325	15	1.78E-02	2.29E+07	2.48E+06				7.04E+12	2.06E+11		
16-ROB-039-SSU	2018_03_29	a	1225	15	2.12E-02	1.67E+09	2.83E+07	1.69E+09	2.84E+07	1.68E+00	3.55E+14	9.18E+12	3.60E+14	9.18104E+12
16-ROB-039-SSU	2018_03_29	a	1325	15	2.12E-02	2.29E+07	2.18E+06				5.31E+12	1.46E+11		
16-ROB-039-SSU	2018_03_29	b	1225	15	1.93E-02	1.75E+09	3.02E+07	1.77E+09	3.02E+07	1.70E+00	3.73E+14	9.66E+12	3.77E+14	9.66438E+12
16-ROB-039-SSU	2018_03_29	b	1325	15	1.93E-02	2.40E+07	2.04E+06				4.47E+12	1.57E+11		
16-ROB-040-SSU	2018_03_29	a	1225	15	2.20E-02	2.09E+09	3.51E+07	2.10E+09	3.51E+07	1.67E+00	7.97E+13	2.08E+12	8.01E+13	2.07726E+12
16-ROB-040-SSU	2018_03_29	a	1325	15	2.20E-02	1.09E+07	1.72E+06				4.85E+11	4.17E+10		
16-ROB-040-SSU	2018_03_29	b	1225	15	1.79E-02	2.09E+09	3.54E+07	2.12E+09	3.55E+07	1.67E+00	7.20E+13	1.90E+12	7.28E+13	1.9013E+12
16-ROB-040-SSU	2018_03_29	b	1325	15	1.79E-02	2.99E+07	2.50E+06				8.02E+11	5.22E+10		
16-ROB-041-SSU	2018_03_29	a	1225	15	2.03E-02	2.10E+09	3.52E+07	2.12E+09	3.52E+07	1.66E+00	6.37E+13	1.65E+12	6.41E+13	1.64916E+12

Table C.1 continued.

Sample ID	Date analyzed	Aliquot	Heating temperature (°C)	Heating time (min)	Aliquot weight (g)	[He-3] (atoms/g)	δ[He-3] (atoms/g)	[He-3] (atoms/g)	δ[He-3] (atoms/g)	% error	[He-4] (atoms/g)	δ[He-4] (atoms/g)	[He-4] (atoms/g)	δ[He-4] (atoms/g)
16-ROB-041-SSU	2018_03_29	a	1325	15	2.03E-02	2.80E+07	2.36E+06				3.77E+11	5.71E+10		
16-ROB-041-SSU	2018_03_29	b	1225	15	1.83E-02	2.08E+09	3.51E+07	2.11E+09	3.52E+07	1.67E+00	5.81E+13	2.42E+12	5.85E+13	2.41943E+12
16-ROB-041-SSU	2018_03_29	b	1325	15	1.83E-02	3.03E+07	2.67E+06				3.56E+11	5.21E+10		
16-ROB-042-SSU	2018_03_29	a	1225	15	1.85E-02	2.16E+09	3.65E+07	2.17E+09	3.66E+07	1.68E+00	3.82E+14	9.88E+12	3.85E+14	9.88451E+12
16-ROB-042-SSU	2018_03_29	a	1325	15	1.85E-02	1.41E+07	1.78E+06				2.83E+12	1.05E+11		
16-ROB-042-SSU	2018_03_29	b	1225	15	1.84E-02	2.21E+09	3.76E+07	2.23E+09	3.77E+07	1.69E+00	3.76E+14	1.13E+13	3.78E+14	1.12618E+13
16-ROB-042-SSU	2018_03_29	b	1325	15	1.84E-02	1.35E+07	2.22E+06				1.93E+12	8.33E+10		
16-ROB-043-SSU	2018_03_29	a	1225	15	2.19E-02	2.44E+09	4.03E+07	2.53E+09	4.04E+07	1.59E+00	5.70E+13	1.49E+12	5.79E+13	1.49461E+12
16-ROB-043-SSU	2018_03_29	a	1325	15	2.19E-02	9.21E+07	2.88E+06				8.64E+11	5.90E+10		
16-ROB-043-SSU	2018_03_29	b	1225	15	1.80E-02	2.35E+09	4.01E+07	2.46E+09	4.03E+07	1.64E+00	4.13E+13	1.09E+12	4.29E+13	1.09494E+12
16-ROB-043-SSU	2018_03_29	b	1325	15	1.80E-02	1.05E+08	3.78E+06				1.52E+12	6.90E+10		
16-ROB-044-SSU	2018_03_29	a	1225	15	2.20E-02	1.63E+09	2.80E+07	1.64E+09	2.81E+07	1.71E+00	3.28E+13	8.53E+11	3.30E+13	8.53851E+11
16-ROB-044-SSU	2018_03_29	a	1325	15	2.20E-02	1.27E+07	1.99E+06				1.37E+11	3.99E+10		
16-ROB-044-SSU	2018_03_29	b	1225	15	2.31E-02	1.57E+09	2.69E+07	1.58E+09	2.70E+07	1.71E+00	3.26E+13	8.48E+11	3.27E+13	8.53159E+11
16-ROB-044-SSU	2018_03_29	b	1325	15	2.31E-02	9.92E+06	1.88E+06				1.10E+11	9.12E+10		
16-ROB-045-HDY	2017_09_2	b	1225	15	0.02066	2.41E+09	6.34E+07	2.42E+09	6.34E+07	2.62	3.58E+14	2.92E+12	3.59E+14	2.92E+12
16-ROB-045-HDY	2017_09_2	b	1325	15	0.02066	1.07E+07	1.61E+06				9.83E+11	5.70E+10		
16-ROB-046-HDY	2017_09_1	b	1225	15	0.02501	2.38E+09	6.96E+07	2.39E+09	6.96E+07	2.91	2.45E+14	3.16E+12	2.46E+14	3.16E+12
16-ROB-046-HDY	2017_09_1	b	1325	15	0.02501	1.05E+07	1.19E+06				4.95E+11	6.67E+10		
16-ROB-046-HDY	2017_09_2	c	1225	15	0.02045	2.42E+09	6.38E+07	2.43E+09	6.39E+07	2.63	2.37E+14	1.88E+12	2.38E+14	1.88E+12
16-ROB-046-HDY	2017_09_3	c	1225	15	0.02375	2.52E+09	7.36E+07	2.53E+09	7.36E+07	2.91	2.71E+14	2.23E+12	2.71E+14	2.24E+12
16-ROB-046-HDY	2017_09_2	c	1325	15	0.02045	8.39E+06	1.45E+06				7.14E+11	5.90E+10		
16-ROB-046-HDY	2017_09_3	c	1325	15	0.02375	8.26E+06	1.19E+06				3.98E+11	1.89E+11		
16-ROB-047-HDY	2017_09_1	b	1225	15	0.05299	1.76E+09	5.12E+07	1.79E+09	5.13E+07	2.87	6.16E+13	7.93E+11	6.24E+13	7.94E+11
16-ROB-047-HDY	2017_09_1	b	1325	15	0.05299	2.28E+07	1.16E+06				7.61E+11	3.78E+10		

Table C.1 continued.

Sample ID	Date analyzed	Aliquot	Heating temperature (°C)	Heating time (min)	Aliquot weight (g)	[He-3] (atoms/g)	δ[He-3] (atoms/g)	[He-3] (atoms/g)	δ[He-3] (atoms/g)	% error	[He-4] (atoms/g)	δ[He-4] (atoms/g)	[He-4] (atoms/g)	δ[He-4] (atoms/g)
16-ROB-048-HDY	2017_09_1	b	1225	15	0.02891	2.38E+09	6.95E+07	2.39E+09	6.95E+07	2.91	2.75E+14	3.54E+12	2.76E+14	3.54E+12
16-ROB-048-HDY	2017_09_1	b	1325	15	0.02891	8.71E+06	1.11E+06				1.35E+12	6.25E+10		
16-ROB-048-HDY	2017_09_2	c	1225	15	0.02022	2.34E+09	6.14E+07	2.35E+09	6.14E+07	2.61	2.68E+14	2.12E+12	2.69E+14	2.12E+12
16-ROB-048-HDY	2017_09_2	c	1325	15	0.02022	9.33E+06	1.45E+06				5.53E+11	6.15E+10		
16-ROB-049-HDY	2017_09_1	b	1225	15	0.02445	2.55E+09	7.45E+07	2.56E+09	7.45E+07	2.91	2.56E+14	3.31E+12	2.57E+14	3.31E+12
16-ROB-049-HDY	2017_09_1	b	1325	15	0.02445	3.74E+06	9.49E+05				2.07E+11	6.71E+10		
16-ROB-050-HDY	2017_09_2	b	1225	15	0.02593	3.01E+09	8.53E+07	3.02E+09	8.53E+07	2.83	4.65E+14	4.22E+12	4.66E+14	4.22E+12
16-ROB-050-HDY	2017_09_2	b	1325	15	0.02593	6.48E+06	1.07E+06				9.25E+11	6.59E+10		
16-ROB-051-HDY	2017_09_2	b	1225	15	0.02034	2.42E+09	6.94E+07	2.43E+09	6.94E+07	2.85	4.70E+14	4.28E+12	4.73E+14	4.28E+12
16-ROB-051-HDY	2017_09_2	b	1325	15	0.02034	1.82E+07	1.79E+06				3.47E+12	7.23E+10		
16-ROB-052-BAS	2017_09_2	b	1225	15	0.03916	2.56E+09	6.63E+07	2.59E+09	6.64E+07	2.56	9.03E+13	7.14E+11	9.15E+13	7.16E+11
16-ROB-052-BAS	2017_09_2	b	1325	15	0.03916	3.37E+07	1.51E+06				1.20E+12	4.49E+10		
16-ROB-053-BAS	2017_09_1	b	1225	15	0.0211	2.58E+09	8.00E+07	2.65E+09	8.00E+07	3.02	4.37E+14	5.98E+12	4.51E+14	5.99E+12
16-ROB-053-BAS	2017_09_1	b	1325	15	0.0211	6.77E+07	3.47E+06				1.40E+13	3.76E+11		
16-ROB-053-BAS	2017_09_1	c	1225	15	0.0251	2.57E+09	8.02E+07	2.64E+09	8.03E+07	3.05	4.12E+14	5.64E+12	4.24E+14	5.65E+12
16-ROB-053-BAS	2017_09_1	c	1325	15	0.0251	6.57E+07	3.13E+06				1.19E+13	3.21E+11		
16-ROB-054-BAS	2017_09_2	b	1225	15	0.02201	2.53E+09	7.20E+07	2.53E+09	7.20E+07	2.84	8.78E+14	7.97E+12	8.80E+14	7.97E+12
16-ROB-054-BAS	2017_09_2	b	1325	15	0.02201	5.77E+06	1.17E+06				2.56E+12	7.37E+10		
16-ROB-055-BAS	2017_09_1	b	1225	15	0.04472	2.70E+09	7.81E+07	2.76E+09	7.81E+07	2.82	6.39E+13	8.23E+11	6.56E+13	8.25E+11
16-ROB-055-BAS	2017_09_1	b	1325	15	0.04472	6.90E+07	2.57E+06				1.77E+12	6.74E+10		
16-ROB-056-BAS	2017_09_2	b	1225	15	0.0361	2.36E+09	6.15E+07	2.40E+09	6.15E+07	2.56	7.42E+13	5.93E+11	7.53E+13	5.94E+11
16-ROB-056-BAS	2017_09_2	b	1325	15	0.0361	3.47E+07	1.60E+06				1.05E+12	4.10E+10		
16-ROB-057-BAS	2017_09_1	a	1225	15	0.02454	2.41E+09	7.03E+07	2.49E+09	7.04E+07	2.82	2.77E+14	3.57E+12	2.89E+14	3.58E+12
16-ROB-057-BAS	2017_09_1	a	1325	15	0.02454	7.85E+07	3.15E+06				1.16E+13	3.12E+11		
16-ROB-057-BAS	2017_09_3	b	1225	15	0.02421	2.54E+09	7.89E+07	2.59E+09	7.89E+07	3.04	3.55E+14	3.12E+12	3.65E+14	3.13E+12

Table C.1 continued.

Sample ID	Date analyzed	Aliquot	Heating temperature (°C)	Heating time (min)	Aliquot weight (g)	[He-3] (atoms/g)	δ[He-3] (atoms/g)	[He-3] (atoms/g)	δ[He-3] (atoms/g)	% error	[He-4] (atoms/g)	δ[He-4] (atoms/g)	[He-4] (atoms/g)	δ[He-4] (atoms/g)
16-ROB-057-BAS	2017_09_3	b	1325	15	0.02421	5.82E+07	2.63E+06				9.83E+12	1.64E+11		
16-ROB-058-BAS	2017_05_5	a	1275	15	0.02605	2.46E+09	5.69E+07	2.50E+09	5.69E+07	2.28	8.32E+13	1.78E+12	8.42E+13	1.78E+12
16-ROB-058-BAS	2017_05_5	a	1350	15	0.02605	3.71E+07	2.05E+06				9.61E+11	5.25E+10		
16-ROB-058-BAS	2017_05_6	b	1275	15	0.03973	2.46E+09	3.73E+07	2.48E+09	3.74E+07	1.51	9.25E+13	1.11E+12	9.30E+13	1.11E+12
16-ROB-058-BAS	2017_05_6	b	1350	15	0.03973	2.03E+07	1.16E+06				5.20E+11	4.02E+10		
16-ROB-059-RIN	2017_05_5	a	1275	15	0.01769	2.73E+09	4.63E+07	2.73E+09	4.63E+07	1.69	3.48E+14	4.63E+12	3.48E+14	4.63E+12
16-ROB-059-RIN	2017_05_5	a	1350	15	0.01769	8.43E+06	1.43E+06				3.20E+11	5.51E+10		
16-ROB-061-RIN	2017_05_5	a	1275	15	0.02169	2.54E+09	5.83E+07	2.56E+09	5.83E+07	2.27	4.88E+13	1.04E+12	4.90E+13	1.04E+12
16-ROB-061-RIN	2017_05_5	a	1350	15	0.02169	2.25E+07	2.01E+06				2.37E+11	7.28E+10		
16-ROB-061-RIN	2017_05_6	b	1275	15	0.04304	2.47E+09	5.66E+07	2.51E+09	5.66E+07	2.26	5.13E+13	1.10E+12	5.19E+13	1.10E+12
16-ROB-061-RIN	2017_05_6	b	1350	15	0.04304	4.32E+07	1.80E+06				5.71E+11	3.04E+10		
16-ROB-063-RIN	2017_05_5	a	1275	15	0.01894	3.64E+09	6.06E+07	3.65E+09	6.06E+07	1.66	3.61E+14	5.00E+12	3.61E+14	5.00E+12
16-ROB-063-RIN	2017_05_5	a	1350	15	0.01894	7.83E+06	1.24E+06				4.09E+11	8.69E+10		
16-ROB-063-RIN	2017_09_4	b	1225	15	0.02426	3.55E+09	1.28E+08	3.57E+09	1.28E+08	3.59	4.08E+14	2.63E+12	4.09E+14	2.63E+12
16-ROB-063-RIN	2017_09_4	b	1325	15	0.02426	1.05E+07	1.37E+06				1.41E+12	5.61E+10		
16-ROB-064-RIN	2017_05_5	a	1275	15	0.02211	3.01E+09	6.91E+07	3.03E+09	6.91E+07	2.28	5.35E+13	1.15E+12	5.37E+13	1.15E+12
16-ROB-064-RIN	2017_05_5	a	1350	15	0.02211	2.00E+07	1.55E+06				1.58E+11	5.76E+10		
16-ROB-065-RIN	2017_09_1	a	1225	15	0.02609	2.05E+09	6.42E+07	2.06E+09	6.42E+07	3.12	3.78E+14	5.15E+12	3.79E+14	5.15E+12
16-ROB-065-RIN	2017_09_1	a	1325	15	0.02609	9.59E+06	1.16E+06				9.07E+11	6.79E+10		
16-ROB-065-RIN	2017_09_4	b	1225	15	0.02068	1.85E+09	6.88E+07	1.85E+09	6.88E+07	3.71	3.60E+14	3.32E+12	3.60E+14	3.32E+12
16-ROB-065-RIN	2017_09_4	b	1325	15	0.02068	5.27E+06	1.23E+06				3.02E+11	6.67E+10		
16-ROB-066-MNM	2017_09_3	a	1225	15	0.02515	1.45E+09	4.54E+07	1.46E+09	4.54E+07	3.12	5.95E+14	5.23E+12	5.99E+14	5.23E+12
16-ROB-066-MNM	2017_09_3	a	1325	15	0.02515	9.76E+06	1.19E+06				4.09E+12	9.03E+10		
16-ROB-067-MNM	2017_09_3	a	1225	15	0.02229	6.75E+08	2.10E+07	6.78E+08	2.10E+07	3.09	2.85E+14	2.37E+12	2.86E+14	2.37E+12
16-ROB-067-MNM	2017_09_3	a	1325	15	0.02229	3.26E+06	9.41E+05				1.23E+12	6.78E+10		

Table C.1 continued.

Sample ID	Date analyzed	Aliquot	Heating temperature (°C)	Heating time (min)	Aliquot weight (g)	[He-3] (atoms/g)	δ[He-3] (atoms/g)	[He-3] (atoms/g)	δ[He-3] (atoms/g)	% error	[He-4] (atoms/g)	δ[He-4] (atoms/g)	[He-4] (atoms/g)	δ[He-4] (atoms/g)
16-ROB-067-MNM	2017_09_4	b	1225	15	0.02168	6.35E+08	2.44E+07	6.39E+08	2.45E+07	3.83	2.94E+14	2.70E+12	2.95E+14	2.71E+12
16-ROB-067-MNM	2017_09_4	b	1325	15	0.02168	4.11E+06	1.01E+06				1.28E+12	8.56E+10		
16-ROB-068-MNM	2017_09_3	a	1225	15	0.02562	1.14E+09	3.74E+07	1.15E+09	3.74E+07	3.26	4.05E+14	3.56E+12	4.05E+14	3.56E+12
16-ROB-068-MNM	2017_09_3	a	1325	15	0.02562	1.01E+06	6.81E+05				2.79E+11	5.27E+10		
16-ROB-069-MNM	2017_09_4	a	1225	15	0.02831	3.93E+08	1.49E+07	4.03E+08	1.49E+07	3.71	6.66E+14	4.36E+12	6.86E+14	4.38E+12
16-ROB-069-MNM	2017_09_4	a	1325	15	0.02831	9.64E+06	1.33E+06				2.01E+13	4.01E+11		
16-ROB-070-MNM	2017_09_4	a	1225	15	0.03093	1.16E+09	4.20E+07	1.16E+09	4.20E+07	3.61	3.10E+14	2.02E+12	3.10E+14	2.02E+12
16-ROB-070-MNM	2017_09_4	a	1325	15	0.03093	2.75E+06	7.23E+05				3.06E+11	5.30E+10		
16-ROB-070-MNM	2017_09_4	b	1225	15	0.01938	1.08E+09	4.11E+07	1.09E+09	4.11E+07	3.79	2.84E+14	2.56E+12	2.84E+14	2.56E+12
16-ROB-070-MNM	2017_09_4	b	1325	15	0.01938	3.32E+06	1.05E+06				4.96E+11	7.91E+10		
16-ROB-071-MNM	2017_09_4	a	1225	15	0.02645	5.36E+08	2.00E+07	5.38E+08	2.00E+07	3.71	5.53E+14	3.54E+12	5.53E+14	3.54E+12
16-ROB-071-MNM	2017_09_4	a	1325	15	0.02645	1.69E+06	6.94E+05				3.76E+11	6.51E+10		
16-ROB-072-MNM	2017_09_3	a	1225	15	0.02535	3.10E+08	1.04E+07	3.14E+08	1.04E+07	3.32	3.01E+14	2.47E+12	3.05E+14	2.47E+12
16-ROB-072-MNM	2017_09_3	a	1325	15	0.02535	3.52E+06	9.46E+05				3.67E+12	9.35E+10		
16-ROB-072-MNM	2017_09_4	b	1225	15	0.02446	3.02E+08	1.22E+07	3.06E+08	1.22E+07	3.98	3.18E+14	2.89E+12	3.22E+14	2.89E+12
16-ROB-072-MNM	2017_09_4	b	1325	15	0.02446	4.37E+06	8.56E+05				3.46E+12	8.38E+10		
16-ROB-076-MON	2017_09_3	a	1225	15	0.02788	4.10E+08	1.36E+07	4.18E+08	1.36E+07	3.26	9.94E+14	8.75E+12	1.02E+15	8.84E+12
16-ROB-076-MON	2017_09_3	a	1325	15	0.02788	7.93E+06	1.09E+06				2.52E+13	1.30E+12		
16-ROB-077-MON	2017_09_3	a	1225	15	0.02499	4.15E+08	1.35E+07	4.20E+08	1.36E+07	3.23	2.87E+14	2.40E+12	2.89E+14	2.40E+12
16-ROB-077-MON	2017_09_3	a	1325	15	0.02499	4.66E+06	9.82E+05				1.86E+12	1.68E+11		
16-ROB-077-MON	2017_09_4	b	1225	15	0.03115	4.38E+08	1.65E+07	4.41E+08	1.65E+07	3.73	2.95E+14	1.89E+12	2.96E+14	1.89E+12
16-ROB-077-MON	2017_09_4	b	1325	15	0.03115	3.18E+06	7.19E+05				8.74E+11	5.95E+10		
16-ROB-079-WIN	2017_09_3	a	1225	15	0.0247	6.40E+08	2.00E+07	6.42E+08	2.00E+07	3.11	1.96E+14	1.62E+12	1.97E+14	1.62E+12
16-ROB-079-WIN	2017_09_3	a	1325	15	0.0247	2.56E+06	7.68E+05				4.99E+11	5.16E+10		
16-ROB-080-WIN	2017_09_4	a	1225	15	0.02503	6.37E+08	2.42E+07	6.71E+08	2.43E+07	3.62	8.36E+14	5.41E+12	9.21E+14	5.67E+12

Table C.1 continued.

Sample ID	Date analyzed	Aliquot	Heating temperature (°C)	Heating time (min)	Aliquot weight (g)	[He-3] (atoms/g)	δ[He-3] (atoms/g)	[He-3] (atoms/g)	δ[He-3] (atoms/g)	% error	[He-4] (atoms/g)	δ[He-4] (atoms/g)	[He-4] (atoms/g)	δ[He-4] (atoms/g)
16-ROB-080-WIN	2017_09_4	a	1325	15	0.02503	3.42E+07	2.13E+06				8.52E+13	1.67E+12		
16-ROB-081-WIN	2017_09_2	a	1225	15	0.02652	5.90E+08	1.77E+07	6.00E+08	1.77E+07	2.95	3.21E+13	1.33E+12	3.25E+13	1.34E+12
16-ROB-081-WIN	2017_09_2	a	1325	15	0.02652	9.80E+06	1.16E+06				4.01E+11	8.85E+10		
16-ROB-081-WIN	2017_09_4	b	1225	15	0.02716	5.76E+08	2.07E+07	5.84E+08	2.07E+07	3.55	3.41E+13	1.47E+12	3.45E+13	1.47E+12
16-ROB-081-WIN	2017_09_4	b	1325	15	0.02716	7.97E+06	1.05E+06				4.58E+11	5.67E+10		
16-ROB-082-WIN	2017_09_3	a	1225	15	0.02759	4.03E+08	1.39E+07	4.06E+08	1.39E+07	3.43	5.74E+13	2.96E+12	5.78E+13	2.96E+12
16-ROB-082-WIN	2017_09_3	a	1325	15	0.02759	2.58E+06	7.24E+05				3.49E+11	3.98E+10		
16-ROB-082-WIN	2017_09_4	b	1225	15	0.04487	4.14E+08	1.58E+07	4.17E+08	1.58E+07	3.78	5.74E+13	5.19E+11	5.79E+13	5.21E+11
16-ROB-082-WIN	2017_09_4	b	1325	15	0.04487	3.13E+06	5.45E+05				5.65E+11	3.93E+10		
16-ROB-083-WIN	2017_09_4	a	1225	15	0.02835	7.49E+08	2.80E+07	7.54E+08	2.80E+07	3.71	3.56E+14	2.30E+12	3.58E+14	2.30E+12
16-ROB-083-WIN	2017_09_4	a	1325	15	0.02835	5.17E+06	8.64E+05				2.04E+12	5.83E+10		
16-ROB-084-WIN	2017_09_3	a	1225	15	0.02928	6.23E+08	1.95E+07	6.29E+08	1.95E+07	3.11	1.08E+14	8.89E+11	1.09E+14	8.90E+11
16-ROB-084-WIN	2017_09_3	a	1325	15	0.02928	5.78E+06	8.77E+05				3.14E+11	5.13E+10		
16-ROB-084-WIN	2017_09_4	b	1225	15	0.02119	6.37E+08	2.46E+07	6.42E+08	2.46E+07	3.83	1.15E+14	1.04E+12	1.16E+14	1.04E+12
16-ROB-084-WIN	2017_09_4	b	1325	15	0.02119	4.79E+06	1.22E+06				3.31E+11	7.61E+10		
16-ROB-085-WIN	2017_09_3	a	1225	15	0.03074	7.91E+08	2.52E+07	7.92E+08	2.52E+07	3.18	3.75E+14	3.29E+12	3.75E+14	3.29E+12
16-ROB-085-WIN	2017_09_3	a	1325	15	0.03074	1.54E+06	6.81E+05				1.51E+11	4.80E+10		
16-ROB-104-WAL	2017_09_2	a	-132	15	0.02438	2.49E+06	9.47E+05				4.80E+11	5.45E+10		
16-ROB-104-WAL	2017_09_2	a	-122	15	0.02438	1.68E+09	4.83E+07	1.68E+09	4.83E+07	2.87	3.42E+14	3.08E+12	3.42E+14	3.08E+12
16-ROB-104-WAL	2017_09_2	b	-132	15	0.02831	8.56E+06	9.47E+05				1.84E+12	4.97E+10		
16-ROB-104-WAL	2017_09_2	b	-122	15	0.02831	1.70E+09	4.88E+07	1.71E+09	4.88E+07	2.86	3.89E+14	3.50E+12	3.91E+14	3.50E+12
16-ROB-105-WAL	2017_09_2	a	1225	15	0.0245	2.02E+09	5.79E+07	2.02E+09	5.79E+07	2.86	6.16E+14	5.52E+12	6.16E+14	5.52E+12
16-ROB-105-WAL	2017_09_2	a	1325	15	0.0245	2.36E+06	8.61E+05				5.89E+11	6.48E+10		
16-ROB-106-WAL	2017_09_2	a	1225	15	0.02546	2.37E+09	6.77E+07	2.38E+09	6.77E+07	2.85	5.08E+14	4.60E+12	5.09E+14	4.60E+12
16-ROB-106-WAL	2017_09_2	a	1325	15	0.02546	7.49E+06	1.05E+06				8.05E+11	4.22E+10		

Table C.1 continued.

Sample ID	Date analyzed	Aliquot	Heating temperature (°C)	Heating time (min)	Aliquot weight (g)	[He-3] (atoms/g)	δ[He-3] (atoms/g)	[He-3] (atoms/g)	δ[He-3] (atoms/g)	% error	[He-4] (atoms/g)	δ[He-4] (atoms/g)	[He-4] (atoms/g)	δ[He-4] (atoms/g)
16-ROB-106-WAL	2017_09_4	b	1225	15	0.02033	2.33E+09	8.33E+07	2.34E+09	8.33E+07	3.56	5.04E+14	3.25E+12	5.06E+14	3.25E+12
16-ROB-106-WAL	2017_09_4	b	1325	15	0.02033	1.03E+07	1.41E+06				2.59E+12	8.04E+10		
16-ROB-107-WAL	2017_09_2	a	1225	15	0.02529	1.31E+09	3.78E+07	1.36E+09	3.79E+07	2.78	5.35E+14	4.86E+12	5.58E+14	4.86E+12
16-ROB-107-WAL	2017_09_2	a	1325	15	0.02529	5.14E+07	2.50E+06				2.27E+13	2.89E+11		
16-ROB-108-WAL	2017_09_2	a	1225	15	0.02605	1.98E+09	5.64E+07	2.01E+09	5.65E+07	2.82	3.82E+14	3.45E+12	3.88E+14	3.45E+12
16-ROB-108-WAL	2017_09_2	a	1325	15	0.02605	2.82E+07	1.78E+06				5.91E+12	1.06E+11		
16-ROB-109-WAL	2017_09_2	a	1225	15	0.0231	1.28E+09	3.75E+07	1.28E+09	3.75E+07	2.92	4.15E+14	3.72E+12	4.15E+14	3.73E+12
16-ROB-109-WAL	2017_09_2	a	1325	15	0.0231	9.34E+05	8.26E+05				1.92E+11	5.63E+10		
16-ROB-110-WAL	2017_09_2	a	1225	15	0.02601	1.57E+09	4.14E+07	1.57E+09	4.14E+07	2.63	2.25E+14	1.81E+12	2.26E+14	1.82E+12
16-ROB-110-WAL	2017_09_2	a	1325	15	0.02601	4.09E+06	9.28E+05				4.38E+11	5.19E+10		
16-ROB-110-WAL	2017_09_4	b	1225	15	0.02829	1.56E+09	5.82E+07	1.57E+09	5.82E+07	3.71	2.59E+14	2.36E+12	2.59E+14	2.36E+12
16-ROB-110-WAL	2017_09_4	b	1325	15	0.02829	2.29E+06	6.85E+05				6.11E+11	5.95E+10		
16-ROB-111-BGE	2017_09_2	a	1225	15	0.01655	1.51E+09	4.12E+07	1.53E+09	4.12E+07	2.69	2.48E+14	1.96E+12	2.50E+14	1.96E+12
16-ROB-111-BGE	2017_09_2	a	1325	15	0.01655	1.53E+07	1.74E+06				1.36E+12	8.15E+10		
16-ROB-111-BGE	2017_09_4	b	1225	15	0.02633	1.53E+09	5.70E+07	1.54E+09	5.71E+07	3.70	2.52E+14	2.30E+12	2.54E+14	2.30E+12
16-ROB-111-BGE	2017_09_4	b	1325	15	0.02633	9.89E+06	1.15E+06				1.36E+12	5.29E+10		
16-ROB-112-BGE	2017_09_1	a	1225	15	0.02879	1.25E+09	3.94E+07	1.28E+09	3.95E+07	3.09	4.69E+14	6.41E+12	4.80E+14	6.42E+12
16-ROB-112-BGE	2017_09_1	a	1325	15	0.02879	3.01E+07	1.84E+06				1.10E+13	2.93E+11		
16-ROB-112-BGE	2017_09_4	b	1225	15	0.01852	1.13E+09	4.14E+07	1.17E+09	4.15E+07	3.54	4.60E+14	3.20E+12	4.73E+14	3.22E+12
16-ROB-112-BGE	2017_09_4	b	1325	15	0.01852	3.80E+07	2.72E+06				1.34E+13	2.83E+11		
16-ROB-113-BGE	2017_09_1	a	1225	15	0.02742	2.51E+09	7.84E+07	2.54E+09	7.85E+07	3.09	6.60E+14	9.04E+12	6.67E+14	9.05E+12
16-ROB-113-BGE	2017_09_1	a	1325	15	0.02742	2.89E+07	1.77E+06				6.89E+12	1.91E+11		
16-ROB-114-BGE	2017_09_2	a	1225	15	0.02563	2.06E+09	5.87E+07	2.08E+09	5.87E+07	2.83	3.92E+14	3.51E+12	3.94E+14	3.51E+12
16-ROB-114-BGE	2017_09_2	a	1325	15	0.02563	1.54E+07	1.45E+06				1.79E+12	6.45E+10		
16-ROB-114-BGE	2017_09_4	b	1225	15	0.02044	2.10E+09	7.60E+07	2.11E+09	7.60E+07	3.59	4.16E+14	2.69E+12	4.18E+14	2.69E+12

Table C.1 continued.

Sample ID	Date analyzed	Aliquot	Heating temperature (°C)	Heating time (min)	Aliquot weight (g)	[He-3] (atoms/g)	δ[He-3] (atoms/g)	[He-3] (atoms/g)	δ[He-3] (atoms/g)	% error	[He-4] (atoms/g)	δ[He-4] (atoms/g)	[He-4] (atoms/g)	δ[He-4] (atoms/g)
16-ROB-114-BGE	2017_09_4	b	1325	15	0.02044	1.10E+07	1.45E+06				2.23E+12	8.63E+10		
16-ROB-115-BGE	2017_09_2	a	1225	15	0.02197	2.40E+09	6.91E+07	2.45E+09	6.91E+07	2.82	4.62E+14	4.17E+12	4.72E+14	4.18E+12
16-ROB-115-BGE	2017_09_2	a	1325	15	0.02197	4.79E+07	2.53E+06				9.28E+12	2.74E+11		
16-ROB-116-BGE	2017_09_2	a	1225	15	0.0276	3.51E+09	9.94E+07	3.63E+09	9.95E+07	2.74	7.29E+14	6.61E+12	7.51E+14	6.62E+12
16-ROB-116-BGE	2017_09_2	a	1325	15	0.0276	1.11E+08	3.28E+06				2.20E+13	2.76E+11		
16-ROB-116-BGE	2017_09_4	b	1225	15	0.0149	3.38E+09	1.21E+08	3.44E+09	1.22E+08	3.53	6.86E+14	4.38E+12	6.96E+14	4.39E+12
16-ROB-116-BGE	2017_09_4	b	1325	15	0.0149	5.80E+07	3.69E+06				9.77E+12	2.28E+11		
16-ROB-117-BGE	2017_09_1	a	1225	15	0.02473	2.44E+09	7.15E+07	2.45E+09	7.15E+07	2.91	8.74E+13	1.13E+12	8.81E+13	1.13E+12
16-ROB-117-BGE	2017_09_1	a	1325	15	0.02473	1.11E+07	1.30E+06				7.14E+11	5.63E+10		
16-ROB-118-BBY	2017_09_1	a	1225	15	0.02426	2.28E+09	7.10E+07	2.29E+09	7.10E+07	3.10	3.77E+14	5.15E+12	3.79E+14	5.16E+12
16-ROB-118-BBY	2017_09_1	a	1325	15	0.02426	8.20E+06	1.07E+06				2.14E+12	7.89E+10		
16-ROB-119-BBY	2017_09_1	a	1225	15	0.02529	1.38E+09	4.35E+07	1.47E+09	4.36E+07	2.97	5.07E+14	6.93E+12	5.52E+14	7.03E+12
16-ROB-119-BBY	2017_09_1	a	1325	15	0.02529	8.30E+07	3.29E+06				4.53E+13	1.20E+12		
16-ROB-120-BBY	2017_09_2	a	1225	15	0.02924	1.39E+09	4.00E+07	1.41E+09	4.00E+07	2.84	2.89E+14	2.61E+12	2.91E+14	2.61E+12
16-ROB-120-BBY	2017_09_2	a	1325	15	0.02924	1.99E+07	1.40E+06				2.02E+12	7.35E+10		
16-ROB-121-BBY	2017_09_1	a	1225	15	0.02683	1.29E+09	4.08E+07	1.34E+09	4.09E+07	3.06	4.55E+14	6.23E+12	4.79E+14	6.26E+12
16-ROB-121-BBY	2017_09_1	a	1325	15	0.02683	4.76E+07	2.56E+06				2.36E+13	6.26E+11		
16-ROB-121-BBY	2017_09_3	b	1225	15	0.0177	1.27E+09	3.86E+07	1.31E+09	3.87E+07	2.95	4.12E+14	3.39E+12	4.31E+14	3.41E+12
16-ROB-121-BBY	2017_09_3	b	1325	15	0.0177	4.61E+07	3.09E+06				1.97E+13	3.10E+11		
16-ROB-122-BBY	2017_09_1	a	1225	15	0.02592	2.01E+09	6.29E+07	2.03E+09	6.30E+07	3.11	5.08E+14	6.98E+12	5.12E+14	6.98E+12
16-ROB-122-BBY	2017_09_1	a	1325	15	0.02592	1.36E+07	1.39E+06				3.77E+12	1.16E+11		
16-ROB-134-MZZ	2017_05_5	a	1275	15	0.02341	1.71E+09	3.99E+07	1.72E+09	4.00E+07	2.33	8.90E+13	1.90E+12	8.93E+13	1.90E+12
16-ROB-134-MZZ	2017_05_5	a	1350	15	0.02341	1.03E+07	1.23E+06				2.89E+11	6.33E+10		
16-ROB-135-MZZ	2017_05_5	a	1275	15	0.02485	2.39E+09	3.98E+07	2.40E+09	3.98E+07	1.66	3.10E+14	4.11E+12	3.10E+14	4.11E+12
16-ROB-135-MZZ	2017_05_5	a	1350	15	0.02485	1.13E+07	1.19E+06				3.50E+11	5.16E+10		

Table C.1 continued.

Sample ID	Date analyzed	Aliquot	Heating temperature (°C)	Heating time (min)	Aliquot weight (g)	[He-3] (atoms/g)	δ[He-3] (atoms/g)	[He-3] (atoms/g)	δ[He-3] (atoms/g)	% error	[He-4] (atoms/g)	δ[He-4] (atoms/g)	[He-4] (atoms/g)	δ[He-4] (atoms/g)
16-ROB-135-MZZ	2017_05_6	b	1275	15	0.02776	2.38E+09	3.76E+07	2.40E+09	3.76E+07	1.57	3.04E+14	3.84E+12	3.05E+14	3.84E+12
16-ROB-135-MZZ	2017_05_6	b	1350	15	0.02776	1.35E+07	1.21E+06				7.48E+11	8.90E+10		
16-ROB-138-MZZ	2017_05_5	a	1275	15	0.01936	1.47E+09	3.50E+07	1.48E+09	3.51E+07	2.37	3.71E+13	7.94E+11	3.72E+13	7.99E+11
16-ROB-138-MZZ	2017_05_5	a	1350	15	0.01936	1.38E+07	1.58E+06				1.79E+11	9.51E+10		
16-ROB-139-MZZ	2017_05_5	a	1275	15	0.01975	2.29E+09	5.34E+07	2.30E+09	5.34E+07	2.32	4.20E+13	8.98E+11	4.22E+13	9.02E+11
16-ROB-139-MZZ	2017_05_5	a	1350	15	0.01975	1.20E+07	1.65E+06				2.03E+11	7.74E+10		
16-ROB-139-MZZ	2017_05_6	b	1275	15	0.03207	2.24E+09	5.21E+07	2.27E+09	5.21E+07	2.30	4.15E+13	8.93E+11	4.19E+13	8.94E+11
16-ROB-139-MZZ	2017_05_6	b	1350	15	0.03207	2.70E+07	1.66E+06				3.94E+11	3.67E+10		
16-ROB-140-MZZ	2017_05_5	a	1275	15	0.01817	3.25E+09	7.46E+07	3.28E+09	7.46E+07	2.27	8.56E+13	1.82E+12	8.60E+13	1.83E+12
16-ROB-140-MZZ	2017_05_5	a	1350	15	0.01817	2.62E+07	2.27E+06				4.61E+11	6.61E+10		
16-ROB-141-JSO	2017_05_5	a	1275	15	0.02375	2.10E+09	4.90E+07	2.12E+09	4.91E+07	2.31	6.88E+13	1.47E+12	6.94E+13	1.47E+12
16-ROB-141-JSO	2017_05_5	a	1350	15	0.02375	2.18E+07	1.62E+06				6.35E+11	6.51E+10		
16-ROB-156A-EVN	2017_05_5	a	1275	15	0.02553	4.40E+09	9.97E+07	4.40E+09	9.97E+07	2.27	5.35E+13	1.14E+12	5.36E+13	1.14E+12
16-ROB-156A-EVN	2017_05_5	a	1350	15	0.02553	3.65E+06	9.05E+05				1.11E+11	5.71E+10		
16-ROB-156A-EVN	2017_05_6	b	1275	15	0.03228	4.41E+09	1.01E+08	4.42E+09	1.01E+08	2.29	5.42E+13	1.17E+12	5.43E+13	1.17E+12
16-ROB-156A-EVN	2017_05_6	b	1350	15	0.03228	8.49E+06	1.15E+06				7.34E+10	3.57E+10		
16-ROB-156B-EVN	2017_05_6	a	1275	15	0.03288	3.42E+09	7.84E+07	3.42E+09	7.84E+07	2.29	6.81E+13	1.47E+12	6.82E+13	1.47E+12
16-ROB-156B-EVN	2017_05_6	a	1350	15	0.03288	6.41E+06	1.02E+06				1.19E+11	4.84E+10		

APPENDIX D

APPARENT EXPOSURE AGES OF ALL ALIQUOTS

Table D.1 Apparent exposure ages of all sample aliquots.

Sample Name	Nuclide	Age (LSDn) (Ma)	Internal error (LSDn) (Ma)	External error (LSDn) (Ma)	Age (St) (Ma)	Internal error (St) (Ma)	External error (St) (Ma)
Roberts Col							
Misery A							
15-ROB-001-MZA	^{3}He	8.16	0.07	0.90	9.14	0.08	1.01
15-ROB-001-MZA	^{3}He	7.89	0.07	0.87	8.84	0.08	0.98
15-ROB-002-MZA	^{3}He	5.69	0.05	0.63	6.37	0.05	0.70
15-ROB-002-MZA	^{3}He	5.69	0.05	0.63	6.37	0.05	0.70
15-ROB-003-MZA	^{3}He	6.11	0.05	0.67	6.84	0.06	0.75
15-ROB-003-MZA	^{3}He	6.12	0.05	0.67	6.85	0.06	0.76
15-ROB-004-MZA	^{3}He	4.23	0.03	0.47	4.74	0.04	0.52
15-ROB-004-MZA	^{3}He	4.52	0.04	0.50	5.06	0.05	0.56
15-ROB-005-MZA	^{3}He	6.23	0.05	0.69	6.97	0.06	0.77
15-ROB-005-MZA	^{3}He	6.22	0.05	0.69	6.96	0.06	0.77
Misery B							
15-ROB-006-MZB	^{3}He	8.14	0.15	0.91	9.15	0.17	1.02
15-ROB-006-MZB	^{3}He	7.84	0.13	0.87	8.82	0.15	0.98
15-ROB-007-MZB	^{3}He	8.31	0.14	0.93	9.35	0.16	1.04
15-ROB-007-MZB	^{3}He	8.09	0.13	0.90	9.10	0.14	1.01
15-ROB-008-MZB	^{3}He	8.10	0.13	0.90	9.12	0.15	1.01
15-ROB-008-MZB	^{3}He	8.06	0.13	0.90	9.06	0.14	1.01
15-ROB-009-MZB	^{3}He	8.21	0.16	0.92	9.24	0.18	1.03
15-ROB-009-MZB	^{3}He	8.05	0.13	0.90	9.06	0.14	1.01
15-ROB-010-MZB	^{3}He	8.04	0.15	0.90	9.04	0.16	1.01
15-ROB-010-MZB	^{3}He	8.09	0.11	0.90	9.10	0.12	1.01
15-ROB-011-MZB	^{3}He	8.10	0.16	0.90	9.10	0.18	1.02
15-ROB-011-MZB	^{3}He	8.07	0.13	0.90	9.07	0.14	1.01
15-ROB-012-MZB	^{3}He	8.15	0.14	0.91	9.17	0.16	1.02
15-ROB-013-MZB	^{3}He	8.07	0.16	0.90	9.08	0.17	1.01
Misery C							
15-ROB-014-MZC	^{3}He	7.96	0.13	0.89	8.93	0.15	0.99
15-ROB-014-MZC	^{3}He	7.90	0.12	0.88	8.87	0.13	0.98
15-ROB-015-MZC	^{3}He	7.99	0.13	0.89	8.97	0.15	1.00
15-ROB-015-MZC	^{3}He	7.98	0.12	0.89	8.96	0.14	0.99
15-ROB-016-MZC	^{3}He	7.79	0.13	0.87	8.74	0.15	0.97
15-ROB-016-MZC	^{3}He	7.83	0.12	0.87	8.78	0.13	0.98
15-ROB-017-MZC	^{3}He	8.06	0.13	0.90	9.04	0.14	1.00
15-ROB-018-MZC	^{3}He	7.65	0.08	0.85	8.58	0.09	0.95
15-ROB-018-MZC	^{3}He	7.40	0.07	0.82	8.30	0.08	0.92

Table D.1 continued.

Sample Name	Nuclide	Age (LSDn) (Ma)	Internal error (LSDn) (Ma)	External error (LSDn) (Ma)	Age (St) (Ma)	Internal error (St) (Ma)	External error (St) (Ma)
15-ROB-018-MZC	^{3}He	7.59	0.13	0.85	8.51	0.15	0.95
15-ROB-019-MZC	^{3}He	7.26	0.07	0.80	8.14	0.08	0.90
15-ROB-019-MZC	^{3}He	7.38	0.08	0.82	8.27	0.09	0.91
15-ROB-020-MZC	^{3}He	7.29	0.07	0.81	8.18	0.08	0.90
15-ROB-020-MZC	^{3}He	7.59	0.07	0.84	8.51	0.08	0.94
15-ROB-021-MZC	^{3}He	5.05	0.05	0.56	5.66	0.06	0.63
15-ROB-021-MZC	^{3}He	4.97	0.05	0.55	5.58	0.06	0.62
15-ROB-022-MZC	^{3}He	4.72	0.05	0.52	5.29	0.06	0.59
15-ROB-022-MZC	^{3}He	4.80	0.05	0.53	5.37	0.06	0.59
Misery D							
15-ROB-023-MZD	^{3}He	8.02	0.14	0.89	9.02	0.16	1.00
15-ROB-024-MZD	^{3}He	7.75	0.12	0.86	8.72	0.14	0.97
15-ROB-025-MZD	^{3}He	8.08	0.13	0.90	9.09	0.15	1.01
15-ROB-026-MZD	^{3}He	7.52	0.13	0.84	8.46	0.15	0.94
15-ROB-027-MZD	^{3}He	8.25	0.14	0.92	9.27	0.15	1.03
15-ROB-027-MZD	^{3}He	8.38	0.13	0.93	9.42	0.15	1.05
Roberts Col							
15-ROB-028-COL	^{3}He	11.29	0.11	1.25	12.83	0.13	1.42
15-ROB-028-COL	^{3}He	11.03	0.14	1.22	12.54	0.16	1.39
15-ROB-029-COL	^{10}Be	9.88	2.97	16.60	0.00	0.00	0.00
15-ROB-029-COL	^{21}Ne	11.92	0.25	0.97	14.51	0.30	1.19
15-ROB-029-COL	^{21}Ne	11.68	0.19	0.94	14.22	0.23	1.15
15-ROB-029-COL	^{21}Ne	11.56	0.15	0.93	14.08	0.19	1.13
15-ROB-029-COL	^{21}Ne	11.83	0.14	0.94	14.40	0.17	1.15
15-ROB-030-COL	^{3}He	10.22	0.13	1.13	11.63	0.15	1.29
15-ROB-030-COL	^{3}He	9.81	0.14	1.09	11.16	0.16	1.24
15-ROB-031-COL	^{3}He	8.86	0.12	0.98	10.07	0.13	1.12
15-ROB-031-COL	^{3}He	8.63	0.12	0.96	9.80	0.14	1.09
15-ROB-031-COL	^{3}He	8.68	0.17	0.97	9.86	0.19	1.10
15-ROB-032-COL	^{10}Be	10.70	4.82	25.17	0.00	0.00	0.00
15-ROB-032-COL	^{21}Ne	13.18	0.27	1.08	16.05	0.33	1.31
15-ROB-032-COL	^{21}Ne	12.98	0.21	1.05	15.80	0.25	1.27
15-ROB-032-COL	^{21}Ne	12.84	0.17	1.03	15.63	0.21	1.25
15-ROB-032-COL	^{21}Ne	12.86	0.15	1.03	15.65	0.18	1.25
15-ROB-033-COL	^{10}Be	10.61	5.36	24.22	0.00	0.00	0.00
15-ROB-033-COL	^{21}Ne	11.97	0.19	0.96	14.58	0.23	1.17
15-ROB-033-COL	^{21}Ne	11.91	0.15	0.95	14.51	0.18	1.16
15-ROB-033-COL	^{21}Ne	11.86	0.14	0.95	14.44	0.17	1.15
15-ROB-034-COL	^{10}Be	9.33	2.37	12.63	0.00	0.00	0.00
15-ROB-034-COL	^{21}Ne	9.35	0.15	0.75	11.37	0.19	0.92
15-ROB-034-COL	^{21}Ne	9.28	0.12	0.74	11.29	0.15	0.90

Table D.1 continued.

Sample Name	Nuclide	Age (LSDn) (Ma)	Internal error (LSDn) (Ma)	External error (LSDn) (Ma)	Age (St) (Ma)	Internal error (St) (Ma)	External error (St) (Ma)
15-ROB-034-COL	^{21}Ne	9.18	0.11	0.73	11.17	0.13	0.89
Upper Roberts							
Arena Moraine							
15-ROB-035-ARM	^{3}He	2.58	0.03	0.28	2.91	0.03	0.32
15-ROB-035-ARM	^{3}He	2.67	0.04	0.30	3.02	0.04	0.33
15-ROB-036-ARM	^{3}He	2.92	0.04	0.32	3.29	0.04	0.36
15-ROB-036-ARM	^{3}He	2.85	0.04	0.32	3.22	0.04	0.36
15-ROB-038-ARM	^{3}He	2.49	0.03	0.28	2.81	0.03	0.31
15-ROB-038-ARM	^{3}He	2.66	0.04	0.30	3.01	0.04	0.33
15-ROB-039-ARM	^{3}He	2.48	0.03	0.28	2.80	0.04	0.31
15-ROB-039-ARM	^{3}He	2.58	0.03	0.29	2.92	0.04	0.32
15-ROB-040-ARM	^{3}He	2.71	0.03	0.30	3.05	0.04	0.34
15-ROB-040-ARM	^{3}He	2.67	0.04	0.30	3.02	0.04	0.33
15-ROB-041-ARM	^{3}He	2.72	0.03	0.30	3.07	0.04	0.34
15-ROB-041-ARM	^{3}He	2.79	0.03	0.31	3.15	0.03	0.35
Eine Moraine							
15-ROB-042-EIN	^{3}He	1.31	0.02	0.15	1.48	0.02	0.16
15-ROB-042-EIN	^{3}He	1.30	0.02	0.14	1.47	0.02	0.16
15-ROB-042-EIN	^{3}He	1.24	0.01	0.14	1.40	0.02	0.15
15-ROB-043-EIN	^{3}He	1.24	0.02	0.14	1.40	0.02	0.15
15-ROB-043-EIN	^{3}He	1.25	0.02	0.14	1.40	0.03	0.16
15-ROB-043-EIN	^{3}He	1.19	0.02	0.13	1.34	0.02	0.15
15-ROB-044-EIN	^{3}He	0.84	0.01	0.09	0.95	0.01	0.10
15-ROB-044-EIN	^{3}He	0.92	0.01	0.10	1.04	0.01	0.11
15-ROB-044-EIN	^{3}He	0.94	0.01	0.10	1.05	0.02	0.12
15-ROB-045-EIN	^{3}He	1.38	0.02	0.15	1.55	0.02	0.17
15-ROB-045-EIN	^{3}He	1.40	0.02	0.16	1.58	0.02	0.18
15-ROB-046-EIN	^{3}He	2.14	0.03	0.24	2.41	0.03	0.27
15-ROB-046-EIN	^{3}He	2.05	0.03	0.23	2.31	0.03	0.26
15-ROB-047-EIN	^{3}He	1.04	0.02	0.12	1.17	0.02	0.13
15-ROB-047-EIN	^{3}He	1.19	0.02	0.13	1.33	0.02	0.15
15-ROB-048-EIN	^{3}He	1.03	0.02	0.11	1.16	0.02	0.13
15-ROB-048-EIN	^{3}He	1.05	0.02	0.12	1.18	0.02	0.13
Kleine Moraine							
15-ROB-049-KLE	^{3}He	1.08	0.02	0.12	1.22	0.02	0.14
15-ROB-050-KLE	^{3}He	1.09	0.02	0.12	1.22	0.02	0.14
15-ROB-050-KLE	^{3}He	1.12	0.02	0.12	1.25	0.02	0.14
15-ROB-050-KLE	^{3}He	1.07	0.01	0.12	1.20	0.01	0.13
15-ROB-051-KLE	^{3}He	1.38	0.02	0.15	1.56	0.02	0.17
15-ROB-052-KLE	^{3}He	1.30	0.02	0.14	1.46	0.02	0.16
15-ROB-053-KLE	^{3}He	1.00	0.02	0.11	1.13	0.02	0.13

Table D.1 continued.

Sample Name	Nuclide	Age (LSDn) (Ma)	Internal error (LSDn) (Ma)	External error (LSDn) (Ma)	Age (St) (Ma)	Internal error (St) (Ma)	External error (St) (Ma)
15-ROB-053-KLE	^{3}He	0.97	0.01	0.11	1.09	0.02	0.12
15-ROB-054-KLE	^{3}He	1.32	0.01	0.15	1.48	0.01	0.16
15-ROB-054-KLE	^{3}He	1.33	0.01	0.15	1.49	0.02	0.16
Nacht Moraine							
15-ROB-055-NAC	^{3}He	1.07	0.02	0.12	1.20	0.02	0.13
15-ROB-055-NAC	^{3}He	1.07	0.02	0.12	1.20	0.02	0.13
15-ROB-056-NAC	^{3}He	1.07	0.02	0.12	1.20	0.02	0.13
15-ROB-056-NAC	^{3}He	1.02	0.02	0.11	1.14	0.02	0.13
15-ROB-057-NAC	^{3}He	1.23	0.02	0.14	1.38	0.03	0.15
15-ROB-057-NAC	^{3}He	1.29	0.02	0.14	1.45	0.03	0.16
15-ROB-058-NAC	^{3}He	1.25	0.02	0.14	1.40	0.03	0.16
15-ROB-059-NAC	^{3}He	1.06	0.02	0.12	1.18	0.02	0.13
15-ROB-059-NAC	^{3}He	1.11	0.02	0.12	1.24	0.02	0.14
15-ROB-060-NAC	^{3}He	1.54	0.03	0.17	1.72	0.03	0.19
15-ROB-061-NAC	^{3}He	1.08	0.02	0.12	1.21	0.02	0.14
Musik Moraine							
15-ROB-062-MUS	^{3}He	1.12	0.02	0.12	1.25	0.02	0.14
15-ROB-063-MUS	^{3}He	1.07	0.02	0.12	1.20	0.02	0.13
15-ROB-064-MUS	^{3}He	0.62	0.01	0.07	0.69	0.01	0.08
Lower Roberts							
NLO Moraine							
16-ROB-009-NLO	^{10}Be	1.20	0.02	0.10	1.37	0.03	0.16
Andrew Moraine							
16-ROB-015-AND	^{3}He	1.59	0.04	0.18	1.73	0.04	0.20
16-ROB-015-AND	^{3}He	1.66	0.04	0.19	1.80	0.04	0.20
16-ROB-016-AND	^{3}He	1.30	0.03	0.15	1.41	0.03	0.16
16-ROB-016-AND	^{3}He	1.31	0.03	0.15	1.42	0.03	0.16
16-ROB-020-AND	^{10}Be	1.43	0.03	0.13	1.66	0.03	0.21
POS Moraines							
16-ROB-023-PSO	^{3}He	1.39	0.03	0.16	1.52	0.04	0.17
16-ROB-023-PSO	^{3}He	1.38	0.03	0.16	1.51	0.04	0.17
16-ROB-024-PSO	^{3}He	1.17	0.03	0.13	1.27	0.03	0.14
16-ROB-028-PSI	^{3}He	1.81	0.04	0.20	1.97	0.04	0.22
16-ROB-028-PSI	^{3}He	1.76	0.04	0.20	1.92	0.04	0.22
16-ROB-029-PSI	^{3}He	2.05	0.05	0.23	2.24	0.05	0.25
16-ROB-030-PSI	^{3}He	1.57	0.04	0.18	1.72	0.04	0.19
WBK Moraine							
16-ROB-031-WBK	^{3}He	2.43	0.04	0.27	2.65	0.04	0.30
16-ROB-031-WBK	^{3}He	2.59	0.04	0.29	2.82	0.05	0.31
16-ROB-032-WBK	^{3}He	2.86	0.07	0.32	3.12	0.07	0.35
16-ROB-032-WBK	^{3}He	2.81	0.06	0.32	3.07	0.07	0.34

Table D.1 continued.

Sample Name	Nuclide	Age (LSDn) (Ma)	Internal error (LSDn) (Ma)	External error (LSDn) (Ma)	Age (St) (Ma)	Internal error (St) (Ma)	External error (St) (Ma)
16-ROB-033-WBK	^{3}He	1.78	0.04	0.20	1.95	0.05	0.22
16-ROB-034-WBK	^{3}He	3.64	0.06	0.41	3.98	0.06	0.44
16-ROB-034-WBK	^{3}He	3.66	0.06	0.41	4.00	0.07	0.44
16-ROB-036-WBK	^{3}He	2.82	0.05	0.31	3.07	0.05	0.34
16-ROB-036-WBK	^{3}He	2.83	0.05	0.31	3.09	0.05	0.34
16-ROB-037-WBK	^{3}He	2.35	0.05	0.26	2.57	0.06	0.29
16-ROB-037-WBK	^{3}He	2.38	0.06	0.27	2.60	0.06	0.29
SSU Moraine							
16-ROB-038-SSU	^{3}He	2.07	0.03	0.23	2.26	0.04	0.25
16-ROB-038-SSU	^{3}He	2.13	0.04	0.24	2.32	0.04	0.26
16-ROB-039-SSU	^{3}He	2.01	0.03	0.22	2.20	0.04	0.24
16-ROB-039-SSU	^{3}He	2.11	0.04	0.24	2.31	0.04	0.26
16-ROB-040-SSU	^{3}He	2.48	0.04	0.28	2.71	0.05	0.30
16-ROB-040-SSU	^{3}He	2.51	0.04	0.28	2.74	0.05	0.30
16-ROB-041-SSU	^{3}He	2.50	0.04	0.28	2.73	0.05	0.30
16-ROB-041-SSU	^{3}He	2.49	0.04	0.28	2.72	0.05	0.30
16-ROB-042-SSU	^{3}He	2.56	0.04	0.28	2.79	0.05	0.31
16-ROB-042-SSU	^{3}He	2.62	0.04	0.29	2.86	0.05	0.32
16-ROB-043-SSU	^{3}He	2.97	0.05	0.33	3.25	0.05	0.36
16-ROB-043-SSU	^{3}He	2.89	0.05	0.32	3.15	0.05	0.35
16-ROB-044-SSU	^{3}He	1.93	0.03	0.22	2.11	0.04	0.24
16-ROB-044-SSU	^{3}He	1.86	0.03	0.21	2.03	0.03	0.23
HDY Moraine							
16-ROB-045-HDY	^{3}He	2.76	0.07	0.31	3.02	0.08	0.34
16-ROB-046-HDY	^{3}He	2.71	0.08	0.31	2.96	0.09	0.34
16-ROB-046-HDY	^{3}He	2.77	0.07	0.31	3.03	0.08	0.34
16-ROB-046-HDY	^{3}He	2.88	0.08	0.33	3.16	0.09	0.36
16-ROB-047-HDY	^{3}He	2.03	0.06	0.23	2.22	0.06	0.25
16-ROB-048-HDY	^{3}He	2.70	0.08	0.31	2.95	0.09	0.34
16-ROB-048-HDY	^{3}He	2.68	0.07	0.30	2.93	0.08	0.33
16-ROB-049-HDY	^{3}He	2.89	0.08	0.33	3.16	0.09	0.36
16-ROB-050-HDY	^{3}He	3.45	0.10	0.39	3.77	0.11	0.43
16-ROB-051-HDY	^{3}He	2.77	0.08	0.32	3.03	0.09	0.34
BAS Moraine							
16-ROB-052-BAS	^{3}He	2.89	0.07	0.33	3.17	0.08	0.36
16-ROB-053-BAS	^{3}He	2.96	0.09	0.34	3.25	0.10	0.37
16-ROB-053-BAS	^{3}He	2.95	0.09	0.34	3.23	0.10	0.37
16-ROB-054-BAS	^{3}He	2.84	0.08	0.32	3.11	0.09	0.35
16-ROB-055-BAS	^{3}He	3.09	0.09	0.35	3.39	0.10	0.38
16-ROB-056-BAS	^{3}He	2.70	0.07	0.31	2.96	0.08	0.33
16-ROB-057-BAS	^{3}He	2.77	0.08	0.31	3.04	0.09	0.34

Table D.1 continued.

Sample Name	Nuclide	Age (LSDn) (Ma)	Internal error (LSDn) (Ma)	External error (LSDn) (Ma)	Age (St) (Ma)	Internal error (St) (Ma)	External error (St) (Ma)
16-ROB-057-BAS	^{3}He	2.91	0.09	0.33	3.19	0.10	0.36
16-ROB-058-BAS	^{3}He	2.91	0.07	0.33	3.18	0.07	0.36
16-ROB-058-BAS	^{3}He	2.87	0.04	0.32	3.15	0.05	0.35
Ringleader Moraine							
16-ROB-059-RIN	^{3}He	3.09	0.05	0.34	3.40	0.06	0.38
16-ROB-060-RIN	^{10}Be	2.67	0.08	0.34	3.39	0.12	0.71
16-ROB-061-RIN	^{3}He	2.88	0.07	0.32	3.17	0.07	0.36
16-ROB-061-RIN	^{3}He	2.81	0.06	0.32	3.09	0.07	0.35
16-ROB-062-RIN	^{10}Be	3.03	0.10	0.43	4.00	0.17	1.02
16-ROB-063-RIN	^{3}He	4.14	0.07	0.46	4.54	0.08	0.51
16-ROB-063-RIN	^{3}He	3.91	0.14	0.45	4.29	0.15	0.50
16-ROB-064-RIN	^{3}He	3.41	0.08	0.38	3.75	0.09	0.42
16-ROB-065-RIN	^{3}He	2.21	0.07	0.25	2.43	0.08	0.28
16-ROB-065-RIN	^{3}He	2.01	0.07	0.23	2.21	0.08	0.26
MNM Moraine							
16-ROB-066-MNM	^{3}He	1.87	0.06	0.21	2.03	0.06	0.23
16-ROB-067-MNM	^{3}He	0.87	0.03	0.10	0.95	0.03	0.11
16-ROB-067-MNM	^{3}He	0.82	0.03	0.10	0.89	0.03	0.10
16-ROB-068-MNM	^{3}He	1.46	0.05	0.17	1.58	0.05	0.18
16-ROB-069-MNM	^{3}He	0.51	0.02	0.06	0.56	0.02	0.06
16-ROB-070-MNM	^{3}He	1.48	0.05	0.17	1.61	0.06	0.19
16-ROB-070-MNM	^{3}He	1.38	0.05	0.16	1.50	0.06	0.17
16-ROB-071-MNM	^{3}He	0.70	0.03	0.08	0.76	0.03	0.09
16-ROB-072-MNM	^{3}He	0.40	0.01	0.05	0.43	0.01	0.05
16-ROB-072-MNM	^{3}He	0.39	0.02	0.05	0.42	0.02	0.05
MON Moraine							
16-ROB-073-MON	^{10}Be	0.65	0.01	0.05	0.72	0.01	0.07
16-ROB-074-MON	^{10}Be	0.82	0.01	0.06	0.92	0.01	0.09
16-ROB-075-MON	^{10}Be	1.03	0.02	0.08	1.17	0.02	0.13
16-ROB-076-MON	^{3}He	0.53	0.02	0.06	0.57	0.02	0.07
16-ROB-077-MON	^{3}He	0.53	0.02	0.06	0.57	0.02	0.07
16-ROB-077-MON	^{3}He	0.55	0.02	0.06	0.60	0.02	0.07
16-ROB-078-MON	^{10}Be	0.94	0.01	0.07	1.07	0.02	0.11
WIN Moraine							
16-ROB-079-WIN	^{3}He	0.79	0.02	0.09	0.86	0.03	0.10
16-ROB-080-WIN	^{3}He	0.82	0.03	0.10	0.89	0.03	0.10
16-ROB-081-WIN	^{3}He	0.73	0.02	0.08	0.79	0.02	0.09
16-ROB-081-WIN	^{3}He	0.71	0.03	0.08	0.77	0.03	0.09
16-ROB-082-WIN	^{3}He	0.49	0.02	0.06	0.54	0.02	0.06
16-ROB-082-WIN	^{3}He	0.51	0.02	0.06	0.55	0.02	0.06
16-ROB-083-WIN	^{3}He	0.92	0.03	0.11	1.00	0.04	0.12

Table D.1 continued.

Sample Name	Nuclide	Age (LSDn) (Ma)	Internal error (LSDn) (Ma)	External error (LSDn) (Ma)	Age (St) (Ma)	Internal error (St) (Ma)	External error (St) (Ma)
16-ROB-084-WIN	^{3}He	0.77	0.02	0.09	0.83	0.03	0.10
16-ROB-084-WIN	^{3}He	0.78	0.03	0.09	0.85	0.03	0.10
16-ROB-085-WIN	^{3}He	0.98	0.03	0.11	1.06	0.03	0.12
16-ROB-086-WIN	^{10}Be	0.38	0.01	0.03	0.42	0.01	0.04
WAL Moraine							
16-ROB-104-WAL	^{3}He	1.95	0.06	0.22	2.13	0.06	0.24
16-ROB-104-WAL	^{3}He	1.92	0.06	0.22	2.10	0.06	0.24
16-ROB-105-WAL	^{3}He	2.30	0.07	0.26	2.52	0.07	0.29
16-ROB-106-WAL	^{3}He	2.76	0.08	0.31	3.02	0.09	0.34
16-ROB-106-WAL	^{3}He	2.72	0.10	0.31	2.98	0.11	0.34
16-ROB-107-WAL	^{3}He	1.56	0.04	0.18	1.70	0.05	0.19
16-ROB-108-WAL	^{3}He	2.30	0.06	0.26	2.52	0.07	0.29
16-ROB-109-WAL	^{3}He	1.51	0.04	0.17	1.65	0.05	0.19
16-ROB-110-WAL	^{3}He	1.80	0.05	0.20	1.97	0.05	0.22
16-ROB-110-WAL	^{3}He	1.79	0.07	0.21	1.96	0.07	0.23
BGE Moraine							
16-ROB-111-BGE	^{3}He	1.72	0.05	0.19	1.88	0.05	0.21
16-ROB-111-BGE	^{3}He	1.73	0.06	0.20	1.90	0.07	0.22
16-ROB-112-BGE	^{3}He	1.43	0.04	0.16	1.56	0.05	0.18
16-ROB-112-BGE	^{3}He	1.32	0.05	0.15	1.44	0.05	0.17
16-ROB-113-BGE	^{3}He	2.85	0.09	0.33	3.12	0.10	0.36
16-ROB-114-BGE	^{3}He	2.34	0.07	0.27	2.56	0.07	0.29
16-ROB-114-BGE	^{3}He	2.38	0.09	0.28	2.61	0.09	0.30
16-ROB-115-BGE	^{3}He	2.78	0.08	0.32	3.04	0.09	0.34
16-ROB-116-BGE	^{3}He	4.12	0.11	0.47	4.51	0.12	0.51
16-ROB-116-BGE	^{3}He	3.91	0.14	0.45	4.28	0.15	0.49
16-ROB-117-BGE	^{3}He	2.76	0.08	0.31	3.02	0.09	0.34
BBY Moraine							
16-ROB-118-BBY	^{3}He	2.62	0.08	0.30	2.86	0.09	0.33
16-ROB-119-BBY	^{3}He	1.65	0.05	0.19	1.80	0.05	0.21
16-ROB-120-BBY	^{3}He	1.61	0.05	0.18	1.76	0.05	0.20
16-ROB-121-BBY	^{3}He	1.52	0.05	0.17	1.66	0.05	0.19
16-ROB-121-BBY	^{3}He	1.51	0.04	0.17	1.65	0.05	0.19
16-ROB-122-BBY	^{3}He	2.27	0.07	0.26	2.49	0.08	0.28

APPENDIX E

MATLAB SCRIPT FOR DETERMINING BOULDER AGE AND UNCERTAINTY

For each sample for which multiple aliquots were measured, the age and internal uncertainty were calculated for each aliquot. The following script was then used to determine the most appropriate age and uncertainty for the sample as described in Chapter 2.4.

```
%this script performs a chi-squared test for multiple measurements of a
%single sample. If the measurements pass the chi-squared test, the true age
%is take as the EWM and the uncertainty as the standard error. If they do
%not pass, the mean and SD are used.

clear all; close all;

T =
readtable('Users/alexandrabalter/Documents/UMaine/Thesis/SQL_scripts_for_tabl
es/SQL_table_compilation.xlsx', 'Sheet', 'ages', "ReadRowNames", false);
T.Sample_ID = categorical(T.Sample_ID);
T.Site = categorical(T.Site);
T.Subsite = categorical(T.Subsite);
T.Nuclide = categorical(T.Nuclide);

%Separate into tables by nuclide

he3 = T(T.Nuclide=='He3', :);
ne21 = T(T.Nuclide == 'Ne21', :);
be10 = T(T.Nuclide == 'Be10', :);

%get mean age of each sample

mean_age_he3 = varfun(@mean, he3, 'GroupingVariables', 'Sample_ID',
'InputVariables', [5, 8]);
mean_age_ne21 = varfun(@mean, ne21, 'GroupingVariables', 'Sample_ID',
'InputVariables', [5, 8]);
mean_age_be10 = varfun(@mean, be10, 'GroupingVariables', 'Sample_ID',
'InputVariables', [5, 8]);

std_age_he3 = varfun(@std, he3, 'GroupingVariables', 'Sample_ID',
'InputVariables', [5, 8]);
    std_he3 = table(std_age_he3.std_LSD_age, std_age_he3.std_St_age);
    std_he3.Properties.VariableNames{'Var1'} = 'std_LSD';
    std_he3.Properties.VariableNames{'Var2'} = 'std_St';
std_age_ne21 = varfun(@std, ne21, 'GroupingVariables', 'Sample_ID',
'InputVariables', [5, 8]);
    std_ne21 = table(std_age_ne21.std_LSD_age, std_age_ne21.std_St_age);
    std_ne21.Properties.VariableNames{'Var1'} = 'std_LSD';
    std_ne21.Properties.VariableNames{'Var2'} = 'std_St';

sig_age_he3 = varfun(@mean, he3, 'GroupingVariables', 'Sample_ID',
'InputVariables', [6, 9]);
    sig_he3 = table(sig_age_he3.mean_LSD_Interr, sig_age_he3.mean_St_Interr);
```

```
    sig_he3.Properties.VariableNames{'Var1'} = 'sig_LSD';
    sig_he3.Properties.VariableNames{'Var2'} = 'sig_St';
sig_age_ne21 = varfun(@mean, ne21, 'GroupingVariables', 'Sample_ID',
'InputVariables', [6, 9]);
    sig_ne21 = table(sig_age_ne21.mean_LSD_Interr,
sig_age_ne21.mean_St_Interr);
    sig_ne21.Properties.VariableNames{'Var1'} = 'sig_LSD';
    sig_ne21.Properties.VariableNames{'Var2'} = 'sig_St';

%chi-squared test to see if measurements agree within error

%3he

he3_LSD = he3.LSD_age;
he3_St = he3.St_age;

 for a = 1:size(he3, 1)
     sID_he = he3.Sample_ID(a);
     herows_mean_LSD = mean_age_he3.Sample_ID == sID_he;
        hemean_age_LSD = table2array(mean_age_he3(herows_mean_LSD, 3));
     h_LSD{a, :} = ((he3_LSD(a) -
hemean_age_LSD).^2)./((he3.LSD_Interr(a)).^2);
 end

 for a = 1:size(he3, 1)
     sID_he = he3.Sample_ID(a);
     herows_mean_St = mean_age_he3.Sample_ID == sID_he;
        hemean_age_St = table2array(mean_age_he3(herows_mean_St, 4));
     h_St{a, :} = ((he3_St(a) - hemean_age_St).^2)./((he3.St_Interr(a)).^2);
 end

%ne21

ne21_LSD = ne21.LSD_age;
ne21_St = ne21.St_age;

 for b = 1:size(ne21, 1)
     sID_ne = ne21.Sample_ID(b);
     nerows_mean_LSD = mean_age_ne21.Sample_ID == sID_ne;
        nemean_age_LSD = table2array(mean_age_ne21(nerows_mean_LSD, 3));
     n_LSD{b, :} = ((ne21_LSD(b) -
nemean_age_LSD).^2)./((ne21.LSD_Interr(b)).^2);
 end

 for b = 1:size(ne21, 1)
     sID_ne = ne21.Sample_ID(b);
     nerows_mean_St = mean_age_ne21.Sample_ID == sID_ne;
        nemean_age_St = table2array(mean_age_ne21(nerows_mean_St, 4));
     n_St{b, :} = ((ne21_St(b) -
nemean_age_St).^2)./((ne21.St_Interr(b)).^2);
 end

%add parameters for calculating chi-squared to nuclide tables

h_LSD = array2table(h_LSD);
h_St = array2table(h_St);
```

```
n_LSD = array2table(n_LSD);
n_St = array2table(n_St);

he3 = [he3, h_LSD, h_St];
he3.h_LSD = cell2mat(he3.h_LSD);
he3.h_St = cell2mat(he3.h_St);

ne21 = [ne21, n_LSD, n_St];
ne21.n_LSD = cell2mat(ne21.n_LSD);
ne21.n_St = cell2mat(ne21.n_St);

%get chi-squared values

G1 = findgroups(he3.Sample_ID);
G2 = findgroups(ne21.Sample_ID);
func = @(x) sum(x);
he_chi_LSD = splitapply(func, he3.h_LSD, G1);
    he_chi_LSD = array2table(he_chi_LSD);
ne_chi_LSD = splitapply(func, ne21.n_LSD, G2);
    ne_chi_LSD = array2table(ne_chi_LSD);
he_chi_St = splitapply(func, he3.h_St, G1);
    he_chi_St = array2table(he_chi_St);
ne_chi_St = splitapply(func, ne21.n_St, G2);
    ne_chi_St = array2table(ne_chi_St);

he_stats = [mean_age_he3, he_chi_LSD, he_chi_St];
ne_stats = [mean_age_ne21, ne_chi_LSD, ne_chi_St];

he_dof = he_stats.GroupCount - 1;
    he_dof = array2table(he_dof);
ne_dof = ne_stats.GroupCount - 1;
    ne_dof = array2table(ne_dof);

he_stats = [he_stats, he_dof];
ne_stats = [ne_stats, ne_dof];


yn_he = [];
for g = 1:size(he_stats, 1)
if he_stats.he_dof(g) == 1
   yn_he(g, 1) = he_stats.he_chi_LSD(g) > 3.84;
elseif he_stats.he_dof(g) == 2
    yn_he(g,1) = he_stats.he_chi_LSD(g) > 5.99;
elseif he_stats.he_dof(g) == 3
    yn_he(g,1) = he_stats.he_chi_LSD(g) > 7.81;
else yn_he(g, 1) = 0;
end
end

yn_he = array2table(yn_he);

yn_ne = [];
for g = 1:size(ne_stats, 1)
if ne_stats.ne_dof(g) == 1
   yn_ne(g, 1) = ne_stats.ne_chi_LSD(g) > 3.84;
```

```
elseif ne_stats.ne_dof(g) == 2
    yn_ne(g,1) = ne_stats.ne_chi_LSD(g) > 5.99;
elseif ne_stats.ne_dof(g) == 3
    yn_ne(g,1) = ne_stats.ne_chi_LSD(g) > 7.81;
else yn_ne(g, 1) = 0;
end
end

yn_ne = array2table(yn_ne);

he_stats = [he_stats, std_he3, yn_he];
ne_stats = [ne_stats, std_ne21, yn_ne];


%get EWM for each sample

func2 = @(y, z) ewmean(y, z);

he_ewm_LSD = splitapply(func2, he3.LSD_age, he3.LSD_Interr, G1);
    he_ewm_LSD = array2table(he_ewm_LSD);
he_ewm_St = splitapply(func2, he3.St_age, he3.St_Interr, G1);
    he_ewm_St = array2table(he_ewm_St);

ne_ewm_LSD = splitapply(func2,ne21.LSD_age, ne21.LSD_Interr, G2);
    ne_ewm_LSD = array2table(ne_ewm_LSD);
ne_ewm_St = splitapply(func2, ne21.St_age, ne21.St_Interr, G2);
    ne_ewm_St = array2table(ne_ewm_St);

he_stats = [he_stats, he_ewm_LSD, he_ewm_St];
ne_stats = [ne_stats, ne_ewm_LSD, ne_ewm_St];

%get standard error for each sample

se_he_LSD = he_stats.std_LSD ./ sqrt(he_stats.GroupCount);
se_he_St = he_stats.std_St ./ sqrt(he_stats.GroupCount);
se_ne_LSD = ne_stats.std_LSD ./ sqrt(ne_stats.GroupCount);
se_ne_St = ne_stats.std_St ./ sqrt(ne_stats.GroupCount);

se_he_LSD = array2table(se_he_LSD);
se_he_St = array2table(se_he_St);
se_ne_LSD = array2table(se_ne_LSD);
se_ne_St = array2table(se_ne_St);

%make one large stats table

he_stats = [he_stats, se_he_LSD, se_he_St, sig_he3];
ne_stats = [ne_stats, se_ne_LSD, se_ne_St, sig_ne21];

%if n = 1, sample age and uncertainty = measurements; if n>1, and pass
%chi-squared (0), then age = EWM and error = SE; if n> and fail chi-squared
%(1), age = mean? and error = SD.

he_age_LSD = [];
he_sig_LSD = [];
he_age_St = [];
```

```
he_sig_St = [];

ne_age_LSD = [];
ne_sig_LSD = [];
ne_age_St = [];
ne_sig_St = [];

for c = 1:size(he_stats, 1)
    if he_stats.GroupCount(c) == 1
       he_age_LSD(c,1) = he_stats.mean_LSD_age(c);
       he_sig_LSD(c,1) = he_stats.sig_LSD(c);
       he_age_St(c,1) = he_stats.mean_St_age(c);
       he_sig_St(c,1) = he_stats.sig_St(c);

    elseif he_stats.GroupCount(c) > 1 & he_stats.yn_he(c) == 0
        he_age_LSD(c,1) = he_stats.he_ewm_LSD(c);
        he_sig_LSD(c,1) = he_stats.se_he_LSD(c);
        he_age_St(c,1) = he_stats.he_ewm_St(c);
        he_sig_St(c,1) = he_stats.se_he_St(c);

    elseif he_stats.GroupCount(c) > 1 & he_stats.yn_he(c) == 1
       he_age_LSD(c,1) = he_stats.mean_LSD_age(c);
       he_sig_LSD(c,1) = he_stats.std_LSD(c);
       he_age_St(c,1) = he_stats.mean_St_age(c);
       he_sig_St(c,1) = he_stats.std_St(c);
    end
end

for d = 1:size(ne_stats, 1)
    if ne_stats.GroupCount(d) == 1
       ne_age_LSD(d,1) = ne_stats.mean_LSD_age(d);
       ne_sig_LSD(d,1) = ne_stats.sig_LSD(d);
       ne_age_St(d,1) = ne_stats.mean_St_age(d);
       ne_sig_St(d,1) = ne_stats.sig_St(d);

    elseif ne_stats.GroupCount(d) > 1 & ne_stats.yn_ne(d) == 0
       ne_age_LSD(d,1) = ne_stats.ne_ewm_LSD(d);
       ne_sig_LSD(d,1) = ne_stats.se_ne_LSD(d);
       ne_age_St(d,1) = ne_stats.ne_ewm_St(d);
       ne_sig_St(d,1) = ne_stats.se_ne_St(d);

    elseif ne_stats.GroupCount(d) > 1 & ne_stats.yn_ne(d) == 1
       ne_age_LSD(d,1) = ne_stats.mean_LSD_age(d);
       ne_sig_LSD(d,1) = ne_stats.std_LSD(d);
       ne_age_St(d,1) = ne_stats.mean_St_age(d);
       ne_sig_St(d,1) = ne_stats.std_St(d);
    end
end

he_age_LSD = array2table(he_age_LSD);
he_sig_LSD = array2table(he_sig_LSD);
he_age_St = array2table(he_age_St);
he_sig_St = array2table(he_sig_St);

ne_age_LSD = array2table(ne_age_LSD);
ne_sig_LSD = array2table(ne_sig_LSD);
```

```
ne_age_St = array2table(ne_age_St);
ne_sig_St = array2table(ne_sig_St);

%get sample info from other tables.
he_info = he3(:, 1:4);
ne_info = ne21(:, 1:4);

he_info.Sample_ID = char(he_info.Sample_ID);
ne_info.Sample_ID = char(ne_info.Sample_ID);

he_info = unique(he_info);
ne_info = unique(ne_info);

he_info.Sample_ID = categorical(cellstr(he_info.Sample_ID));
ne_info.Sample_ID = categorical(cellstr(ne_info.Sample_ID));

%combine all he and ne info

he3_all = [he_info, he_age_LSD, he_sig_LSD, he_age_St, he_sig_St];
    he3_all.Properties.VariableNames{'he_age_LSD'} = 'LSD_age';
    he3_all.Properties.VariableNames{'he_sig_LSD'} = 'LSD_Interr';
    he3_all.Properties.VariableNames{'he_age_St'} = 'St_age';
    he3_all.Properties.VariableNames{'he_sig_St'} = 'St_Interr';
ne21_all = [ne_info, ne_age_LSD, ne_sig_LSD, ne_age_St, ne_sig_St];
    ne21_all.Properties.VariableNames{'ne_age_LSD'} = 'LSD_age';
    ne21_all.Properties.VariableNames{'ne_sig_LSD'} = 'LSD_Interr';
    ne21_all.Properties.VariableNames{'ne_age_St'} = 'St_age';
    ne21_all.Properties.VariableNames{'ne_sig_St'} = 'St_Interr';
be10_all = [be10(:, 1:6), be10(:, 8:9)];

tt = [he3_all; ne21_all; be10_all];

tt2 = table2array(tt(:, 5:8));

for s = 1:size(tt2, 1)
    if (tt2(s,2) ./ tt2(s,1)).*100 <2
        tt2(s,2) = tt2(s,1).*0.02;
    else tt2(s, 2) = tt2(s, 2);
    end

    if (tt2(s, 4) ./ tt2(s, 3)).*100 <2
        tt2(s, 4) = tt2(s, 3).*0.02;
    else tt2(s, 4) = tt2(s, 4);
    end
end

tt2 = array2table(tt2);
    tt2.Properties.VariableNames{'tt21'} = 'LSD_age';
    tt2.Properties.VariableNames{'tt22'} = 'LSD_Interr';
    tt2.Properties.VariableNames{'tt23'} = 'St_age';
    tt2.Properties.VariableNames{'tt24'} ='St_Interr';
tt = [tt(:, 1:4), tt2(:, 1:4)];
filename =
'/Users/alexandrabalter/Documents/UMaine/Thesis/Results/avg_aliquot_data_2504
18.xlsx';
writetable(tt, filename)
```

APPENDIX F

MATLAB SCRIPTS FOR DETERMINING OUTLIERS

F.1 Nostrat function

```
%given a cosmogenic sampling dataset, this script eliminates outliers
%assuming that no boulder on a given moraine can be older (younger) than
%the oldest (youngest) boulder on the next oldest (youngest) moraine.

function [out] = nostrat_agro(excel, sheet, subsite, sites)

%load data

T_noelim = readtable(excel, 'Sheet', sheet, 'ReadRowNames', false);

%eliminate outliers based on stratigraphic relationship.

%first, isolate subsite in table, then sort based on values of moraine to
%get in stratigraphic order.

%set parameter for including/not including RINGLEADER

if any(strcmp(sites, 'RINGLEADER'))
    toggle_top = 1;
else toggle_top = 0;
end

if toggle_top == 1
    rows_noelim = strcmp(T_noelim.Subsite, subsite) |
strcmp(T_noelim.Subsite, 'top');
else rows_noelim = strcmp(T_noelim.Subsite, subsite);
end
    noelim2 = T_noelim(rows_noelim, :);
    noelim2.Site = categorical(noelim2.Site, sites, 'Ordinal', true);
    noelim2 = sortrows(noelim2, 'Site');

%now, eliminate based on stratigraphic order.

minima = varfun(@min, noelim2, 'InputVariables', 'LSD_min',
'GroupingVariables', 'Site');
    minima_A = table2array(minima(:,3));
maxima = varfun(@max, noelim2, 'InputVariables', 'LSD_max',
'GroupingVariables', 'Site');
    maxima_A = table2array(maxima(:,3));

elimstrat = noelim2;
table2cell(elimstrat);


for a = 1:length(sites)
    for c = 1:size(elimstrat, 1)
            if a == 1
                if elimstrat.Site(c) == sites{a}
```

```
                    if elimstrat.LSD_min(c)>maxima_A(a+1, :)
                        elimstrat(c, 13) = {'0'};
                    else elimstrat(c, 13) = {'1'};
                    end
                end


            elseif a > 1 & a < length(sites)
                if elimstrat.Site(c) == sites{a}
                    if elimstrat.LSD_min(c)>maxima_A(a+1, :);
                        elimstrat(c, 13) = {'0'};
                    elseif elimstrat.LSD_max(c)<minima_A(a-1, :);
                        elimstrat(c, 13) = {'0'};
                    else elimstrat(c, 13) = {'1'};
                end
                end


            elseif a == length(sites)
                if elimstrat.Site(c) == sites{a}
                    if elimstrat.LSD_max(c)<minima_A(a-1, :)
                        elimstrat(c, 13) =  {'0'};
                    else elimstrat(c, 13) = {'1'};
                    end
                end
            end
        end
    end;


elimstrat2 = elimstrat;
      elimstrat2.Var13 = categorical(elimstrat2.Var13);
      elimstrat2(elimstrat2.Var13=='0', :) = [];
           minimaB = varfun(@min, elimstrat2, 'InputVariables', 'LSD_min',
'GroupingVariables', 'Site');
                minima_B = table2array(minimaB(:,3));
           maximaB = varfun(@max, elimstrat2, 'InputVariables', 'LSD_max',
'GroupingVariables', 'Site');
                maxima_B = table2array(maximaB(:,3));

for a = 1:length(sites)
    for c = 1:size(elimstrat, 1)
        if a == 1
            if elimstrat.Site(c) == sites{a}
                if elimstrat.LSD_min(c)>maxima_B(a+1, :)
                    elimstrat(c, 13) = {'0'};
                else elimstrat(c, 13) = {'1'};
                end
            end
        end

        if a > 1 & a < length(sites)
            if elimstrat.Site(c) == sites{a}
                if elimstrat.LSD_min(c)>maxima_B(a+1, :)
                    elimstrat(c, 13) = {'0'};
                elseif elimstrat.LSD_max(c)<minima_B(a-1, :)
                   elimstrat(c, 13) = {'0'};
```

```
                else elimstrat(c, 13) = {'1'};
                end
            end
        end

        if a == length(sites)
            if elimstrat.Site(c) == sites{a}
                if elimstrat.LSD_max(c)<minima_B(a-1, :)
                    elimstrat(c, 13) =  {'0'};
                else elimstrat(c, 13) = {'1'};
                end
            end
        end
    end
end;

out = elimstrat;
```

F.2 Script to eliminate outliers

```
%given a cosmogenic sampling dataset, this script eliminates outliers
%assuming that no boulder on a given moraine can be older (younger) than
%the oldest (youngest) boulder on the next oldest (youngest) moraine.

clear all;
close all;

%define moraines in each site. for this script (unlike others), RINGLEADER is
only included
%in lowrobN.

upperROB = {'MUSIK', 'NACHT', 'KLEINE', 'EINE', 'ROBARM'};
lowrobN = {'NOLO', 'ANDREW', 'POS', 'WBKSSU', 'HUNKY','BANANA','RINGLEADER'};
lowrobS = {'EMINEM', 'MONET', 'WINTERFELL','BGEWALBBY', 'RINGLEADER'};
misery = {'MISERYC', 'MISERYB', 'MISERYA', 'MISERYD', 'ROBSCOL'};
otway = {'MOGUL', 'DUTCH', 'JOSHUA', 'MONTANA', 'CHARLIE', 'OTWEBAS'};

%load raw data

excel =
'/Users/alexandrabalter/Documents/UMaine/Thesis/Results/avg_aliquot_data_2604
18.xlsx';
sheet = 'Sheet1';

%NEED TO ENTER INFO HERE! LOW ROB S

subsite_lowrobS = {'lowrobS'}; %define sub-site of interest
sites_lowrobS = lowrobS;       %re-enter subsite of interest (this will
assign moraines to the sub-site)
%run nostrat function
lowrobS_elim = nostrat_agro(excel, sheet, subsite_lowrobS, sites_lowrobS);
lowrobS_elim.Site = categorical(lowrobS_elim.Site, 'Ordinal', false);
rows_remove = lowrobS_elim.Site == 'RINGLEADER';
lowrobS_elim(rows_remove, :) = [];
```

```
%NEED TO ENTER INFO HERE! LOW ROB N

subsite_lowrobN = {'lowrobN'}; %define sub-site of interest
sites_lowrobN = lowrobN;       %re-enter subsite of interest (this will
assign moraines to the sub-site)
%run nostrat function
lowrobN_elim = nostrat_agro(excel, sheet, subsite_lowrobN, sites_lowrobN);
lowrobN_elim.Site = categorical(lowrobN_elim.Site, 'Ordinal', false);

%NEED TO ENTER INFO HERE! UPPER ROB

subsite_upperROB = {'upperROB'}; %define sub-site of interest
sites_upperROB = upperROB;       %re-enter subsite of interest (this will
assign moraines to the sub-site)
%run nostrat function
upperROB_elim = nostrat_agro(excel, sheet, subsite_upperROB, sites_upperROB);
upperROB_elim.Site = categorical(upperROB_elim.Site, 'Ordinal', false);

%NEED TO ENTER INFO HERE! OTWAY

subsite_otway = {'otway'}; %define sub-site of interest
sites_otway = otway;       %re-enter subsite of interest (this will assign
moraines to the sub-site)
%run nostrat function
otway_elim = nostrat_agro(excel, sheet, subsite_otway, sites_otway);
otway_elim.Site = categorical(otway_elim.Site, 'Ordinal', false);

%NEED TO ENTER INFO HERE! MISERY

subsite_misery = {'misery'}; %define sub-site of interest
sites_misery = misery;       %re-enter subsite of interest (this will assign
moraines to the sub-site)
%run nostrat function
misery_elim = nostrat_agro(excel, sheet, subsite_misery, sites_misery);
misery_elim.Site = categorical(misery_elim.Site, 'Ordinal', false);

all_nostrat = [lowrobS_elim; lowrobN_elim; upperROB_elim; otway_elim;
misery_elim];
all_nostrat.Properties.VariableNames([13]) = {'nostrat'};

%if want to keep all misery samples, uncomment the following:
%for d = 1:size(all_nostrat, 1)
    %if strcmp(all_nostrat.Subsite(d), 'misery');
       %all_nostrat{d,13} = {'1'};
    %end
%end

filename =
'/Users/alexandrabalter/Documents/UMaine/Thesis/Results/eliminate_outliers/wi
th_MATLAB/nostrat_agro_all_020518.xlsx';
writetable(all_nostrat, filename)
```

APPENDIX G

MATLAB SCRIPT FOR GENERATING BOXPLOTS

```
%this script creates boxplots for each subsite

clear all;

%define moraines in each site

upperROB = {'MUSIK', 'NACHT', 'KLEINE', 'EINE', 'ROBARM'};
lowrobN = {'NOLO', 'ANDREW', 'POS', 'WINDBREAK', 'SUNNYSIDE',
'HUNKY','BANANA','RINGLEADER'};
lowrobS = {'EMINEM', 'MONET', 'WINTERFELL','ROBWALL', 'BARRAGE', 'ROBBABY',
'RINGLEADER'};
misery = {'MISERYC', 'MISERYB', 'MISERYA', 'MISERYD', 'ROBSCOL'};
otway = {'MOGUL', 'DUTCH', 'JOSHUA', 'MONTANA', 'CHARLIE', 'OTWEBAS'};

%load outlier-eliminated data

T_nostrat_agro_old =
readtable('/Users/alexandrabalter/Documents/UMaine/Thesis/Results/eliminate_o
utliers/with_MATLAB/nostrat_agro_all_250418_2.xlsx', 'Sheet', 'Sheet1',
'ReadRowNames', false);

%%NEED TO DO STUFF HERE

subsite = {'lowrobS'}; %define subsite. make sure use the same case/name as
the sites defined
                       %above (i.e. misery, lowrobS). Make sure to put
between ''.

sites  = lowrobS;      %give the name "sites" to table of whatever subsite we
are using.

%code is good to run, don't need to mess with anything below.

%select table rows from subsite
if any(strcmp(sites, 'RINGLEADER'))
    toggle_top = 1;
else toggle_top = 0;
end

    if toggle_top == 1
    rows_nostrat_agro_old = strcmp(T_nostrat_agro_old.Subsite, subsite) |
strcmp(T_nostrat_agro_old.Subsite, 'top');
else rows_nostrat_agro_old = strcmp(T_nostrat_agro_old.Subsite, subsite);
end
    T_nostrat2_agro_old_all = T_nostrat_agro_old(rows_nostrat_agro_old, :);
    T_nostrat2_agro_old = T_nostrat2_agro_old_all;
    T_nostrat2_agro_old.nostrat = categorical(T_nostrat2_agro_old.nostrat);
    T_nostrat2_agro_old(T_nostrat2_agro_old.nostrat=='0', :) = [];
    T_nostrat2_agro_old_all.Site = categorical(T_nostrat2_agro_old_all.Site);
    T_nostrat2_agro_old_all.Site = reordercats(T_nostrat2_agro_old_all.Site,
sites);
```

```
    T_nostrat2_agro_old_all.nostrat =
categorical(T_nostrat2_agro_old_all.nostrat);
    T_nostrat2_agro_old.Site = categorical(T_nostrat2_agro_old.Site);
    T_nostrat2_agro_old.Site = reordercats(T_nostrat2_agro_old.Site, sites);


%get stats for each method

S_nostrat_agro_old = grpstats(T_nostrat2_agro_old, 'Site', {'mean', 'std',
'min', 'max'}, 'DataVars', 'LSD_age');

%separate nuclides for scatter plots

T_nostrat2_agro_old_all.Nuclide =
categorical(T_nostrat2_agro_old_all.Nuclide);

he_rows = T_nostrat2_agro_old_all.Nuclide == 'He3';
    he = T_nostrat2_agro_old_all(he_rows, :);
be_rows = T_nostrat2_agro_old_all.Nuclide == 'Be10';
    be = T_nostrat2_agro_old_all(be_rows, :);
ne_rows = T_nostrat2_agro_old_all.Nuclide == 'Ne21';
    ne = T_nostrat2_agro_old_all(ne_rows, :);

%make boxplots for each method. Also include all data with eliminated
%outliers shown in unfilled circles and average

figure

yyaxis left
set(gca, 'ycolor', 'k')
g = boxplot(T_nostrat2_agro_old.LSD_age, T_nostrat2_agro_old.Site,
'Orientation', 'horizontal', 'GroupOrder', sites, 'Symbol', '', 'Colors',
'k');
title(sprintf('%s - NoStrat Agro', subsite{:}));
yyaxis right
set(gca, 'ycolor', 'k')
set(gca, 'YGrid', 'on', 'XGrid', 'off')
h = scatter(he.LSD_age(he.nostrat=='1'), he.Site(he.nostrat=='1'), 80, 'k',
'o', 'filled', 'MarkerFaceAlpha', 0.55);
hold on
i = scatter(be.LSD_age(be.nostrat=='1'), be.Site(be.nostrat=='1'), 80, 'r',
'o', 'filled', 'MarkerFaceAlpha', 0.55);
hold on
j = scatter(ne.LSD_age(ne.nostrat=='1'), ne.Site(ne.nostrat=='1'), 80, 'b',
'o', 'filled', 'MarkerFaceAlpha', 0.55);


hold on
k = scatter(he.LSD_age(he.nostrat=='0'), he.Site(he.nostrat=='0'), 80, 'k',
'o', 'MarkerEdgeAlpha', 0.55);
hold on
l = scatter(be.LSD_age(be.nostrat=='0'), be.Site(be.nostrat=='0'), 80, 'r',
'o', 'MarkerEdgeAlpha', 0.55);
hold on
m = scatter(ne.LSD_age(ne.nostrat=='0'), ne.Site(ne.nostrat=='0'), 80, 'b',
'o', 'MarkerEdgeAlpha', 0.55);
```

```
xlim([000000 5000000]);
set(gca, 'YTickLabel', []);
legend('off');
set(findobj(gcf,'LineStyle','--'),'LineStyle','-')
hold on
s = scatter(S_nostrat_agro_old.mean_LSD_age, S_nostrat_agro_old.Site,150,
'd', 'filled', 'm', 'MarkerFaceAlpha', 0.55, 'MarkerEdgeColor', 'k');
```

APPENDIX H

MATLAB SCRIPT FOR BOULDER AGE RESAMPLING

```
%this script resamples a given moraine with seven sampled boulders for all
combinations of 6 (5,4,3) boulders, and a histogram of mean ages is
generated.

clear all
close all

%first, get data from excel in table T

T =
readtable('/Users/alexandrabalter/Documents/UMaine/Thesis/Results/avg_aliquot
_data_200418.xlsx', 'ReadRowNames', false);

site = {'RINGLEADER'}; %enter moraine name you wish to run the script for


%get all combinations of 6 (5,4,3) boulders from each moraine. Plot
%histograms of average age to see how much the average can shift.
thissite = T(strcmp(T.Site, site),:);
    getnumber = size(thissite,1);
    v = table2array(thissite(:,7));
    avg_start = mean(v);
    if (getnumber-1) >= 3
     comb = nchoosek(v, (getnumber-1));
     avg_run = mean(comb, 2);
     stdev_run = std(comb, 0, 2);
    end


    if (getnumber-2) >= 3
     comb2 = nchoosek(v, (getnumber-2));
     avg_run2 = mean(comb2, 2);
     stdev_run2 = std(comb2, 0, 2);
    end


    if (getnumber-3) >= 3
     comb3 = nchoosek(v, (getnumber-3));
     avg_run3 = mean(comb3, 2);
     stdev_run3 = std(comb3, 0, 2);
    end


    if (getnumber-4) >= 3
     comb4 = nchoosek(v, (getnumber-4));
     avg_run4 = mean(comb4, 2);
     stdev_run4 = std(comb4, 0, 2);
    end

figure
```

```
ax.xLim = [-inf,inf];
title('noelim')

ax1 = subplot(4, 1, 1);
histogram(avg_run)
hold on
scatter(avg_start, 2)

ax2 = subplot(4, 1, 2);

histogram(avg_run2)

ax3 = subplot(4, 1, 3);
histogram(avg_run3)

ax4 = subplot(4, 1, 4);
histogram(avg_run4)

linkaxes([ax1, ax2, ax3, ax4], 'x');
```

BIOGRAPHY OF THE AUTHOR

Allie Balter was born in Houston, Texas, and grew up in Wayland, Massachusetts. She graduated from the Dana Hall School in Wellesley, Massachusetts, in 2010. Allie attended Bates College in Lewiston, Maine, where she received a B.S. in Geology. After Bates, Allie taught math and wilderness travel at the High Mountain Institute in Leadville, Colorado. She then worked as an Assistant Geologist for the environmental consulting firm WESTON Solutions, Inc. Allie entered the University of Maine in August 2016. She is a candidate for the Master of Science degree in Earth and Climate Sciences from The University of Maine in August 2018.